

Dresden Integrated Center for Applied Physics and Photonic
Materials
Technische Universität Dresden

Influence of processing conditions on morphology and performance of vacuum deposited organic solar cells

Dissertation
zur Erlangung des akademischen Grades
Doctor rerum naturalium
(Dr. rer. nat.) vorgelegt von

Felix Holzmüller
geboren am 17.10.1986 in Pirna

Dresden 2016

Eingereicht am 24.11.2016

Verteidigt am 30.03.2017

1. Gutachter: Prof. Dr. Karl Leo
2. Gutachter: Prof. Dr. Carsten Deibel

Abstract

This thesis discusses vacuum deposited organic solar cells. It focuses on the investigation of new donor molecules blended with the standard electron acceptor C_{60} . These donor-acceptor heterojunctions form the photoactive system of organic solar cells. In addition, the influence of the processing conditions on the morphology of the blend layers is investigated, as the morphology is crucial for an efficient generation of free charge carriers upon photon absorption.

Bulk heterojunction solar cells with the donor DTDCTB are deposited at different substrate temperatures. We identify three substrate temperature regimes, discriminated by the behavior of the fill factor (FF) as a function of the blend layer thickness. Devices deposited at RT have a maximum FF between 50 and 70 nm blend thickness, while devices deposited at 110 °C have a monotonically decreasing FF . At $T_{\text{sub}}=85$ °C, the devices have an S-kinked current-voltage curve. Grazing incidence wide angle X-ray scattering measurements show that this peculiar behavior of the FF is not correlated with a change in the crystallinity of the DTDCTB, which stays amorphous. Absorption measurements show that the average alignment of the molecules inside the blend also remains unchanged. Charge extraction measurements (OTRACE) reveal a mobility for the 110 °C device that is an order of magnitude higher than for the RT device. The difference in mobility can be explained by a higher trap density for the RT samples as measured by impedance spectroscopy. Despite slightly higher carrier lifetimes for the RT device obtained by transient photovoltage measurements, its mobility-lifetime product is still lower than for the 110 °C devices.

Based on DTDCTB, three new donor materials are designed to have a higher thermal stability in order to achieve higher yields upon material purification using gradient sublimation. For PRTF, the thermal stability is increased demonstrated by a higher yield upon sublimation. However, all new materials have a reduced absorption as compared to DTDCTB, which limits the short current density, and the FF is more sensitive to an increase of the blend layer thickness. The highest power conversion efficiency is achieved for a PRTF: C_{60} solar cell with 3.8%. Interestingly, PRTF: C_{60} solar cells show exceptionally low nonradiative voltage losses of only 0.26 V.

Another absorber molecule is the push-pull chromophore QM1. Scanning electron microscope (SEM) measurements show a growth of the molecule in nanowires on several substrates. The nanowires have lengths up to several micrometers and are several tens of nanometers wide. The formation of the nanowires is accompanied by a strong blue shift (650 meV) of the thin film absorption spectrum in comparison to the absorption in solution, which is attributed to H-aggregation of the molecules. Furthermore, the thin film absorption onset reaches up to 1100 nm, making the material a suitable candidate for a near infrared absorber in organic solar cells. For a solar cell in combination with C_{60} , a power conversion

Abstract

efficiency of 1.9% was achieved with an external quantum efficiency of over 19% for the spectral range between 600 and 1000 nm.

The method of “co-evaporant induced crystallization” as a means to increase the crystallinity of blend layers without increasing the substrate temperature during the deposition is investigated. Mass spectrometry (LDI-ToF-MS) measurements show that polydimethylsiloxane (PDMS), which is used as a co-evaporant, decomposes during the evaporation and only lighter oligomers evaporate. Quartz crystal microbalance (QCM) measurements prove that the detection of PDMS saturates at higher amounts of evaporated material. LDI-ToF-MS measurements show further that the determination of the volatilization temperature by QCM measurements is highly error prone. The method was applied to zinc phthalocyanine (ZnPc):C₆₀ solar cells, accepting the insertion of PDMS into the blend layer. Diffraction (GIXRD) measurements show a large increase in crystallinity. ZnPc:C₆₀ solar cells produced by applying the method reveal a similar behavior as solar cells processed at a higher substrate temperature.

Kurzfassung

Diese Arbeit behandelt vakuumprozessierte, organische Solarzellen. Der Schwerpunkt liegt dabei auf neuen Donatormolekülen, welche in Mischschichten mit dem Standardakzeptor C₆₀ untersucht werden. Diese Donator-Akzeptor Heteroübergänge bilden das photoaktive System organischer Solarzellen. Weiterhin wird der Einfluss der Prozessierungsbedingungen auf die Morphologie dieser Mischschichten untersucht, da die Morphologie entscheidend für die Erzeugung freier Ladungsträger ist.

Bei der Herstellung von Solarzellen mit einem Volumenheteroübergang aus DTDCTB und C₆₀ werden verschiedene Substrattemperaturen (T_{sub}) verwendet. Wir ermitteln drei Temperaturbereiche, welche sich durch das Verhalten des Füllfaktors (FF) als Funktion der Mischschichtdicke unterscheiden. Solarzellen, welche bei Raumtemperatur hergestellt wurden, zeigen ein Maximum im Füllfaktor zwischen 50 und 70 nm Schichtdicke. Bei Solarzellen, welche bei 110 °C Substrattemperatur hergestellt wurden, fällt der FF monoton mit steigender Mischschichtdicke. Bei $T_{\text{sub}}=85$ °C haben die Solarzellen einen S-Knick in der Strom-Spannungs-Kennlinie. Weitwinkelröntgenstreuexperimente unter streifendem Einfall zeigen keine Änderung der Kristallinität der bei verschiedenen Substrattemperaturen hergestellten DTDCTB:C₆₀ Mischschichten, welche immer amorph sind. Absorptionmessungen beweisen, dass sich die durchschnittliche Ausrichtung der Moleküle in der Mischschicht ebenfalls nicht ändert. Aus Ladungsträgerextraktionsmessungen (OTRACE) erhält man eine um eine Größenordnung größere Beweglichkeit für die bei 110 °C hergestellten Solarzelle, verglichen zu den RT-Solarzellen. Der Unterschied in den Beweglichkeiten kann mit Impedanzspektroskopiemessungen erklärt werden, welche eine höhere Fallendichte bei den RT-Proben zeigen. Trotz geringfügig höherer Ladungsträgerlebensdauern für die RT-Proben, welche mittels Messung der Transienten der Photospannung ermittelt werden, ist das Beweglichkeits-Lebensdauer Produkt für die RT-Solarzellen geringer als für die Solarzellen, die bei 110 °C hergestellt wurden.

Basierend auf DTDCTB wurden drei neue Donatormoleküle entworfen, welche eine höhere Thermostabilität haben sollten, um höhere Ausbeuten bei der Aufreinigung der Materialien durch Gradientensublimation zu erreichen. Für PRTF konnte die erwartete Erhöhung der Ausbeute bei Gradientensublimation durch bessere thermische Stabilität erreicht werden. Die neuen Materialien haben alle einen geringeren Absorptionskoeffizienten als DTDCTB, was die Kurzschlussstromdichte in der Solarzelle reduziert. Weiterhin sinkt der Füllfaktor stärker bei Erhöhung der Schichtdicke des Volumenheteroübergangs als dies bei DTDCTB:C₆₀ Solarzellen beobachtet wurde. Der höchste Wirkungsgrad von 3,8% wurde für PRTF:C₆₀ Solarzellen erreicht. PRTF:C₆₀ Solarzellen zeigen außergewöhnlich geringe nicht-strahlende Spannungsverluste von 0,26 V.

Ein weiteres Absorbermolekül ist das Donator-Akzeptor Molekül QM1. Rasterelektronenmikroskop (SEM) Aufnahmen zeigen, dass die Moleküle beim Aufdampfen auf verschiedenen

Kurzfassung

Substraten Nanodrahtstrukturen bilden. Die Nanodrähte können bis zu mehreren Mikrometern lang sein und einige zehn Nanometer Durchmesser aufweisen. Die Bildung der Nanodrähte wird von einer starken Blauverschiebung (650 meV) der Dünnschichtabsorption im Vergleich zur Absorption in Lösung begleitet, welche auf H-Aggregation der Moleküle zurückzuführen ist. Da die Dünnschichtabsorption von NGX1 bis 1100 nm reicht, ist das Material auch ein geeigneter Kandidat für einen Nahinfrarotabsorber in organischen Solarzellen. In Verbindung mit C₆₀ als Akzeptor erreichen die Solarzellen Wirkungsgrade von 1,9% in Verbindung mit einer externen Quanteneffizienz von über 19% im Bereich von 600-1000 nm.

Abschließend wird die Methode der "durch Dampfzusätze induzierten Kristallisation" als Mittel zur Erhöhung der Kristallinität von Mischschichten ohne Erhöhung der Substrattemperatur während der Prozessierung untersucht. Massenspektrometriemessungen (LDI-ToF-MS) an aufgedampften Schichten zeigen, dass sich Polydimethylsiloxan (PDMS), welches als Dampfzusatz verwendet wurde, in leichtere Oligomere zersetzt. Messungen mit Quarzkristall-Mikrowaagen (QCM) belegen, dass die Detektion von PDMS für größere Mengen von verdampftem Material sättigt. Aus LDI-ToF-MS Messungen geht hervor, dass die Bestimmung der Volatilisierungstemperatur mit QCMs sehr fehleranfällig ist. Die Methode wurde auf Zink Phthalocyanin (ZnPc) :C₆₀ Solarzellen angewandt. Röntgendiffraktometrie-messungen unter streifendem Einfall zeigen einen starken Zuwachs an Kristallinität. Die so hergestellten Solarzellen, zeigen ein vergleichbares Verhalten zu Solarzellen, welche bei höheren Substrattemperaturen hergestellt wurden.

Publications

Articles

- J. Meiss, F. Holzmüller, R. Gresser, K. Leo, M. Riede, Near-infrared absorbing semi-transparent organic solar cells, *Applied Physical Letters*, 99, 193307 (2011)
- F. Holzmueller, L. Wilde, F. Wölzl, C. Körner, K. Vandewal, K. Leo, Co-evaporant induced crystallization of zinc phthalocyanine:C60 blends for solar cells, *Organic Electronics* 27, 133-136 (2015)
- T. Moench, P. Friederich, F. Holzmueller, B. Rutkowski, J. Benduhn, T. Strunk, C. Koerner, K. Vandewal, A. Czyska-Filemonowicz, W. Wenzel, K. Leo, Influence of Meso- and Nanoscale Structure on the Properties of Highly Efficient Small Molecule Solar Cells, *Advanced Energy Materials*, 6, 4 (2015)
- L. Fang, F. Holzmueller, T. Matulaitis, A. Baasner, C. Hauenstein, J. Benduhn, M. Schwarze, A. Petrich, F. Piersimoni, R. Scholz, O. Zeika, C. Koerner, D. Neher, K. Vandewal, K. Leo, Thermally Stable Fluorine-Containing Low-Energy-Gap Organic Dyes with Low Voltage Losses for Organic Solar Cells, *Synthetic Metals* 222, 232-239 (2016)
- F. Holzmüller, N. Gräßler, M. Sedighi, E. Müller, M. Knupfer, O. Zeika, K. Vandewal, C. Koerner, K. Leo, H-aggregated small molecular nanowires as near infrared absorbers in organic solar cells, *Organic Electronics* 17, 198-202 (2017)

Conference Contributions

- F. Holzmüller, J. J. Alex, J. Meiß, A. Petrich, C. Schuenemann, W. Tress, M. Hummert, K. Leo, M. Riede. Diindenoperylene derivatives as green donors for organic solar cells. DPG Frühjahrstagung, 13.03.-18.03.2011, Dresden (Poster)
- F. Holzmüller, L. Wilde, C. Körner, K. Leo. The influence of co-evaporated polydimethylsiloxane oil on small molecule bulk heterojunction solar cells. DPG Frühjahrstagung, 30.03. - 04.04.2014, Dresden (Poster)
- F. Holzmüller, L. Wilde, F. Wölzl, J. Jankowski, C. Körner, K. Leo. "Co-evaporant induced crystallization" applied to C60 single and blend layers using polysdimethylsiloxane. 10th International conference on Electroluminescence and Organic Optoelectronics, 31.08. - 03.09.2014, Köln (Vortrag)

Publications

- F. Holz Müller, L. Fang, C. Hauenstein, S. Ullbrich, D. Spoltore, O. Zeika, C. Koerner, K. Vandewal, K. Leo. Influence of substrate heating on a new benzothiadiazole derivative blended with C60 in organic solar cells. 8th International Symposium on Flexible Organic Electronics, 06.07. - 09.07.15, Thessaloniki (Griechenland) (Vortrag)
- F. Holz Müller, Co-evaporant induced crystallization of donor:acceptor blend layers in organic solar cells, OPKM Seminar Chemnitz, 21.10.15

Patents

- T. Matulaitis, L. Fang, O. Zeika, C. Körner, K. Leo, F. Holz Müller, K. Vandewal „Organische Donor-Akzeptor-Farbstoffe für die Verwendung in elektronischen und optoelektronischen Bauteilen“, application number: 10 2014 217 817.7, date of filing 05.09.2014

Contents

Abstract	iii
Kurzfassung	v
Publications	vii
1. Introduction	1
2. Theory	3
2.1. Organic molecules	3
2.2. Organic semiconductors	8
2.2.1. Thin film growth and morphology	8
2.2.2. Optical properties	10
2.2.3. Charge transport	15
2.3. Solar cells	20
2.3.1. General concepts	20
2.3.2. Organic solar cells	27
3. Experimental	35
3.1. Materials	35
3.1.1. Sublimation	39
3.2. Preparation methods	40
3.2.1. Sample design	40
3.2.2. Substrate cleaning	40
3.2.3. Vacuum deposition	41
3.2.4. Quartz crystal microbalances	44
3.3. Measurement setups	45
3.3.1. UPS	45
3.3.2. Mass spectrometry	46
3.3.3. UV/vis-spectrometer	47
3.3.4. AFM	47
3.3.5. X-ray measurements	48
3.3.6. SEM/TEM/ED	50
3.3.7. EQE measurement	50
3.3.8. Mismatch correction	52
3.3.9. Current-voltage measurement	52
3.3.10. V_0 measurement	54
3.3.11. Impedance Spectroscopy	55

Contents

3.3.12. OTRACE	56
3.3.13. Transient Photovoltage	57
3.3.14. V_{oc} - I_{sc} method	57
4. DTDCTB	61
4.1. Introduction	61
4.1.1. Previous work	61
4.2. Solar cells	65
4.2.1. Sublayer	69
4.3. Morphology	69
4.3.1. Absorption	70
4.4. Charge carrier mobility	72
4.5. Impedance spectroscopy	73
4.6. Lifetime and Recombination	75
4.7. Conclusion	77
5. Thermally stable benzothiadiazole compounds	81
5.1. Introduction	81
5.2. Thin film investigation	83
5.2.1. Morphology	84
5.2.2. Absorption	84
5.2.3. Energy levels	86
5.3. Solar cells	87
5.3.1. Initial characterization	87
5.3.2. Optimization of the solar cells	88
5.3.3. Comparison to DTDCTB	89
5.3.4. Voltage losses	91
5.4. Conclusion	94
6. QM1	95
6.1. Introduction	95
6.2. Preliminary experiments	96
6.2.1. Solution spectrum	96
6.2.2. Neat QM1 films	97
6.2.3. Blends with C_{60}	104
6.3. Solar cells	106
6.3.1. PHJ	107
6.3.2. BHJ	107
6.3.3. Aging	111
6.4. Conclusion	113
7. Investigations on co-evaporant induced crystallization	115
7.1. Introduction	115
7.1.1. Motivation	115

7.1.2. Preliminary work in literature	115
7.2. Analysis of PDMS	117
7.3. Detection of PDMS with QCMs and volatilization temperature	121
7.4. Morphology effects of PDMS co-evaporation with ZnPc:C ₆₀ blend layers . . .	125
7.5. Usage in organic solar cells	129
7.6. PDMS co-evaporation applied to DTDCTB and DCV ₂ -5T-Me(3,3) blends . .	132
7.7. Conclusion	132
8. Conclusion and Outlook	135
A. Appendix	139
A.1. DTDCTB	139
A.1.1. Sublayers	139
A.1.2. Solar cell set 2	139
A.1.3. IS on ITO blend Al devices	142
A.1.4. IS on complete solar cells	143
A.1.5. sensitive EQE	147
A.2. QM1	147
A.3. PDMS	148
B. Lists	151
Bibliography	161
C. Acknowledgements	179

1. Introduction

In recent years, an increasing number of devices using organic semiconductors entered the market. The most successful application so far are displays using organic light emitting diodes (OLEDs). Whereas large area displays, e.g. in OLED-TVs, are still rather expensive, smaller displays as in smartphones have become affordable for the average consumer. This work deals with the opposite application of organic semiconductors - solar cells. While organic solar cells are not as far in the commercialization phase as OLEDs, pioneering companies have started to produce organic solar cells on an industrial scale. Heliatek, founded in 2006 in Dresden, produces organic solar cells in a role-to-role process. Recently, the company has raised 80 million euros to further scale up the production to a web width of 1200 mm. The new production line will have the capability to produce one million square meter of organic solar cells per year.[1]

Photovoltaics, in general, allows the generation of energy without the emission of CO₂ or other greenhouse gases as a by-product. This is important as these gases are responsible for global warming. Organic photovoltaics (OPV), in particular, uses materials based on hydrocarbons for the generation of electrical energy. These materials offer the advantage of an extraordinarily high thin film absorption in the range of 10⁵ cm⁻¹. Based on this property, 100-200 nm thick layers are sufficient to absorb a considerable amount of the incoming sun light. The low thickness enables the production on flexible substrates, allowing the above mentioned role-to-role production. The devices can be processed from solution or thermally evaporated in vacuum. The involved temperatures are considerably lower than for the production of solar cells from inorganic semiconductors - for example silicon. Accordingly, energy payback times of only a few days are possible.[2] These reasons allow a potentially low-cost mass production.

Organic dyes have narrower absorption bands than inorganic semiconductors. At first glance, this is a drawback. However, it also offers new possibilities. The combination of absorber materials with different absorption spectra allows the production of solar cells in different colors and also semitransparent solar cells are possible. This opens new fields of application, e.g. the integration in buildings, cars, or bags. These alternative markets are necessary, as the power conversion efficiencies of organic solar cells are nowadays not competitive with inorganic solar cells. At the moment, the highest power conversion efficiency for organic solar cells is 13.2% in the laboratory.[3]

In contrast to inorganic semiconductors, the electron hole pairs or excitons in organic semiconductors are strongly bound and cannot be dissociated by thermal energy at room temperature. In order to dissociate the excitons, heterojunctions – a certain combination of organic semiconductors with differing energy levels are necessary. This meets another strength of organic photovoltaics: the multitude of possible organic compounds. Organic chemistry with its century-long history can provide millions of molecules. The crucial question is:

1. Introduction

How to find the suitable molecule (combination)? Molecular properties such as the energy levels or the geometry of the molecule can be calculated. In addition, the calculation of properties of molecular single crystals is possible. However, organic solar cells use amorphous or polycrystalline materials, often in blended layers. A forecast of e.g. optical or electrical properties via simulation of such complex layers from the structural formula of the molecule alone is not possible so far. Accordingly, newly synthesized molecules have to be tested and evaluated by experiment. In addition, the quantitative prediction of device properties based on values obtained by the characterization of single layers alone is rather an exception. Under these circumstances, the testing and optimization of new organic semiconductors in the solar cell happens in series of experiments guided by experience.

The properties of organic thin films are an interplay between the properties of the molecules and the arrangement of these molecules in the layer. The processing conditions during the layer deposition influence strongly the growth of the thin film. For this reason, the investigation of the morphology allows us to study the effect of the processing conditions on the electrical/optical properties of the layer and eventually the performance in a device. In this work, we test molecules for their suitability as absorber materials in organic solar cells and investigate the relationship between processing conditions and morphology. In short, the identification of suitable absorber molecules from the large variety provided by organic chemistry as well as their successful implementation in solar cells by carefully choosing the right processing conditions are among the top challenges of OPV research.

Chapter 2 provides an overview about the theoretical background of organic molecules and thin films as well as solar cells in general and organic solar cells in particular. Chapter 3 summarizes the materials, experimental infrastructure and techniques, and the evaluation methods used in this work. The investigations on the green absorber molecule DTDCTB are presented in chapter 4. The focus in this chapter lies on the investigation of the solar cell performance as a function of bulk heterojunction thickness and substrate temperature during the deposition. In addition, derivatives of DTDCTB are investigated in chapter 5. These absorber molecules have a higher thermostability than DTDCTB, resulting in higher yields during the sublimation of the materials. Though not reaching the power conversion efficiency of the original material, the voltage losses could be significantly reduced. The near infrared absorber QM1 is presented in chapter 6. QM1, a known molecule from literature, is applied as an absorber in organic solar cells. With an EQE of 19% at 1000 nm, this NIR absorber covers a significant part of the NIR spectrum, which is often unused by other organic solar cells. The absorption in the near infrared is related to the aggregation of the QM1 molecules in nanowires. Chapter 7 presents the investigations on a new processing method called "co-evaporant induced crystallization". This method promotes a crystallization of the materials in the blend, providing an opportunity to adjust the phase separation in the blend, which is a critical parameter for bulk heterojunction solar cells. The results are summarized in the last chapter, providing a conclusion and outlook.

2. Theory

The following chapter provides an overview about the theoretical basics of organic photovoltaics. Organic semiconductors appear in two forms – small molecules and polymers, which differ in molecular weight. As this work deals with small molecules, the text will focus on this topic, too. However, polymers are widely used in organic photovoltaics as they can be easily processed from solution. The theory chapter is divided into three sections: organic molecules, organic semiconductors, and photovoltaics. The first part introduces the reader to the concepts of hybrid orbitals, intramolecular bonding, and properties of π -systems. The second part explains characteristic properties of organic semiconductors: thin film growth mechanisms, optical properties with a focus on excitons, and the properties of charge transport. Eventually, physical principles of photovoltaics in general and organic photovoltaics in particular are presented, including key concepts such as quasi-Fermi levels and general limitations to power conversion efficiency. The heterojunction concept is outlined along with the assumed mechanism of charge separation as well as the p - i - n concept.

2.1. Organic molecules

The term “organic” defines carbon-based compounds, with the exception of allotropes of carbon, oxides of carbon, carbonic acid, and carbonates.[4] The extraordinary diversity of carbon-based compounds in contrast to other elements mainly results from its electronic configuration ($1s^2 2s^2 2p^2$).

The different properties of carbon can be explained by the concept of hybrid orbitals, assuming a linear combination of atomic orbitals yielding molecular orbitals of equal energy. In case of carbon, the electrons of the $2s$ - and $2p$ -orbitals are involved in the formation of hybrid orbitals. They are formed in molecules, where the hybrid orbitals enable an energetically more favorable arrangement of the molecules than atomic orbitals. Three types of hybridization are possible: sp -, sp^2 - and sp^3 - hybridization. The superscript represents the number of p -orbitals involved in the hybridization. Each hybridization is characterized by a specific orbital symmetry, restraining the final molecular geometry. The sp^3 -hybridization results in a tetrahedral arrangement with four surrounding atoms, as for instance observed in methyl groups. If two carbon atoms of sp^3 -hybridization bind with each other, the created single or σ -bond will connect straightly the two centers. Rotations along the σ -bond are possible. The sp^2 -hybridization binds three atoms to the central carbon. These atoms are arranged in a plane with angles of 120° as shown in the sketch of benzene in Figure 2.1(a). The orientation of the remaining p -orbital, not affected by the hybridization, is orthogonal to this plane. If two adjacent carbon atoms of sp^2 - hybridization bind together, a double bond is formed. The double bond consists of a σ -bond and an additional π -bond that is formed

2. Theory

by the orthogonal p-orbitals. Therefore, rotations around the σ -bond are hindered. The arrangement of multiple carbon atoms in sp^2 -configuration allows the formation of unsaturated chains and ring structures, which are crucial for organic electronics. Hydrocarbons with at least one double (or triple bond) are called unsaturated. The sp -hybridization, which forms the triple bond, binds two atoms to the central carbon in a linear arrangement. In this case, the bonding consists of one σ - and two π -bonds. The second π -bond is perpendicular to the plane of the first π -bond. Ethyne or cyano groups are examples that both contain triple bonds with carbon.

The next paragraph describes the differences in the energy levels of molecular orbitals in comparison to atomic orbitals in the single atom. For that purpose, Figure 2.1(b) depicts the energy levels of a carbon atom in a benzene ring. On the left hand side, the two sp^2 -orbitals and the p_z -orbital are depicted. The third sp^2 -orbital that forms a bond with a hydrogen atom is omitted for clarity.

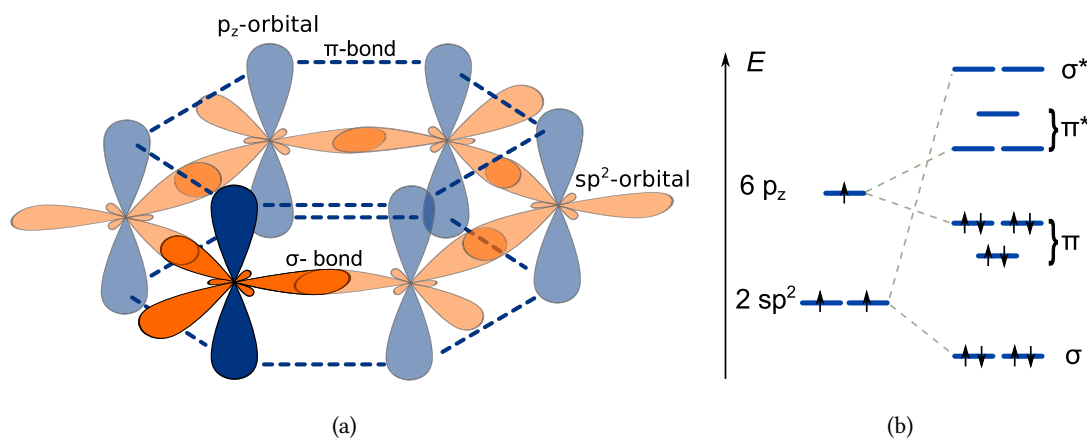


Figure 2.1.: (a) Sketch of the carbon atoms of benzene in sp^2 -configuration. The hydrogen atoms are omitted for clarity. (b) Sketch of selected energy levels of a carbon atom in a benzene molecule. The left side shows the (hybrid-) orbitals sp^2 and p_z of a single carbon atom. The right side shows the molecular orbitals σ , σ^* , π and π^* in benzene.

The right hand side depicts the energy levels in the molecule. There, the two sp^2 -orbitals form σ - and σ^* -orbitals due to the interaction with the sp^2 -orbitals of the neighboring carbon atoms. In contrast, the p_z -orbital interacts with the p_z -orbitals of all the other carbons in the benzene ring and three π - and π^* -orbitals are formed. Thereby, the total number of atomic orbitals equals the total number of molecular orbitals. σ - and π - orbitals are called bonding orbitals, because their energy is decreased with respect to the atomic orbitals. The population of these orbitals has, therefore, a binding character. Accordingly, σ^* - and π^* -orbitals are anti-bonding orbitals, their energy is increased in comparison to the atomic orbitals.

The increase in energy of the anti-bonding orbitals with respect to the atomic orbitals is always larger than the decrease in energy of the bonding orbitals with respect to the atomic orbitals.[5] Accordingly, a bond between the atoms forms when the number of the occupied bonding orbitals is higher than the number of the occupied anti-bonding orbitals. The strength of the energy splitting between bonding and anti-bonding orbitals is proportional to the overlap of the former atomic orbitals.[5]

The energy difference between σ - and σ^* -orbitals is more than 6 eV[6], since the symmetry of σ -bonds allows a large overlap of the connected orbitals and, therefore, a strong interaction. This energy corresponds to a photon wavelength lower than 200 nm, which is in the far ultraviolet region of the electromagnetic spectrum. Radiance with such energies is only a small part of the sun spectrum. However, it can degrade organic molecules in a solar cell, if they are not properly protected.[7, 8] The difference in energy between π - and π^* -orbitals is in the range between 1.5 eV and 6 eV.[6] This corresponds to wavelengths up to 800 nm, where the sun provides considerably higher photon fluxes. Lower transition energies are achieved by the interaction of multiple π -orbitals. This is possible since the parallel alignment of the former p_z - orbitals allows the formation of π -bonds with up to three neighboring orbitals. The electrons, occupying these orbitals, delocalize over the so-called conjugated π -system. The dashed lines in Figure 2.1(a) represent the π -system of benzene. It has a shape of two rings that extend to both face sides of the molecule. A larger π -system reduces the energy gap between the highest occupied molecular orbital (HOMO) and the lowest unoccupied molecular orbital (LUMO) and leads to a smaller energy gap. The standard example for this relationship is the change in the energy gap from benzene to pentacene.[9, 10] The molecular structures and their continuous increase of the lowest-energy optical absorption are shown in Figure 2.2. Benzene, with six π -electrons the smallest π -system, has the lowest-energy absorption at 254 nm, which corresponds to an optical gap of 4.9 eV. The lowest-energy absorption increases for anthracene with 14 π -electrons to 375 nm. The molecule with the largest π -system in this example is pentacene with 22 π -electrons. Its lowest-energy absorption is located at 582 nm, which corresponds to an optical gap of 2.1 eV.

Another possibility to alter the energy levels is the addition of heteroatoms or functional groups to the molecules. These can cause inductive or mesomeric effects. Often, a functional group imposes both effects, however one effect is usually more prominent than the other. The inductive effect is caused by a different electronegativity of the atoms bound to each other, hence leading to a polarization of the electron density between the two. Strongly electronegative atoms like fluorine or chlorine attract the electron density ($-I$ effect), causing a decrease in the energy levels of the molecular orbitals.[11] Schlettwein *et al.* performed gas phase ultraviolet photospectroscopy (UPS) measurements on zinc-phthalocyanine (ZnPc, $E_{\text{HOMO}}=5.3$ eV) and hexadecafluoro-zinc-phthalocyanine (F_{16}ZnPc , $E_{\text{HOMO}}=6.7$ eV) and found a reduction of the HOMO by 1.4 eV.[12] In contrast, the $+I$ effect increases the energy levels of the molecular orbitals. It can be caused by alkyl groups like methyl or ethyl. The inductive effect has a rather small range and takes only effect over a few bonding lengths.

2. Theory

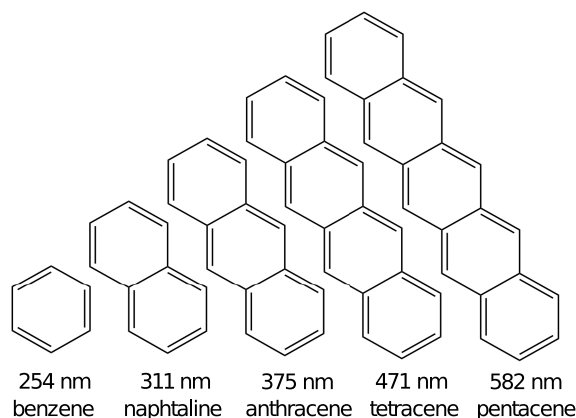


Figure 2.2.: Homologous series of benzene up to pentacene with their respective lowest-energy absorption in solution at room temperature. The values were taken from ref. [9].

The mesomeric effect is an interaction of a substitute with the π -system, in which the substitute pushes electron density into the π -system (+M effect) or pulls electron density out (-M effect). Accordingly, the energy levels shift to higher energies, respectively lower energies. The contributing structures of the molecule help to understand this effect. Figure 2.3 presents the contributing structures of benzonitrile. In this example, the nitrile group, which causes a -M effect, pulls electron density out of the aromatic system. The structures (i) - (v) show possible contributing structures. Neither one of the contributing structures alone correctly describes the molecule in a state, where it is possible to isolate. However, they contribute to the representation (vi), which should be understood in the following way: an increased electron density on the nitrogen of the nitrile group, and a slightly reduced π -electron density in the aromatic ring compared to the unsubstituted benzene, as indicated by the partial charges. This example also illustrates that the mesomeric effect, in contrast to the inductive effect, interacts with the complete aromatic system.

Common functional groups which cause an -M effect are the nitrile group, often used in form of a dicyanovinyl group (e.g. in DCV-nT[13], DTDCTB[14]) or keto groups (e.g. in NTCDA[15], Bis-FI-NTCDI[16]). The +M effect can be caused by amine groups or aryl groups (e.g. in DTDCTB[14], BF-DPB[17], BPAPF[18]), but also by halogene atoms (e.g. in F₆-TCNNQ[19], C₆₀F₃₆[20]). In the latter case, the inductive and mesomeric effect are present at the same time.[4] Molecules that contain functional groups causing a -M effect as well as functional groups causing a +M effect are called push-pull chromophores or D-A type molecules.¹[21, 22] The π -system between the functional groups is then called spacer. The mesomeric/inductive effects or the size of the π -system do not shift all energy levels in the same way. The magnitude of the shift depends on the electron density distribution for the specific orbital. For instance, Fitzner *et al.* reported this effect for the class of dicyanovinyl

¹The D stands for electron-donating functional group and the A for an electron-accepting functional group.

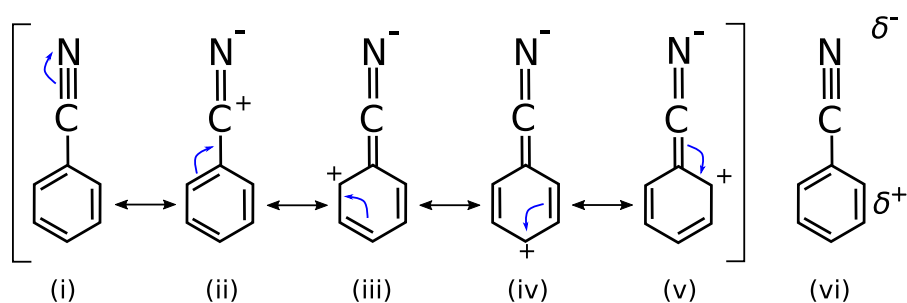


Figure 2.3.: $-M$ effect in benzonitrile in the concept of contributing structures. (i)-(v) represent the contributing structures of benzonitrile. + and - indicate positive and negative net charges. (i) The nitrogen atom of the nitrile group pulls a conjugated electron pair from the triple bond with the carbon atom and (ii) positive and negative net charges are created. (iii)-(v) Through switching of the conjugated electron pairs, also several positions of the positive net charge within the aromatic ring are possible. Structures (i)-(v) contribute to the overall distribution of the partial charges in benzonitrile (vi). δ^+ and δ^- symbolize the resulting positive and negative partial charges.

oligothiophenes, where the number of thiophenes was varied from one to six.[13] In this type of molecules, the electron density of the LUMO is increased on the terminal thiophenes and the two cyanovinyl groups, still otherwise equally distributed over the whole molecule. In contrast, the HOMO electron density is strongly located on the thiophene backbone. Henceforth, the energy gap between HOMO and LUMO decreases with increasing number of thiophenes, as discussed above. Due to the increased electron density on the thiophene backbone in the HOMO, it shifts by 1.07 eV, while the LUMO shifts only by 0.18 eV for an increase from two to six thiophene rings.[13] In contrast, an equal shift of HOMO and LUMO level was observed for the fluorination of ZnPc to F_{16} ZnPc or pentacene to perfluoropentacene.[12, 23] However, the quantitative effect of functional groups can only be calculated with DFT and quantum chemistry.

Finally, an important requirement for small molecules arising from processing conditions is discussed. For vacuum processing, the flyability (dispersibility) of a molecule is necessary. As a rule of thumb, a molecule should not be significantly heavier than 1500 g/mol. The p-dopant $C_{70}F_{56}$ represents an exception with a molecular mass of 1905 g/mol. Furthermore, the decomposition temperature of the molecule should be significantly higher than the evaporation/sublimation temperature of the molecule. This is important for two reasons. Firstly, it is preferable when the materials are purified, e.g. by vacuum gradient sublimation. The purification guarantees the removal of remainders from the synthesis as well as the batch to batch reproducibility. Secondly, this temperature gap enables higher evaporation rates, which are beneficial for a possible large-scale production. In case of solution processing, the solubility of the materials needs to be ensured, e.g. through attached alkyl side chains.

2.2. Organic semiconductors

2.2.1. Thin film growth and morphology

This section deals with the different growth mechanisms, the Van-der-Waals forces and methods to influence the morphology of organic thin films. The main literature sources for this section are the review paper about pentacene by Ruiz[24] and the book of Steudel[5].

Thin film growth of vacuum deposited small molecules

Upon the deposition of small molecules on a substrate surface, the molecules aggregate and form thin films. The different growth mechanisms can be classified into three archetypes. Figure 2.4(a) shows the layer-by-layer growth (Frank-van der Merwe), in which a layer is closed before the next layer forms. In this case, the growth in the xy -plane proceeds much faster than the growth in the z -direction. The second growth mechanism, the island growth (Volmer-Weber), is presented in Figure 2.4(b). As the name suggests, islands form and grow in all three dimensions, rather than only in two dimensions as in the layer-by-layer growth. Here, the interaction between the molecules is stronger than the interaction between the molecules and the substrate. The third growth mechanism, depicted in Figure 2.4(c), is the layer-plus-island growth (Stranski-Krastanov), which begins with the formation of closed layers and changes afterwards to the formation of three dimensional islands. In this case, the interaction with the substrate is stronger than the interaction among the molecules. However, the balance of interactions changes after the first layer is closed and the interaction between the molecules and the substrate is no longer possible. Now, the interaction takes only place between molecules and the growth of the thin film proceeds in three dimensions.[24]

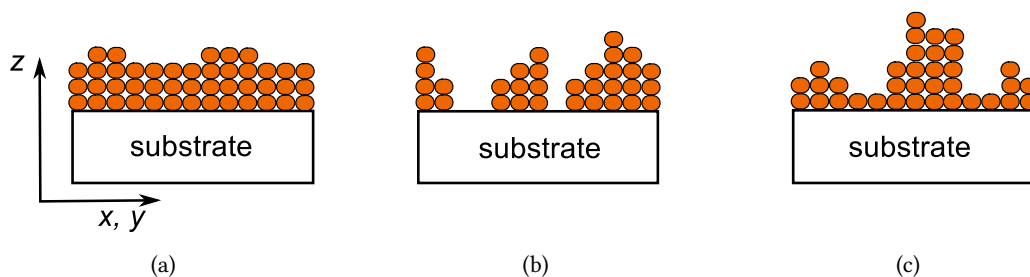


Figure 2.4.: Three models for growth mechanisms: (a) layer-by-layer growth (Frank-van der Merwe), (b) island growth (Volmer-Weber) and (c) layer-plus-island growth (Stranski-Krastanov).

Van-der-Waals force

The bonds between the atoms in an organic molecule are mainly covalent with binding energies in the range between 1 eV and 5 eV.[5] Organic solids or thin films consist of organic

molecules, which are bound by the relatively weak Van-der-Waals force. The binding energy is in the range from tens of millielectronvolts up to ≈ 200 meV.[5] Contributions to the Van-der-Waals force arise from the dipole-dipole force, the Debye force, and the London dispersion force. They are based on different interactions of permanent and induced dipoles among themselves and the interaction of dipoles with polarizable matter.[5] The Pauli principle and Coulomb repulsion act as repulsive forces for small distances. The combination of the Van-der-Waals force and the repulsive forces can be approximated by the Lennard-Jones potential $V(r)$. It is described by

$$V(r) = \frac{a}{r^{12}} - \frac{b}{r^6} \quad (2.1)$$

where r is the distance between the molecules and a and b are material-specific constants.[5]

H- and J-aggregation

Special types of molecular assembly are H- and J-aggregation. These aggregates were first observed for dyes in solution.[25] Due to the aggregation, the transition dipole moments of the single molecules interact and cause a collective excitation that shifts the absorption spectrum of the single molecule. For J-aggregates, the absorption of the aggregate is redshifted and strongly narrowed.[26] In addition, a strong fluorescence is observed. In contrast, for H-aggregation the absorption of the aggregate is blueshifted in comparison to the absorption of the single molecule.[26] Furthermore, the fluorescence in H-aggregates is strongly suppressed. Several thousand molecules can be assembled in both types of aggregates.[25] The change in the optical properties can be understood by considering the interaction of two molecules. As mentioned above, the changes in the optical spectra are caused by the interaction of the transition dipole moments. Kasha showed that the main consequences can be understood classically by consideration of two point dipoles.[27] Figure 2.5 shows three scenarios: the parallel arrangement, the head-to-tail arrangement, and the oblique arrangement of the dipoles. The diagrams below show the corresponding splitting of the energy levels. As the wavelength of the light is much longer than the distance between the molecules, the anti-parallel orientation of the transition dipoles is forbidden in each case.

In the oblique case, a vectorial addition of the dipoles leads to the resulting dipole moments. For co-planar dipoles, a slippage angle of 54.7° marks the border between J- and H-aggregation.[28, 29] Besides the appearance in solution, H- and J-aggregation can be also present in nanowires.[29–31]

Layer control by processing conditions

The morphology of organic layers has several aspects, such as crystallinity, roughness, and orientation of the molecules. Besides the molecular design by chemistry, also processing conditions can have a significant influence on the morphology. Concerning crystallinity, the most common ways are the choice of the substrate[32] and the regulation of deposition rate[33] and substrate temperature[34, 35]. For the latter two, a higher crystallinity can be

2. Theory

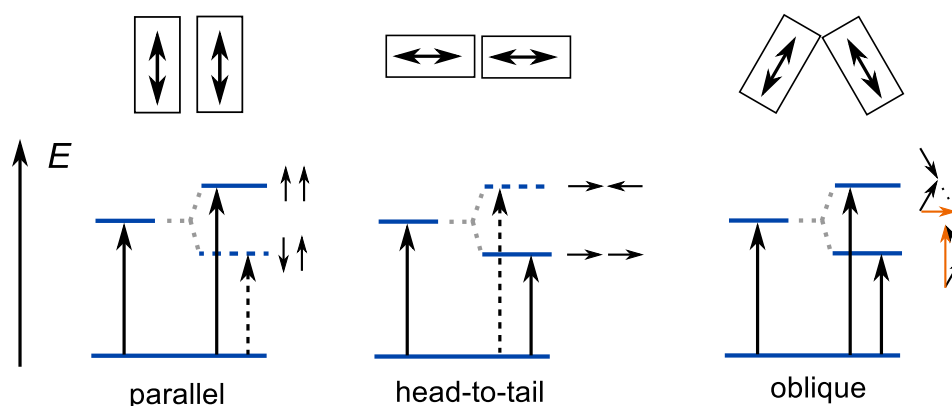


Figure 2.5.: Sketch of possible types of molecular aggregation. The arrows in the boxes indicate the position of the transition dipole moments relative to each other. The diagrams below show the corresponding energy levels. The dashed arrows indicate forbidden transitions. The parallel arrangement corresponds to H-aggregation and the head-to-tail arrangement to J-aggregation.

achieved by a lowering of the deposition rate or increasing the substrate temperature.[24] The higher substrate temperature supports the mobility of the molecules on the substrate surface and the lower deposition rate gives the molecules more time to arrange themselves on the substrate. Figure 2.6 shows exemplarily the complex interplay between substrate temperature and deposition rate for pentacene thin films. Here, Ruiz *et al.* assembled information from several publications to a scheme about the single layer growth of the molecule and depicted them in dependence of the two processing parameters.[24] The single layer growth is limited by a low-temperature limit and a fast-rate limit. If the substrate temperature is set too high or the rate too low, one reaches the regime of low supersaturation where the layer-by-layer growth is disturbed by dislocations. The forth border of the single layer growth is set by the beginning of the nucleation of the bulk phase, which appears at high substrate temperatures.[24]

2.2.2. Optical properties

This section follows mainly the books of Schwöerer/Wolf[9] and Simon/André[36] as well as Lanzani[28].

Jablonski diagramm

The absorption and emission spectrum of organic molecules and solids is determined by the dipole selection rules. This perturbation-theory approximation states that the probability of an optical transition between energy levels is dependent on the overall spin of the system,

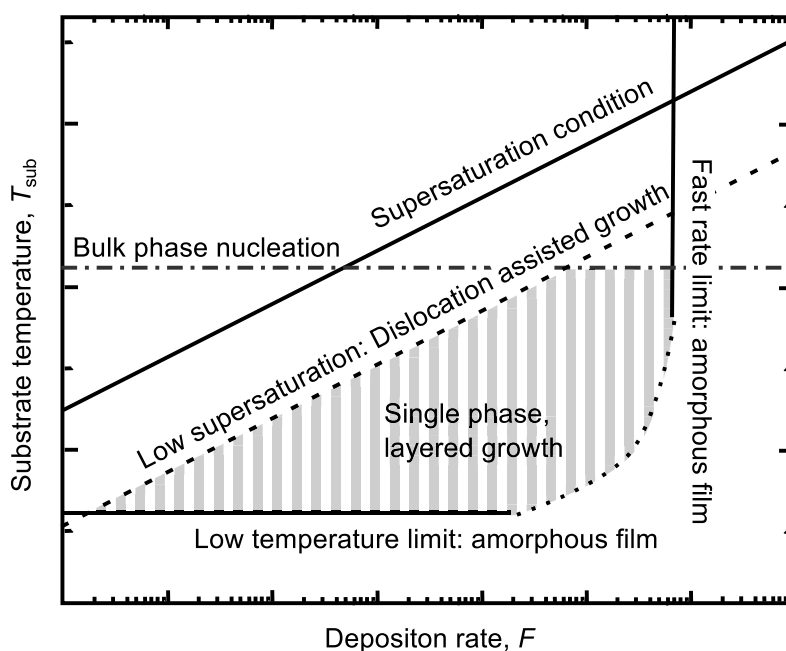


Figure 2.6.: (b) Qualitative overview about the different growth mechanisms of pentacene as a function of material deposition rate and substrate temperature during the deposition. Adapted with permission from [24]. Copyright (2004) American Chemical Society.

which has to be conserved. Transitions requiring a change of the overall spin are called nonradiative, whereas radiative transitions have a conserved overall spin. The transitions are described in the Jablonski diagram shown in Figure 2.7.

S_x stands for singlets, where the overall spin $S=0$ and T_x represents triplets with an overall spin of $S=1$. When the HOMO is fully occupied with electrons, which is usually the case for organic molecules, the overall spin of the ground state is $S(S_0)=0$. Hence, the transition to higher singlet states upon photon absorption is preferred against transition to triplet states, where a spin-flip has to take place. The first excited singlet state S_1 has a lifetime of ca. $10^{-9} - 10^{-6}$ s. The radiative decay from a singlet state to the ground state is called fluorescence. Practically, this transition happens only from S_1 to S_0 , because the higher excited singlet states decay rapidly on a time scale of $10^{-14} - 10^{-13}$ s over internal conversion and vibrational relaxation to the S_1 state. Also triplet states have practically only one (radiative) transition from the first excited state T_1 to ground state, where the transition is called phosphorescence. The lifetime of the T_1 is ca. $10^{-4} - 20$ s. An exchange between singlets and triplets is called intersystem crossing. The probability for intersystem crossing is dependent on the spin-orbit coupling, which is usually quite low in molecules with only light atoms and higher for molecules containing heavy atoms.[9]

2. Theory

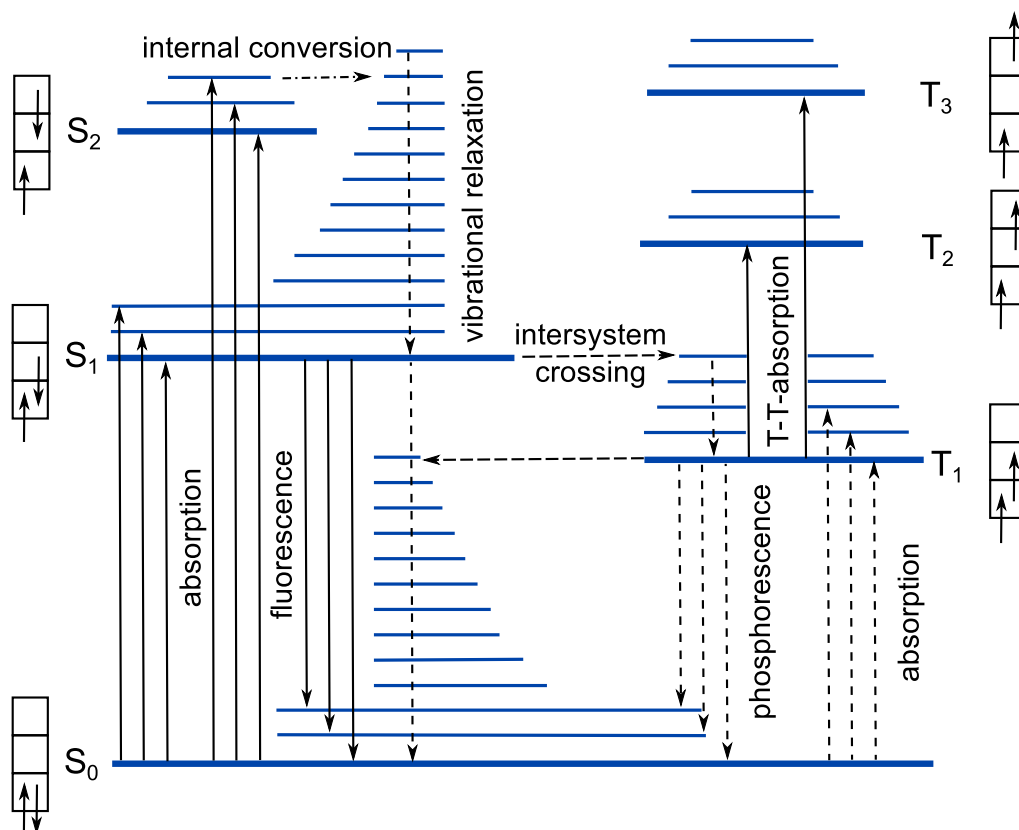


Figure 2.7.: Jablonski diagram with term scheme for the absorption/emission in organic molecules and solids. S_x (T_x) represents singlet (triplet) states. The small arrows in the boxes on the side of the diagram stand for the spin state of the electron. The vertical solid arrows represent allowed transitions, while the vertical dashed lines indicate nonradiative transitions. Adapted from ref [9].

Excitons

Excitons are Coulombically bound electron-hole pairs. Depending on the strength of the binding energy, one can distinguish different types of excitons. The first group are Wannier-Mott excitons that appear in inorganic semiconductors. These excitons are loosely bound with binding energies in the range of 25 meV. Therefore, Wannier-Mott excitons can dissociate up at room temperature and create free charge carriers. The binding energy is small, because the relative permittivity in inorganic semiconductors is quite high, e.g. silicon has a relative permittivity of $\epsilon_r=11.9$. [37] The relative permittivity for organic materials is usually between 3.5 and 5.5. [38] Accordingly, their exciton binding energies are in the range between 0.4 eV and 1.4 eV. [39] Consequently, the probability that ambient heat at room temperature dissociates these so called Frenkel excitons is very low. A third type of exciton is the charge-transfer state. Lanzani defines it as “[...] a molecular state with ionic character where

regions of positive and negative charge are bound together by Coulomb attraction.”[28] This definition means for organic semiconductors that the electron and the hole are bound and located on two neighboring molecules. Thereby, the molecules can be of the same kind or two completely different molecular structures. The CT state plays an important role in the exciton splitting in organic solar cells and will be discussed in detail in the organic solar cell section.

Frenkel excitons in organic semiconductors are basically excitations of a single molecule, which can move through the bulk. The excitons are not charged and consequently not affected by an externally applied electric field. However, a diffusive transport is possible by three types of transport mechanisms: reabsorption, Förster transfer, and Dexter transfer. In the following, two molecules are considered in order to explain each transfer mechanism. The exciton donor D is the molecule at which the exciton is originally located and the exciton acceptor A is the molecule that receives the exciton. Thereby, only energy is transferred and no material transport takes place. In the case of reabsorption, which is depicted in Figure 2.8(a), the donor relaxes under emission of a photon



that is consecutively absorbed by the acceptor



Therefore, a spectral overlap between the fluorescence spectrum of the donor and the absorption spectrum of the acceptor is necessary.[36]

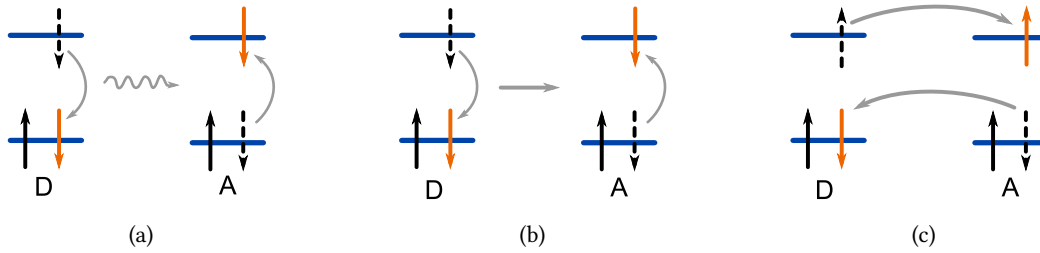


Figure 2.8.: Energy levels of exciton donor (D) and exciton acceptor (A) during (a) reabsorption, (b) Förster transfer, and (c) Dexter transfer. The dashed black arrows indicate the position of the electrons before the energy transfer and the orange arrows after the transfer.

Radiationless interactions between molecules can be divided into two groups: Coulombic interaction and exchange interactions.[36] The Coulombic interactions are the sum of dif-

2. Theory

ferent multipole interactions of the electrostatic potential. Since the distance dependence of such interactions increases with the order of the interacting multipoles, in first approximation only the dipole-dipole interaction, the so called Förster transfer, is important. The rate k is given by

$$k = J_{\text{ov}} \frac{2\pi}{\hbar} c \frac{\xi^{\text{D}} \xi^{\text{A}}}{r^6 \nu^2} \theta_a^2 \quad (2.4)$$

where J_{ov} is the spectral overlap between D and A, ξ^{D} and ξ^{A} are the oscillator strengths for the donor and acceptor transitions, ν is the average wavenumber for the transitions, r is the distance, and θ_a is the angle between the molecules. The Förster transfer requires a separate spin conservation for the donor and the acceptor, so that only a singlet-singlet transfer is allowed, as it is depicted in Figure 2.8(b). Due to the $\sim r^{-6}$ dependence, the transfer can only happen on length scales of 50-100 Å.

The exchange interaction (Dexter transfer) is based on the indistinguishability of electrons and the symmetry properties of the transfer integral with respect to space, time, and spin. This type of transfer requires an orbital overlap, which reflects itself in the distance dependence of $\sim \exp(-cr)$ and limits the range to 5-10 Å. However, due to the symmetry of the spin also triplet transfer is allowed. The cartoon in Figure 2.8(c) presents an example, where the donor changes its multiplicity from triplet to singlet and the acceptor accordingly from singlet to triplet. In general, the transfer rate is given by

$$k = J_{\text{ov}} \frac{2\pi}{\hbar} K \exp\left(-\frac{2r}{L}\right) \quad (2.5)$$

in which K is a constant and L is the measure for the average orbital radius.[36] Both interactions happen isoenergetically, which is reflected by the proportionality of the transfer rates to the spectral overlap between donor and acceptor. Förster and Dexter transfer happen only in materials in which the molecules are vibrationally relaxed before the exciton transfer happens. These materials have usually a thin film absorption that is very similar to the single molecule absorption.[36]

The exciton diffusion is a crucial process in organic solar cells. The exciton diffusion length L_{D} is used to quantify and compare the exciton diffusion in organic semiconductors. It is defined by

$$L_{\text{D}} = \sqrt{D_{\text{E}} \tau}. \quad (2.6)$$

D_{E} represents the exciton diffusion constant and τ the lifetime of the exciton. The exciton diffusion length is usually in the range of a few nanometers.[40]

2.2.3. Charge transport

The charge transport in organic semiconductors differs in some aspects from the charge transport in inorganic semiconductors. The following paragraphs will give an overview about typical phenomena in organic semiconductors, starting with the anisotropy of electrical properties on the example of organic crystals and the polaronic properties of the charge carriers. However, organic thin films as used in optoelectronic devices are normally only partly crystalline or even amorphous, which prohibits the formation of electronic band structures. Two criteria are introduced that allow the distinction between band transport and hopping transport. Accordingly, some considerations on the hopping transport are discussed and the assumptions and main conclusions of the Bässler model are shortly summarized. In the end, the interactions between the electrodes and the organic semiconductor are covered and the Mott-Gurney law is presented. The subsequent paragraphs follow the reviews of Bässler, Tessler *et al.*, and Coropceanu *et al.* as well as the textbook of Schwoerer/Wolf.[9, 41–43]

Anisotropy of charge transport

Organic semiconductors often exhibit anisotropic electrical properties. Angular dependent field effect transistor (FET) measurements on single crystals give an instructive example for this anisotropy.[44, 45] Mobility measurements on pentacene performed by Lee *et al.* showed (FET-) mobilities from 0.66 cm²/Vs up to 2.33 cm²/Vs, depending on the direction of the applied electric field.[44] The reasons for this anisotropy are the molecular geometries and their packing in the crystal structure. The π -system that promotes the charge transport is usually located on the face of a molecule. The coupling between the π -systems of the molecules depends on their stacking pattern respectively the orientation of the molecules to each other. Directions with a better coupling of the π -systems enable a better transport.[46] The current density \vec{j} is not necessarily parallel to the applied electric field \vec{F} in these cases. Thus, the conductivity $\underline{\sigma}$ has to be considered as a tensor

$$\vec{j} = \underline{\sigma}\vec{F}. \quad (2.7)$$

Similar to inorganic semiconductors, the concept of holes is applied to describe the charge transport of defect electrons. Accordingly, the conductivity is given by

$$\underline{\sigma} = e(n_e\underline{\mu}_e + n_p\underline{\mu}_p), \quad (2.8)$$

where n_e , n_p are the electron/hole density and $\underline{\mu}_e/\underline{\mu}_p$ are the respective mobilities.[9]

Polarons

A free charge carrier in an organic solid means that a molecule is ionized.[28] Thus, a free electron (hole) is always associated with an anion (cation). Charge transport is consequently

2. Theory

the serial ionization and recombination of organic molecules.² The excess charge of a newly formed ion polarizes its environment and leads to a small displacement or realignment of the ion itself and the surrounding molecules. The relaxation time of the surrounding molecules is two orders of magnitude lower than typical times for charge transport from one molecule to another.[9] Hence, the induced changes in the molecular environment are confined to the immediate surrounding of the ionized molecule. The excess charge carrier on the ion in combination with the induced polarization of the environment is called polaron. The energy of the average polarization is given by

$$\overline{P}_h = E_{\text{HOMO}} - IP \quad \text{for holes and} \quad (2.9)$$

$$\overline{P}_e = EA - E_{\text{LUMO}} \quad \text{for electrons,} \quad (2.10)$$

in which IP refers to the ionization potential of the solid and EA refers to the corresponding electron affinity. Figure 2.9 shows the relation between the energy levels of a single molecule, the energy levels in a solid and the average polarization energy.

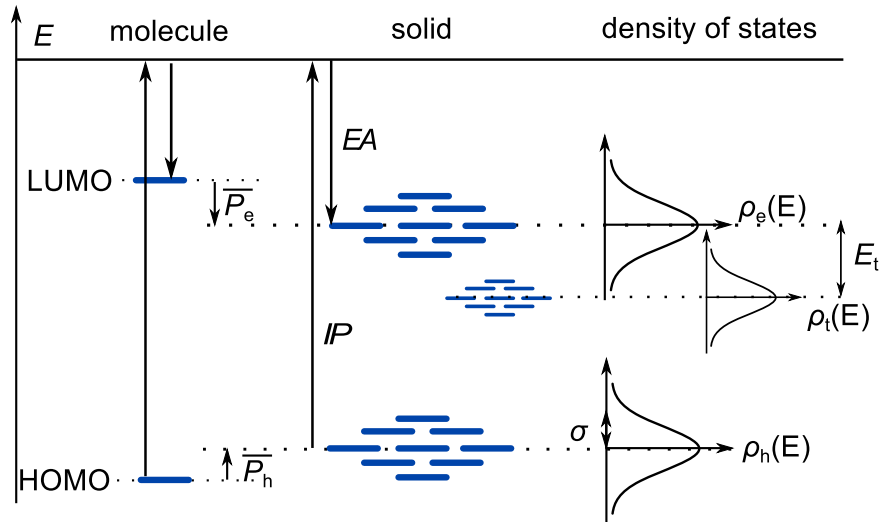


Figure 2.9.: Energy levels of a single molecule (left) and the corresponding disordered solid (right). $\overline{P}_{e/h}$ refer to the polarization energies, IP to the ionization potential and EA to the electron affinity. E_t is the mean energy of the trap states. $\rho_{h/e/t}(E)$ describes the respective density of states of holes, electrons, and traps. σ is the diagonal disorder. Adapted from [9].

²Please, note that “recombination” in this regard means that a charged molecule obtains its neutral configuration by the transfer of the additional/missing charge carrier to a neighboring molecule. It has to be distinguished from the “recombination” of a free hole and a free electron on a molecule by mutual annihilation.

Band transport vs. hopping transport

With increasing disorder in an organic semiconductor, the energy bands become thinner and single sites appear at the band edges up to the point at which only localized sites exist. Then hopping transport models have to be applied to describe the charge transport. There are two criteria in order to discriminate between these transport mechanisms.[9, 36] The first criterion for band transport is that the mean free path length of a charge carrier has to be significantly larger than the lattice constant. This condition means that the charge carrier is not localized on one molecule. The second criterion for band transport states that the lifetime τ of a charge carrier has to be longer than

$$\tau \gg \frac{\hbar}{W} \quad (2.11)$$

where \hbar is the reduced Planck constant and W is the band width. This equation can be derived from the energy-time uncertainty relationship $\Delta Et \gg \hbar$. [36] If the energy is measured between two scattering events, the energy uncertainty has to be lower than the bandwidth, otherwise a state in the energy gap would be occupied, which is not possible. Cheng *et al.* report band widths of 0.1-0.5 eV for polyacene crystals[47], which correspond, according to ref. [9], to $\tau > 10^{-15}$ s. If the criteria are not fulfilled, a hopping model has to be applied to describe the transport.[9, 36]

Hopping transport

In disordered materials, the formation of an electronic band structure is not possible, because the necessary long-range periodicity of a lattice is not present. Thus, charge carriers occupy localized states (sites). Due to disorder, every molecule has a different environment and, consequently, these sites have slightly different energy levels as shown in Figure 2.10.

This leads usually to a Gaussian density of states as depicted in Figure 2.9. Its standard deviation is described by the “diagonal” disorder (σ) that is a measure for the fluctuation of the polarization energies. States within the energy gap are called trap states, since they can “trap” charge carriers. The de-trapping of trapped charge carriers depends on the depth of the trap. The trapping energy E_t of shallow traps is in the order of $k_B T$ and allows de-trapping by thermal heat. In contrast, deep traps have trapping energies much larger than $k_B T$. [43] Traps can be caused by material impurities, depending on their energy levels. Figure 2.9 shows a trap distribution with a Gaussian density of states in the energy gap.

Bässler model

The most popular model to describe hopping transport in disordered organic solids is the Bässler model.[41] It refers to a Monte Carlo simulation using the Miller-Abrahams equations as transition rates. The simulations contained 70x70x70 sites. Their energy levels were distributed according to a Gaussian density of states

2. Theory

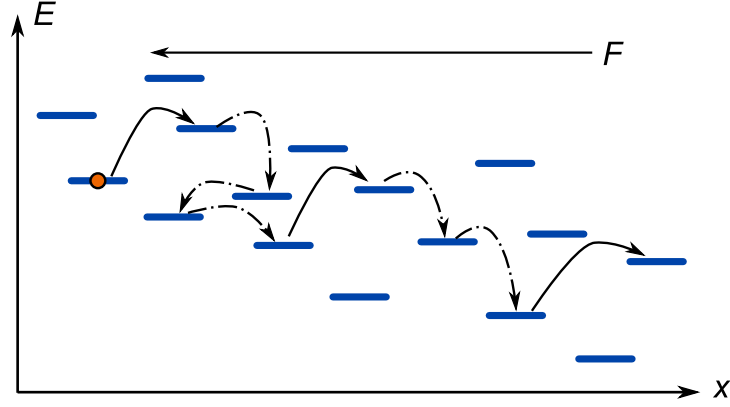


Figure 2.10.: Energy of an ensemble of randomly distributed sites (blue bars) as a function of distance under an external electric field F . A possible movement of a charge carrier (orange circle) is depicted. The solid arrow indicates transport by thermal activation and the dashed arrow transport by tunneling.

$$\rho(E) = \frac{1}{\sqrt{2\pi\sigma^2}} \exp\left(-\frac{E^2}{2\sigma^2}\right). \quad (2.12)$$

E is the energy of a site and σ represents the diagonal disorder. The transitions between the sites were modelled with the Miller-Abrahams equations

$$W_{ij} = v_0 \exp(-2\gamma R_{ij}) \begin{cases} \exp\left(-\frac{E_j - E_i}{k_B T}\right) & \text{if } E_j > E_i \\ 1 & \text{else} \end{cases} \quad (2.13)$$

where the first term describes the tunneling process with v_0 as the attempt hopping frequency, γ as the overlap factor and R_{ij} as the distance between the sites i and j . R_{ij} is also Gaussian distributed due to varying distances and coupling strengths between the sites. While the distances vary mostly due to spatial disorder, the differences in coupling strength are also related to the flat form of the molecules as explained before (see section 2.2.3). The influence of these phenomena is described by the ‘‘off-diagonal’’ disorder parameter Σ . The second term is a Boltzmann factor and describes a thermal activation for the case that the initial site i has a lower energy than the final site j . The simulation predicts the necessity of a thermal activation of the charge carriers, because the initially randomly distributed charge carriers relax into a equilibrium energy $\langle E_\infty \rangle$. This energy is then

$$\langle E_\infty \rangle = -\frac{\sigma^2}{k_B T} \quad (2.14)$$

and is dependent only on the diagonal disorder and the temperature. Furthermore, the charge carrier mobility is obtained by

$$\mu(\sigma, \Sigma, F, T) = \mu_0 \exp \left[- \left(\frac{2\sigma}{3k_B T} \right)^2 + C \left(\left(\frac{\sigma}{k_B T} \right)^2 - 1.5^2 \right) \sqrt{F} \right] \text{ for } \Sigma < 1.5 \quad (2.15)$$

$$\mu(\sigma, \Sigma, F, T) = \mu_0 \exp \left[- \left(\frac{2\sigma}{3k_B T} \right)^2 + C \left(\left(\frac{\sigma}{k_B T} \right)^2 - \Sigma^2 \right) \sqrt{F} \right] \text{ for } \Sigma \geq 1.5 \quad (2.16)$$

where μ_0 is the mobility for an ideal disorder free material and $C=3 \cdot 10^{-4} \sqrt{\text{cm}/\text{V}}$ is an experimentally determined constant.

Current regimes

For the usage of organic semiconductors in devices, the material has to be contacted to electrodes to allow injection and extraction of charge carriers. The current through an organic semiconductor can be limited either by the contacts or by the semiconductor itself. For the former case, the system is named “contact limited” and for the latter case the contact is called “ohmic”. If the system is ohmic, the current will follow Ohm’s law $j \sim V$ for low applied fields. For higher applied voltages, too many charges are injected into the organic semiconductor. They cannot be transported through the layer and pile up. These excess charge carriers create an electric field that limits the current. This is called space charge limited current. For an organic semiconductor with a small amount of traps between two equal metal electrodes, the Mott-Gurney law was derived. It reads

$$j = \frac{9}{8} \varepsilon_r \varepsilon_0 \mu \frac{V^2}{d^3}, \quad (2.17)$$

where ε_r is the relative permittivity, ε_0 is the vacuum permittivity, and d is the thickness of the organic semiconductor.[9]

Doping

Like inorganic semiconductors, organic semiconductors can be doped by integrating specific chemical impurities into the host material. The aim is to increase the charge carrier concentration in the layer to enhance the conductivity. However, doping is also used to provide an ohmic contact between organic and metal layers or between organic and organic layers. Dopants can be single atoms like caesium[48], metal oxides like MoO_x [49] or small molecules like $\text{C}_{60}\text{F}_{36}$ [50]. In contrast to inorganic semiconductors with typical doping densities of $10^{12} - 10^{18} \text{ cm}^{-3}$ for silicon[37], for organic semiconductors doping densities of a few weight percent are needed.[51] Figure 2.11(a) shows the principle of p-doping. In this case, the p-dopant must have an electron affinity that is lower than the ionization potential of the matrix material. Then a charge transfer from a matrix molecule to the dopant can happen. This leads to a shift of the Fermi level to lower energies. Figure 2.11(b) shows the analogous

2. Theory

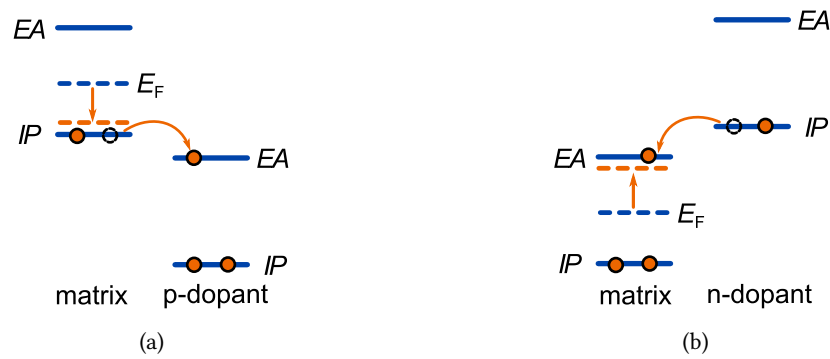


Figure 2.11.: (a) Model for p-doping and (b) model for n-doping. The blue dashed line represents the Fermi-level for the intrinsic case and orange for a doped sample.

situation for n-doping. Here, the n-dopant needs to have a higher ionization potential than the electron affinity of the matrix material. However, this is only a simple model to describe the doping process. An in-depth model of the doping process is still under investigation.[52] Besides the generation of excess charge carriers, doping can also enhance the mobility of an organic layer by filling of trap states.[53]

2.3. Solar cells

This section gives an overview about the physical principles of photovoltaics in general and organic photovoltaics in particular. The subsections about the general concepts follow mainly the book of Würfel.[54] The subsections about organic solar cells base mainly on these references [55–59].

2.3.1. General concepts

Sun spectrum

The standard reporting conditions advice to measure non-concentrator solar cells under the AM1.5G spectrum. The characters AM stand for Air-Mass and the digits indicate the length of the path through the atmosphere (l). It is calculated by

$$AM = \frac{l}{l_0} = \frac{1}{\cos \alpha} \quad (2.18)$$

in which l_0 is the thickness of the atmosphere and α the angle between the incoming light of the sun and the normal to the surface of the earth.[54] AM0, which is displayed in Figure 2.12, refers to the sun spectrum outside the earth atmosphere. Accordingly, AM1 stands for irradiance under an angle of 90° and AM1.5 means irradiance under an angle of 48° . [54] The character “G” means global tilt and is in contrast to the direct (plus circumsolar) radi-

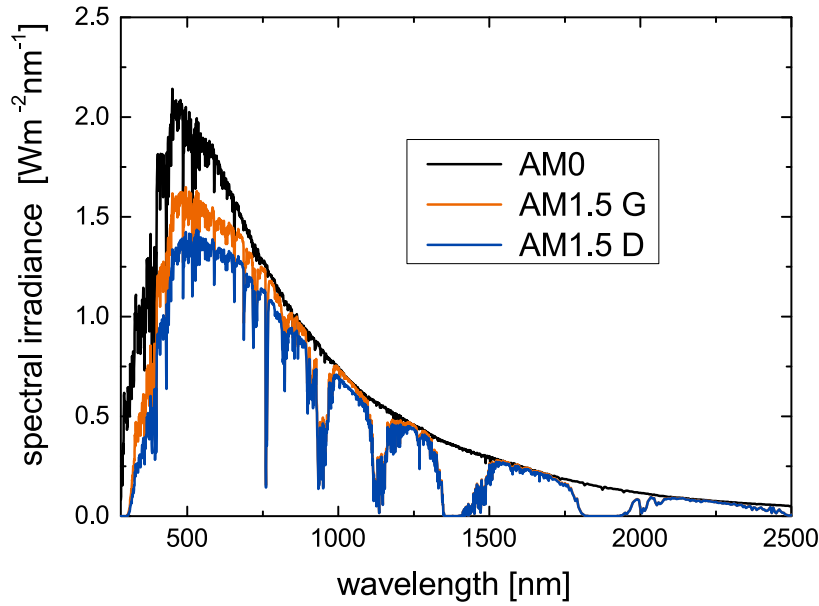


Figure 2.12.: Spectral irradiance of AM0, AM1.5G and AM1.5D. The spectra are taken from ref. [60].

ation “D”.[60] The global irradiance includes light which was scattered by particles in the atmosphere or the ground, namely “[...] spectral radiation from solar disk plus sky diffuse and diffuse reflected from ground on south facing surface tilted 37° from horizontal.”[60] The intensity of the integrated AM1.5G spectrum is 100 mW/cm^2 , while the intensity of AM1.5D is 90 mW/cm^2 . Figure 2.12 presents a comparison between the AM1.5D and AM1.5G spectra.

Limits to power conversion efficiency

In the following section, general limits to the power conversion efficiency of photovoltaics are discussed. The first limitation was presented by Würfel and arises mainly from thermodynamics.[54] Accordingly, η_{\max} is given by

$$\eta_{\max} = \left(1 - \frac{T_A^4}{T_S^4}\right) \left(1 - \frac{T_0}{T_A}\right), \quad (2.19)$$

in which $T_S=5800 \text{ K}$ is the temperature of the sun, T_0 is the ambient temperature and T_A the temperature of the absorber. For ideal conditions, the absorber is located in a cavity with ideal reflecting mirrors with a single opening that points at the sun.[54] An equilibrium between the sun and the absorber arises in which the absorber can in principle reach the

2. Theory

temperature of the sun, if no energy is removed. This relationship is represented by the first term in equation (2.19). The four in the exponent stems from the Stefan-Boltzmann law that describes the radiative nature of the energy transfer. The second term characterizes the power conversion efficiency of a Carnot process – the maximum power conversion efficiency of a heat engine. The maximum power conversion efficiency of 85% is achieved at an absorber temperature of 2478 K.[54]

A second limitation is connected to the band or energy gap of semiconductors and was derived by Shockley and Queisser for pn-single-junctions.[61] It describes the relationship between the size of the band gap and the number of absorbed photons, which leads to a trade-off between V_{oc} and j_{sc} . This means that on the one hand, a small band gap can absorb more photons. On the other hand, the electrons can only gain the energy of the band gap. The additional energy of electrons, which were excited by photons with an energy higher than the band gap is transferred into heat by relaxation of the electron. Using the assumption that only radiative recombination is present in the solar cell, Shockley and Queisser found that the highest power conversion efficiency is approximately 30% for a semiconductor with a bandgap of 1.3 eV.[61]

Quasi-Fermi level

Quasi-Fermi levels describe the distribution of excess charge carriers in semiconductors, e.g. by photoexcitation or charge carrier injection. This concept is of great importance for (organic) solar cells. Here, it is motivated for three dimensional semiconductors that have an electronic band structure. This assumption can be valid for organic single crystals, but is usually not the case for organic thin films. However, it is instructive to use this example as it allows the Boltzmann approximation that leads to an analytical expression for the quasi-Fermi levels.

The Fermi - Dirac distribution $f(E)$ describes the occupation of states for particles with spin $\frac{1}{2}$ – fermions

$$f(E) = \frac{1}{\exp\left(\frac{E-\mu}{k_B T}\right) + 1}. \quad (2.20)$$

μ denotes the chemical potential. At 0 K the distribution has an energy up to which every state is occupied, which is called chemical potential. In this case, it is also called Fermi level (E_F).³ For temperatures higher than 0 K, the chemical potential marks the energy at which the half of the states are occupied. The density of states is given by

³Strictly speaking, the Fermi level is only defined for 0 K and is a special case of the chemical potential $\mu(T=0 \text{ K}) \equiv E_F$, which is defined for all temperatures. However, the terms “Fermi level” and “chemical potential” are often used synonymously.

$$\rho(E) = 4\pi \left(\frac{2m^*}{h^2} \right)^{\frac{3}{2}} \sqrt{E}, \quad (2.21)$$

in which m^* is the reduced mass. The electron (hole) population density n_e (n_h) is now the result of the integral over the product of the density of states $\rho(E)$ and the distribution function according to

$$n_e = \int \rho(E) f(E) dE, \quad (2.22)$$

$$n_h = \int \rho(E) (1 - f(E)) dE \quad (2.23)$$

This integral can be analytically solved, if the Fermi distribution is approximated by a Boltzmann distribution (Boltzmann approximation). This approximation is valid at low doping concentrations and temperatures ($k_B T$) that are considerably smaller than the band gap. The first assumption is valid, since organic semiconductors have usually larger energy gaps[62] than conventional inorganic semiconductors like silicon or germanium[37]. Also the second assumption is fulfilled, as the photoactive layers in organic solar cells are generally not doped. Using the Boltzmann approximation, the results for the population density for electrons n_e and holes n_h are

$$n_e = N_c \exp\left(-\frac{E_e - E_F}{k_B T}\right) \quad (2.24)$$

$$n_h = N_v \exp\left(\frac{E_h - E_F}{k_B T}\right). \quad (2.25)$$

N_c (N_v) is the effective density of states for the conduction (valence) band and E_e (E_h) is the energy of the edge of the conduction (valence) band. As discussed in a previous section for an (amorphous) organic thin film, a Gaussian density of states is usually assumed. This is no obstacle for the concept of the quasi-Fermi levels. However, the evaluation of the integral becomes unnecessary difficult for the purpose of explaining the concept. Figure 2.13(a) shows the population density (blue area) for a semiconductor in the dark.

The Fermi level is, in first order approximation and in case of low temperatures, located in the middle of the energy gap and describes the electron density as well as the hole density. Figure 2.13(b) depicts an illuminated semiconductor. Electron and hole density are increased due to photoexcitation and cannot be characterized by a single Fermi level. Hence, separate quasi-Fermi levels for electrons and holes are assumed to describe the population density at illuminated conditions:

2. Theory

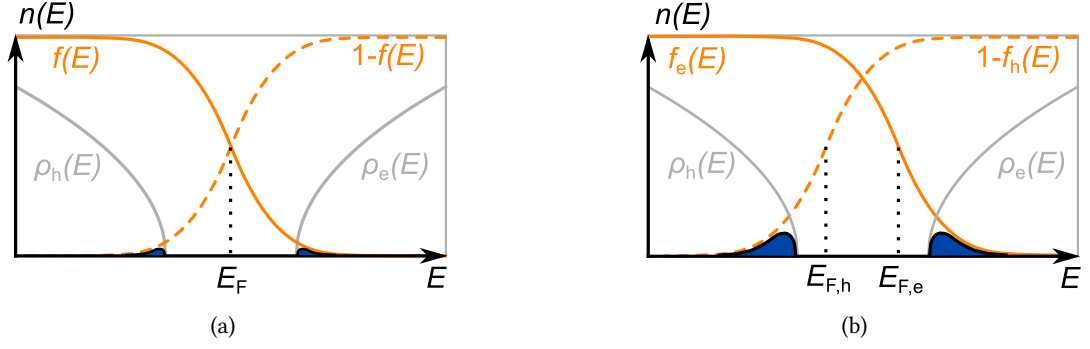


Figure 2.13.: (a) Electron and hole density (blue) of a semiconductor in the dark as a function of energy. It is depicted as a product of the density of states (grey) and the Fermi-Dirac distribution (orange). E_F marks the Fermi level. (b) The same situation in an illuminated semiconductor. $E_{F,h}$ and $E_{F,e}$ are the respective quasi-Fermi levels for the holes and electrons. Note that the Fermi-Dirac distribution for the holes is depicted mirrored in $E_F/E_{F,h}$ for illustration.

$$n_e = N_c \exp\left(-\frac{E_e - E_{F,e}}{k_B T}\right), \quad (2.26)$$

$$n_h = N_v \exp\left(\frac{E_h - E_{F,h}}{k_B T}\right). \quad (2.27)$$

$E_{F,e}$ represents the quasi-Fermi level of the electrons and $E_{F,h}$ stands for the quasi-Fermi level of the holes. The difference between both quasi-Fermi levels

$$E_{F,e} - E_{F,h} \geq eV_{oc} \quad (2.28)$$

sets an upper boundary for the open circuit voltage of a solar cell for the specific illumination conditions.

Ideal solar cell stack

After the creation of charge carriers in a photoactive layer, one needs to separate the holes from the electrons and extract the charge carriers from the device. For this purpose, Würfel proposed an ideal solar cell that is discussed in the subsequent paragraphs.[54] Figure 2.14 depicts a sketch of such a solar cell.

It consists of three parts: an electron transport layer (n), an intrinsic absorber layer (i), and a hole transport layer (p). Würfel demands that the transport layers do not absorb any light and work similar under illumination and in darkness.[54] Furthermore, the transport layers should be doped to ensure a good conductivity and enough charge carriers to avoid an in-

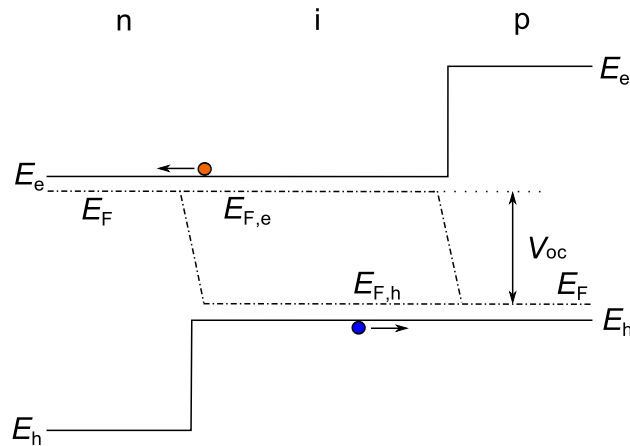


Figure 2.14.: Energy band diagram of an ideal solar cell according to Würfel.[54] The dash-dotted line represents the Fermi levels in the transport layers and the splitted quasi-Fermi levels in the absorption layer.

crease in entropy when extracting the photogenerated charge carriers.[54] The requirement of transparent transport layers can be approximately fulfilled by using materials with a large band gap that absorb only little light from the sun spectrum. These wide-gap materials also provide the benefit of acting as selective membranes for the charge carriers. By considering e.g. the junction between the electron transport layer (n) and the absorber layer (i), one sees that the large band gap of the electron transport layer acts as a barrier for the holes and ensures barrier-free transport for the electrons. In combination with an analogously working hole transport layer, this results in an effective separation of the electrons and holes, which is beneficial for a solar cell.[54]

Parameters

Figure 2.15 shows the current – voltage characteristics of a solar cell in darkness and under illumination. The simplest model to describe this behavior is the Shockley equation

$$I = I_s \left(\exp \left(\frac{qV}{n_{id}k_B T} \right) - 1 \right) - I_{ph} \quad (2.29)$$

modified by the photocurrent I_{ph} . I_s is the saturation current in darkness under reverse bias and n_{id} is the diode ideality factor. The intersection between the curve and the current axis at 0 V is called short circuit current (I_{sc}), the intersection with the voltage axis is called open circuit voltage (V_{oc}). A solar cell can only produce power in the fourth quadrant, where a positive bias voltage is applied and the current flows in reverse direction. An important

2. Theory

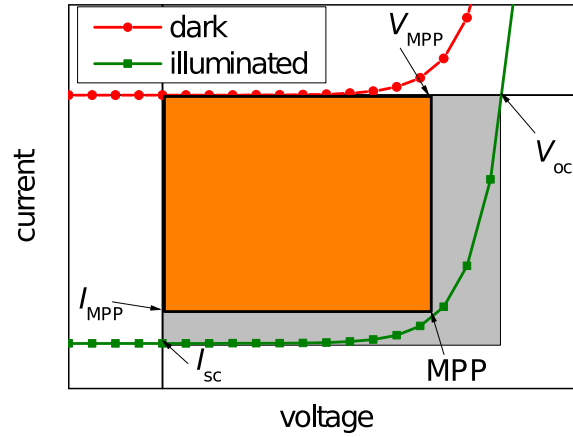


Figure 2.15.: Dark and illuminated current - voltage curves of a solar cell. The gray square marks the product of V_{oc} and I_{sc} . The orange square is proportional to the power in the maximum power point. The ratio of both areas defines the fill factor.

parameter for the extraction of power is the fill factor (FF). It is the ratio of the power that can be extracted at the point of maximum power (MPP) and the product of V_{oc} and I_{sc}

$$FF = \frac{P_{MPP}}{V_{oc}I_{sc}}. \quad (2.30)$$

A graphic description of the fill factor is displayed by the ratio between the orange and gray square in Figure 2.15. In a first approximation, the fill factor is a measure for the mobility-lifetime product, the ability of the solar cell to extract photogenerated charge carriers.[63] It is a complex, interference-prone parameter that can be influenced by many factors, such as barriers to the transport layers[64] or imbalanced mobility between electrons and holes in the absorber layer[65]. The power conversion efficiency (η_{PCE}) of a solar cell is given by

$$\eta_{PCE} = \frac{I_{sc}V_{oc}FF}{P_{ill}}. \quad (2.31)$$

P_{ill} is the irradiated power. The last parameter is the saturation, it is calculated by

$$Sat = \frac{I(V = -1V)}{I_{sc}}. \quad (2.32)$$

It gives information about the blocking behavior of the solar cell. It can be influenced by photo-shunts or S-kinks[66], which appear in the third quadrant e.g. for extraction barriers[64]. The next step in the analytical description of a solar cell is usually the model with

an equivalent circuit like in Figure 2.16. Therefore, the solar cell is connected with a parallel and a serial resistor and a parallel current source, which reflects the photocurrent.

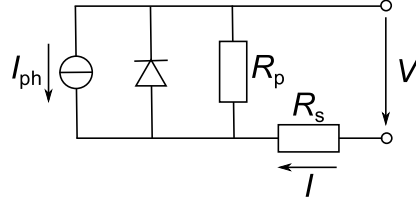


Figure 2.16.: Equivalent circuit for a solar cell. The parallel circuit consists of a resistor R_p , an ideal diode, and a current source, which provides the photocurrent I_{ph} . An additional resistor is connected in series to model the series resistance of the solar cell.

The current of this circuit is then described by

$$I = I_s \left\{ \exp \left(\frac{q(V - IR_s)}{n_{id}k_B T} \right) - 1 \right\} + \frac{V - IR_s}{R_p} - I_{ph}. \quad (2.33)$$

This model is important for the evaluation of impedance spectroscopy measurements, in which the ideal solar cell is replaced by a capacitor. Figure 2.17(a) shows the influence of an increasing series resistance on the IV curve. In the first quadrant, the curve flattens in forward direction. Accordingly, the fill factor decreases and for very high series resistances even I_{sc} decreases. V_{oc} is not affected. The opposite behavior can be seen in Figure 2.17(b) for a decreasing parallel resistance. Here, V_{oc} decreases and the saturation increases, while I_{sc} remains unaffected.

2.3.2. Organic solar cells

Heterojunctions

A heterojunction is an interface between two semiconductors with different energy levels. An example is depicted in Figure 2.18(a). The material with the higher energy levels is named donor, because it “donates” the electron that the acceptor “accepts”. This concept is vital for organic photovoltaics, because the offsets in electron affinity and ionization potential enable the dissociation of the Frenkel excitons into a charge separated state (CS). At the heterojunction, a charge-transfer state (CT) manifold forms, which is depicted in Figure 2.18(b).[58] These are excited states in which the bound electron-hole pair is distributed over a donor and an acceptor molecule. The excited electron is located on the acceptor molecule, while the hole is located on a neighboring donor molecule. This configuration can be reached by excitons that diffused to the heterojunction interface or directly by photoabsorption from the ground state.[67]

2. Theory

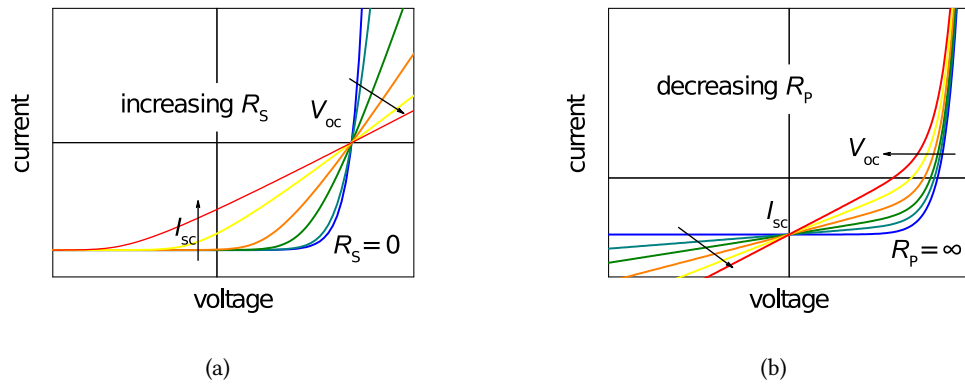


Figure 2.17.: Influence of an (a) increasing series resistance and (b) decreasing parallel resistance on the IV curve.

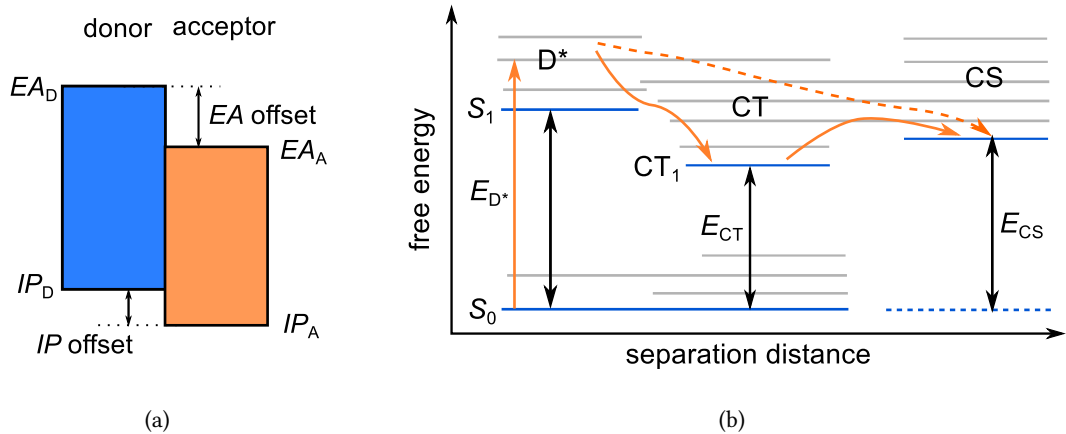


Figure 2.18.: (a) Heterojunction in single electron picture. (b) Heterojunction in a two-particle picture. The solid orange arrows indicate processes that lead to the formation of free charge carriers. Adapted from [67].

Charge generation upon photoexcitation

The external quantum efficiency (EQE) describes the probability of the conversion of a photon, which arrives at the solar cell, into charge carriers that are extracted at the electrodes. For organic solar cells, the external quantum efficiency can be written as a product of part-efficiencies that describe the subsequent processes during the charge generation[55]:

$$EQE(\lambda) = \eta_A(\lambda)\eta_{ED}\eta_{CT}(V)\eta_{CC}(V) \quad (2.34)$$

$$= \eta_A(\lambda)IQE(V). \quad (2.35)$$

η_A describes the probability that an incoming photon is absorbed and an exciton forms. This parameter depends mainly on the absorption coefficient of the donor (acceptor) material and is thus dependent on the wavelength of the photon. The probability that an exciton reaches the heterojunction is given by η_{ED} . Since the exciton has no net charge, it is not influenced by electric field. Consequently, η_{ED} depends mainly on the exciton diffusion length of the exciton in the specific material. However, also the geometry/design of the heterojunction is important. η_{CT} is the probability that an exciton that reached the heterojunction is dissociated into free charge carriers. This process is described in detail in the next section. η_{CC} is the charge carrier collection efficiency that deals with the processes after the free charge carriers are created. It is related to the charge transport properties of the absorber materials as well as the properties of transport/blocking layers and their contact to the electrodes. The product of η_{ED} , η_{CT} , and η_{CC} is also called internal quantum efficiency (*IQE*). The calculation of the internal quantum efficiency is, concerning the absorption, ambiguous and depends on the circumstances. There are basically two cases: in the first case the absorption of the whole solar cell is considered. In the second case only the absorption of the active layers are considered. While the first case is experimentally easier accessible, the second case requires supporting optical calculations and knowledge of the (complex) refractive indices of all layers in the solar cell. The usage of both methods depends on the conclusion that is desired. State-of-the-art organic solar cells can reach *IQEs* higher than 90%. [68]

Charge-transfer state

Figure 2.18(b) shows a scheme of the processes from the absorption of a photon over the dissociation of an exciton into free charge carriers with a focus on the charge-transfer state. The free energy of the participating states is therefore depicted as a function of the distance between electron and hole. In the cartoon, a donor molecule is excited and an exciton is formed. When the exciton arrives at the heterojunction, a CT state is formed. Subsequently, the CT state is split into free charge carriers. There is a debate whether this splitting happens using the fully relaxed CT state CT_1 or using excited, so called “hot” CT states. In case of a hot CT state, the transfer to the charge separated state happens without relaxation to a relaxed CT state. Thereby, the excess energy from the transfer is considered to support the splitting process. Vandewal *et al.* proved for several systems that for an efficient charge separation, the path over the relaxed CT state is sufficient. [67] For this purpose, they photo-excited organic solar cells at different wavelengths and determined the internal quantum efficiency. The *IQEs* were independent of the incoming photon energies down to an energy that corresponds to the – fully relaxed – CT_1 state. [67] A correlation has been observed between the energy of the CT state and eV_{oc} . The energy of the CT state determines the maximum achievable open circuit voltage in an organic solar cell. Accordingly, a high CT energy is favorable. However, the CT state should be lower than the triplet state to avoid a relaxation

2. Theory

path of the CT state to the triplet state. This case was discussed by Schueppel *et al.* and leads to low current densities.[69] Veldman *et al.* suggest therefore a maximum energy difference between the triplet state and the CT state of 0.2 eV.[70]

Recombination

For every step of the charge separation, there is also the chance that the charge carriers recombine and are lost for the current generation. The recombination processes can be divided into geminate and non-geminate recombination. The former describes all relaxations to the ground state in which the electron and the hole stem from a single photon absorption (geminus lat. twin). Hence, exciton recombination and the recombination of a CT-state are classified into geminate recombination. Nongeminate recombination describes all other recombination events. This includes e.g. recombination events after the separation of electron and hole and recombination with injected charge carriers. Bimolecular-, trap-assisted- and Auger recombination fall into this category.[59] Bimolecular recombination describes the recombination of a mobile hole and a mobile electron. It can be described by a Langevin-type equation. The second mechanism is trap-assisted recombination, in which a free charge carrier gets bound by a trap state. Subsequently, an opposite charge carrier recombines with the trapped charge carrier. In addition, recombination processes with a recombination order higher than two are observed. The reasons and mechanisms of this effect are still unclear.[59]

Relationship between V_{oc} and dark current

Vandewal *et al.* derived an equation formally equal to the Shockley equation.[58] The starting point was the reciprocity relationship derived by Rau[71]

$$\Phi_{EL}(E, V) = EQE(E)\Phi_{BB}(E) \left(\exp\left(\frac{qV}{k_B T}\right) - 1 \right). \quad (2.36)$$

This equation relates the excess electroluminescence (Φ_{EL}) of a solar cell, when driven as a photodiode, with the photovoltaic properties – namely the EQE. The electroluminescence spectrum is the product of the external quantum efficiency and the black body spectrum at ambient conditions (Φ_{BB}). The authors state that for organic solar cells the black body spectrum at ambient conditions overlaps mainly the absorption spectrum of the CT state and found a convincing agreement between the measured and calculated electroluminescence values.[58] Assuming an ideal diode characteristic

$$j_{inj}(V) = j_0 \left(\exp\left(\frac{qV}{k_B T}\right) - 1 \right) \quad (2.37)$$

for the injection current (j_{inj}) with j_0 as the dark saturation current, they deduced

$$j_0 EQE_{EL}(E) = qEQE(E)\Phi_{BB}(E). \quad (2.38)$$

EQE_{EL} is the external quantum efficiency for the electroluminescence. Hence, EQE_{EL} is the quotient from Φ_{EL} and j_{inj} . The integral over the photon energy leads to the expression

$$j_0 = \frac{q}{EQE_{EL}} \int EQE(E)\Phi_{BB}(E)dE \quad (2.39)$$

where EQE_{EL} is the integral of the measured $EQE_{EL}(E)$ over all photon energies. The dark saturation current is therefore attributed to measurable electro-optical properties of the CT-state.[58] By inserting j_0 into equation (2.37) and considering it at open circuit conditions, Vandewal *et al.* derived

$$V_{oc} = \frac{k_B T}{q} \ln \left(\frac{j_{sc}}{j_0} + 1 \right) \quad (2.40)$$

and could achieve a good agreement between measured and calculated V_{oc} .[58]

Losses in V_{oc}

In order to further quantify the losses from the CT state energy to qV_{oc} , Vandewal *et al.* deduced the following equation [72]

$$qV_{oc} = E_{CT} + \underbrace{k_B T \ln \left(\frac{j_{sc} h^3 c^2}{f_{CT} q 2\pi (E_{CT} - \lambda_{reorg})} \right)}_{\text{radiative losses}} + \underbrace{k_B T \ln (EQE_{EL})}_{\text{nonradiative losses}}. \quad (2.41)$$

In this formula, λ_{reorg} represents the reorganization energy and f_{CT} is a measure for the number of CT states in a solar cell.[72] The voltage losses from E_{CT} to qV_{oc} are classified into radiative losses (ΔV_{rad}) and nonradiative voltage losses (ΔV_{nonrad}). Both terms are negative. The radiation losses are in principle unavoidable, as stated in the reciprocity relationship (2.36). The nonradiative voltage losses can be reduced by eliminating nonradiative pathways.[58] Vandewal *et al.* found that typical values for ΔV_{rad} in organic solar cells are 0.25 V and 0.35 V for ΔV_{nonrad} .[72]

Forms of heterojunctions

Figure 2.19 shows two types of heterojunctions: (a) planar heterojunctions (PHJ) and (b) bulk heterojunctions (BHJ).[73,74] The PHJ approach was invented in 1986 by Tang *et al.* and was a milestone in the research on organic photovoltaics.[73] In this concept, the donor and the acceptor layer are stacked on top of each other. The stack design leads to good charge carrier extraction properties, resulting in high fill factors. For a diindenoperylene derivative in

2. Theory

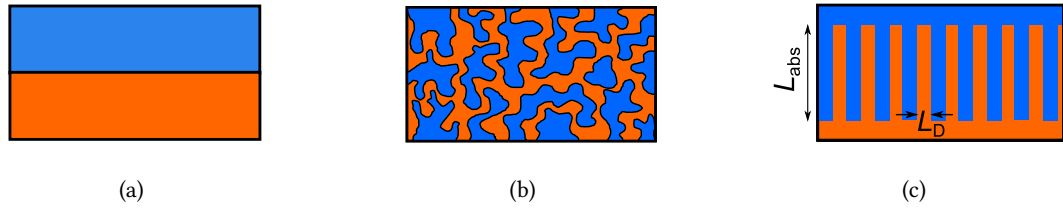


Figure 2.19.: (a) Planar heterojunction and (b) bulk heterojunction. The donor is depicted in blue and the acceptor in orange. (c) An ideal bulk heterojunction with a pillar structure. The length of the pillars corresponds is in the range of the characteristic absorption length L_{abs} and the thickness in the range of the exciton diffusion length L_{D} .

combination with C_{60} , Meiss *et al.* reported fill factors up to 76% in PHJ solar cells.[75] The drawback of the PHJ concept is the thickness limitation of the donor and acceptor layer by their exciton diffusion lengths. Though small organic molecules have very high absorption coefficients, there is still nearly one order of magnitude difference between the characteristic absorption length and the exciton diffusion length. For this reason, the j_{sc} of a PHJ is in general much smaller than in a BHJ. This concept was invented by Hiramoto *et al.* in 1991.[74] The main challenge in this approach is to adjust material phases to the exciton diffusion length. When the phase separation is too large, excitons recombine before they reach a heterojunction and the solar cell suffers from current losses. When the phase separation is too fine the exciton separation is high, but the charge extraction is reduced due to recombination of charge carriers.[76] A common way to increase the phase separation is the increase of the crystallinity by substrate heating or lowering of the deposition rate.[34, 77] Figure 2.19(c) shows the ideal bulk heterojunction, which was among others investigated by Yang *et al.*[78] It is an interpenetrating network with two (nanocrystalline) phases that are arranged like pillars. The width of the percolation paths is then in the range of the exciton diffusion length. Furthermore, the length of the pillars are in the range of the characteristic absorption length of the material. A promising approach to form the ideal BHJ structure is the technique of glancing angle deposition.[79, 80]

The p-i-n concept

Doped wide-gap materials used as transport layers form the centerpiece of the p-i-n concept. The scheme is displayed in Figure 2.20(a), in which the intrinsic absorber layers (i) are sandwiched between a p-doped hole transport layer (HTL) and an n-doped electron transport layer (ETL).[57] In an ideal case, the transport layers have a large optical gap to avoid parasitic absorption. An optical gap larger than 3 eV is often noted as a benchmark.[16] The energy levels of the transport layer have to be adjusted to the donor/acceptor layer to ensure charge transport without barriers.[57] As shown in Figure 2.20(a), the ionization potential of donor and HTL have to be aligned as well as the electron affinity of the acceptor and the ETL. The large energy gap of the transport layers in conjunction with the aligned energy levels

form selective membranes for the charge carriers as proposed by Würfel.[54] This is especially important for BHJs in which e.g. the acceptor phase has an interface with the HTL. Furthermore, the quenching of excitons at the transport layer is prohibited. Doped transport layers with typical conductivities of 10^{-4} - 10^{-5} S/cm[57] enable transport layers with ≈ 100 nm thickness without a significant increase in series resistance. The tunable thicknesses of both transport layers become free parameters. These parameters can be used to manipulate the optical field, which is the spatial distribution of the light intensity in the solar cell. It is a standing wave as schematically shown in Figure 2.20(a), which forms in the cavity between the electrodes. The right choice of the transport layer thicknesses maximizes the absorption in the absorber layers. For example, Figure 2.20(b) shows the simulation of the spatial absorption of two p-i-n solar cells.⁴ The only difference between these solar cells is the thickness of the HTL with 50 nm and 150 nm. One can see that the absorption in the absorber layer of the solar cell with the 50 nm thick HTL layer is significantly stronger than in the 150 nm HTL solar cell.

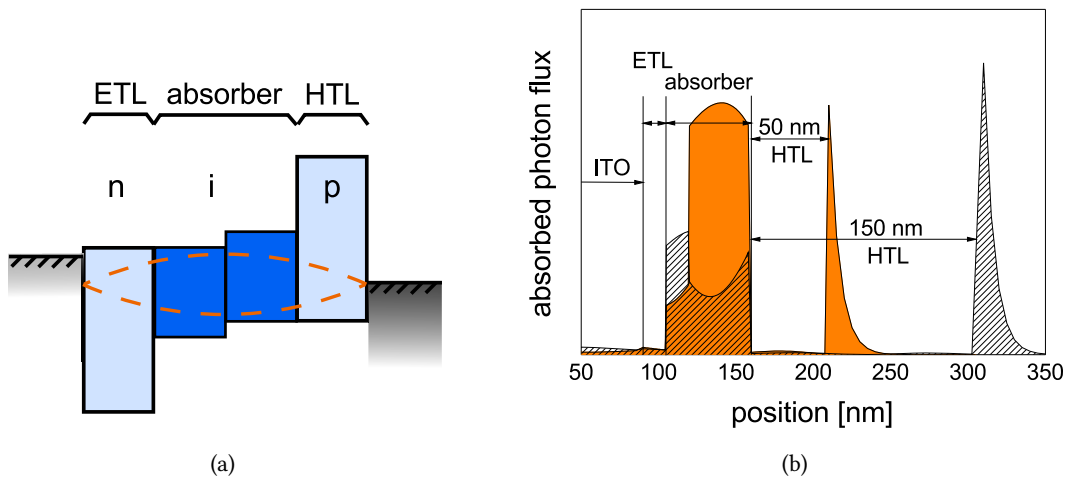


Figure 2.20.: (a) Schematic stack design of a p-i-n organic solar cell. The light blue squares indicate transport layers and the light green squares are the donor and the acceptor layer. The gray squares represent the electrodes which form an optical cavity. The dashed lines represent a standing wave of the optical field. (b) Absorption profiles of two solar cells with an HTL thickness of 50 nm (orange) and 150 nm (shaded). The device with 50 nm HTL thickness absorbs significantly more photons than the device with 150 nm HTL thickness.

In addition, the relatively free choice of the transport layer thicknesses enables the usage as a smoothing layer for relatively rough absorber layers to prevent short circuits. Since the

⁴The calculation was performed using OSOLemio, a software written by Dr. Mauro Furno (formerly IAPP) based on a transfer-matrix-algorithm.

2. Theory

built-in field is determined by the work function in the doped transport layers and not by the work function of the electrodes[81,82], it is also possible to invert the stack design (n-i-p configuration) with respect to the electrodes. This can be an advantage if the morphology of a donor or acceptor layer depends on the underlying layer.[83] A typical hole transport layer at the IAPP consists of three separate layers: an intrinsic matrix layer next to the donor of about 5 nm, a p-doped matrix layer with variable thickness and a 1-2 nm thick layer of pure p-dopant. The intrinsic matrix layer acts as a spacer between the p-doped layer and the intrinsic absorber layers. Since the acceptor phase of a bulk heterojunction can have contact with the hole transport layer, this spacer prevents the recombination of generated electrons in the acceptor phase with the high concentration of free holes in the p-doped transport layer. The 1-2 nm pure dopant do not form a closed layer, it is rather a very high doping of the adjacent p-doped layer to ensure an ohmic contact to the electrode by creating a Schottky barrier.

3. Experimental

This chapter presents the materials, instruments, and methods used in this work. At the beginning, Section 3.1 gives an overview of the properties of the materials. Additionally, thermal gradient sublimation as a means of material purification is explained. Section 3.2 covers all aspects of the preparation of organic thin films, including the design of the different substrates and the substrate cleaning procedure. Furthermore, the different evaporation chambers are presented. A focus is set on the properties of quartz crystal microbalances as this measurement system is important for chapter 7. The first part of section 3.3 describes measurement techniques and evaluation methods that are applied to organic thin films. The second part presents methods to characterize solar cells.

3.1. Materials

Table 3.1 gives a summary about the densities, energy levels, and suppliers of the used materials. In addition, data that were obtained in this work are added to give an overview. In the case of bulk heterojunctions and doped layers, two or more materials are blended in one layer. The denotation of the composition of these layers differs for bulk heterojunctions and doped layers. The composition of doped layers is expressed in weight percent (wt%). Typical doping concentrations are in the range of 3-10 wt%. The doping concentration is then achieved through the adjustment of the deposition rates of matrix and dopant materials. Thereby, the density of the dopants is considered equal to the density of the matrix materials. In contrast, the composition of bulk heterojunctions is given in a volume ratio, e.g. 2:1, in which the first number refers to the donor and the second number to the acceptor. Figure 3.1 gives an overview of the molecular structures of materials used in this work. The molecular structure of NDP9 is not published.

Figure 3.2 shows the extinction coefficients (k) of the matrix materials to give an impression of the (low) parasitic absorption of the transport layers. Furthermore, C₆₀ is included as it is used as an absorber as well as a transport material. Accordingly, its extinction coefficient is a bit higher than for the other materials, which are solely used as matrix materials for transport layers. However, the superior charge transport properties of (n-doped) C₆₀ account for the higher absorption.[84] In addition, Figure 3.2 comprises a comparison of the extinction coefficients of pure and p-doped BF-DPB (10 wt% F₆-TCNNQ). The additional absorption peak at 500 nm for the doped BF-DPB demonstrates that the absorption of the dopant should be also considered. Now, selected properties of the materials are briefly summarized.

3. Experimental

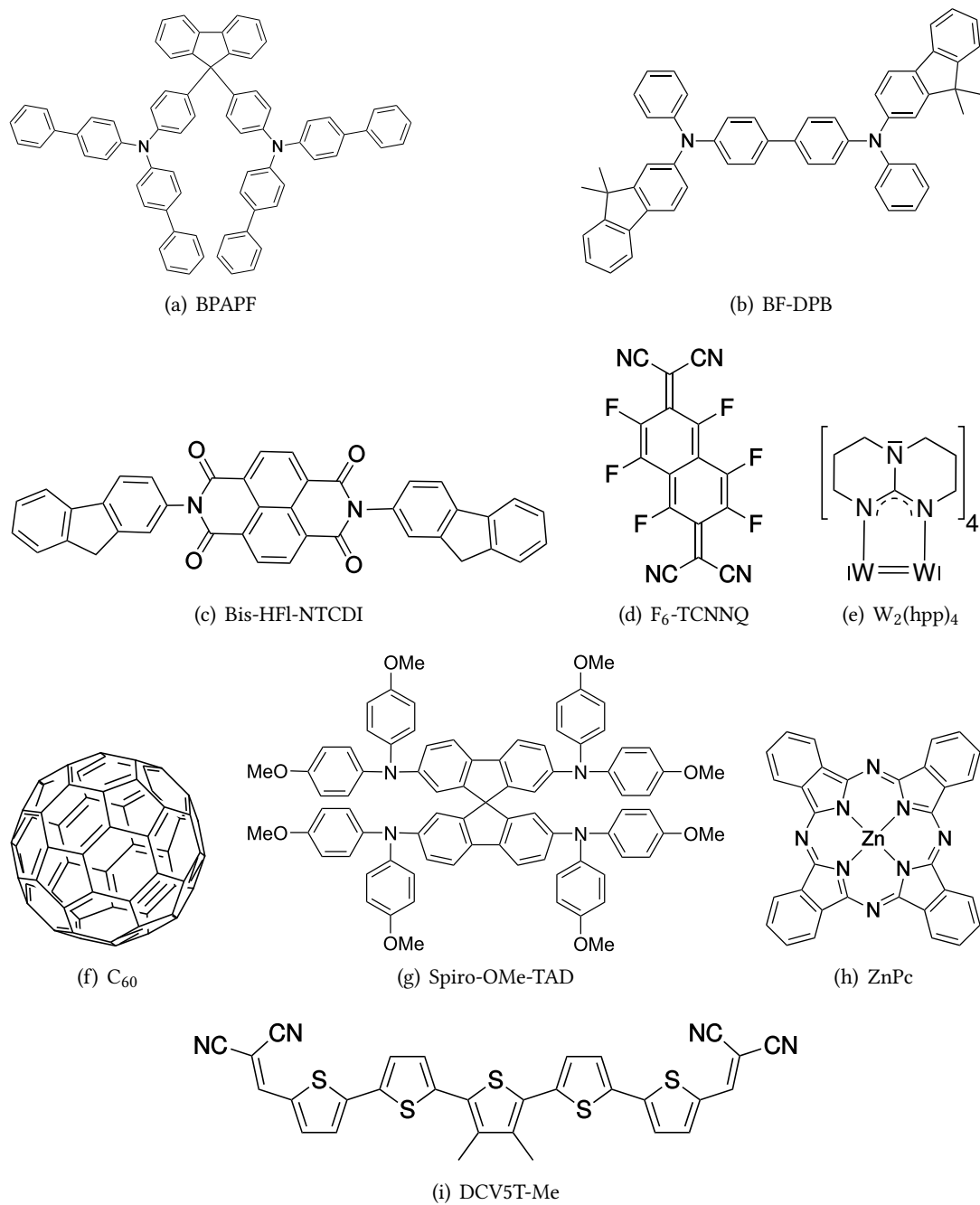


Figure 3.1.: Overview about the molecular structures used in this work.

short name	long name	supplier	density [g/cm ³]	I_P [eV]	EA [eV]
C ₆₀	fullerene	CreaPhys	1.63 [∇]	6.4 [△]	4.0 [85]
ZnPc	zinc-phthalocyanine	CreaPhys	1.55 [∇]	5.1 [‡]	3.34 [86]
BPAPF	9,9-bis[4-(N,N-bis-biphenyl-4-yl-amino)phenyl]-9H-fluorene	LumTec	1.2 [*]	5.6 [△]	2.2 [87]
BF-DPB	N,N'-((Diphenyl-N,N'-bis)9,9'-dimethyl-fluoren-2-yl)-benzidine	IAPP	1.21 [∇]	5.23 [50]	
Spiro-OMe-TAD	2,2',7,7'-Tetrakis[N,N-di(4-methoxyphenyl)amino]-9,9'-spirobifluorene	Feiming [■]	1.3 [*]	5.0 [88]	
Bis-HF1-NTCDI	N,N-Bis(fluoren-2-yl)-naphthalenetetracarboxylic diimide	IAPP	1.25 [∇]	6.55 [16]	
F ₆ -TCNNQ	2,2'-(perfluoronaphthalene-2,6-diylidene)dimalononitrile	Novaled	1.5 [*] ◇		
W ₂ (hpp) ₄	tetrakis(1,3,4,6,7,8-hexahydro-2H-pyrimido[1,2-a]pyrimidato)ditungsten (II)	Novaled	◇	2.68 [89]	
NDP9	-	Novaled	1.3 [*] ◇		
DCV-5T-Me(3,3)	2,2'-(3'',4''-dimethyl-[2,2':5',2'':5'',2''':5''',2''''-quinque thiophene]-5,5''-diyl)bis(methanylylidene)dimalononitrile	Synthon	1.3 [*]	5.75 [‡]	
DTDCTB	2-[7-(5-N,N-ditolylaminothiophen-2-yl)-2,1,3-benzothiazol-4-yl]methylenemalononitrile	IAPP	1.364 [14]	5.4 [†]	
PRTF	(Z)-3-(7-(5-(di-p-tolylamino)thiophen-2-yl)benzo-2,1,3-thiadiazol-4-yl)-2-(perfluoropyridin-4-yl)acrylonitrile	IAPP	1.3 [*]	5.55 [†]	
CNTF	(Z)-4-(1-cyano-2-(7-(5-(di-p-tolylamino)thiophen-2-yl)benzo-2,1,3-thiadiazol-4-yl)vinyl)-2,3,5,6-tetrafluorobenzonitrile	IAPP	1.3 [*]	5.65 [†]	
TFTF	(Z)-3-(7-(5-(di-p-tolylamino)thiophen-2-yl)benzo-2,1,3-thiadiazol-4-yl)-2-(2,3,5,6-tetrafluoro-4-(trifluoromethyl)phenyl)acrylonitrile	IAPP	1.3 [*]	5.65 [†]	
QM1	2-(dicyanomethylene)-5'-(1,3-dithiol-2-ylidene)-5,5'-dihydro-Delta2,2'-bithiophene	IAPP	1.3 [*]	4.95 [*]	

Table 3.1.: Physical properties and suppliers of the materials used in this work. ◇ When the dopant is used for doping of a matrix material, the density of the respective matrix material is used. ‡ measured by Dr. Max Tietze (IAPP) using UPS. △ measured by Dr. Selina Olthof (IAPP) using UPS. * measured by Anton Kirch (IAPP) by V_0 -method (see section A.2 in the Appendix). † measured by Martin Schwarze (IAPP) using UPS. ∇ measured with profilometer at IAPP. ■ assumed density. Feiming Chemical Limited.

3. Experimental

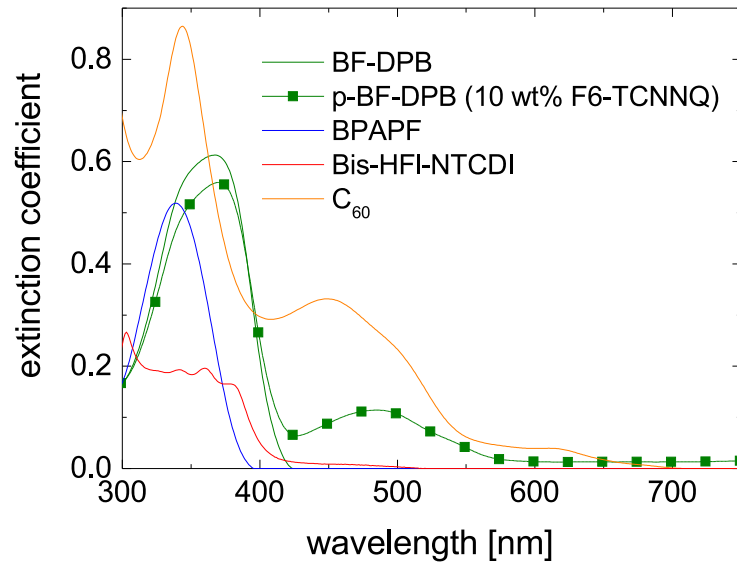


Figure 3.2.: Extinction coefficients (k) of common hole and electron transport materials. The extinction coefficient of Bis-HFI-NTCDI was determined by Dr. Christiane Falkenberg (IAPP), the other values by Dr. André Merten (IAPP).

BPAPF is the matrix material with the highest ionization potential (5.6 eV) used in this work. It has a high glass transition temperature of 167 °C[18] and is usually doped with 10 wt% NDP9.[90, 91] BPAPF forms amorphous layers at room temperature.[92]

BF-DPB has an ionization potential of 5.23 eV, which is not as high as BPAPF. In this work, it is doped with 10 wt% F₆-TCNNQ, which corresponds to a conductivity of 10⁻⁴ S/cm[84], but it is also dopable with NDP9. It has a glass transition temperature of 121 °C.[17] The donors ZnPc and QM1 are used in combination with p-doped BF-DPB as hole transport layer.

Bis-HFI-NTCDI is a low absorbing electron transport material designed to contact C₆₀. It has a lower extinction coefficient than C₆₀, and with an optical gap of 3.0 eV it meets the requirement, discussed in the p-i-n section (Section 2.3.2).[16] It forms polycrystalline layers at room temperature as well as on a heated substrate.[92] Bis-HFI-NTCDI is usually doped with 7 wt% W₂(hpp)₄, which results in a conductivity of 10⁻⁴ S/cm.[16]

C₆₀ is the most used acceptor in vacuum deposited small molecular solar cells. It has an electron affinity of 4.0 eV[85]. Due to its good charge transport properties, C₆₀ is also used as an electron transport material. When used as an electron transport layer, C₆₀ is doped with 3 wt% W₂(hpp)₄. C₆₀ has a polymorph crystalline thin film phase.[93] In the thin film,

C_{60} has two characteristic absorption peaks at 350 nm and 450 nm. However, it absorbs up to 700 nm, as shown in Figure 3.2.

ZnPc is a common red absorber that belongs to the class of metal phthalocyanines. In pure thin films, it is polycrystalline and occurs in a triclinic α -phase and a monoclinic β -phase, depending on the processing conditions.[94] It is used in combination with p-BF-DPB as hole transport layer.

DCV₂-5T-Me is a donor that absorbs mainly around 600 nm.[90] In combination with C_{60} as an acceptor, it achieved power conversion efficiencies of 8.3 % in a single heterojunction solar cell.[95] The optimum morphology of the BHJ is achieved in a 2:1 ratio at 80 °C using a deposition rate of 0.07 Å/s for DCV₂-5T-Me.[90] For higher substrate temperatures of 90 °C, faster deposition rates of 0.2 Å/s are necessary.[95] However, for too high deposition temperatures the yield of evaporated mass to deposited thickness drops significantly.[90] With an ionization potential of 5.75 eV, DCV₂-5T-Me is used in combination with p-BPAPF as hole transport layer.[90]

3.1.1. Sublimation

Before the organic materials are evaporated in one of the vacuum chambers, they are usually purified from remainders from the synthesis.¹ The purification is done by thermal gradient sublimation. Figure 3.3 shows a sublimation tube after a sublimation. Initially, the material is filled in the left side of the tube. The rest of the tube is filled with glass rings. Afterwards, the tube is evacuated and the material is heated. Additional heating elements are positioned along the tube to create a negative temperature gradient. When the sublimation temperature is reached, the molecules fly through the tube. After a certain path length, the molecules condense on the rings in the tube. The path length is dependent on the mass of the molecules, their sublimation temperature, and the applied temperature gradient. In general, lighter molecules with low sublimation temperatures fly farther than heavy molecules with a high sublimation temperature. Often, two to three subsequent sublimation steps are performed to purify the material. The thermal gradient sublimation is performed by Annette Petrich (IAPP).



Figure 3.3.: Picture of a sublimation tube after sublimation. On the left end of the tube, remainders of the original material are visible. The image was taken by Annette Petrich.

¹Dopants are used as purchased.

3. Experimental

3.2. Preparation methods

3.2.1. Sample design

Figure 3.4 shows the design of a standard solar cell used at IAPP. It consists of a 1 mm thick glass substrate with a pre-structured 90 nm thick layer of indium tin oxide (ITO). The ITO is the semi-transparent bottom contact of the solar cells and arranged in a structure consisting of four fingers. The substrates are purchased (Thin Film Devices Inc., USA) in 6x6 matrices (150x150 mm²) and – if necessary – cut into single substrates.

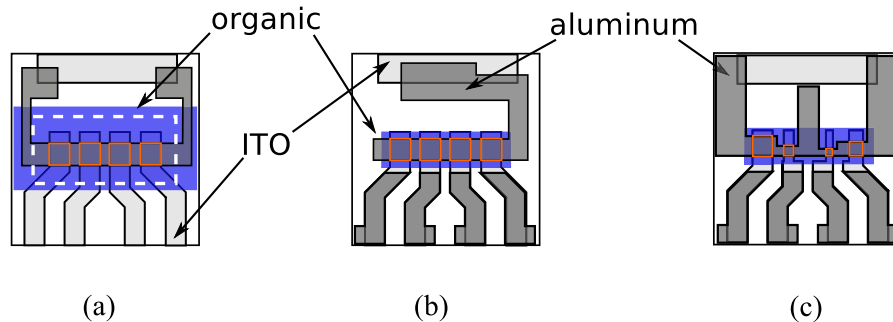


Figure 3.4.: Sample layout of (a) single samples, (b) samples produced within a 6x6 or 4x4 matrix, and (c) samples with different active areas. The orange contour marks the active area that is given by the geometrical overlap of the bottom contact (ITO) and the top electrode (aluminum). The dashed white square in (a) marks the position of the cover glass.

The sample size of a single substrate is 25x25 mm². Each substrate can support four 6.44 mm² large solar cells, which are usually referred to as pixels. The area of the solar cells is defined by the geometrical overlap of bottom- and top contact. For some measurement techniques (e.g. OTRACE), smaller areas are advantageous, because the capacitance of a solar cell is proportional to its area, which limits the detection of fast signals in form of the RC -time. Therefore, a layout as shown in Figure 3.4 (c) with 6.44 / 1.68 / 0.88 / 3.27 mm² pixel area can be used. It is produced from a normal substrate by laser-structuring. After the solar cells are processed, they are encapsulated with a cover glass using a UV-hardening glue. For samples on a 4x4 or 6x6 matrix, a moisture getter is included. The encapsulation is performed by a technician.

3.2.2. Substrate cleaning

The following paragraph describes the substrate cleaning procedure for single glass and ITO-substrates. However, most steps apply also to the 150x150 mm² substrates. The procedure is performed by a technician of the institute. It starts by cleaning the 150x150 mm² substrates with an acetone soaked cotton tissue. Subsequently, this step is repeated with ethanol. Afterwards, the substrates are cut into single samples. The substrates are then blown clean

with nitrogen to remove possible dust remainders from the cutting. Shortly after, the substrates are put into an ultrasonic bath with a N-Methyl-2-pyrrolidone (NMP) solution for 20 min. Then, the substrates are put into pure water and rinsed for 5 min. Subsequently, the substrates are put in an ultrasonic bath with pure water for 10 min and afterwards with high purity ethanol for additional 15 min. The substrates are then put in a spin rinser, where they are first rinsed with pure water and afterwards blown dry with nitrogen. At the end of the procedure, the single substrates are plasma cleaned using an oxygen plasma for 10 min. Note, that the plasma cleaning step is not applied to the uncut 150x150 mm² substrates. After the cleaning steps, the single samples are stored in a box until they are used for sample preparation.

3.2.3. Vacuum deposition

Four evaporation tools are used for the deposition of organic thin films: The multi-chamber system “UFO 1”, the vacuum chambers “Lesker A” and “Lesker B” and the material test chamber “MTC”. All systems are evacuated with a combination of forepump and turbo molecular pump to achieve high vacuum or ultra high vacuum (UHV). Figure 3.5(a) shows the basic principle of vacuum deposition on the example of co-evaporation. The organic material, in form of a powder is put into an aluminum oxide crucible, which is resistively heated with copper wires. The temperature of the crucible is measured at the bottom with a thermocouple type K. Upon heating, the powder sublimates or evaporates from the crucible. Due to vacuum, an evaporation cone forms that is directed to the substrate. The evaporation rate is controlled via a quartz crystal microbalance (QCM). For blend layers, two or more materials are evaporated at the same time. For this case, Figure 3.5(a) shows that crosstalk between the QCMs can be avoided by appropriate positioning or shielding.

UFO 1

The UFO 1 is a multi-chamber system (Bestec, Germany) with a central chamber for the distribution of the samples. Several chambers are connected to the central chamber: two chambers for the evaporation of intrinsic organic layers, one for p-doping, one for n-doping, and one for metal evaporation. Furthermore, the central chamber provides access to a substrate holder storage with a connection to the “UPS/XPS” chamber. The base pressure is 10⁻¹⁰ - 10⁻⁸ mbar depending on the chamber. In addition, the chamber system has a connection to a glovebox with a nitrogen atmosphere, which enables the transport of organic thin films under nitrogen to encapsulation.

Figure 3.5(b) shows an image of a typical substrate holder that is used in UFO 1 and in the MTC chamber. Such a substrate holder can consist of teflon or Macor. Teflon substrate holders are used for substrate temperatures below approximately 90 °C. Substrate holders out of Macor, a special ceramic, are used for higher substrate temperatures. The substrate is heated via resistive heating. For this purpose, a fully covered ITO substrate is put behind the actual substrate into the substrate holder, as shown in Figure 3.5(c). Heating wires are attached on the holohedral ITO substrate at the backside of the substrate holder using liquid silver. The temperature is measured with a thermocouple type K on the (device-) substrate

3. Experimental

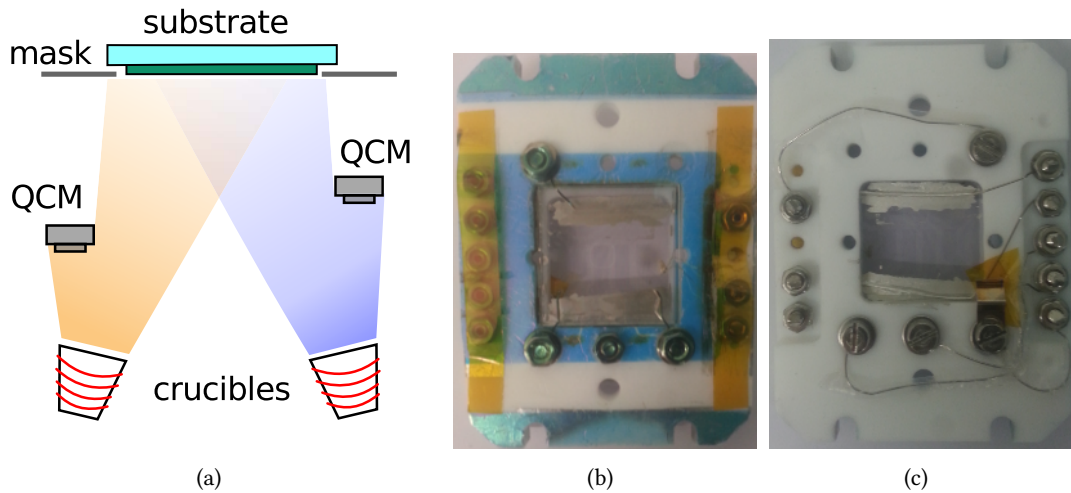


Figure 3.5.: (a) Principle of co-evaporation. The red lines indicate heating wires. (b) Front view of a single substrate holder. A thermocouple type K is attached next to the pixels using liquid silver. The pins fix the substrate and contact the electrodes of the device. (c) Rear view of a single substrate holder. A fully covered ITO substrate is contacted with heating wires using liquid silver. The other wires contact the pins on the front side for electric measurements.

itself. It is placed directly next to the pixels, as the temperature gradient towards the edges of the substrate is quite steep mounting up to 10 K. A heat image of the temperature distribution can be found in ref. [93]. If not stated otherwise, the single layer samples in chapters 4-6 are processed at the UFO 1.

Lesker A/B

There are two evaporation chambers at IAPP that are able to evaporate sample matrices of 4x4 samples (Lesker A) and 6x6 samples (Lesker B). Both chambers are attached to glove-boxes containing a nitrogen atmosphere. These chambers are operated by the “Lesker team” (Tobias Günther, Caroline Walde, and Andreas Wendel – IAPP). Figure 3.6 shows a picture of a 6x6 sample matrix. With the support of different masks and movable covers (wedges), specific areas of the matrix can be shadowed, respectively addressed. Basically, one vary the columns and rows. Such a variation can be seen on the different colors of the active areas of the devices presented in Figure 3.6. During the layer deposition, the substrate is constantly rotated to ensure a homogenous deposition across the 150x150 mm² sample. Nevertheless, there is a thickness gradient from the center of the substrate to the corners.[96] Accordingly, the thickness in the corner can be up to 13% lower than in the center of the substrate.[96] The thickness profile depends on the position and alignment of the source, the material, and the evaporation rate.[96]

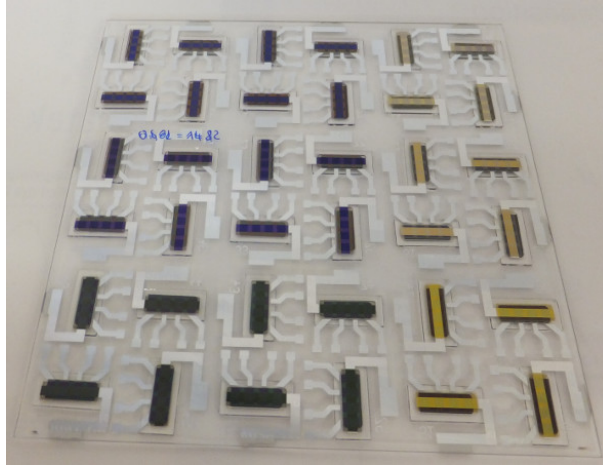


Figure 3.6.: 6x6 sample matrix of solar cells. The variations in the color of the devices indicate differences in the preparation using the wedging system.

Four quartz lamps at the backside of the substrate in Lesker B enable substrate heating up to 150 °C. The substrate temperature is not measured during the preparation of samples. However, a temperature sensor is located behind the substrates. The offset between the sensor temperature and substrate temperature is known from a calibration with temperature indicators on the substrate with an accuracy of ± 5 K. At a nominal substrate temperature of, e.g., 100 °C in the middle of the substrate, the substrate temperature at the edges is 95 °C and in the corners 90 °C. If not stated otherwise, the solar cells in chapters 4-6 are processed at the Lesker chambers.

MTC

The material test chamber (MTC) is used for the co-evaporation of liquid additives. Figure 3.7(a) shows a view inside the chamber. The MTC has three sources and three water cooled QCMs. Two triple sources (CreaPhys, Germany) and one single source are used to increase the amount of available materials. Cross talk among the QCMs is prohibited by metal sheets that block the evaporation path accordingly. The MTC has no direct connection to a nitrogen atmosphere and has to be loaded under ambient conditions. The chamber achieves a base pressure of 10^{-8} - 10^{-7} mbar. For the investigations on the volatilization temperature of PDMS (see chapter 7), a QCM with temperature control was necessary. Figure 3.7(b) shows a cartoon of the heatable QCM, which can also be seen in the lower left side of Figure 3.7(a). It was custom-made by Sven Kunze (IAPP) and consists of a normal QCM, heating wires, and a temperature sensor. The heating wires are made of Kanthal and meander on the top of the QCM. They are put in ceramic tubes for a better positioning. A thermocouple type K is positioned on the downside of the QCM, next to the quartz. If not stated otherwise, the samples in chapter 7 are processed in the MTC.

3. Experimental

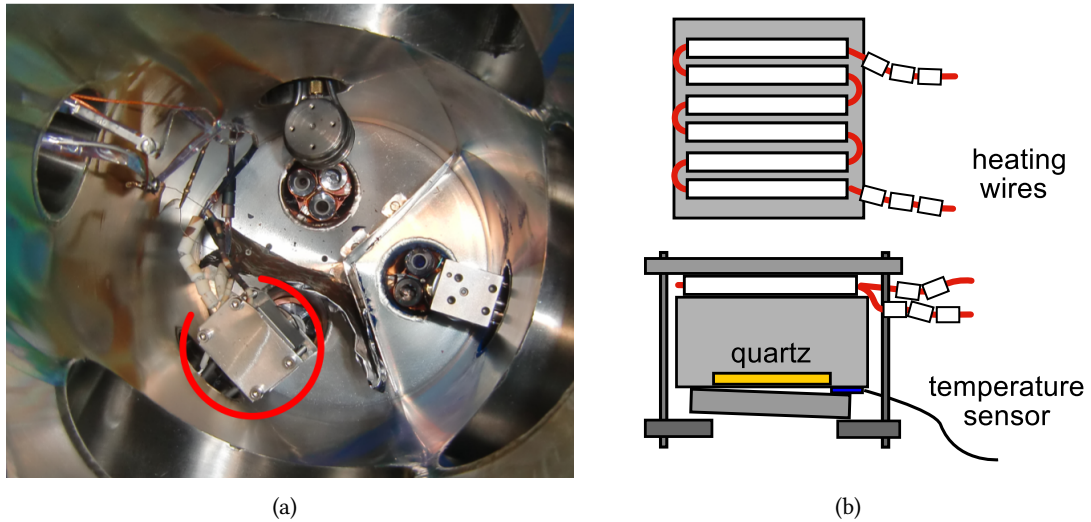


Figure 3.7.: (a) Top view into the MTC chamber. On the lower left corner of the chamber, the temperature controlled QCM (red arc) is visible. (b) Scheme of the heatable QCM with temperature sensor in top- and side view.

3.2.4. Quartz crystal microbalances

Quartz crystal microbalances (QCM) measure the thickness of thin films during the deposition. For this purpose, an AT-cut quartz is electrically excited to oscillate at its resonance frequency of $f_0=6$ MHz. This frequency decreases when mass is deposited onto the quartz. The QCM detects the frequency shift of the quartz and with the knowledge of the material density the thin film thickness can be calculated. Since the Z-ratio is commonly unknown for the applied materials, it is usually set to unity. This limits the frequency range of the QCM to a relative frequency shift $< 5\%$, because otherwise the deviations between real and measured thickness would be too large.² Figure 3.8 shows the temperature dependence of the resonance frequency of an AT-cut quartz. The relative frequency shift of the quartz resonance frequency is plotted as a function of the temperature of the quartz. Between 10°C and 35°C , the resonance frequency is nearly independent of temperature changes. At higher temperatures, the resonance frequency shifts to higher frequencies and small changes in temperature lead to large shifts in frequency. Therefore, the QCMs used in this work are water cooled to avoid temperature shifts, unless stated differently.

²empirical knowledge from the institute.

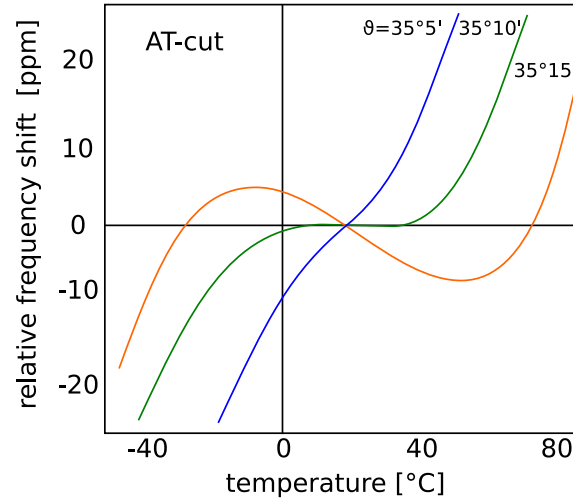


Figure 3.8.: Sketch of the temperature dependence of the resonance frequency of an AT-cut quartz crystal for different cutting angles ϑ . Adapted from ref. [97].

3.3. Measurement setups

3.3.1. UPS

Ultraviolet photoelectron spectroscopy (UPS) is based on the photoelectric effect. Figure 3.9(a) depicts the principle of UPS: Photons with a specific energy ($h\nu$) illuminate a sample. For UPS, the He I emission line (21.22 eV) of a helium discharge lamp is used. The photons are absorbed on the length scale of a few micrometers within the sample. Upon absorption, an electron becomes free with a kinetic energy that equals the difference between $h\nu$ and the binding energy of the electron. The surface sensitivity of this method stems from the mean free path length of the free electrons within the sample, which is only 1-2 nm. Interactions of highly energetic free electrons with the sample lead to secondary events, which result in an increased background signal near the high binding energy cutoff (HBEC). The ionization potential can be calculated using

$$IP = h\nu - (E_{\text{HBEC}} - E_{\text{HOMO}}). \quad (3.1)$$

E_{HOMO} refers to the energy of the electrons at the HOMO onset. The determination of both values is depicted in Figure 3.9(b). The UPS samples are evaporated on sputter-cleaned metal foils. Usually, a 5 nm interlayer of C_{60} is inserted to mimic the conditions in the solar cell. The UPS-chamber has a base pressure of 10^{-11} mbar. The analyzer is a Phoibos 100 (Specs,

3. Experimental

Germany) with an energy resolution of 140 meV. The UPS measurements were performed and evaluated by Martin Schwarze (IAPP).

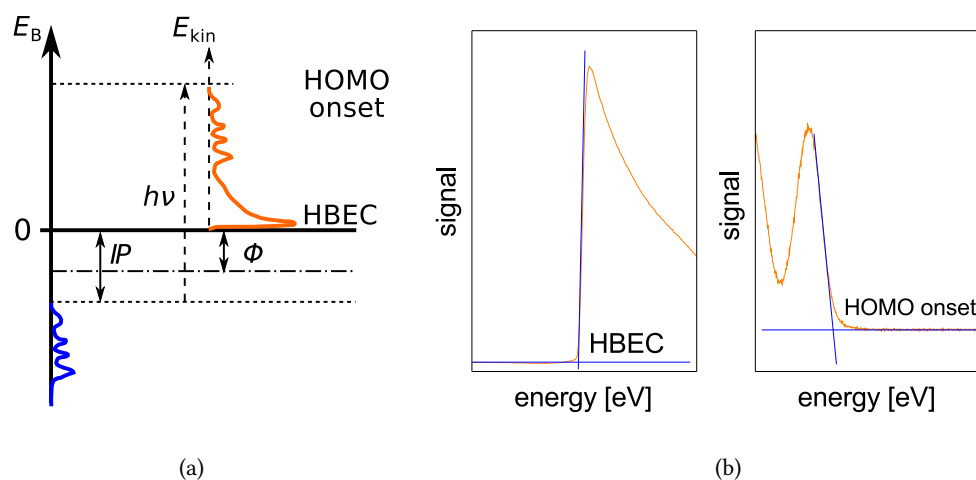


Figure 3.9.: (a) Principle of an UPS measurement. (b) Determination of the high binding energy cutoff (HBEC) and the HOMO onset. Both values are located at the intersection between the tangent through the slope and the background.

3.3.2. Mass spectrometry

MALDI-ToF-MS is the acronym for matrix assisted laser desorption/ionization time-of-flight mass spectrometry. For this technique, the material of interest (analyte) is diluted in a matrix material and casted on a substrate. Salts are added to the solution to enhance the ionization. After drying, a high voltage is applied to the substrate and the film is irradiated with a laser in order to ionize and desorb the material. The wavelength of the laser and the absorption maximum of the matrix are well adjusted. During the desorption of the matrix molecules some energy is transferred to the analyte, which desorbs as well. This procedure allows the desorption of very heavy analyte molecules without decomposition. Therefore, this technique is widely used for analyzing polymers and biomolecules[98,99]. After the desorption and ionization of the analyte molecules, a time of flight measurement is performed to determine the mass of the molecules. These measurements are taken on an Autoflex Speed TOF/TOF System (Bruker Daltonics GmbH). Dithranol is used as a matrix material in combination with sodium trifluoroacetate (NaTFAc) as salt. The acceleration voltage is 20 kV and the measurement mode is linear with positive polarity. The MALDI-ToF-MS measurements were performed and evaluated by Dr. Karin Sahre (Leibniz Institute of Polymer Research (IPF) Dresden, Germany).

LDI-ToF-MS measurements base on the same principle as MALDI-ToF-MS measurements. However, the analyte is used without an additional matrix. The LDI-ToF-MS measurements

are recorded with a MALDI-ToF spectrometer autoflex (Bruker Daltonics, Billerica, USA) using a nitrogen laser with a wavelength of 337 nm. The used laser intensity is 75 μJ /pulse. The LDI-ToF-MS measurements were performed by Dr. Florian Wölzl (IAPP).

Pyrolysis-GC-MS analyzes the degradation products of a molecule upon thermal decomposition in the absence of reactions with oxygen. The terms “GC” and “MS” refer to the analysis techniques: gas chromatography and mass spectrometry. For the pyrolysis a Pyroprobe 5000 pyrolysator (CDS Analytical, Inc.) with a platinum filament is used. The pyrolysis temperatures are 300 °C and 500 °C. The interface (CDS model 1500) is heated to 280 °C. The gas chromatograph GC7890A (Agilent Technologies) has an inlet temperature of 280 °C. The electron ionization energy of the mass spectrometer, an Agilent 5975C inert XL MSD EI/CI, is 70 eV with a detection range of 15-550 u. The pyrolysis-GC-MS measurements were performed by Eileen Schierz (IPF).

3.3.3. UV/vis-spectrometer

For transmission (T) and reflexion (R) measurements, the “MPC 3100” and “solidspec-3700” (both Shimadzu) are used. Direct and integrated measurements are possible in both devices. The slit width is 1-5 nm for transmission measurements and 20 nm for reflexion measurements. The absorption (A) is calculated using

$$A(\lambda) = 100\% - R(\lambda) - T(\lambda). \quad (3.2)$$

In some cases, the absorbance/optical density (OD) is calculated using

$$OD = -\log_{10} T(\lambda). \quad (3.3)$$

3.3.4. AFM

Two atomic force microscopes (AFM) are used: the Nanoscope IIIa (Digital Instruments, Tonawanda, USA) and the Combiscope (AIST-nt, Russia). The Combiscope can measure the standard sample sizes with 25 x 25 mm^2 , while the Nanoscope is limited to 7 x 7 mm^2 . Both microscopes are used in intermittent mode. The AFM tips for the Combiscope are TAP-AI-G purchased from BudgetSensors. The tips operate at a resonance frequency of approximately (300 \pm 20) kHz with a spring constant of 40 N/m. For the Nanoscope non-contact tips “NSC15/AIBS” (μmasch , Estonia) are used. They have a resonance frequency of ca. 325 kHz and a spring constant of 40 N/m. The tip radius is below 10 nm. Scan sizes are between 1 and 10 μm with scan rates of 0.2 - 1.0 Hz with 512 measurement points per line. The obtained images are evaluated with the software “Gwyddion”.³ The program provides several filter-tools for image processing. Often applied filters are the adjustment of lines to

³Gwyddion is a free, open-source software for the visualization and analysis of scanning probe microscopy measurements. The software is available at <http://gwyddion.net/>

3. Experimental

the height median, correction for horizontal defects and the subtraction of a plane to account for a tilt of the sample. The roughness of the sample is determined by evaluating the root-mean-square value of the height distribution according to

$$R_{\text{RMS}} = \sqrt{\frac{1}{MN} \sum_{m=1}^M \sum_{n=1}^N (z(x_m, y_n) - \langle z \rangle)^2}, \quad (3.4)$$

in which the height z is dependent on the coordinates x and y . The term $\langle z \rangle$ refers to the average height. The sums over m and n run up to 512, the number of the pixels per line. All AFM measurements are conducted in ambient conditions. Therefore, at least one monolayer of water is present on the sample surface.

3.3.5. X-ray measurements

X-ray reflectometry (XRR) measurements can provide information about the thickness, density, and roughness of thin films.[100] These measurements are performed in a Bragg-Bretano geometry as shown in Figure 3.10(a). Here, the angle of incidence ω equals the detection angle. Figure 3.11 shows an example of an XRR measurement. The intensity of the reflected X-ray beam is logarithmically plotted against 2ω . The inset shows the local minimum at $2\omega=0.4^\circ$. This minimum marks the critical angle of the total reflection at which the X-ray beam propagates along the surface of the thin film. The position of the critical angle gives information about the density of a thin film. Above this angle, the X-ray beam propagates through the thin film and the intensity of the reflected signal decreases rapidly. The prominent oscillations at $0.5^\circ - 2^\circ$ are called Kiessig fringes.[101] The angle between two fringes gives information about the thickness of the thin film and their amplitude depends on the surface roughness. However, for quantitative statements a fitting of the data is necessary. The XRR measurements are performed on a Bruker D8 Discover diffractometer (Bruker, Karlsruhe, Germany). Cu K- α -radiation with a wavelength of $\lambda=1.54 \text{ \AA}$ is used as X-ray source. The radiation is parallelized by a Göbel mirror and after reflection detected by a scintillation counter. The measurement range is $2\omega=0 \dots 5^\circ$ with a step size of 0.01° . The measurements took place at room temperature in ambient conditions and were performed by Dr. Lutz Wilde (Fraunhofer IPMS-CNT, Dresden, Germany). The determination of the film thickness, density, and surface roughness is done with the RefSim software (Bruker GmbH, Germany).

Grazing incidence X-ray diffraction (GIXRD) is a special geometry of a diffraction experiment, which is especially useful for thin films on nanometer scale.[102] Figure 3.10(b) depicts a diffraction experiment on an organic thin film in grazing incidence geometry. The angle of incidence ω is fixed at a value that is above the critical angle of the organic-air interface, however, below the critical angle of the organic-substrate interface. This situation is shown in Figure 3.10(c) (black line), where the X-ray beam propagates mainly through the organic layer. Therefore, the scattering volume is confined to the organic layer and scattering in the substrate is diminished. The angle of incidence for the measurement is about 0.2° . A second measurement (gray line) is conducted to account for the scattering of the radiation on

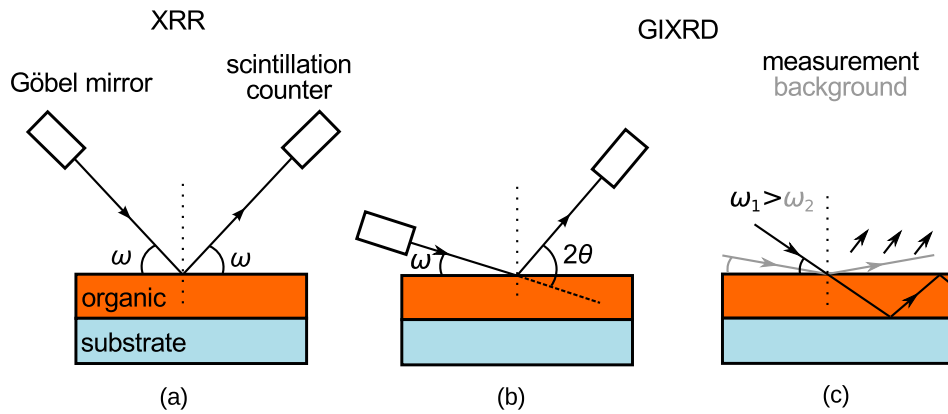


Figure 3.10.: (a) XRR measurement in Bragg-Bretano geometry. (b) Measurement setup in GIXRD geometry under an angle of incidence ω and a reflection angle 2θ . (c) Measurement in GIXRD geometry under ω_1 (black). Background measurement in GIXRD geometry under ω_2 (gray).

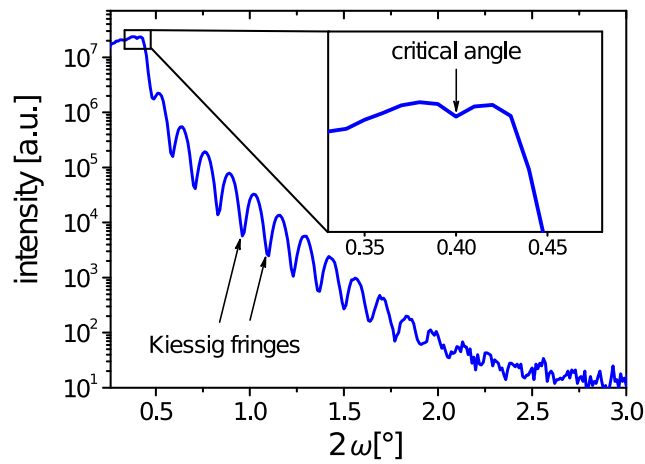


Figure 3.11.: Example for an XRR measurement. The inset shows the critical angle for total reflection. The oscillations are called Kiessig fringes.

3. Experimental

the thin-film air interface. The angle for the background correction measurement is usually around 0.12° . These angles are determined from the XRR measurement and a rocking curve, further details related to this protocol can be found in ref. [102], in which the measurement and correction procedures are described in greater detail. For the background correction, the signal of the background is scaled to the signal of the measurement and subsequently subtracted from the measurement. This procedure has the benefit that parameters like the full width half maximum (FWHM) can be determined more easily. The range for both measurements is $2\theta=3 \dots 90^\circ$ at a step width of 0.1° . Conclusions made from these measurements are based upon the assumption that the samples do not change their morphology significantly when they have contact to ambient conditions. The GIXRD measurements are performed on a Bruker D8 Discover diffractometer by Dr. Lutz Wilde. In chapter 7, the Scherrer equation is applied to quantify changes in crystallinity. Therefore, the coherence length is calculated according to

$$L_{\text{coh}} = \frac{K\lambda}{\Delta_{2\theta} \cos(\theta_0)}. \quad (3.5)$$

K is the shape-factor, λ is the wavelength of the X-rays, $\Delta_{2\theta}$ is the full width half maximum of the peaks in radiant, θ_0 is the angle of the peak and L_{coh} is the coherence length. The values for K are typically between 0.8 and 1.0.[103]

3.3.6. SEM/TEM/ED

For the scanning electron microscopy (SEM) measurements a Gemini 500 (Zeiss, Germany) microscope was used. The images were taken with an in-lens detector at acceleration voltages of 0.5 - 1 kV. The transmission electron microscopy (TEM) measurements were performed at a LIBRA200 microscope (Zeiss, Germany) at an acceleration voltage of 200 kV. The used TEM grids were silicon substrates with a $100 \mu\text{m}$ frame thickness. In the window the silicon was 9 nm thick and covered with a 40 nm silicon oxide film. All SEM/TEM measurements were performed by Mona Sedighi (Dresden Center for Nanoanalysis (DCN)).

The electron diffraction measurements were performed on an electron energy loss spectrometer by Eric Müller (Leibniz Institute for Solid state and materials research (IFW)). Details about this setup can be found in ref. [104].

3.3.7. EQE measurement

The EQE, as the number of extracted charge carriers per incident photon, is the dimensionless counterpart of the spectral response (SR). Both quantities are linked by

$$SR(\lambda) = \frac{j(\lambda)}{I_{\text{ill}}(\lambda)} = \frac{e\lambda}{hc} EQE(\lambda). \quad (3.6)$$

The SR , as the ratio of current density and illumination intensity, is experimentally easier accessible. The quantity is measured at a custom-made fully automatic setup, which can mea-

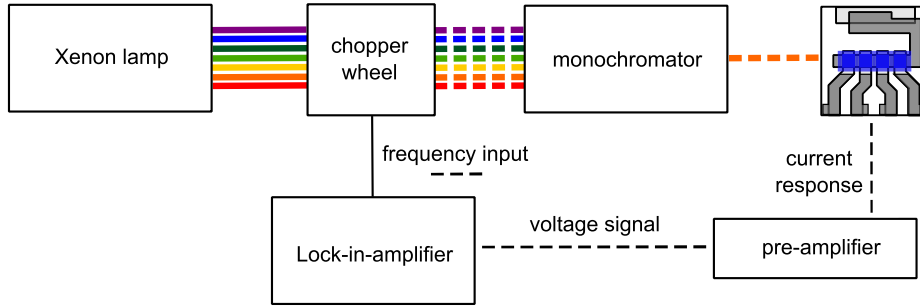


Figure 3.12.: Scheme of the EQE-setup for the measurement of the SR and EQE. The dashed lines indicate the modulated signals.

sure single samples as well as 6x6 Lesker wafers. Figure 3.12 shows a scheme of the setup. Light, which is generated by a Xenon lamp (Apex Illuminator), passes a chopper wheel which rotates with a frequency of ca. 230 Hz. Afterwards, the chopped light passes a Cornerstone 260 monochromator (Newport Oriel, USA) and illuminates the solar cell through a 2.89 mm² mask. The current response produced by the solar cells is pre-amplified, converted into a voltage signal, and then measured by an SR 7265 lock-in amplifier (Signal Recovery, USA). The lock-in amplifier receives the modulation frequency from the chopper wheel. The intensity of the different wavelengths is determined with a calibrated Hamamatsu S1337-33BQ Si-photodiode (Hamamatsu-Photonics, Japan) directly before the actual measurement. Figure 3.13 depicts the SR of the Hamamatsu diode.

The knowledge of the EQE allows the calculation of j_{sc}^{EQE} under the AM1.5G reference spectrum. As the EQE is measured without bias illumination at low intensities, this value is often higher than the j_{sc} measured under the sun simulator at 100 mW/cm². This behavior is known from literature, as j_{sc} can have a sublinear dependence on the intensity with $j_{sc} \propto I_{ill}^\alpha$ with an α of 0.85 - 1.[105, 106] This leads to an overestimation of the calculated j_{sc}^{EQE} . For this reason, we normalize the EQE spectra presented in this work to the j_{sc} measured under mismatch corrected 1 sun illumination conditions.

CT state measurement For the determination of the CT state, the sensitive EQE setup in combination with an electroluminescence setup is used. The sensitive EQE setup is based on the same principle as the regular EQE setup. However, some the devices are different. The lock-in amplifier is a DSP 7280 (Signal Recovery, USA) and an indium-gallium-arsenide (InGaAs) photodetector is used. The sEQE measurements were performed by Johannes Benduhn (IAPP). The electroluminescence setup uses an Andor SR3931-B spectrometer with a silicon-detector (DU420ABR-DD) and an InGaAs photodetector (DU491A-1.7.). The measurements were done by Dr. Fortunato Piersimoni (University of Potsdam). The evaluation of the data, including calculation of E_{CT} , V_{rad} , ΔV_{rad} , ΔV_{nonrad} and plotting of the graphs was done by Johannes Benduhn. More details can be found in ref. [107].

3. Experimental

3.3.8. Mismatch correction

Since a sun simulator replicates the solar spectrum only to a certain degree, a mismatch correction has to be applied. Figure 3.13 depicts the spectra of AM1.5G and the spectrum of the 16S-003-300-AM1.5 simulator spectrum, which is used at the IV-Robot. The largest deviations between both spectra appear between 750 nm and 1000 nm, where xenon has sharp emission lines. The mismatch correction procedure adjusts the illumination intensity of the sun simulator in a way that the organic solar cell gives the same current as under illumination with AM1.5G spectrum. The procedure for the applied mismatch correction was published by Shrotriya *et al.*[108]. Accordingly, the mismatch factor (MM) is calculated by

$$MM = \frac{\int_{\lambda_1}^{\lambda_2} E_{\text{sun}}(\lambda)SR_{\text{Ref}}(\lambda)d\lambda}{\int_{\lambda_1}^{\lambda_2} E_{\text{sun}}(\lambda)SR_{\text{OSC}}(\lambda)d\lambda} \frac{\int_{\lambda_1}^{\lambda_2} E_{\text{sim}}(\lambda)SR_{\text{OSC}}(\lambda)d\lambda}{\int_{\lambda_1}^{\lambda_2} E_{\text{sim}}(\lambda)SR_{\text{Ref}}(\lambda)d\lambda} = \frac{j_{\text{sun,Ref}}}{j_{\text{sun,OSC}}} \frac{j_{\text{sim,OSC}}}{j_{\text{sim,Ref}}}. \quad (3.7)$$

$E_{\text{sun}}(\lambda)$ and $E_{\text{sim}}(\lambda)$ refer to the AM1.5G spectrum and the illumination spectrum of the sun simulator. $SR_{\text{OSC}}(\lambda)$ and $SR_{\text{Ref}}(\lambda)$ stand for the spectral responses of the organic solar cell and the reference diode. The integral of the product of illumination spectrum and spectral response over wavelength equals the current density for each combination. For a correct measurement, the requirement

$$j_{\text{sun,OSC}} = j_{\text{sim,OSC}} \quad (3.8)$$

has to be fulfilled, which expresses that the organic solar cell should give the same current density under the simulator spectrum as under AM1.5G. Equation (3.8) inserted in equation (3.7) leads to the following relationship (here, in terms of currents):

$$I_{\text{sim,Ref}}^* = \frac{I_{\text{sun,Ref}}}{MM} = \frac{0.780 \text{ mA}}{MM}. \quad (3.9)$$

The value for $I_{\text{sun,Ref}}=0.780 \text{ mA}$ is known from the calibration at Fraunhofer ISE (Freiburg, Germany) and the MM is calculated from the SR -measurements. $I_{\text{sim,Ref}}^*$ is the current that the reference diode has to produce under the simulator spectrum to ensure equation (3.8) is fulfilled. An adjustment of the intensity of the sun simulator leads to the necessary $I_{\text{sim,Ref}}^*$.

3.3.9. Current-voltage measurement

Two setups at IAPP can measure current-voltage characteristics under simulated sunlight. One setup is located in the nitrogen atmosphere of the UFO 1 glovebox. It allows the measurement of solar cells without encapsulation. The sun simulator is a ‘‘SoCo 1200 MHG’’ (K.H. Steuernagel GmbH, Germany). Its intensity is monitored with a photodiode and set to a fixed value, which corresponds to 100 mW/cm^2 measured with a calibrated ISE photo-

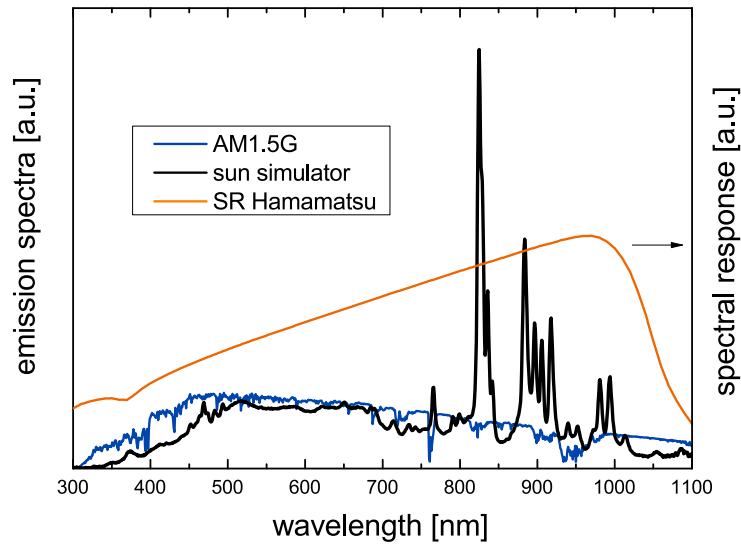


Figure 3.13.: AM1.5G spectrum and 16S-003-300-AM1.5 simulator spectrum as well as the spectral response of the Hamamatsu diode.

diode. Accordingly, a *MM* correction is not possible with this setup. The other setup is a fully automatic setup (IV-Robot) that can measure single substrates as well as Lesker wafers. The setup uses a 16S-003-300-AM1.5 (Solar Light Co., USA) sun simulator. The intensity is monitored by a calibrated Hamamatsu S1337-33BQ Si-photodiode (Hamamatsu-Photonics, Japan). Six neutral density filters (dark, 0.001, 0.01, 0.1, 1, 6 suns) allow the measurement under different intensities. The device parameters are calculated by the user software. The following paragraph describes the sequence of measurements for the characterization of a Lesker wafer.

Sequence of measurements

1. Measurement of the *SR/EQE* and calculation of the *MM* on the basis of a formerly measured sun simulator spectrum.
2. *jV* measurement of the samples using the calculated *MM*.⁴ Directly before the *jV* measurement, the illumination spectrum of the sun simulator is measured with a CAS 140CT spectrometer (Instrument Systems, Germany).

⁴Depending on the planning of the Lesker wafer, the *MMs* of the single devices on the wafer can differ significantly from each other. If the deviations are smaller than $\lesssim 5\%$ an average mismatch factor is calculated for the measurement. For higher deviations, the devices are measured under different *MM*.

3. Experimental

3. Recalculation of the *MM* with the actual simulator spectrum. If necessary, the intensity is recalculated for the determination of j_{sc} and η_{PCE} under 100 mW/cm^2 .⁵

Measurement uncertainties This paragraph gives an overview about the measurement uncertainties for the measurement at the IV-Robot. The step size for the voltages was mainly 0.05 V. This leads to a measurement uncertainty in the measurement of V_{oc} . However, V_{oc} is interpolated between two measurement points, which reduces the uncertainty by a factor of ≈ 10 for devices, without an S-kink around V_{oc} . A second source of uncertainty is the temperature in the box, which varies between 20 °C and 30 °C depending on the season. The standard reporting conditions recommend 25 °C, which results in an uncertainty of $\approx 7 \text{ mV}$. Overall, the relative uncertainty is 2% for typical V_{oc} of 0.5-1.0 V. The main measurement uncertainty for j_{sc} is the area of the solar cell. Usually, the *jV* measurement of the Lesker samples takes place without mask. However, masked measurements are occasionally done to exclude edge effects. The relative uncertainty is $\approx 3\text{-}4\%$. The main uncertainty of the *FF* is also the step size of the voltage. Under the assumption that the source-measurement unit (SMU) can set the voltage and measure the current with sufficient accuracy, the limitation is again the step size of the voltage. Also in this case an interpolation is performed. Since the interpolation works as a secant line, the *FF* is underestimated. Therefore, the relative uncertainty of the *FF* is $\approx 1\%$, depending on the absolute value of V_{MPP} . The relative uncertainty of the intensity is $\approx 2\%$ caused by fluctuations of the lamp and the positioning of the lamp. The overall uncertainty for the η_{PCE} is $\approx 5\%$.

Solar cell absorption The absorption of the solar cells is measured in reflection geometry under the assumption that no light passes the back electrode. This is a reasonable assumption for 100 nm aluminum back electrodes. The absorption is then calculated by $A=100\% - R$. The light source is a combined deuterium-halogen lamp AvaLight-DH-S-BAL (avantes) and the spectrum measured by a custom built spectrometer (OMT, Germany).

3.3.10. V_0 measurement

The measurement of the *IP* is normally performed with a UPS measurement. However, an important requirement for UPS measurements are closed layers of a certain thickness. When the layer is not closed, electrons can be emitted from the sub-layer, which prohibits an evaluation. On the other side, if the layer is too thick and has a low conductivity, which is usually the case for undoped organic thin films, the layer starts charging. This leads to a shift of the HBEC of the UPS signal, which also prohibits the evaluation. A temperature dependent measurement of V_{oc} can offer an alternative for the determination of the *IP*.^[109] For this purpose, V_{oc} is measured at different temperatures and extrapolated to 0 K using

$$V_{oc}(I, T) \approx V_0 + n \frac{k_B T}{e} \ln \left(\frac{I}{I_0} \right). \quad (3.10)$$

⁵For the recalculation of the *MM*, a program written by Toni Meyer (IAPP) is used.

V_0 can be identified with the effective gap between the IP of the donor and the EA of the acceptor.[109] The knowledge of the EA of the acceptor enables the calculation of the IP of the donor. For the adjustment of the temperature, the solar cell is attached to a copper block. This block can be cooled by liquid nitrogen and also heated by electrical heating. A 50 W halogene lamp illuminates the device. The measurement was done by Anton Kirch (IAPP) and the evaluation by Dr. Johannes Widmer (IAPP).

3.3.11. Impedance Spectroscopy

Impedance spectroscopy measures the frequency dependence of the electrical response of a device. Thereto, a small sine voltage $v(t)=\hat{v} \sin(\omega t)$ is applied to a device and the current response $i(t)=\hat{i} \sin(\omega t + \varphi)$ is recorded. ω refers to the circular frequency $\omega=2\pi f$. For the evaluation of the obtained data, the Fourier transform (\mathcal{F}) is computed and the complex impedance is defined

$$Z(\omega) = \frac{V(\omega)}{I(\omega)} = \frac{\mathcal{F}(v(t))}{\mathcal{F}(i(t))}. \quad (3.11)$$

The inverse of the impedance is the admittance $Y(\omega)$, which can be separated in the conductance $G(\omega)$ and the capacitance $C(\omega)$

$$Y(\omega) = \frac{1}{Z(\omega)} = G(\omega) + i\omega C(\omega). \quad (3.12)$$

The capacitance provides information about the trap states in a device. Figure 3.14(b) shows a schematic Cf spectrum of a device with traps that can be modelled by an equivalent circuit as depicted in Figure 3.14(a). If the frequency of the applied voltage signal is low enough, the trap states can be populated and depopulated according to the ac voltage signal. This leads to a plateau in the Cf plot, additionally to the depleted capacitance.

Capacitance-voltage measurement The measurement of the capacitance as a function an applied dc bias voltage can provide information about the built-in-voltage and the trap profile. For this purpose, C^{-2} is plotted as a function of the dc bias voltage (Mott-Schottky plot). The trap profile can be extracted from the slope of the function, according to

$$x = \frac{\epsilon_0 \epsilon_r A}{C}, \quad (3.13)$$

$$N_A(x) = -\frac{2}{q\epsilon_0 \epsilon_r A^2} \left(\frac{dC(x)^{-2}}{dV} \right)^{-1}. \quad (3.14)$$

For devices with a thickness in the range of 100 nm, the obtained values give only an upper limit of the trap density. Further details for the evaluation can be found in reference [110].

3. Experimental

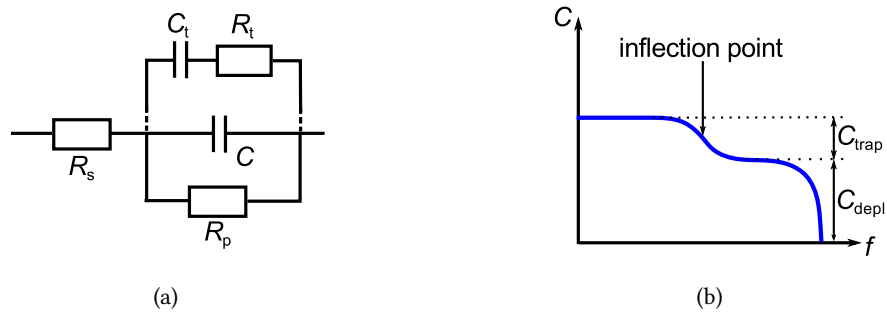


Figure 3.14.: (a) Equivalent circuit for an organic solar cell, consisting of a series resistor, a parallel resistor, and a capacitor. A trap contribution can be modelled by a parallel circuit of an additional capacitor and resistor. (b) The corresponding Cf plot for the equivalent circuit with traps.

Trap distribution Walter *et al.* developed a method to get information about the energetic distribution of the trap states via temperature dependent impedance spectroscopy measurements.[111] For each temperature the inflection point of the capacitance as a function of the frequency is determined. Using

$$\ln(\omega) = \ln(2\nu_0) - \frac{E}{k_B T}, \quad (3.15)$$

the attempt-to-escape frequency (ν_0) and the demarcation energy (E_d) can be calculated. The energetic distribution can then be calculated using

$$E_d = k_B T \ln\left(\frac{2\nu_0}{\omega}\right) \quad (3.16)$$

$$N_t = -\frac{V_{bi}}{qW} \frac{dC}{d\omega} \frac{\omega}{k_B T}, \quad (3.17)$$

in which W is the width of the space charge region. A detailed derivation of the formulas can be found in references [111, 112]. The measurements are performed with a ‘‘AUTOLAB PG-STAT302N’’ from Metrohm. The device allows the measurement of frequencies from 0.1 Hz to 1 MHz. The measurement range of the current is 10 nA to 1 A. A cryostat with Peltier element (HAT Belectronic, Germany) regulates the temperature. The evaluation of the data was performed in cooperation with Natalia Sergeeva (IAPP).

3.3.12. OTRACE

Open circuit corrected charge carrier extraction (OTRACE) is a method to investigate the mobility and recombination of charge carriers in organic solar cells.[113] Figure 3.15 presents a scheme of the current/voltage curves as a function of time. A light pulse creates charge

carriers within the device at open circuit conditions. Subsequently, the light pulse is turned off and a variable bias voltage is applied that keeps the device at open circuit conditions, accounting for the decreasing charge density due to charge recombination. In this time frame (delay time), the excess charge carriers are kept in the device and recombine. Afterwards, a linearly increasing voltage is applied to extract the remaining excess charge carriers. The analysis of the current response provides information about the mobility of the charge carriers as well as the charge carrier density. The mobility is calculated by

$$\mu = \frac{d^2}{2A't_{\max}^2} \left[\frac{1}{6.2 \left(1 + 0.002 \frac{\Delta j}{j_0}\right)} + \frac{1}{1 + 0.12 \frac{\Delta j}{j_0}} \right]^2 \quad (3.18)$$

in which d refers to the device thickness without electrodes.[114] The other parameters are explained in Figure 3.15. The bias voltage signal that keeps the device at open circuit conditions is determined in a preliminary measurement and is combined with the linear increasing voltage signal depending on the delay time. A variation of the delay time enables the correlation between the charge carrier density in the device and the mobility of the charge carriers without changing the intensity of the bias light. The pulse and adaptive bias voltage are generated by a waveform generator from the Agilent 33600A Series. To record the current response and the voltage decay, a Tektronix DPO 7354 C Digital Phosphor Oscilloscope is used. The light pulse is created by Luxeon K2 LEDs. The evaluation of the data was done by Sascha Ullbrich (IAPP).

3.3.13. Transient Photovoltage

The transient photovoltage measurements yield the small perturbation lifetime (τ) of the charge carriers in the device in dependence of the open-circuit voltage.[115] For this purpose, we illuminate the solar cell with a bias light creating an open circuit voltage ($V_{\text{oc,bias}}$) in the device. The bias light is generated by a high power LED. A laser pulse (Ekspla PL2210, 532 nm, 25 ps pulse) creates additional charge carriers in the device that recombine after the pulse ended to the $V_{\text{oc,bias}}$ caused by the bias illumination. The transient is measured by an oscilloscope and fitted by a single exponential function.

$$V = A \exp\left(-\frac{t}{\tau}\right) + V_{\text{oc,bias}} \quad (3.19)$$

The measurement and evaluation was performed by Sascha Ullbrich. The equipment is the same as described in the OTRACE section.

3.3.14. $V_{\text{oc}}-I_{\text{sc}}$ method

The $V_{\text{oc}}-I_{\text{sc}}$ method enables the reconstruction of an $I-V$ curve of a device with strongly reduced influence of the series resistance.[116] This allows a more accurate determination of the diode ideality factor according to ref. [117]

3. Experimental

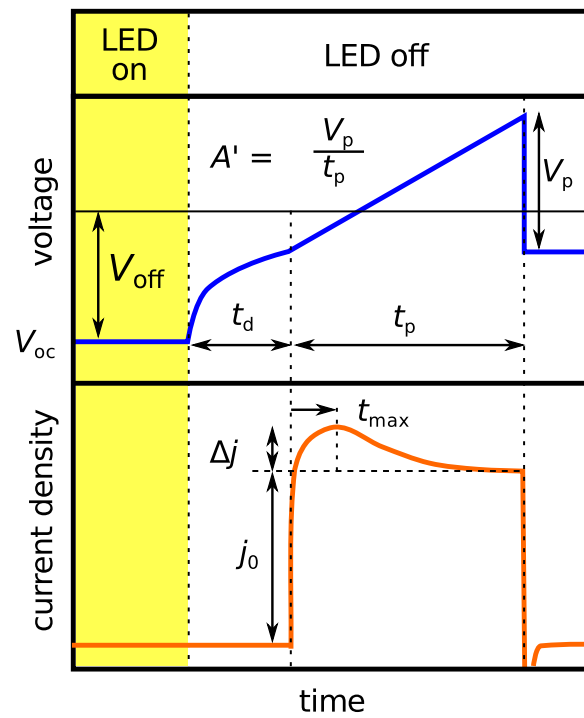


Figure 3.15.: Scheme of the voltage and current signal over time in an OTRACE measurement. In the beginning, an LED creates a light pulse, which illuminates the sample. After the light is off, a variable voltage is applied that keeps the device at open circuit conditions. After a delay time, a linear increasing voltage is applied that extracts the remaining charge carriers.

3.3. Measurement setups

$$n_{\text{id}} = \frac{q}{k_{\text{B}}T} \frac{\partial V_{\text{oc}}}{\partial \ln I_{\text{sc}}}. \quad (3.20)$$

The $V_{\text{oc}}-I_{\text{sc}}$ pairs are measured at different intensities that are created by a white high power LED. The measurement was performed by André Nascimento (Faculdade de Ciências e Tecnologia Universidade Nova de Lisboa, Portugal) and evaluated in cooperation with Sascha Ullbrich.

4. DTDCTB

This chapter focuses on the fill factor of DTDCTB:C₆₀ solar cells, which shows a peculiar dependence on substrate temperature during deposition. The first part describes the change of the jV curves depending on the substrate temperature and blend layer thickness. Three regimes with different fill factor - absorber layer thickness dependence can be identified, depending on the substrate temperature during the deposition. GIWAXS measurements show no change in the crystallinity of the blend layers, deposited at the respective substrate temperatures. Afterwards, we investigate several aspects known to influence the fill factor. We determine the charge carrier mobility using OTRACE, the trap distribution using impedance spectroscopy, and lifetime of the charge carriers using transient photovoltage measurements. In addition, the diode ideality factor is determined using the V_{oc} - I_{sc} method.

4.1. Introduction

Lin *et al.* published the first paper on 2-[7-(5-N,N-ditolylaminothiophen-2-yl)-2,1,3-benzothiadiazol-4-yl]methylenemalononitrile (DTDCTB) in 2011.[118] Figure 4.1 shows the molecule, which is a push-pull chromophore with a D-A-A structure. The electron donating ditolylaminothienyl moiety is linked with two electron accepting groups: benzothiadiazole and dicyanovinyl. The molecule is a red absorber with an absorption maximum at 684 nm and functions as a donor in combination with C₆₀ and C₇₀. The authors of refs. [14, 118] reported a η_{PCE} of 4.41% for DTDCTB:C₆₀ and 5.81% for DTDCTB:C₇₀ solar cells. Further optimization of the blend layer led to an increase of the power conversion efficiency to 5.3% for DTDCTB:C₆₀ and 8.0% for DTDCTB:C₇₀ solar cells.[119, 120] Triple stack cells incorporating DTDCTB:C₆₀ achieved a η_{PCE} of 11.1%.[119]

While DTDCTB has an extinction coefficient <1 in the thin film and an open circuit voltage of ≈ 0.8 V in combination with the fullerenes, the asset of the material system is its charge extraction capability. It allows fill factors of $\approx 60\%$ at a blend layer thickness of 80 nm, compensating the moderate absorption of the material and allowing high short circuit current densities.

4.1.1. Previous work

Jacob König-Otto (née Otto) studied DTDCTB:C₆₀ solar cells in the framework of his Master's thesis.[121] He investigated the influence of substrate heating during the deposition on this material system in blend layers on glass as well as in p-i-n solar cells in the range between RT and 100 °C.¹ The morphology of the DTDCTB:C₆₀ blend layers on glass was

¹Preliminary tests showed that this material system achieved significantly better results in a p-i-n configuration on BPAPF as sublayer instead of a n-i-p configuration on C₆₀ as sublayer. Since the p-dopant NDP9 is

4. DTDCTB

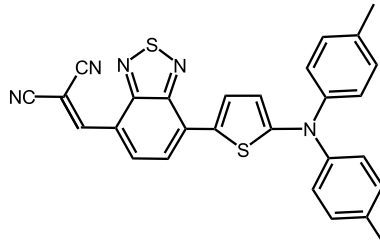
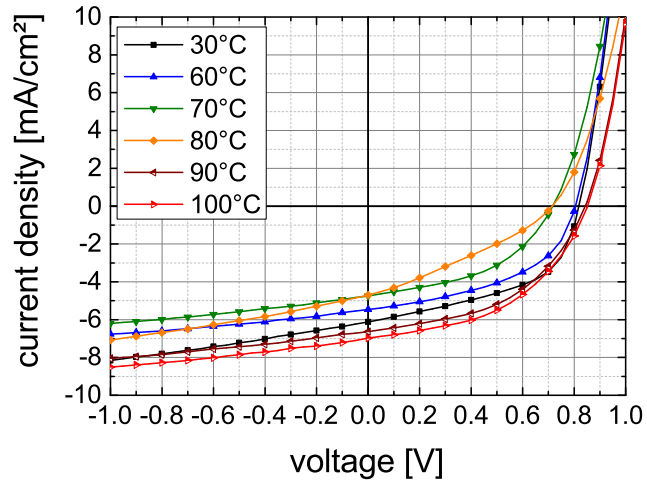


Figure 4.1.: Molecular structure of DTDCTB.

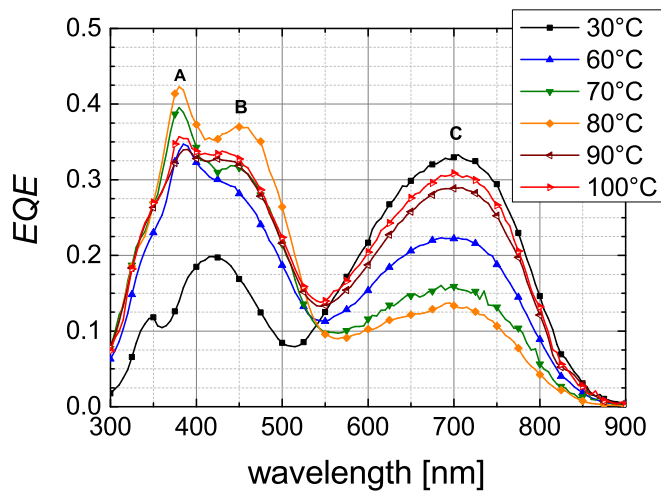
studied using GIXRD and XRR. The diffractogram of the material system exhibited rather amorphous structures and the XRR showed a low surface roughness for all tested substrate temperatures. No change in the absorption spectra was observed for blend layers deposited on differently heated glass substrates.

König-Otto tested the heated blend layers in solar cells with the following stack: ITO | NDP9 (2 nm) | p-BPAPF (30 nm, 10 wt% NDP9) | DTDCTB:C₆₀ (30 nm, var. substrate temp.) | C₆₀ (25 nm) | Bphen (6 nm) | Al (100 nm). Figure 4.2(a) shows the jV measurements of the solar cells and Figure 4.2(b) shows the corresponding EQEs. For a better overview, Figure 4.3 shows the solar cell characteristics as a function of the different substrate temperatures during the deposition. A general trend is visible in the device characteristics. All performance parameters decrease from RT to 80 °C. Up to approximately 60 °C the decrease is relatively small. However, in the range between 70 °C and 80 °C, the parameters reach a pronounced minimum. Besides a decreased V_{oc} and j_{sc} , the fill factor also decreases, due to a slight S-kink. For higher substrate temperatures, the S-kink vanishes and also the other parameters increase again. For the devices processed at $T_{sub}=90$ °C and $T_{sub}=100$ °C, higher j_{sc} are achieved as compared to the RT devices, resulting in a slightly higher η_{PCE} than for the devices prepared at RT. The increase in j_{sc} can be attributed to the increased EQE in the spectral region around 450 nm. In what follows we investigate this peculiar behavior in more detail, including a variation of the blend thickness.

evaporated at temperatures of 120 °C, higher substrate temperatures were excluded in order to prevent the p-BPAPF (10 wt% NDP9) layer against excessive thermal stress.



(a)



(b)

Figure 4.2.: (a) jV characteristics and the corresponding (b) EQE of the solar cells. Adapted from the Master's thesis of Jacob Otto.[121]

4. DTDCTB

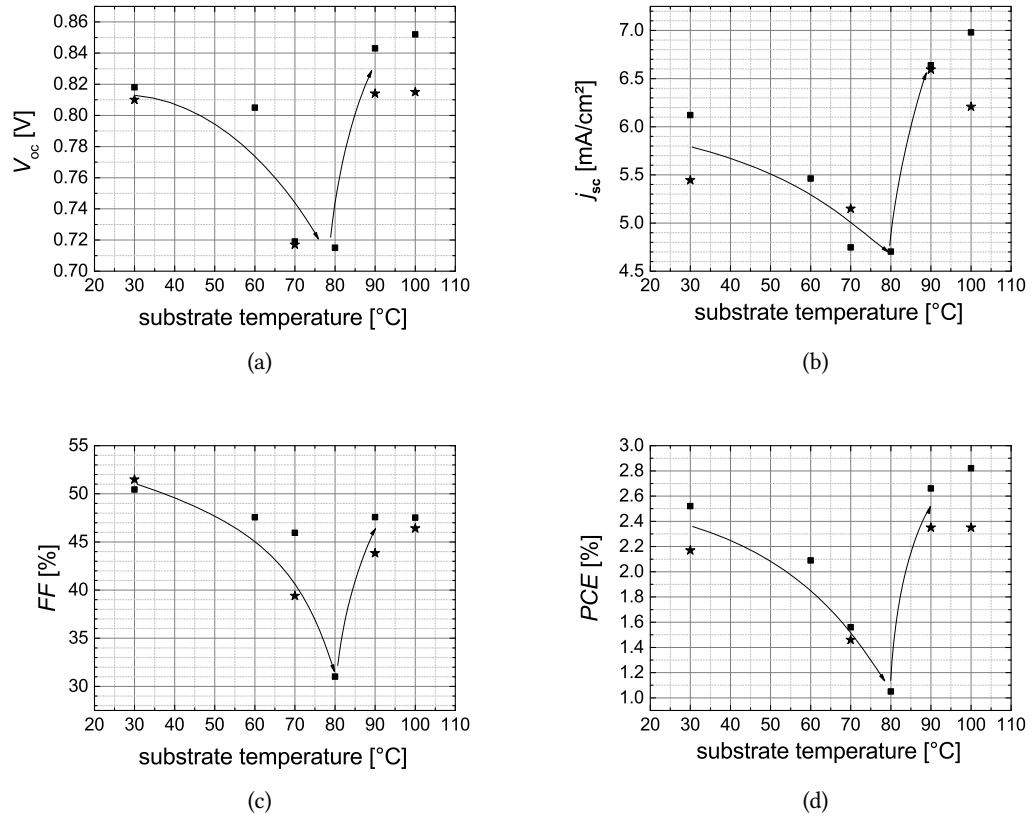


Figure 4.3.: (a) V_{oc} , (b) j_{sc} , (c) FF, and (d) η_{PCE} of the solar cells. The star symbol allows the discrimination of specific devices processed at the same substrate temperature in different graphs. Graphs adapted from reference [121].

4.2. Solar cells

In order to further investigate the results of König-Otto, we designed a coherent device series to investigate the behavior for thicker layers. The solar cell stack (set 1) is adjusted to ITO | NDP9 (2 nm) | p-BPAPF (30 nm, 10 wt% NDP9) | DTDCTB:C₆₀ (var. blend thickness, var. substrate temp.) | C₆₀ (20 nm) | n-Bis-HFI-NTCDI (15 nm, 7 wt%) | Al (100 nm). We chose the substrate temperatures $T_{\text{sub}}=\text{RT}/85/110$ °C, as these temperatures reflect the three regimes, found by König-Otto.² For a comparison to König-Ottos work, Figure 4.4 shows the jV - and EQE curves of our devices with 30 nm blend thickness. Table 4.1 shows the corresponding fingerprints. The comparison with the devices by König-Otto presented in Figure 4.3 shows the same trends in all parameters: A decrease for the transition from RT to 85 °C substrate temperature and a subsequent increase for the transition to 110 °C. However, for the sample processed at 85 °C, the S-kink is more pronounced for our samples, resulting in a FF of only 22%. Considering the steep temperature dependence of the fill factor between 70 °C and 90 °C and the temperature accuracy of around 5 K, this value is still reasonable.

Table 4.1.: Fingerprints of the devices with 30 nm thick blend layer.

T_{sub}	V_{oc} [V]	j_{sc} [mA/cm ²]	FF [%]	η_{PCE} [%]	I_{ill} [mW/cm ²]	j_{sc}^* [mA/cm ²]
RT	0.83	5.7	56.5	2.6	100	5.6
85 °C	0.74	4.7	22.0	0.8	101	4.7
110 °C	0.84	7.0	52.1	3.0	101	6.9

In addition, this device series comprises blend layer thicknesses of 40/50/60/70/100 nm. Figure 4.5 shows the jV curves of the devices. Figure 4.6 shows the corresponding fingerprints as a function of the blend layer thickness. The low performance of the device at 85 °C persists for the devices with higher blend layer thickness. The focus, however, is on the difference in the fill factor between the RT devices and the devices processed at 110 °C. For blend layer thicknesses from 30 nm to 50 nm, the FF of the RT devices increases and stays constant up to at least 70 nm at approximately 60%. For a blend layer thickness of 100 nm the FF drops to 54%. This is a rather unusual behavior of the fill factor for an increasing blend layer thickness. Normally, the FF drops monotonously with increasing blend layer thickness.[63, 122] Here, only for the 110 °C samples the FF decreases from 52% to 32% upon an increase of the blend layer thickness. In addition, this difference in charge extraction for the RT and 110 °C devices affects j_{sc} for blend layer thicknesses over 60 nm. Up to 60 nm blend thickness, the j_{sc} of the RT and the 110 °C devices increases equally. For 70 nm and 100 nm thick blend layers, j_{sc} decreases in the 110 °C devices due to the limited charge extraction at short circuit. The paramount fill factor dependence of the RT devices leads to significantly higher power conversion efficiencies of the thick RT devices compared to the devices processed at 110 °C. As all optical or electrical properties of a small molecular thin film can be attributed roughly

²Since the substrate temperature measurement systems in UFO and Lesker are different, the used temperatures are not directly transferable. The substrate temperatures displayed in the UFO are usually 8 K lower than the temperature in the Lesker chamber. The following substrate temperatures in this chapter are measured in the Lesker chamber.[90]

4. DTDCTB

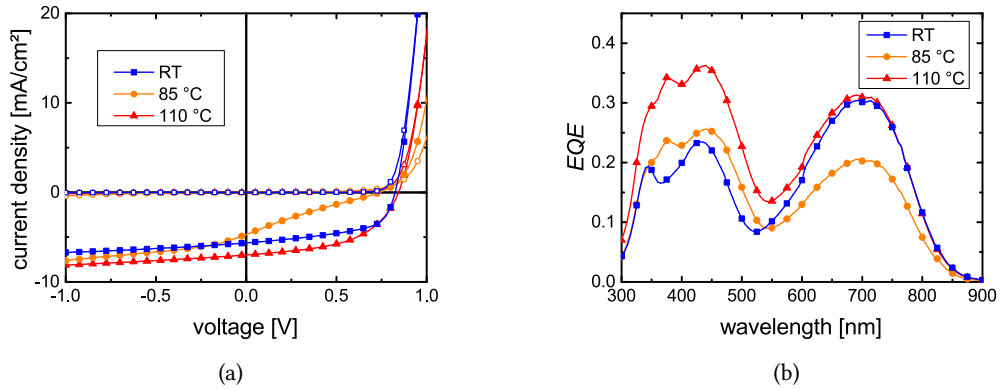


Figure 4.4.: jV curves of the devices with 30 nm thick blend layer, prepared at different substrate temperatures. The open symbols represent the dark measurements, the colored symbols represent the measurements under illumination.

to the properties of the single molecule or the assembly of the molecules, we attribute this change to a different morphology of the blend layer.³ Indeed, the difference in substrate temperature during the deposition of the DTDCTB:C₆₀ layer should neither affect the molecular integrity of DTDCTB nor C₆₀. The following sections investigate the solar cells and blend layers with respect to sublayer influence, absorption, morphology, charge carrier mobility, trap states, lifetime, and recombination to identify the reason for the behavior of the fill factor as a function of thickness and substrate temperature.

³Regardless of the substrate temperature during the deposition of the blend layer, all solar cells of set 1 were processed on one Lesker matrix. Therefore, the HTLs of all solar cells received the same temperature treatment. Accordingly, an influence of differently heated sublayers on the $FF(d)$ characteristics can be excluded.

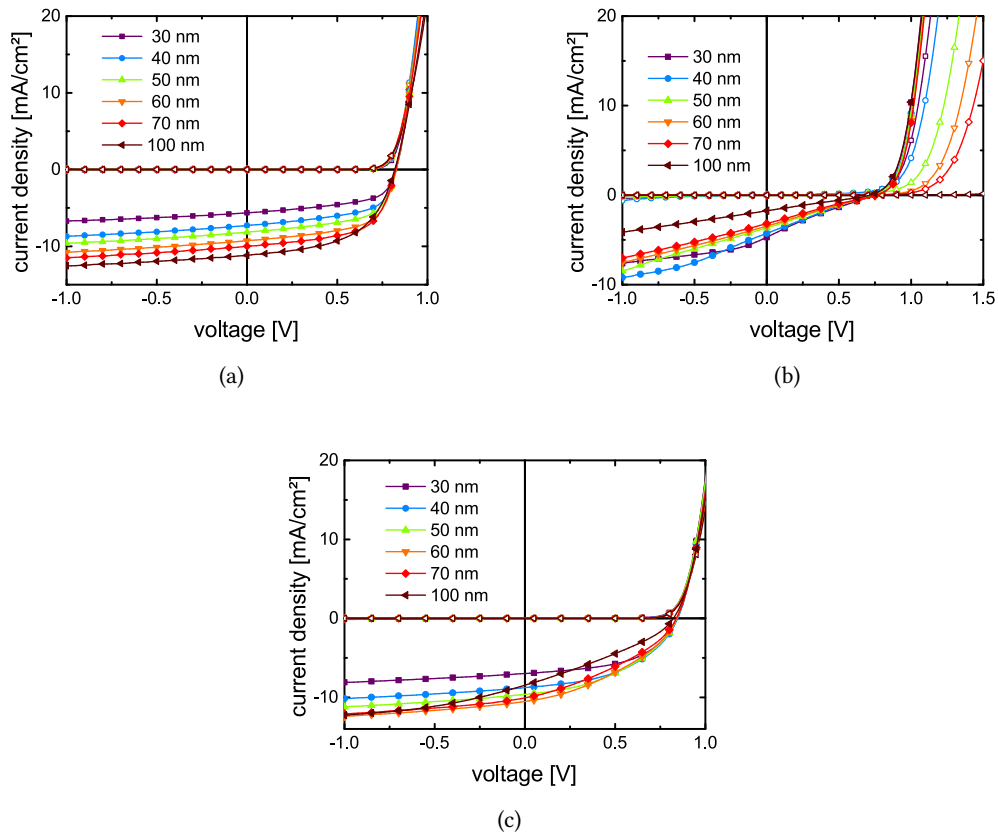


Figure 4.5.: jV curves in dark and under illumination for blend layer thicknesses of 30/40/50/60/70/100 nm deposited at (a) RT, (b) 85 °C, and (c) 110 °C.

4. DTDCTB

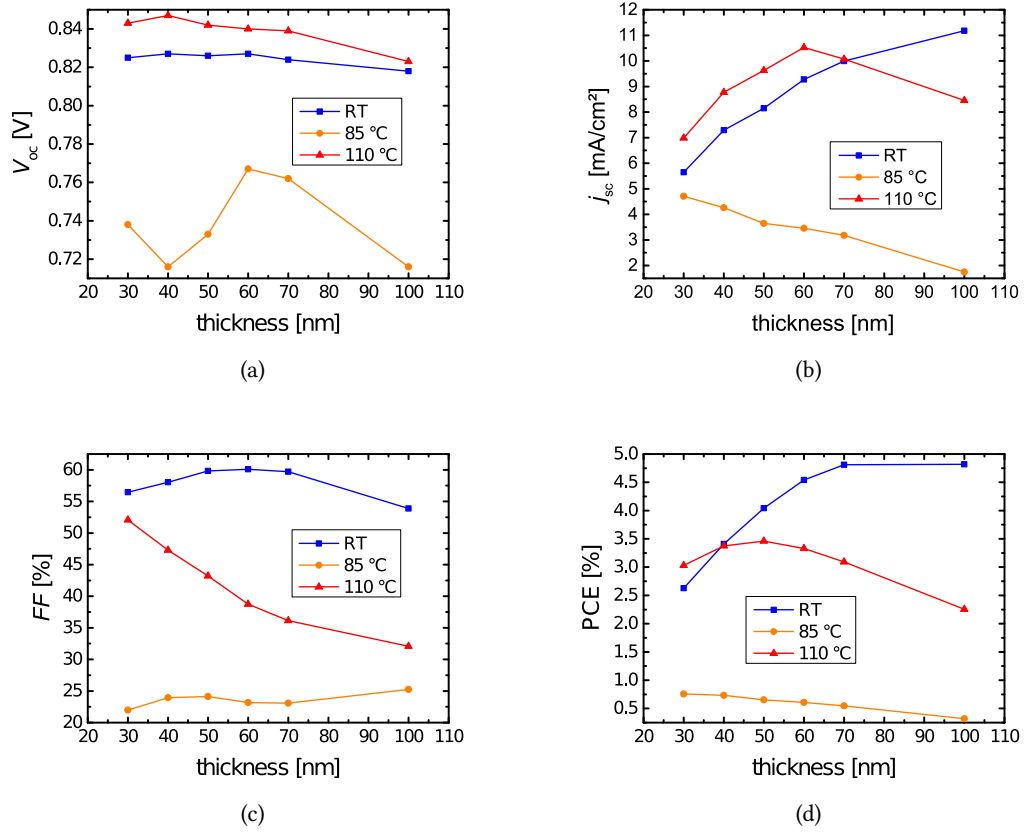


Figure 4.6.: Fingerprints of the jV curves presented in Figure 4.5. The lines are a guide to the eye.

4.2.1. Sublayer

We test other sublayers to exclude a possible influence of the sublayers, especially the p-doped BPAPF layer, on the FF dependence as a function of blend layer thickness at room temperature or in the high substrate temperature regime. Table 4.2 gives an overview of the tested solar cell stacks. The variation includes intrinsic DTDCTB layers and MoO_3 layers in comparison to blend layers deposited on p-BPAPF.

Table 4.2.: Overview of the solar cell stacks for the devices presented in Figure 4.7: hole conducting side (listed in the table) | DTDCTB: C_{60} (var. blend thickness, var. substrate temp.) | C_{60} (20 nm) | n- C_{60} (15 nm, 7 wt%) | Al (100 nm).

stack	hole conducting side
1	ITO NDP9 (2 nm) p-BPAPF (30 nm) BPAPF (5 nm)
2	ITO NDP9 (2 nm) p-BPAPF (30 nm) BPAPF (5 nm) DTDCTB (7 nm)
3	ITO MoO_3 (3 nm) DTDCTB (7 nm)

Figure 4.7 shows the fill factor as a function of the blend layer thickness at different substrate temperatures. The other device fingerprints are listed in Table A.1 in the Appendix. Despite absolute deviations in the range of $\approx 2\%$, the general fill factor-blend layer thickness trend is the same for devices deposited at the same substrate temperature. The FF of the RT samples increases from 55% for 30 nm to 59% for 50 nm blend layer thickness. In contrast, the FF of the samples prepared at 100 °C decreases from 45% for 30 nm to 35% for 50 nm. Note that the fill factor for the 100 °C samples is less than for the 110 °C samples. This is in agreement with the results of König-Otto in Figure 4.3. These results prove that the fill factor dependence for the RT and the high temperature regime are not related to the p-BPAPF as they are also present in devices without p-doped layers. Furthermore, the insertion of intrinsic BPAPF or DTDCTB layers has no influence on the general trend as well. Section A.1.2 of the Appendix shows a second set of solar cells (set 2) with a 5 nm thick intrinsic BPAPF layer between the p-BPAPF and the DTDCTB: C_{60} blend. In this variation, the blend layer thicknesses 30/50/60/70 nm are prepared for RT, 85 °C, and 110 °C. The same $FF(d)$ trends are again clearly visible.

4.3. Morphology

The GIXRD investigations of Jacob Otto showed no change of the DTDCTB: C_{60} blend layers upon substrate heating. In order to check for changes in the in-plane component of the diffraction pattern of the blend layer, we prepare samples for 2D-GIWAXS measurements. Table 4.3 gives an overview of the samples, which are deposited on silicon substrates.⁴ A sublayer of BPAPF is included to mimic the growth conditions in the solar cell. Figure 4.8 (a) shows the results of the intrinsic DTDCTB layer (sample 1). The prominent spots left and right from the center are substrate artefacts and appear also in most of the other images. The small streak right next to the bottom center is also a reflection from the substrate. Except

⁴Samples prepared on glass had too much scattering from the glass substrate.

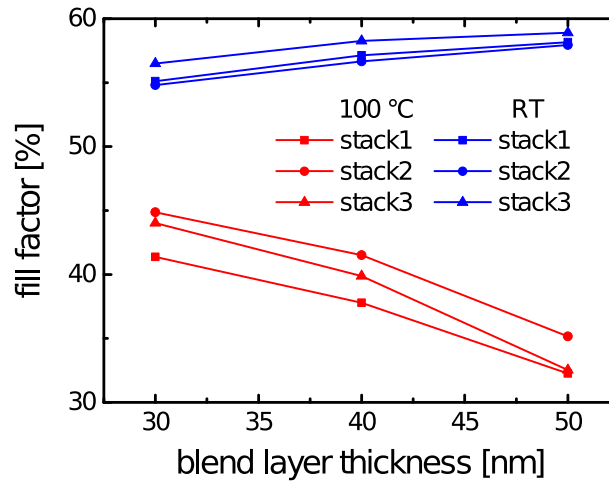


Figure 4.7.: Fill factor as a function of blend layer thickness for the stacks presented in Table 4.2.

for these artefacts, the image is rather featureless, indicating a disordered layer. Figures 4.8 (b)-(d) show the measurements on blend layers with C_{60} at different substrate temperatures during the deposition (samples 2-4). All samples have a broad amorphous ring that can be assigned to C_{60} . In the RT sample (b), the ring has a higher intensity compared to the background than in samples with heated substrate. In summary, also the in-plane diffraction pattern shows no significant changes that could serve as an explanation for the behavior of the solar cells upon substrate heating. The results for the blend at RT are in agreement with literature. Nunomura *et al.* investigated C_{60} layers with selected area electron diffraction and compared the layers to DTDCTB: C_{60} blends.[123] In their work, the authors found that in the blend, the ordering of C_{60} is hampered.[123] A specific diffraction pattern of DTDCTB was not visible.[123] Cheyys *et al.* state that DTDCTB is known to crystallize and quote the original work of Lin from 2011.[118, 124] However, the only X-ray data related to thin films (p. 12 in SI of ref. [118]) showed no indications of crystallinity for the thin film.[118]

In summary, the diffraction patterns indicate a large disorder in the blend layers that is also present when the substrate is heated during deposition. Therefore, a crystallization of DTDCTB as the reason for the changes in the solar cell behavior can be excluded. The changes in the solar cell behavior might be related to changes in the short range order of the molecules, which cannot be detected with GIWAXS. Changes in the average orientation of the molecules are reflected in changes in the thin film absorption spectra. For this reason, we investigate the absorption spectra of the DTDCTB blends in the different temperature regimes.

4.3.1. Absorption

The absorption spectra of the solar cells at different substrate temperatures are investigated. König-Otto already investigated the change in the absorption in blend layers upon heating

Table 4.3.: Sample structures prepared on silicon for GIWAXS measurements. The samples were prepared in collaboration with Daniel Schütze (IAPP).

#	structure
1	BPAPF (5 nm) DTDCTB (30 nm, RT)
2	BPAPF (5 nm) DTDCTB:C ₆₀ (30 nm, RT, 1:1)
3	BPAPF (5 nm) DTDCTB:C ₆₀ (30 nm, 72 °C, 1:1)
4	BPAPF (5 nm) DTDCTB:C ₆₀ (30 nm, 102 °C, 1:1)

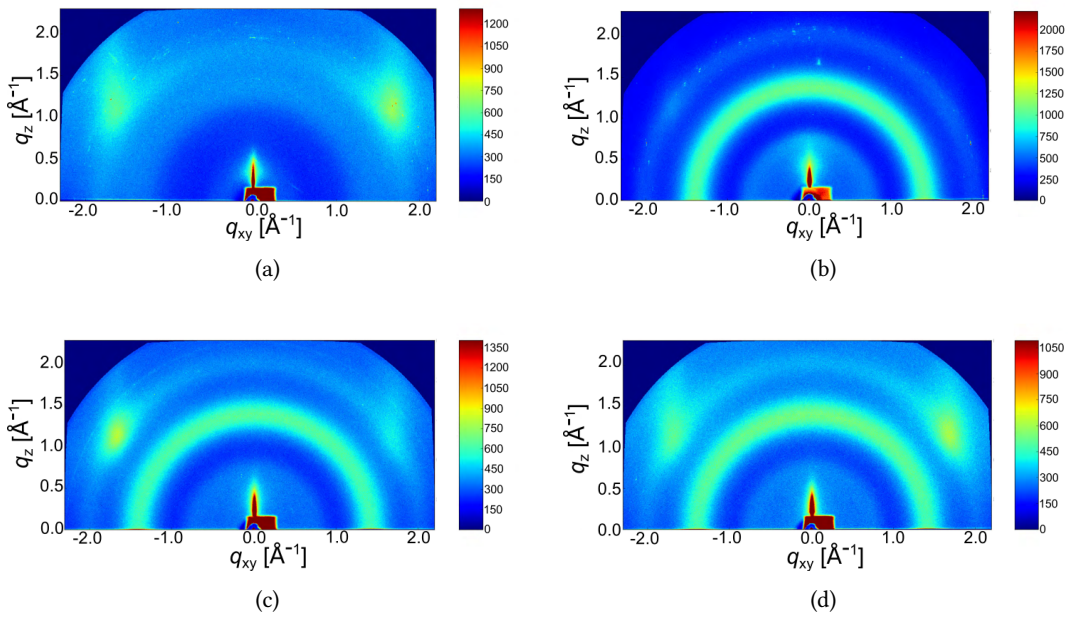


Figure 4.8.: GIWAXS images of (a) neat DTDCTB (sample 1), a DTDCTB:C₆₀ blend prepared at (b) RT (sample 2), (c) $T_{\text{sub}}=72$ °C (sample 3), and (d) $T_{\text{sub}}=102$ °C (sample 4). The measurements were performed and evaluated by Dr. Scott Himmelberger (Stanford University).

4. DTDCTB

substrates for RT/70/90/100 °C (UFO-temperatures) and found no changes. In addition, we demonstrate that the absorption in a solar cell stack does not change. Figure 4.9 shows the absorption spectra of the devices with 30 nm and 70 nm blend layer thickness of set 2. For both blend layer thicknesses, only minor changes in the absorption are visible. The absence of significant changes shows that the average alignment of the molecules inside the blend has not changed.

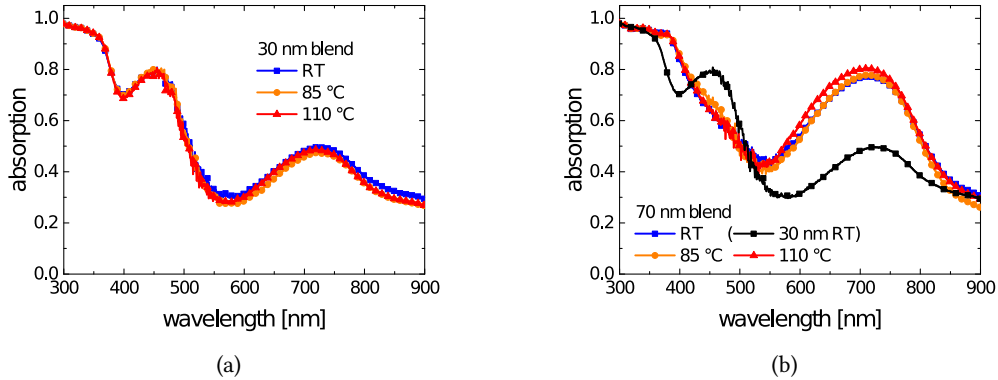


Figure 4.9.: Absorption of solar cells of set 2 with (a) 30 nm blend layer and (b) 70 nm blend layer.

4.4. Charge carrier mobility

We investigate the mobility of the charge carriers using OTRACE, to check whether a change in mobility upon substrate heating is responsible for the different behavior of the FF . We investigate devices with 100 nm thick blend layer, which have the same stack as the devices of set 1 and were discussed in the solar cell section. However, we use solar cells with smaller active areas of 2.85 mm^2 to avoid that the current transients measured in OTRACE are limited by the RC -time.⁵ The OTRACE measurements were performed by André Nascimento (IAPP). The evaluation was done by Sascha Ullbrich (IAPP). Figure 4.10(a) shows the OTRACE curves for a delay time of $1 \mu\text{s}$. The mobility is determined using the formula (3.18). The mobility of the $110 \text{ }^\circ\text{C}$ sample is $6 \cdot 10^{-4} \text{ cm}^2/\text{Vs}$ and roughly one order of magnitude higher than for the $85 \text{ }^\circ\text{C}$ device ($8 \cdot 10^{-5} \text{ cm}^2/\text{Vs}$) and the RT device ($3 \cdot 10^{-5} \text{ cm}^2/\text{Vs}$). Figure 4.10(b) shows the behavior of the mobilities as a function of $(t_{\text{max}} + \Delta t)$, which corresponds to the time delay between the end of the light pulse and the maximum of the current response. The graph shows that the mobilities determined at $\Delta t = 1 \mu\text{s}$ are representative for delay times up to $1 \cdot 10^{-4} \text{ s}$ as the changes in mobility in this time frame are small. In addition, OTRACE measurements are conducted for solar cells with an intrinsic interlayer of BPAPF. These devices have the same stack as the solar cells from set 2 and are prepared in the same Lesker

⁵The solar cells were prepared in the same Lesker run as the solar cells of set 1.

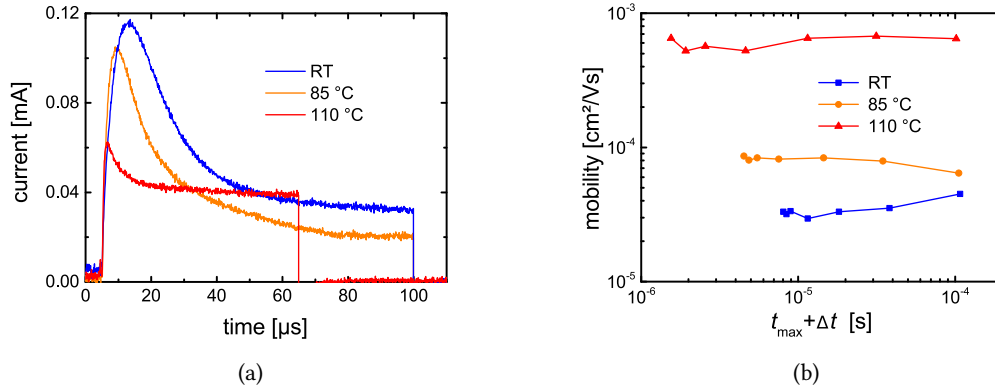


Figure 4.10.: (a) Current transients measured with OTRACE for the 100 nm devices at different T_{sub} after 1 μs delay time. (b) Overview of the determined mobilities for different delay times.

run. The only difference is the smaller area of 1.68 mm^2 . Again, with $\mu = 3 \cdot 10^{-4} \text{ cm}^2/\text{Vs}$, the mobility of the 110 °C sample is one order of magnitude higher than the RT ($5 \cdot 10^{-5} \text{ cm}^2/\text{Vs}$) or the 85 °C ($3 \cdot 10^{-5} \text{ cm}^2/\text{Vs}$) device. As in both measurement series the RT devices have a mobility that is more than one order of magnitude lower than for the 110 °C devices, we exclude a higher mobility as the reason for the beneficial $FF(d)$ dependence of RT devices as compared to the 110 °C devices.

4.5. Impedance spectroscopy

Since trap states can influence the charge transport in organic thin films and, therefore, the fill factor in organic solar cells, we apply impedance spectroscopy to obtain information about the trap distribution in DTDCTB:C₆₀ blend layers. We characterize m-i-m devices consisting of ITO | 100 nm blend | 100 nm Al deposited at RT / 85 °C / 110 °C.⁶ Measurements of jV curves in dark and under illumination can be found in Figure A.4 of the Appendix. Figure 4.11(a) depicts the Cf spectra for these devices. The Cf spectra of the RT- and 85 °C sample exhibit two ω -dependent capacitance plateaus, which is a sign of a capacitance contribution due to trap states. For the 85 °C sample, it is difficult to distinguish between the first and the second plateau, because the second plateau is close to 10^5 Hz and the geometrical capacitance is cut off by the series resistance at 10^6 Hz. The 110 °C sample exhibits only the plateau of the geometrical capacitance without any contribution of trap states.

In order to estimate the amount of the trap states, capacitance-voltage measurements are performed for the RT and 85 °C devices. The Mott-Schottky plot of the measurements is shown in Figure A.4(c) of the Appendix. Using equation (3.14), we calculate the apparent

⁶Note that the samples were prepared on the same Lesker matrix as the devices of set 1, which were discussed in solar cell section.

4. DTDCTB

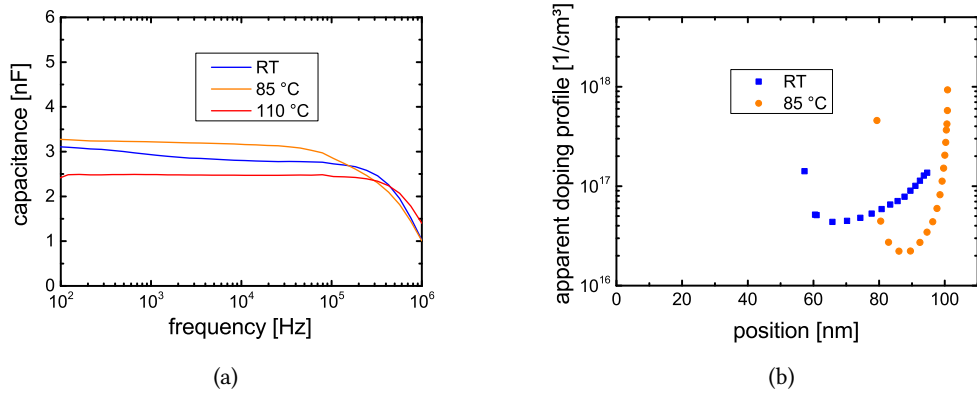


Figure 4.11.: (a) Cf plot of the ITO | DTDCTB:C₆₀ (100 nm) | Al devices, (b) apparent doping profile of the RT and 85 °C sample. The frequency for the RT sample was 10^2 Hz and for the 85 °C sample 10^3 Hz.

doping profile of the devices. According to Kirchartz *et al.*, for thin devices with a thickness of 100 nm or less, only an upper limit of the traps states can be estimated.[110] Figure 4.11(b) shows the apparent doping profile for the RT- and 85 °C samples.⁷ The minima of the apparent doping profiles indicate an upper limit of the trap density of around $2 \cdot 10^{16} \text{ cm}^{-3}$ for the 85 °C sample and $4 \cdot 10^{16} \text{ cm}^{-3}$ for the RT sample. The corresponding slope of the capacitance of the RT sample are recorded at positive bias voltages.⁸ Therefore, injection currents are present that cause a chemical capacitance that superposes the capacitance of the space charge region and leads to an overestimation of the upper limit of the trap density.

We perform temperature dependent measurements and apply the method suggested by Walter *et al.* (see section 3.3.11) to get information about the energetic distribution of the traps.[111, 112] Figure 4.12(a) shows Cf spectra for the three samples for temperatures from -30 °C to 30 °C in steps of 10 K. The corresponding modulus- f and phase- f plot can be found in Figure A.3 in the Appendix. The RT sample and the 85 °C sample exhibit changes in the plateaus upon temperature variation, confirming the trap hypothesis from the first Cf measurements. The 110 °C sample exhibits no change upon the temperature variation, proving that the first plateau corresponds to the geometric capacitance, with no detectable traps. In order to calculate the density of traps per energy, we need the built-in voltage and the width of the space charge region. Since for low trap densities the built-in voltage determined by analysis of the CV plot is unreliable, we estimate the built-in voltage from the difference between the work functions of the electrodes.[110] The work function of aluminum is 4.2 eV. For the ITO work function, values of 4.5 - 4.9 eV can be found.[125–127] Since the voltage of the RT m-i-m device is $V_{oc}=0.65$ V and the $FF=50\%$ (see Figure A.4(a) in the Appendix), we estimate that the

⁷For the calculation of the apparent doping profile, we used $\epsilon_r(\text{RT})=4.82$ and $\epsilon_r(85 \text{ °C})=4.61$, which were calculated from Cf spectra of devices with different blend layer thicknesses. A description of the procedure can be found in section A.1.4 of the Appendix.

⁸compare Figure A.4(c) in the Appendix.

built-in voltage is at least 0.7 V, corresponding to an ITO work function of 4.9 eV. Otherwise the FF should be significantly lower.[110] For the width of the depleted layer, we assume the thickness of the intrinsic layers (100 nm). Figure 4.12(b) shows an Arrhenius plot determined via the Walter method for the RT and 85 °C sample. Furthermore, the determined values for the attempt-to-escape frequency and the trap energy are displayed.

Figure 4.12 shows the calculated trap distributions for the RT sample (c) and the 85 °C sample (d). For the RT sample, we find a Gaussian trap distribution with a standard deviation of 50 meV at 440 meV with respect to the transport level. For the 85 °C sample, a Gaussian distribution at 310 meV with a standard deviation (σ) of 25 meV is measured. The fitted trap densities of $\approx 2 \cdot 10^{16} \text{ cm}^{-3}$ are reasonable, considering the upper limit of the trap densities determined by the CV measurements. Figure 4.13 shows the obtained trap levels in relation to the energy levels of the system. As the gap between the ITO workfunction and the DTDCTB is $\approx 0.5 \text{ eV}$, we conclude that the measured traps are electron traps. Hole traps with a similar trap depth with respect to the hole transport level cannot be measured in the used m-i-m configuration. The trap states for the RT and 85 °C sample provide an explanation for the lower mobility for devices fabricated at these substrate temperatures. For the 110 °C sample, which has the highest mobility, no trap states are detected. However, since the Fermi level of the ITO and the aluminum are different from the Fermi level in n-Bis-HFI-NTCDI and p-BPAPF for the complete solar cell, there might be trap states that cannot be detected in the simplified stack. Though an investigation of complete solar cells is beneficial, the interpretation of the impedance signal is difficult as the doped transport layers can lead to an additional capacitive contribution that makes the evaluation of the bulk traps difficult. For this reason, the impedance spectra of the complete devices are briefly discussed in Section A.1.4 of the Appendix. The main point of the full device measurement is that in the complete solar cell, the RT devices have a significantly higher geometrical capacitance indicating a higher relative permittivity of the blend layer.

4.6. Lifetime and Recombination

A model often discussed in literature links the fill factor of a solar cell with the mobility-lifetime product of the photoactive layer.[63] As we determined the mobility of the devices in a previous section, we now investigate the lifetime of the charge carriers by transient photovoltage measurements. The measurements were performed by Sascha Ullbrich. The evaluation was done in cooperation with Sascha Ullbrich. We ignore the 85 °C sample for the evaluation, as there are barrier effects affecting the measurements. Figure 4.14(a) shows the lifetime as a function of the open circuit voltage. For 0.82 V, which corresponds to both open circuit voltages at 1 sun illumination within the measurement uncertainty, the lifetime of the RT device ($\tau=5.0 \mu\text{s}$) is higher by a factor of approximately two than that of the 110 °C device ($\tau=2.4 \mu\text{s}$).⁹ Carrier lifetimes can only be compared at the same carrier density, which is exponentially related to the difference between V_{oc} and E_{CT} . A sensitive EQE measurement,

⁹The lifetime as a function of the charge carrier density is left out, because the transient photocurrent measurement induces a large spread in the measurement data as a function of the charge carrier density that is not present when analyzed as a function of the open circuit voltage.

4. DTDCTB

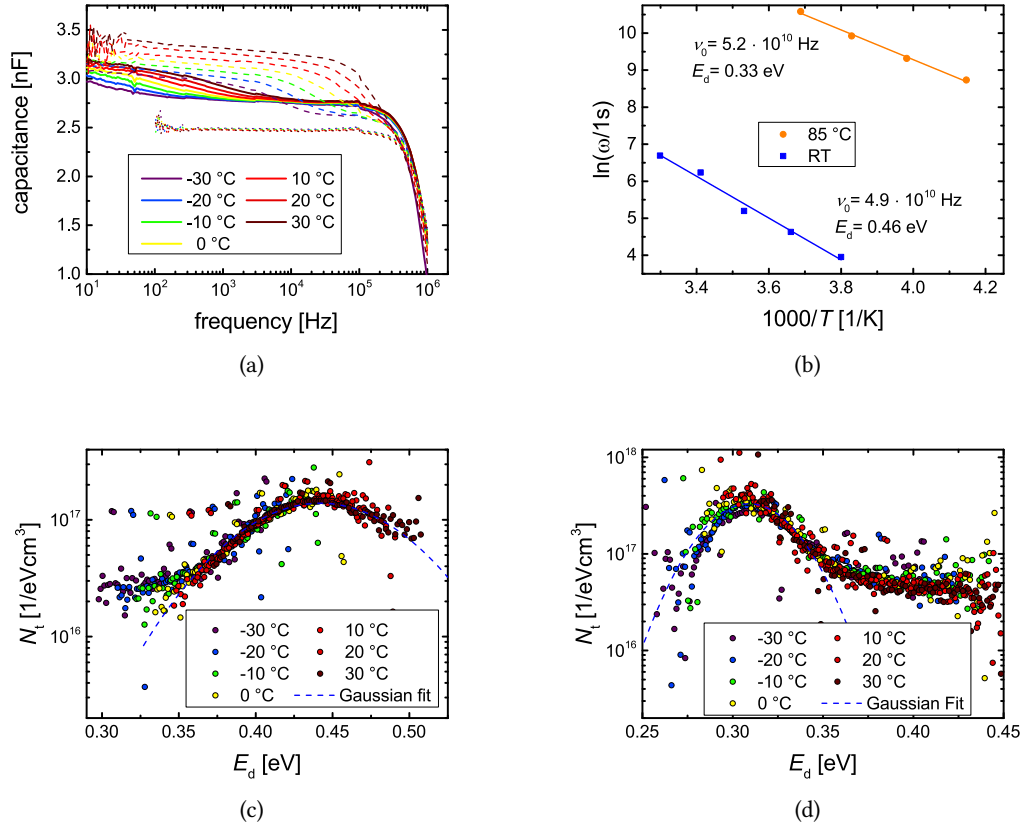


Figure 4.12.: Temperature dependent (a) Cf plot of the RT sample (solid lines), the 85 °C sample (dashed lines), and the 110 °C sample (dotted lines). The data points of the 110 °C sample are removed below 10^2 Hz, since the measured noise mashed the other lines. (b) Arrhenius plot for the determination of the demarcation energy. Trap distribution of the (c) RT- and the (d) 85 °C- sample determined by the Walter method. A built-in voltage of 0.7 V and the attempt-to-escape frequency determined in (b) are used for calculation. The blue line indicates a Gaussian Fit of the trap distribution. The determined parameters are for RT: mean trap energy $E_t=440$ meV, $\sigma=50$ meV, and $N_t = 1.7 \cdot 10^{16} \text{ cm}^{-3}$. For 85 °C, it is $E_t = 310$ meV, $\sigma = 25$ meV, and $N_t=1.9 \cdot 10^{16} \text{ cm}^{-3}$.

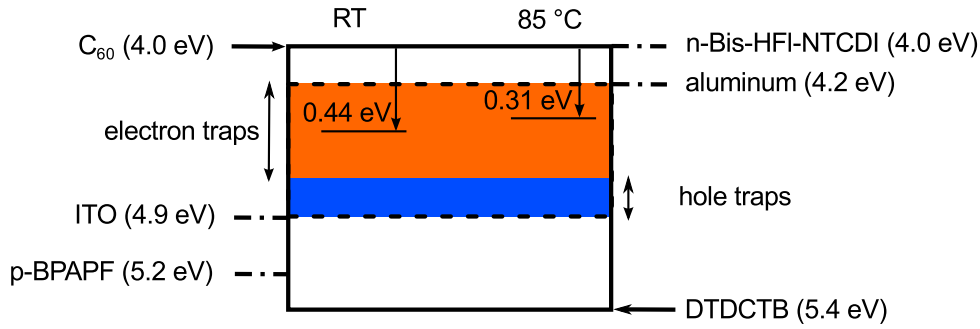


Figure 4.13.: Sketch of the energy levels of the materials, including the determined position of the trap energies at both substrate temperatures.

presented in Figure A.7 in the Appendix, indicates no change of the CT state energies. Thus, we assume that we have equal carrier densities when we have equal V_{oc} . In the framework of the $\mu\tau$ product as a measure for the charge extraction yield and, therefore, the fill factor, this data provides also no reasonable explanation: While the mobility of the 110 °C device is an order of magnitude higher than the RT device, a carrier lifetime of the RT device, which is only a factor 2 higher than the 110 °C device results in a $\mu\tau$ product of the RT sample, which is still five times smaller than for the 110 °C device.

In order to get further insight into the recombination dynamics, we determine the diode ideality factor by evaluating current and voltage measurements as described in section 3.3.14.[116, 117] The measurement was performed by André Nascimento. Figure 4.14(b) shows the open circuit voltage as a function of the short circuit current. From the slope of the curves, we extract the diode ideality factor, which is presented in Figure 4.14(b). The determined diode ideality factors indicate that the recombination for the RT ($n_{id}=1.16$) and the 110 °C sample ($n_{id}=1.21$) is bimolecular. In contrast, the 85 °C sample has a high diode ideality factor of 1.82. In combination with the trap states found in the impedance measurements, this value hints to recombination via traps.

4.7. Conclusion

The behavior of the fill factor with increasing DTDCTB:C₆₀ thickness depends strongly on the substrate temperature during the deposition. Three regimes can be identified: At RT, the fill factor increases up to 50 nm blend layer thickness and stays constant up to 70 nm. In a medium temperature regime around 85 °C an S-kink is present, which keeps the fill factor constantly below 25%. In the high temperature regime at ≈ 100 -110 °C, the fill factor drops monotonically, as usually observed for an increase of the blend layer thickness in organic solar cells. Due to the beneficial $FF(d)$ performance, the optimized RT device has a η_{PCE} of 4.9%, while the optimized 110 °C device reaches only 3.5%. This behavior raises two questions: What causes the fill factor development at RT and: Can this knowledge be applied

4. DTDCTB

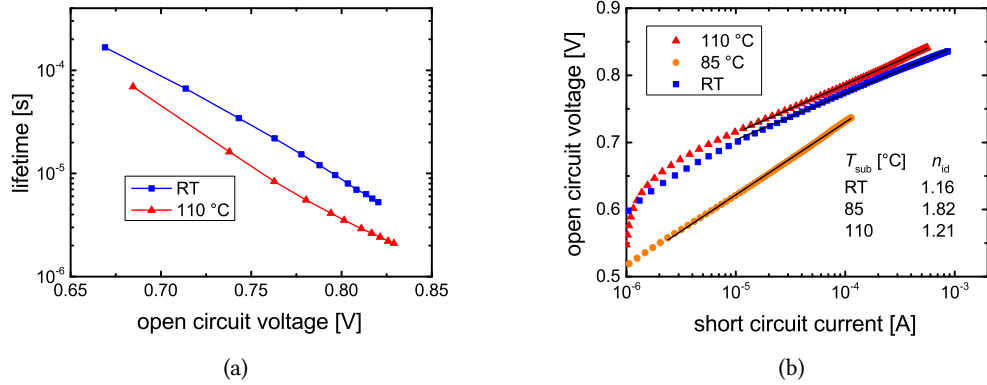


Figure 4.14.: (a) Carrier lifetime as a function of the open circuit voltage for the RT sample and the 85 °C sample. (b) Open circuit voltage as a function of the short circuit current of the RT (blue squares), 85 °C (orange circles), and 110 °C (red triangles) sample. The black lines indicate the measurement data used for fitting the diode ideality factor.

to other photovoltaic blends? As the change is solely induced by substrate heating, it can be attributed to a morphological change in the blend layer. The GIWAXS measurements indicate that the change cannot be explained by an increase in crystallinity of the blend layer as the diffraction patterns do not change upon substrate heating during the deposition. Furthermore, absorption measurements show that the average alignment of the molecules inside the blend layer is not changed. Based on these results, we expect a rather local intermolecular change of the morphology. The reasonable assumption that a higher mobility of the charge carriers causes the higher fill factor at RT is not supported by the OTRACE measurements. Here, the device processed at 110 °C has a mobility ($6 \cdot 10^{-4} \text{ cm}^2/\text{Vs}$) that is an order of magnitude higher than for the RT device ($3 \cdot 10^{-5} \text{ cm}^2/\text{Vs}$). The difference in mobility can be explained by the presence of trap states, detected by impedance spectroscopy measurements in the ITO | blend | Al devices. While the RT- and the 85 °C samples exhibit trap states, no trap contribution is found for the 110 °C device. In addition, the lifetime of the charge carriers is determined for the RT and 110 °C device by transient photovoltage measurements. Though the 110 °C and RT devices have a comparable V_{oc} , the lifetime of the charge carriers in the RT sample ($\tau=5.0 \mu\text{s}$) is roughly two times higher than for the charge carriers in the 110 °C device ($\tau=2.4 \mu\text{s}$). In combination with the mobility values, the $\mu\tau$ product of the 110 °C devices is still five times higher than for the RT devices. Therefore, the $FF(d)$ dependence cannot be explained by an increased $\mu\tau$ product. Furthermore, V_{oc} - I_{sc} measurements were performed to determine the diode ideality factor that is slightly lower for the RT device ($n_{id}=1.16$) compared to the 110 °C device ($n_{id}=1.21$). The values indicate that the recombination is in both cases close to bimolecular. The presented measurements can only exclude approaches to an explanation of the behavior of $FF(d)$ for the different sub-

4.7. Conclusion

strate temperatures. For a conclusive explanation of this behavior further investigations are necessary.

5. Thermally stable benzothiadiazole compounds

This chapter gives an overview of the work on new benzothiadiazole derivatives (PRTF, CNTF, TFTF) based on the known donor molecule DTDCTB. The design motive for these donor molecules is the enhancement of the thermal stability of the molecules against decomposition by stabilizing a vinyl group with an H · · · F bond. For PRTF, higher sublimation yields are achieved. However, the reduced absorption of the new derivatives in comparison to DTDCTB limits the capability to generate current in the organic solar cell. The materials are tested and optimized in organic solar cells with C₆₀ as acceptor, resulting in a maximum power conversion efficiency of 3.8% for PRTF:C₆₀ solar cells. A stable FF over a larger range of active layer thicknesses as for DTDCTB:C₆₀ devices is not observed. While not achieving the power conversion efficiencies of the original DTDCTB molecules, an outstanding reduction of the non-radiative voltage losses to 0.26 V is detected for PRTF:C₆₀ and CNTF:C₆₀ devices. Parts of this chapter are published in reference [107], Copyright 2016, reprinted with permission from Elsevier.

5.1. Introduction

While DTDCTB has a very good performance in organic solar cells, its yield upon vacuum gradient sublimation is rather low. Over 3 sublimation steps, the yield is approximately 18-24%. Since purified materials are a prerequisite for batch to batch reproducibility, DTDCTB was the starting point for plans to new, thermally more stable materials. The vinyl group in the dicyanovinyl moiety of DTDCTB was identified as the weak point for thermal stability, as it is prone to decomposition. Problems with this terminal group in other materials were reported in literature.[90, 128, 129] Consequently, three new materials were designed by Dr. Olaf Zeika and Lijia Fang (both IAPP) to avoid this problem. Figure 5.1 shows the structures of the new materials in comparison to DTDCTB. One cyanide of the dicyanovinyl moiety of DTDCTB is either replaced by a 2,3,5,6-tetrafluoropyridine-4-yl moiety (PRTF), a 4-cyano-2,3,5,6-tetrafluorobenzene-1-yl moiety (CNTF), or a 4-(trifluoromethyl)-2,3,5,6-tetrafluorobenzene-1-yl moiety (TFTF). The principle for enhancing the stability of such materials for sublimation can be ascribed to the formation of a hydrogen-bonding bridge between a fluorine atom and the acidic vinyl proton. This bridge leads to the formation of a closed six-membered ring, thus preventing the decomposition to acrylonitrile as it is often seen with high temperature vacuum sublimation of this series of materials. The following two paragraphs summarize experimental data that indicate that the molecular design worked out for PRTF.

5. Thermally stable benzothiadiazole compounds

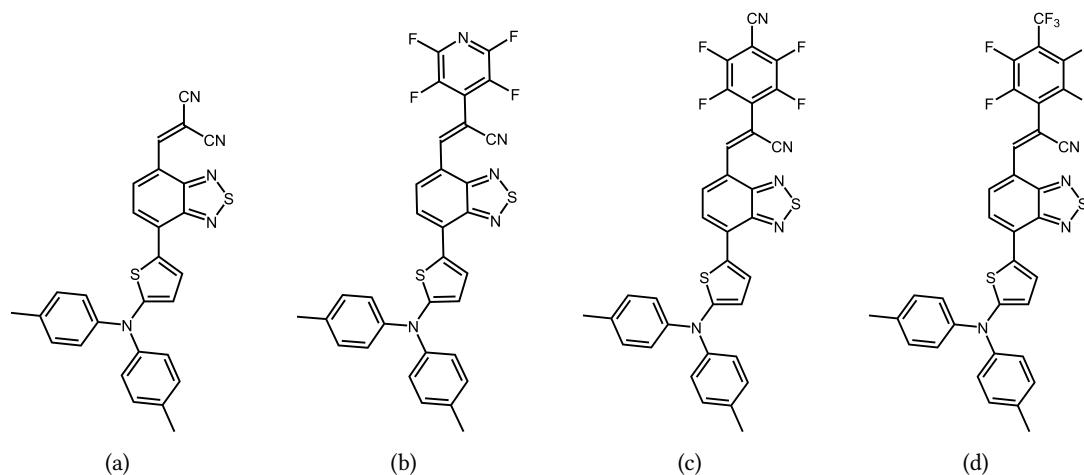


Figure 5.1.: Molecular structures of (a) DTDCTB, (b) PRTF, (c) CNTF, and (d) TFTF.

Thermal gradient sublimation An indicator that the design strategy works for PRTF is the higher yield upon sublimation. Table 5.1 gives an overview of the material yields over three steps of thermal gradient sublimation. DTDCTB has a sublimation yield of 18% to 24%, comparable to the yields of CNTF and TFTF with approximately 25% sublimation yield. PRTF yields 55%, which is more than twice the yield of the other materials. Variations in the sublimation yield as observed for different batches of DTDCTB can be caused e.g. by differences in the purity or amount of the input material or the applied temperature gradient during the sublimation. However, the doubled sublimation yield of PRTF is beyond these uncertainties.

Table 5.1.: Overview of sublimation yields upon 3 steps of thermal gradient sublimation. The sublimation was performed by Annette Petrich (IAPP).

material	starting mass [mg]	end mass [mg]	yield
DTDCTB	2500	460	18%
	2290	560	24%
	1570	340	22%
PRTF	2020	1110	55%
CNTF	1930	480	25%
TFTF	1280	320	25%

Molecular structure The reason for the higher thermal stability of PRTF is the shorter distance between the hydrogen and the fluorine atom in the PRTF molecule compared to TFTF and CNTF. The distances were obtained by X-ray diffraction on single crystals. These measurements were performed by Dr. Jens Hunger (Anorganische Chemie 2, TU Dresden).

The evaluation was done by Lijia Fang. Figure 5.2 presents the determined molecular structures. An analysis of the lengths between the hydrogen atom and the fluorine atom gives values of 2.54 Å for TFTF, 2.53 Å for CNTF, and 2.34 Å for PRTF. The shorter hydrogen bond length of PRTF indicates a better stabilization of the acidic vinyl proton in the acceptor unit, which had been identified to be responsible for the low thermal stability.

Besides the aspect of the thermal stability, PRTF differs in two other properties from the other molecules. The first characteristic is the alignment of the benzothiadiazole unit with respect to the thiophenyl ring. For PRTF, the sulfur atoms of the benzothiadiazole unit and the thiophenyl unit are pointing in the same direction, while for CNTF, TFTF, and DTDCTB they are pointing in opposite directions. Secondly, PRTF has a triclinic crystal structure, while CNTF and TFTF, like DTDCTB, have a monoclinic crystal structure.[118]

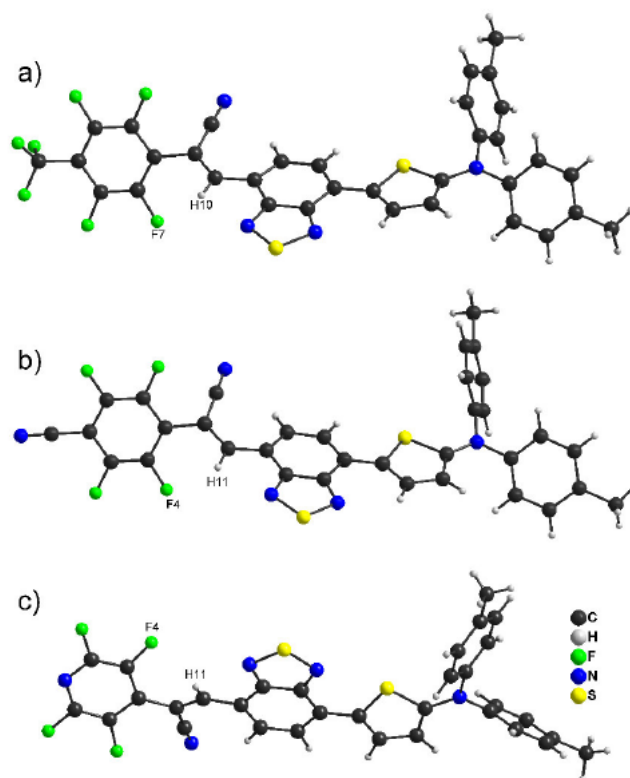


Figure 5.2.: X-ray-characterized molecular structures and intramolecular hydrogen bond lengths of a) TFTF (CH10 \cdots F7, 2.54 Å) b) CNTF (CH11 \cdots F4, 2.53 Å), and c) PRTF (CH11 \cdots F4, 2.34 Å).

5.2. Thin film investigation

This section summarizes the experiments on the evaporated thin films of the materials in neat layers and blends with C₆₀. GIXRD measurements indicate a weak long range order

5. Thermally stable benzothiadiazole compounds

of the donor materials. AFM measurements show a smooth surface in neat layers as well as blends. The absorption of the materials is weaker than for DTDCTB and blueshifted, decreasing the photoresponse of the solar cells. UPS measurements show a deeper lying I^p of the new materials in comparison to DTDCTB.

5.2.1. Morphology

GIXRD measurements provide information about the long range order of the layers, AFM measurements about the surface roughness. Table 5.2 gives an overview of the investigated samples. Figure 5.3(a) shows the diffractograms of the neat layers 1, 5, and 7. All diffractograms have a comparable peak pattern with one broad maximum around 20° . This indicates that the samples have a weak long range order. Figure 5.3(b) shows the GIXRD measurements of the molecules blended with C_{60} (samples 2, 6, and 8). The respective mixing ratio is chosen according to the best mixing ratio for the solar cells. Again, all diffractograms exhibit a similar peak pattern. In this case, it is a three peak structure with maxima at $10.6^\circ \pm 0.3^\circ$, $19.5^\circ \pm 0.2^\circ$, and $28.8^\circ \pm 0.1^\circ$. The maxima can be assigned to a superposition of different Bragg reflexes of C_{60} . The pattern of the donor materials might contribute to the 20° peak. This is a typical peak pattern for a blend consisting of a rather amorphous donor blended with the nanocrystalline C_{60} . Similar diffraction patterns can be found for aza-BODIPY: C_{60} blends.[130] The change in morphology upon substrate heating is exemplarily studied for PRTF, since this donor achieves the highest power conversion efficiencies. Figure 5.3(c) shows the GIXRD diffractograms for PRTF: C_{60} samples for different substrate temperatures during the deposition (samples 2-4) in comparison to neat PRTF (sample 1). The changes upon substrate heating are minor, mainly a reduction in intensity of the Bragg peak at 10.6° associated with C_{60} . Figures 5.3(d) and 5.3(e) show the AFM images of the samples 5 (TFTF) and 7 (CNTF). Both samples exhibit a smooth surface with RMS surface roughnesses below 1 nm, similar to the results for PRTF and DTDCTB.[121, 131] In summary, all three donor materials have a comparable thin film morphology with little long range order in neat film as well as in blend layers with C_{60} . The neat layers have a smooth surface. Substrate heating during the deposition as a means to increase the crystallinity in the blend layer has no measurable effect on the crystallinity of the blend layer. In this regard, the materials are very similar to DTDCTB.[121]

5.2.2. Absorption

Figure 5.4 shows a comparison between the optical densities of 46 nm thick layers of PRTF, TFTF, and CNTF. The absorption maximum of TFTF is located at 636 nm and is blueshifted compared to PRTF (650 nm) or CNTF (657 nm). The optical density of PRTF and CNTF is also higher than the optical density of TFTF. This relationship is also observed in the solution spectra.[107] Furthermore, the absorption of a 44 nm thick DTDCTB layer (686 nm) is depicted. One can clearly see that the new derivatives have the absorption maximum at higher energies and a reduced absorption strength compared to DTDCTB. This is a serious drawback of the materials, because less excitons are generated for the same layer thickness.

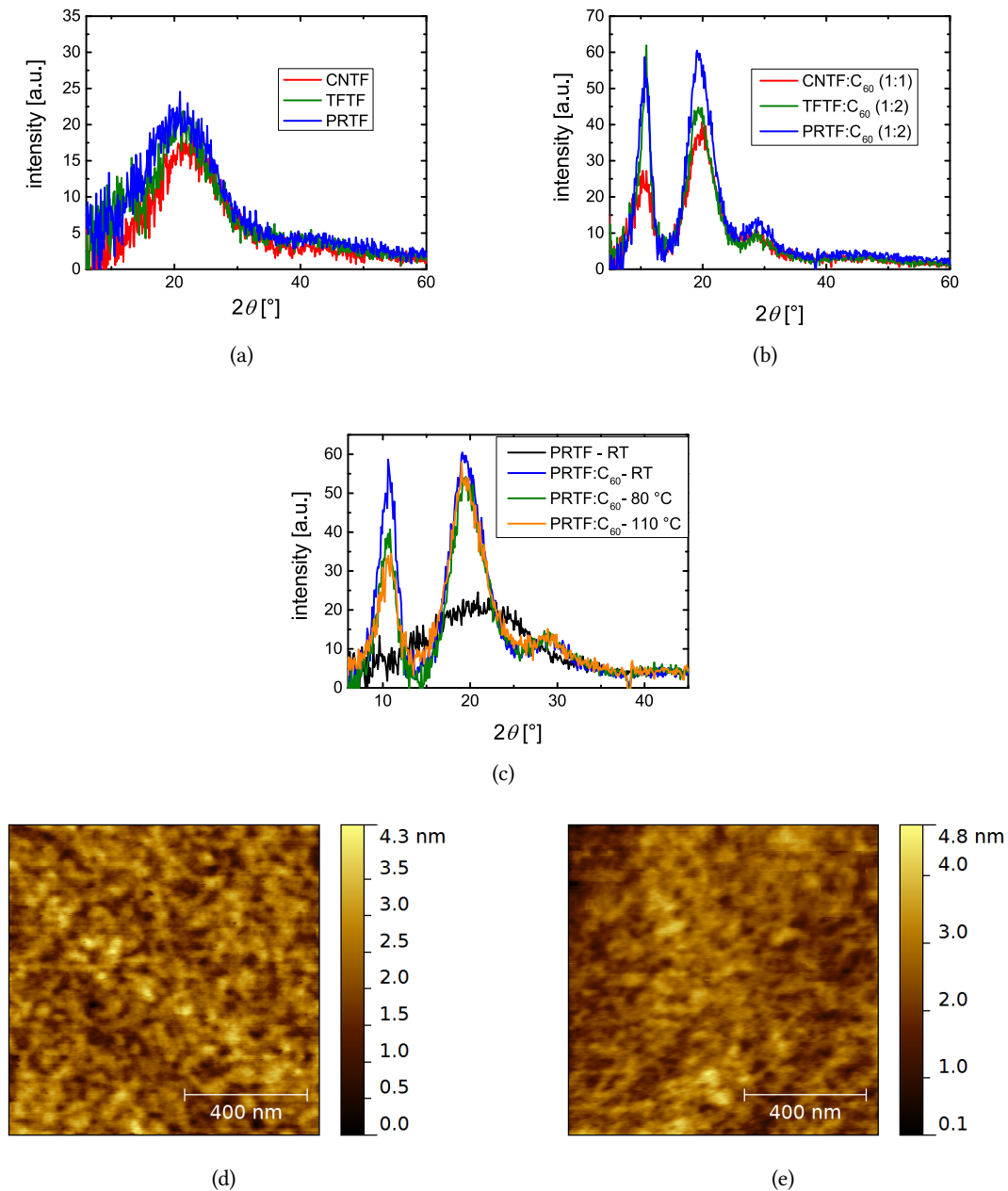


Figure 5.3.: (a) GIXRD measurements of single layers of CNTF (red), TFTF (green), and PRTF (blue). (b) GIXRD measurements of blend layers of CNTF (red), TFTF (green), and PRTF (blue) with C_{60} . (c) GIXRD measurements on PRTF: C_{60} blend layers processed at $T_{\text{sub}}=\text{RT}$ (blue), $T_{\text{sub}}=80\text{ }^{\circ}\text{C}$ (green), and $T_{\text{sub}}=110\text{ }^{\circ}\text{C}$ (orange). AFM images of (d) neat TFTF (sample 5) and (e) neat CNTF layers (sample 7).

5. Thermally stable benzothiadiazole compounds

Table 5.2.: Overview of morphology samples for GIXRD, XRR, and AFM. Samples 1-4 were prepared by Christoph Hauenstein (IAPP), samples 5-8 were prepared by Daniel Schütze (IAPP).

sample	material	thickness [nm]	substrate temperature
1	PRTF	50	RT
2	PRTF:C ₆₀ (1:2)	40	RT
3	PRTF:C ₆₀ (1:2)	40	80 °C
4	PRTF:C ₆₀ (1:2)	40	110 °C
5	TFTF	40	RT
6	TFTF:C ₆₀ (1:2)	40	RT
7	CNTF	40	RT
8	CNTF:C ₆₀ (1:1)	40	RT

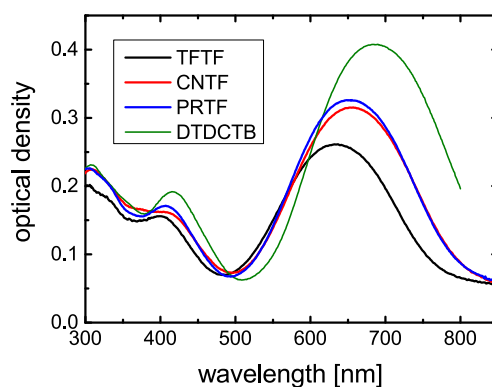


Figure 5.4.: Comparison of PRTF, TFTF, and CNTF layers (46 nm) to a DTDCTB layer (44 nm). All samples are processed on quartz glass. The TFTF and CNTF samples were prepared and measured by Annette Petrich (IAPP).

5.2.3. Energy levels

The ionization potentials of the materials are determined by UPS. The stack of the samples is pre-sputtered Au foil | C₆₀ (5 nm) | donor (10 nm). The 5 nm C₆₀ layer is included in order to mimic the growth conditions in the solar cell, assuming that the growth of C₆₀ is similar on ITO and on the gold substrate. Table 5.3 lists the ionization potentials of the donor materials. The corresponding spectra are presented in reference [107]. TFTF (CNTF) have an *IP* of 5.65 eV (5.63 eV), which is about 0.1 eV lower than measured for PRTF with 5.51 eV. Thereby, all donor materials have a higher *IP* than DTDCTB (5.4 eV) and a higher open circuit voltage in the solar cells is possible.

Table 5.3.: The UPS measurements were done and evaluated by Martin Schwarze (IAPP). The TTF sample was prepared by Daniel Schütze (IAPP).

donor	TTF	CNTF	PRTF
IP [eV]	5.65	5.63	5.51

5.3. Solar cells

The solar cell section is divided into four parts. In the first part, all solar cells are compared within the same stack design for a first overview. In the second part, the solar cells are independently optimized for power conversion efficiency. The third section covers the comparison of the materials with DTDCBTB with regard to the j_{sc}/FF dependence at different film thicknesses and substrate temperatures during the deposition. In the last part, the voltage losses of the materials are investigated.

5.3.1. Initial characterization

All three donor molecules are tested and compared in solar cells with the same device architecture. The stack is glass | ITO | n-C₆₀ (5 nm, 3 wt% W₂(hpp)₄) | C₆₀ (15 nm) | donor:C₆₀ (30 nm, 1:1) | BPAPF (5 nm) | p-BPAPF (40 nm, 10 wt% NDP9) | NDP9 (2 nm) | Al (100 nm).

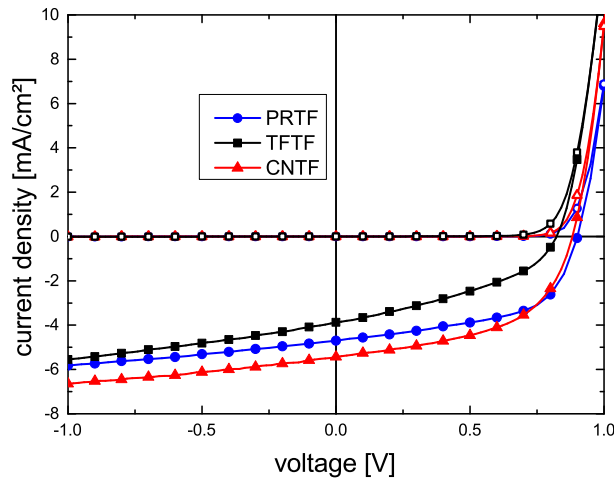


Figure 5.5.: (a) Scheme of the solar cell stack. (b) jV curves, under solar illumination (closed symbols) and in the dark (open symbols) of the solar cells.

Figure 5.5 shows the jV curves of the solar cells and Table 5.4 presents a summary of the solar cell parameters. The best efficiency of the non-optimized solar cells has the CNTF device with a η_{PCE} of 2.4% followed by the PRTF device with a η_{PCE} of 2.3%. The CNTF device has

5. Thermally stable benzothiadiazole compounds

the higher η_{PCE} because its j_{sc}^* of 5.3 mA/cm² is significantly higher than the j_{sc}^* of the PRTF device (4.7 mA/cm²). The slightly higher values for the PRTF device, regarding V_{oc} (0.90 V) and FF (55%) cannot compensate the higher j_{sc}^* of the CNTF device ($V_{\text{oc}}=0.88$ V, $FF=53\%$). The TFTF device has the smallest η_{PCE} (1.2%) as it is inferior in every solar cell parameter ($V_{\text{oc}}=0.82$ V, $FF=39\%$, $j_{\text{sc}}^*=3.8$ mA/cm²). The low FF of the TFTF device is partly related to the blend ratio with C₆₀. In the subsequent optimization of the donor:C₆₀ stoichiometry and the substrate temperature during the deposition, significantly higher FF are achieved (see below).

Table 5.4.: Solar cell parameters of the devices with 30 nm thick blend layer in a 1:1 ratio. j_{sc}^* are the current densities projected to 100 mW/cm².

donor	V_{oc} [V]	j_{sc} [mA/cm ²]	FF [%]	I_{ill} [mW/cm ²]	j_{sc}^* [mA/cm ²]	η_{PCE} [%]
TFTF	0.82	3.9	39	102	3.8	1.2
CNTF	0.88	5.4	53	103	5.3	2.4
PRTF	0.90	4.7	55	100	4.7	2.3

5.3.2. Optimization of the solar cells

All donor materials are separately optimized to further increase the power conversion efficiency. Christoph Hauenstein optimized the 30 nm thick PRTF:C₆₀ solar cells at room temperature with respect to blending ratio in the framework of his Bachelor thesis.[131] Testing blending ratios of 2:1, 1:1, 1:2, 1:3, 1:4, and 1:5, he found that the optimal blending ratio for this material system is 1:2. In addition, he showed in a comparison between BF-DPB ($IP=5.23$ eV) and BPAPF ($IP=5.6$ eV) that BPAPF is the more suitable HTL.[131] This is in accordance with the IP of 5.51 eV for PRTF, determined by UPS. We start the further optimization at this blending ratio and test the following device stack: glass | ITO | n-C₆₀ (5 nm, 3 wt% W₂(hpp)₄) | C₆₀ (15 nm) | donor:C₆₀ (var. thickness, 1:2) | BPAPF (5 nm) | p-BPAPF (40 nm, 10 wt% NDP9) | NDP9 (2 nm) | Al (100 nm). Please note that the three materials were also tested in a p-i-n configuration. However, due to the higher FF in the n-i-p configuration, we proceed the optimization in n-i-p structure. In the course of the measurement series, we optimize the blend layer thickness and substrate temperature during the deposition. The best results are achieved for a blend layer thickness of 60 nm deposited at a substrate temperature of 110 °C. The results for j_{sc}^* and FF are depicted in Figure 5.7 and are discussed below. For the solar cells using TFTF and CNTF, blend ratios of 2:1, 1:1, and 1:2 are tested at room temperature.¹ The best blending ratio for TFTF is 1:2, while it is 1:1 for CNTF. In a second step, substrate temperatures of 80 °C and 110 °C are tested for blend layer thicknesses of 30/40/50/60/70/90 nm. For TFTF, like PRTF, a 60 nm thick blend layer in a 1:2 ratio with C₆₀ deposited at a substrate temperature of 110 °C shows the optimal performance. For the CNTF devices, substrate heating as well as thicker blend layers decrease the power conversion efficiency. However, the insertion of a 3 nm thick intrinsic layer of CNTF on top of the

¹ jV and EQE measurements were performed by Dr. Rico Meerheim (IAPP).

blend layer has a positive effect. The best solar cells for each material are summarized in Table 5.5. The corresponding jV -curves are shown in Figure 5.6(a).

Table 5.5.: Fingerprints of the solar cells. The best configurations for the absorber layers are TFTF:C₆₀ (1:2, 60 nm, $T_{\text{sub}}=110$ °C), CNTF:C₆₀ (1:1, 30 nm, $T_{\text{sub}}=RT$) + 3 nm CNTF, and PRTF:C₆₀ (1:2, 60 nm, $T_{\text{sub}}=110$ °C).

absorber layer	V_{oc} [V]	j_{sc} mA/cm ²	FF [%]	I_{light} [mW/cm ²]	j_{sc}^* [mA/cm ²]	η_{PCE} [%]
TFTF	0.78	6.8	50	104	6.5	2.6
CNTF	0.89	6.1	52	104	5.8	2.7
PRTF	0.89	8.2	56	105	7.8	3.8

The PRTF solar cells have the highest power conversion efficiency among the optimized devices with a η_{PCE} of 3.8%, while the TFTF (2.6%) and CNTF (2.7%) devices yield lower values. The large gain in j_{sc}^* , based on the increased blend layer thickness of up to 60 nm is responsible for the efficiency increase of the PRTF and TFTF device. However, this is only possible because of the positive effect of the substrate heating on FF and j_{sc}^* . The PRTF device (7.8 mA/cm²) has now the highest j_{sc}^* , followed by the TFTF device with 6.5 mA/cm². The j_{sc}^* of the CNTF device (5.8 mA/cm²) gains only 0.5 mA/cm² upon the deposition of the additional pure CNTF layer. This difference in photocurrent between PRTF and TFTF devices can be attributed to both a stronger absorption and an increased internal quantum efficiency for the PRTF device by comparing the EQE spectra (Figure 5.6(b)) to the total absorption spectra of the devices (Figure 5.6(c)). The former is directly concluded from the higher absorption peak, leading to a higher EQE around 630 nm. The latter is inferred from the higher EQE for wavelengths below 550 nm in spite of identical absorption. This is in agreement with a lower FF of the TFTF device (50%) in comparison with the PRTF device ($FF=56\%$). In contrast to the PRTF and TFTF devices, the EQE of the CNTF device is strongly decreased in the region between 400 nm and 500 nm. This reduction is due to the smaller overall absorber layer thickness and the concomitant different thin film optics.

5.3.3. Comparison to DTDCTB

The molecular geometry of PRTF, CNTF, and TFTF differs only in the dicyanovinyl group from DTDCTB. Accordingly, we check whether some of the characteristic features of DTDCTB are also present in the devices with the derivatives. The first characteristic of DTDCTB is the FF of approximately 59%, which stays nearly constant for blend layer thicknesses from 30 nm to 70 nm, while j_{sc} increases steadily. This behavior changes significantly for higher substrate temperatures (see Chapter 4).

Figure 5.7 shows the trend of j_{sc} ((a),(c),(e)) and FF ((b),(d),(f)) as a function of the different blend layer thicknesses for the devices prepared during the optimization. The differently colored symbols represent the different substrate temperatures. None of the devices using the new derivatives exhibits a nearly constant FF for a larger blend layer thickness as it is the case for the DTDCTB devices at RT. Also the sharp kink in j_{sc} and FF is not observed for any of the derivatives. For the PRTF and TFTF devices, j_{sc} as well as FF increase from RT to

5. Thermally stable benzothiadiazole compounds

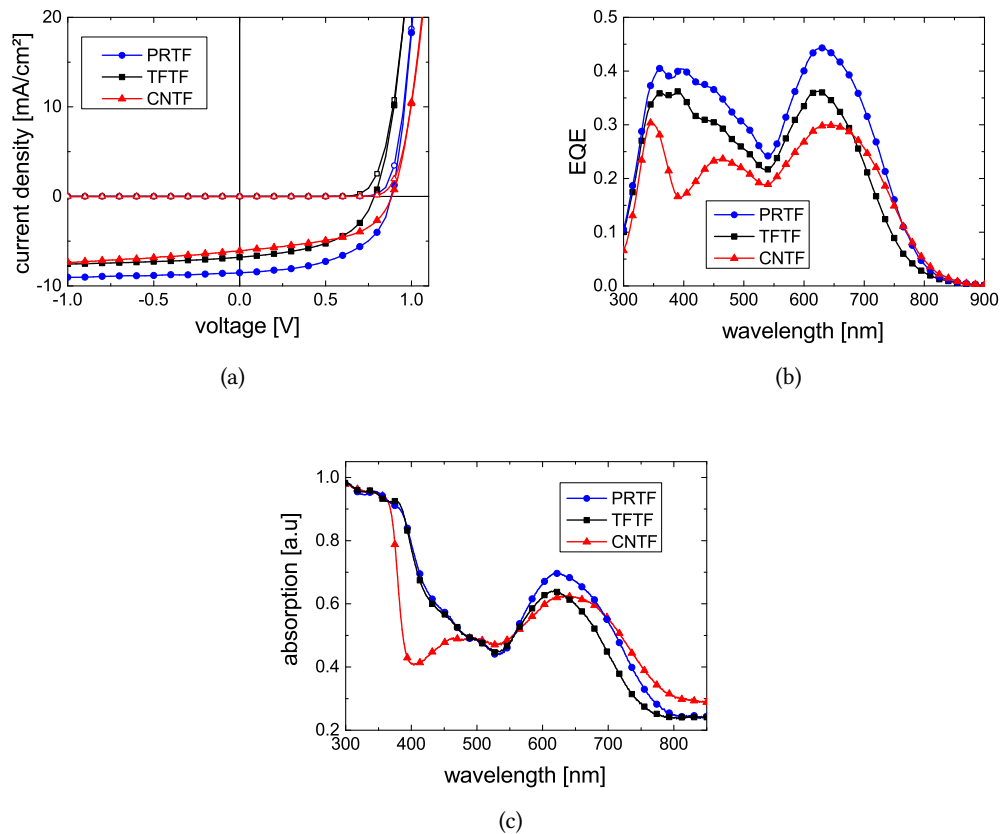


Figure 5.6.: (a) jV curves of the best solar cells with TFTF, CNTF, and PRTF as donor without illumination (open symbols) and under 1 sun illumination (solid symbols). (b) Corresponding EQE spectra of the solar cells. (c) Absorption of the solar cells, determined using their reflection spectra.

110 °C. However, the CNTF devices show a different trend. j_{sc} drops from RT to 80 °C and rises then again for $T_{sub}=110$ °C. Furthermore, j_{sc} as a function of the blend layer thickness differs for the substrate temperatures. While the devices processed at RT and 80 °C have the highest j_{sc} for the devices with 70 nm blend layer thickness, the devices processed at 110 °C achieve a maximum at 40 nm and decrease afterwards. The CNTF devices differ also in the trend of the FF . While for the PRTF and TFTF devices the FF increases with temperature, CNTF has the highest FF for the devices processed at RT. For the 80 °C devices, the FF is shifted to lower values. For the CNTF devices at 110 °C, the trend is more shallow, since the FF changes only from 40% to 36%. In summary, none of the devices processed with the new derivatives exhibits a similar dependence of the FF on the blend layer thickness as DTDCTB at RT. However, CNTF shows some similarities like the discontinuity in the substrate temperature dependence (lowest j_{sc} for 80 °C) and a constantly decreasing FF with increasing

substrate temperature. A further screening of the substrate temperatures during the deposition is expected to show similar trends.

5.3.4. Voltage losses

The fact that the TFTF device has the lowest V_{oc} in both measurement series might be surprising considering the ionization potentials (IP) presented in Table 5.3. The TFTF and CNTF thin films have an IP of 5.65 eV and 5.63 eV – about 0.1 eV larger than the IP of the PRTF film with 5.51 eV. However, the IP is determined for a neat layer, whereas it is known from literature that the IP in neat and blend layers can be significantly different.[132] In order to better understand the voltage differences, we investigate the devices presented in Table 5.4 using sensitive EQE and electroluminescence measurements to determine the energy of the charge transfer (CT) state as well as the voltage losses due to radiative and non-radiative recombination.[72] The sensitive EQE measurements and the overall evaluation of the voltage losses was performed by Johannes Benduhn (IAPP). Fortunato Piersimoni (University of Potsdam) performed the electroluminescence measurements. Figure 5.8 presents the results. The CT state energy is, in contrast to the IP , the decisive parameter for the evaluation of V_{oc} as it can be determined directly from the solar cells.[58] The results are presented in Table 5.6.

Table 5.6.: Overview of the CT state energy, the V_{oc} under the assumption of exclusively radiative recombination (V_{rad}), the non-radiative (ΔV_{nonrad}), and radiative (ΔV_{rad}) voltage losses as well as the overall voltage losses (ΔV_{oc}). The stack of the DTDCTB device differs from the other devices, see main text.

OSC containing	V_{oc} [V]	V_{rad} [V]	E_{CT} [eV]	ΔV_{nonrad} (V)	ΔV_{rad} [V]	ΔV_{oc} [V]
TFTF	0.82	1.14	1.44	0.32	0.30	0.62
CNTF	0.88	1.15	1.44	0.27	0.29	0.56
PRTF	0.90	1.16	1.45	0.26	0.29	0.54
DTDCTB	0.82	1.14	1.44	0.31	0.31	0.62

A similar DTDCTB:C₆₀ solar cell is measured for comparison. However, the device has a p-i-n stack structure, instead of the n-i-p configuration of the other devices. The structure is glass | ITO | NDP9 (2 nm) | p-BPAPF (30 nm, 10 wt% NDP9) | DTDCTB:C₆₀ (30 nm, 1:1) | C₆₀ (20 nm) | n-C₆₀ (5 nm, 3 wt% W₂(hpp)₄) | Al (100 nm). However, the influence of the stack should be negligible. All donor:C₆₀ combinations have a similar CT state energy (E_{CT}) of 1.44-1.45 eV and cannot explain the differences in V_{oc} . The knowledge of the CT state energy allows the calculation of the maximum theoretical V_{oc} under the assumption that all charge carriers recombine radiatively (V_{rad}).[72] Therefore, the overall voltage losses $E_{CT}/e - V_{oc}$ can be itemized to radiative (ΔV_{rad}) and non-radiative voltage losses (ΔV_{nonrad}) (see section 2.3.2).[72] An overview of the values is given in Table 5.6. The values of the radiative losses ΔV_{rad} are with 0.29-0.31 V in the range of commonly observed values in literature.[72] However, the comparatively high V_{oc} of the PRTF and CNTF devices is related to their extraordinary low non-radiative losses of 0.26 V, while typical values ΔV_{nonrad} are larger than 0.34 V.[72, 133]

5. Thermally stable benzothiadiazole compounds

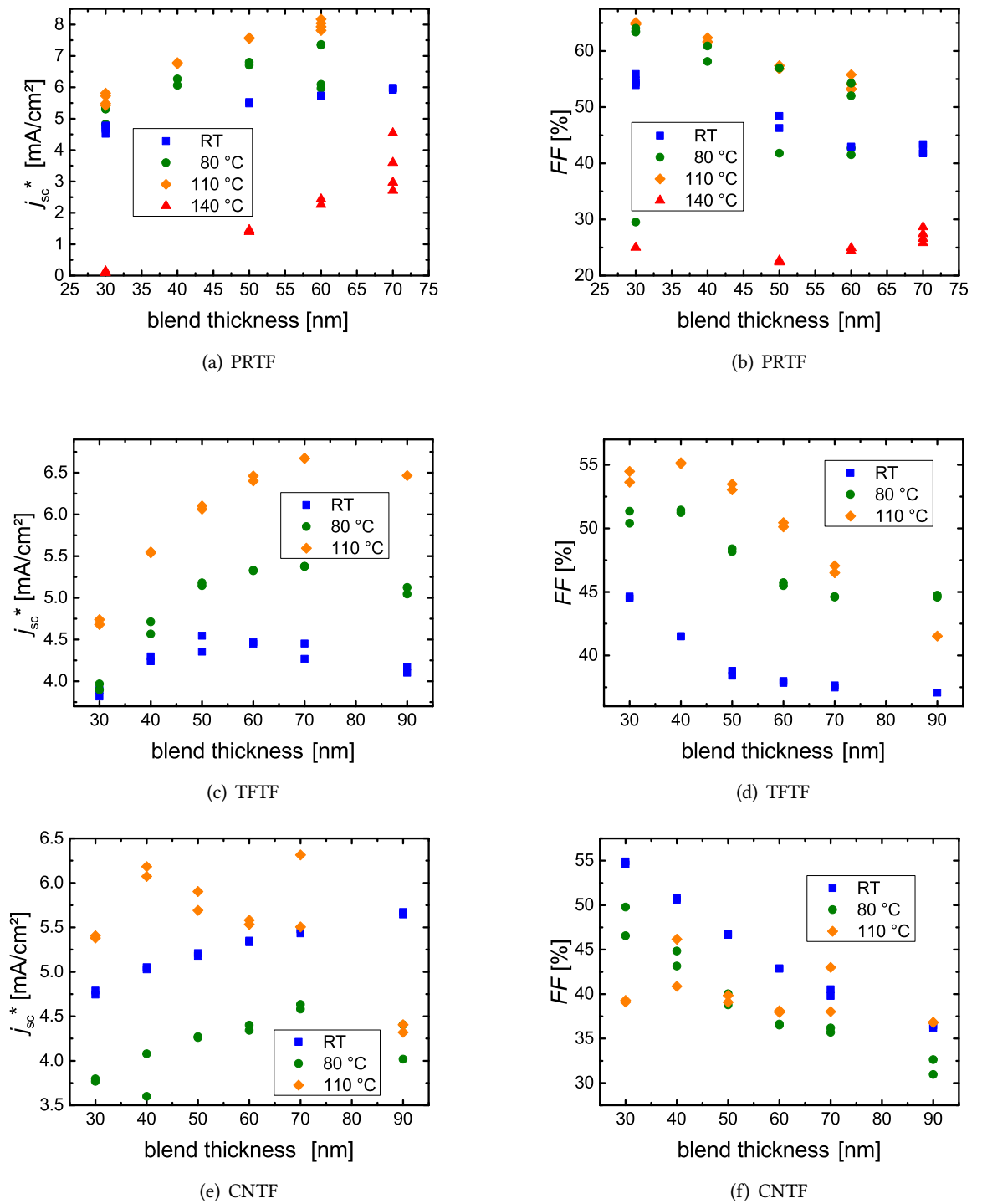


Figure 5.7.: j_{sc}^* (a), (c), (e) and FF (b), (d), (f) of PRTF, TFTF, and CNTF devices as a function of the blend layer thickness and T_{sub} during the deposition. The TFTF and CNTF devices were each processed on one substrate. The RT and 140 °C devices of PRTF are processed on one substrate. The 80 °C and 110 °C samples were processed on another substrate.

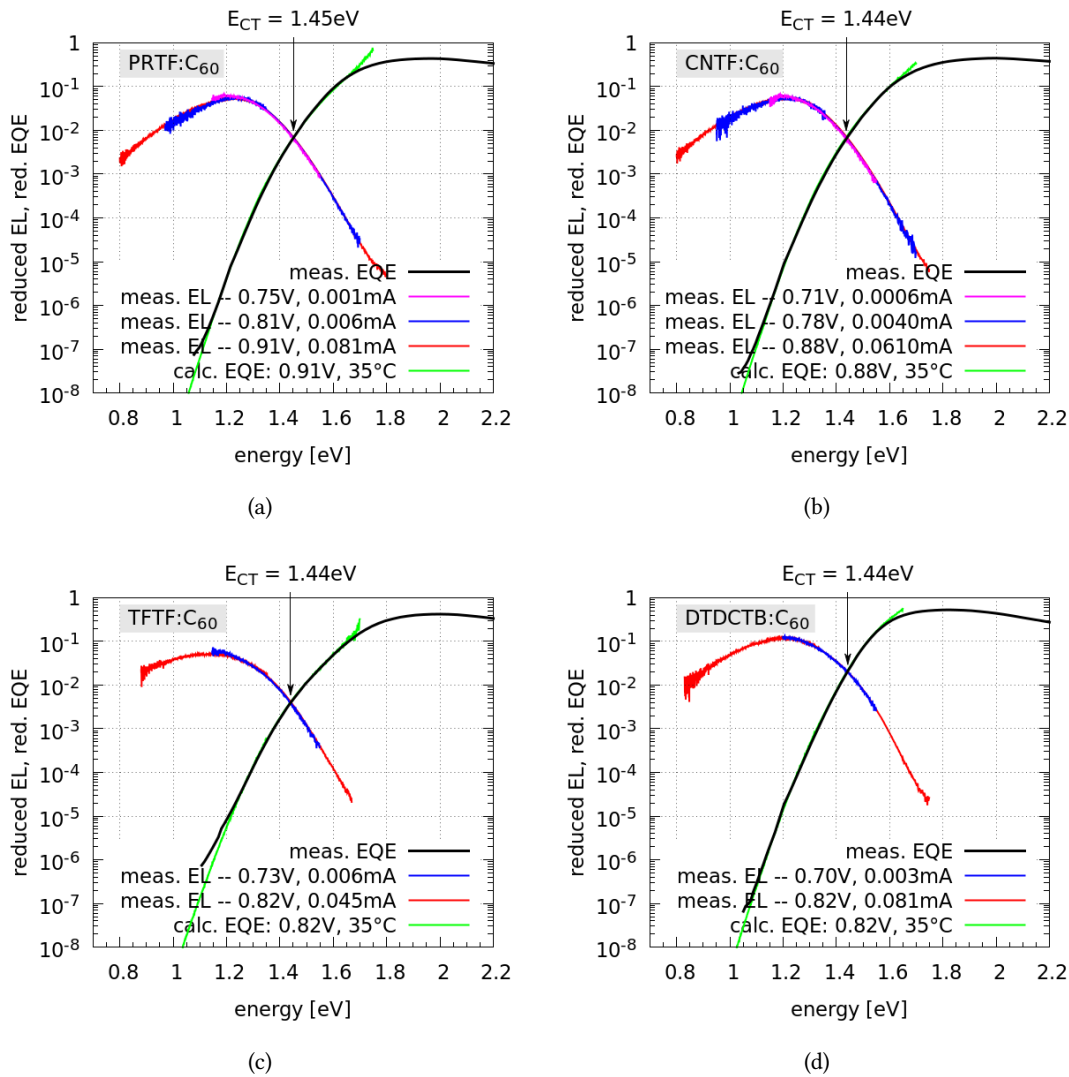


Figure 5.8.: Semi-logarithmic plot of the reduced EQE and reduced EL of the (a) PRTF:C₆₀, (b) CNTF:C₆₀, (c) TFTF:C₆₀, and (d) DTDCTB:C₆₀ solar cell as a function of the photon energy. The red. EL spectrum is aligned to the height of the CT state of the red. EQE data, the crossing point equals the energy of the CT state. Due to the reciprocity relation the EL and the EQE spectrum are related by the black body spectrum at room temperature. The green curve is the EL data divided by the black body spectrum at $T=35^\circ\text{C}$, it accurately fits with the measured EQE data.

In this regard, PRTF and CNTF have better properties than DTDCTB. This aspect deserves further investigation in future work.

5.4. Conclusion

In summary, three new molecules TTF, CNTF, and PRTF were tested in thin films and solar cells. They were designed to overcome the low thermal stability of DTDCTB. For PRTF, a strong increase in sublimation yield was achieved. However, all derivatives have a reduced absorption compared to DTDCTB, making it difficult to achieve comparable short circuit currents. Furthermore, the devices incorporating the new materials have lower fill factors and are more sensitive to higher blend layer thicknesses as the fill factor of DTDCTB:C₆₀ devices. The highest power conversion efficiency was achieved for PRTF with 3.8%, which is clearly lower than the 5.3% of the DTDCTB:C₆₀ devices.[119] However, we find for PRTF that the difference between the open-circuit voltage and the CT state energy ($\Delta V_{oc}=0.54$ V) is exceptionally low compared to typical voltage losses in organic solar cells. This is the result of low non-radiative recombination losses, the origin of which deserves further investigation and might lead to a future design rule for materials that enable higher open circuit voltages.

6. QM1

This chapter covers the work on the molecule QM1. We deposit QM1 thin films by thermal deposition in vacuum and find that the molecule forms nanowires on various surfaces. The molecules aggregate, causing a blueshift and broadening of the absorption, which reaches up to 1100 nm, making the molecule a suitable candidate for a NIR absorber in organic solar cells. In combination with C_{60} as acceptor, the solar cells exhibit an EQE of over 19% from 600 nm up to 1000 nm. Due to a limited FF and the inherent small V_{oc} , the highest η_{PCE} is 1.9% , despite a comparatively large j_{sc} of 9.7 mA/cm^2 . Parts of this chapter are published in reference [134], Copyright 2017, reprinted with permission from Elsevier.

6.1. Introduction

The two main features of QM1 are its nanowire growth and the wide absorption range in the NIR range. Therefore, we use the first part of this section to review the state-of-the-art of small molecular NIR absorbers and motivate the demand for these kind of absorber molecules. A focus is set on molecules in (J-) aggregates as an approach to achieve NIR-absorption. The second part gives a short summary of the literature on molecular nanowires formed by self aggregation. The third part presents an overview about the results in literature about QM1.

NIR-absorber

The power conversion efficiency of organic solar cells has strongly increased over the last two decades.[73, 135] As external quantum efficiencies are already exceeding 70% in the visible regime, the necessity increases for absorber materials that cover the near-infrared regime.[95, 136] For vacuum deposited organic solar cells, few material classes of NIR-absorbers are known. One example are the metal-phthalocyanines (Pc), e.g. lead-Pc (PbPc), chloro-aluminum-Pc (ClAlPc), or tin(II)-Pc (SnPc).[137–139] Another promising class are the azabodipys.[130, 140] However, with the exception of PbPc and SnPc, the absorption and, accordingly, contribution to the EQE reaches in most cases only up to 900 nm, leaving large parts of the solar spectrum unused. An alternative approach to achieve NIR absorption is J-aggregation (see section 2.2.1).[141] In this type of aggregation, a red shifted absorption band arises. While not necessarily focusing on NIR absorption, this strategy was applied to organic solar cells using several molecule classes.[142–147] In 2003, Meng *et al.* used a cyanine dye in a PHJ solar cell. The absorption of the dye in the solar cell showed H- as well as J-type absorption bands. The absorption of the J-band was found at 580 nm, while the monomer absorption was at 530 nm.[142] With PbPc, a more suitable candidate for NIR absorption was investigated by Hiramoto *et al.* and later Yokoyama *et al.*[143, 144] The authors

6. QM1

used co-evaporation of PDMS to influence the morphology and absorption of the PbPc:C₆₀ blend layers. The achieved shifts in absorption were attributed to H- and J-aggregation. Upon applying this technique, the absorption onset was extended up to 1050 nm.[144] In 2012, Deing *et al.* found H- and J-aggregates in squaraine dyes, which were used as donor in combination with PC₆₁BM in solution processed solar cells. For one squaraine derivative a shift of 0.19 eV from the non-aggregated dye in thin film (722 nm) to the J-aggregated thin film (811 nm) was observed.[145] Further investigations on aggregated squaraines in organic solar cells were done by Brück *et al.* and Chen *et al.* leading to power conversion efficiencies of up to 1.7%.

Self aggregated molecular nanowires

Self aggregated molecular nanowires can be formed by several interactions, such as π - π -interaction, metal coordination, hydrogen bonding, the hydrophobic effect, or dipole-dipole interaction.[148] Depending on the interaction, certain properties of the single molecule are beneficial for the growth in nanowires. In case of a dipole-dipole interaction, a strong dipole moment of the molecule is advantageous.[148] Such a static dipole moment can be found for push-pull chromophores. For π - π -stacking, a large π -system is believed to be beneficial.[148]

The formation of nanostructures, such as nanowires, can have a strong influence on the emission and absorption spectra of the molecules. One reason can be the formation of J- or H- aggregates that influence the spectra (see section 2.2.1). However, also the size of a nanoparticle can influence the optical properties of an aggregated molecule.[30, 149, 150]

QM1

The push-pull chromophore 2-(dicyanomethylene)-5'-(1,3-dithiol-2-ylidene)-5,5'-dihydro-Delta2,2'-bithiophene (QM1) was originally prepared by Inoue *et al.* via the procedure of Gopper *et al.*[151, 152] In 2003, Milián *et al.* investigated QM1 and comparable compounds regarding solvatochromism as well as an application in the field of nonlinear optics.[22] The strong dipole moment of QM1 is caused by the electron donating 1,3-dithiol-2-ylidene group and the electron accepting dicyanomethylene group, which are connected by an oligothiophene bridge.[22] Besides a quinoid resonance with double bonds, a zwitterionic resonance contributes to the molecule structure as shown in Figure 6.1.[153] Milián *et al.* also found that the internal rotation of QM1 is hindered, which is beneficial for a close molecular packing and low disorder.[22]

6.2. Preliminary experiments

6.2.1. Solution spectrum

Figure 6.2 shows the absorbance of QM1 in dimethyl sulfoxide (DMSO).¹ QM1 has two absorption peaks at 760 nm (1.64 eV) and 824 nm (1.50 eV). In addition, a shoulder at 700 nm

¹Nico Gräßler (IAPP) synthesized the material used in this study.

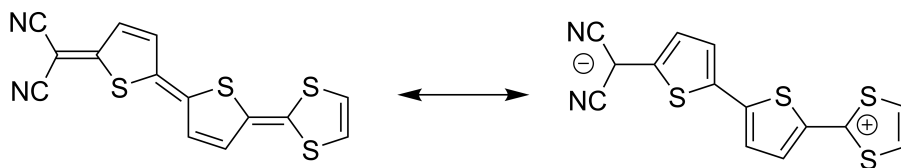


Figure 6.1.: The quinoid (left) and zwitterionic (right) structure as resonant structures of QM1.

and minor peaks between 400 nm and 500 nm are visible. DFT calculations show only one transition at 2.25 eV (551 nm) in the single molecule with a significant oscillator strength of $f=1.28$. The calculations were performed by Dr. Reinhard Scholz (IAPP) using the B3LYP-631G* package and are in agreement with calculations from Milián *et al.* using the B3LYP-6-31G** package.[22, 154, 155] These calculations indicate that the higher energetic absorption peaks are part of the vibronic structure of one electronic transition. Milián *et al.* presented a solution spectrum in acetonitrile or dimethylformamide solution (contradictory information in the paper).[22] The absorption spectrum consists of 7-8 peaks, which form a connected absorption band ranging from 500 nm to 880 nm. The highest three peaks are located at 820 nm, 740 nm, and 680 nm and are roughly in agreement with peaks found in the dimethyl sulfoxide solution. Liptay found that the vibronic structure of the absorption of a molecule with a strong dipole moment is more pronounced in less polar solvents.[156] This explains the difference in the case of dimethylformamide, since Dr. Scholz calculated a dipole moment of 15.6 D for QM1 and dimethylformamide has a lower polarity than DMSO.

6.2.2. Neat QM1 films

Thin film absorption

In order to test the optical properties of QM1 thin films, we deposit 20 nm QM1 on a glass substrate and perform transmission and reflection measurements. Figure 6.2 shows the absorption of the thin film. Two distinct absorption peaks are visible at 510 nm (2.44 eV) and 580 nm (2.15 eV). At higher wavelengths, no distinct absorption peaks are visible - the spectrum is rather one large shoulder that reaches up to 1100 nm. A large blueshift of the maximum absorption from solution with 824 nm (1.50 eV) to thin film with 580 nm (2.15 eV) of 650 meV is visible.

Morphology

QM1 grows in nanowires with a diameter in the range of tens of nanometers and several micrometers length. Table 6.1 gives an overview about the investigated samples and used methods. In the first part, neat QM1 is investigated, followed by an investigation of blend layers with C₆₀, which are important for solar cells.

6. QM1

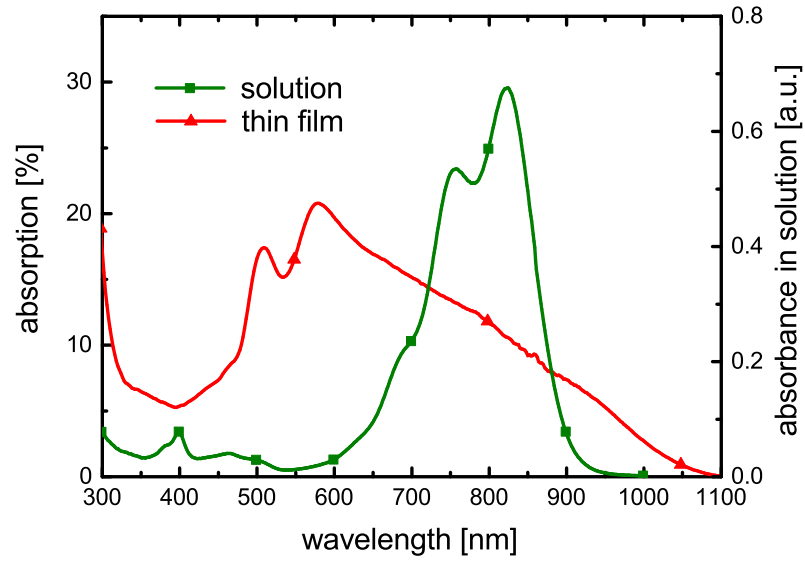


Figure 6.2.: Absorption spectrum of QM1 in DMSO solution (green square) and in a 20 nm thin film on glass (red triangle). The measurement of the solution spectrum was performed by Nico Gräßler (IAPP).

Table 6.1.: Overview about the samples for morphological investigations. The substrate, stack, QM1 deposition rate, substrate temperature during the deposition, and characterization method are given. Sample 4 was prepared by Daniel Schütze; samples 6-9 by Andreas Wendel (both IAPP).

no.	substrate	stack	T_{sub}	method
1	TEM grid	10 nm C_{60} QM1 (20 nm, 0.3 Å/s)	RT	SEM, TEM
2	TEM grid	10 nm C_{60} QM1 (20 nm, 0.1 Å/s)	100 °C	SEM
3	KBr	QM1 (80 nm, 0.3 Å/s)	RT	ED, SEM
4	glass	QM1 (40 nm, 0.4 Å/s)	RT	GIXRD
5	glass with ITO	10 nm C_{60} QM1: C_{60} (20 nm, 0.3 Å/s, 1:1)	RT	SEM
6	TEM grid	10 nm C_{60} QM1: C_{60} (30 nm, 0.6 Å/s, 1:2)	RT	SEM
7	glass	5 nm C_{60} QM1: C_{60} (30 nm, 0.2 Å/s, 1:1)	RT	GIXRD
8	glass	5 nm C_{60} QM1: C_{60} (30 nm, 0.4 Å/s, 1:1)	RT	GIXRD
9	glass	5 nm C_{60} QM1: C_{60} (30 nm, 0.6 Å/s, 1:1)	RT	GIXRD
10	glass	5 nm C_{60} QM1: C_{60} (30 nm, 0.8 Å/s, 1:1)	RT	GIXRD

SEM/TEM

Figure 6.3 presents an SEM image of sample 1. The image shows wires of several hundred nanometers to micrometers length and tens of nanometers width. The wires are randomly aligned and vary from straight to bended to slipknots. Furthermore, the wires lie randomly on top of each other or are entangled. A dangling of the nanowires is partly observed during the scanning process. These observations indicate that the adhesion of the wires to the surface is small compared to a closed layer. In order to get further insight into the structure, TEM measurements are performed. Figure 6.4(a) shows a TEM image of sample 1. As in the SEM images, predominantly wires are visible. An analysis with Gwyddion reveals that the nanowires are 10-18 nm thick. Figure 6.4(c) presents a diffraction pattern of the detail view of $500 \times 500 \text{ nm}^2$ depicted in Figure 6.4(b). The diffraction pattern has broad, diffuse rings that indicate an amorphous structure. This amorphous structure can be caused by radiation damage through the electrons at high magnifications and corresponding electron energies (200 kV). Such a distinguished growth mode as nanowires is unlikely to appear without any crystallinity.

We assume that the nanowires are crystalline, but too thin and too loosely packed to give a measurable diffraction pattern. Therefore, sample 2 is prepared at higher substrate temperature and lower deposition rate, as these conditions are known to induce a higher crystallinity in closed layers (see section 2.2.1). Figure 6.5 shows an SEM image of sample 2. Again, wire-like structures are visible. However, for this sample the wires are on average larger and thicker with diameters up to 100 nm (note the larger scale of the image). Most of the wires are between 40 nm and 70 nm thick. Nevertheless, also nanowires with 10-20 nm are still visible. With increasing wire size, the density of the wires per area decreases and larger void areas are visible between the wires. The strong defocus of some of the wires, e.g., in the upper middle area of Figure 6.5, indicates that some of the nanowires are upright standing on the substrate. However, this behavior is not limited to the heated sample and is also observed at samples prepared at room temperature. The background in Figure 6.5 appears quite uniform. Small grains are visible, which stem from the C_{60} with temperature treatment, due to the substrate heating prior and during the deposition of QM1.[157] However, we still do not find any signature of crystallinity in these samples using TEM in diffraction mode (not shown).

Electron diffractometry

In order to check for crystallinity, sample 3 is evaporated on a cleaved KBr crystal. Afterwards, the potassium bromide (KBr) crystal is dissolved in water such that the QM1 film settles on the water surface. In the next step, the film is moved to a TEM grid, which is transferred to a custom made setup to measure electron diffraction.² Figure 6.6 shows an electron diffraction pattern of this film. The advantage of this measurement is that the detectable area is higher than in conventional TEM. The sharp diffraction pattern indicates that the film is crystalline. In order to check whether the preparation method has an influence on the thin film properties, a similar 80 nm thick QM1 film is transferred to glass. Figure 6.7(a)

²The transfer of the thin film to the TEM grid and the measurement was done by Eric Müller (IFW Dresden).

6. QM1

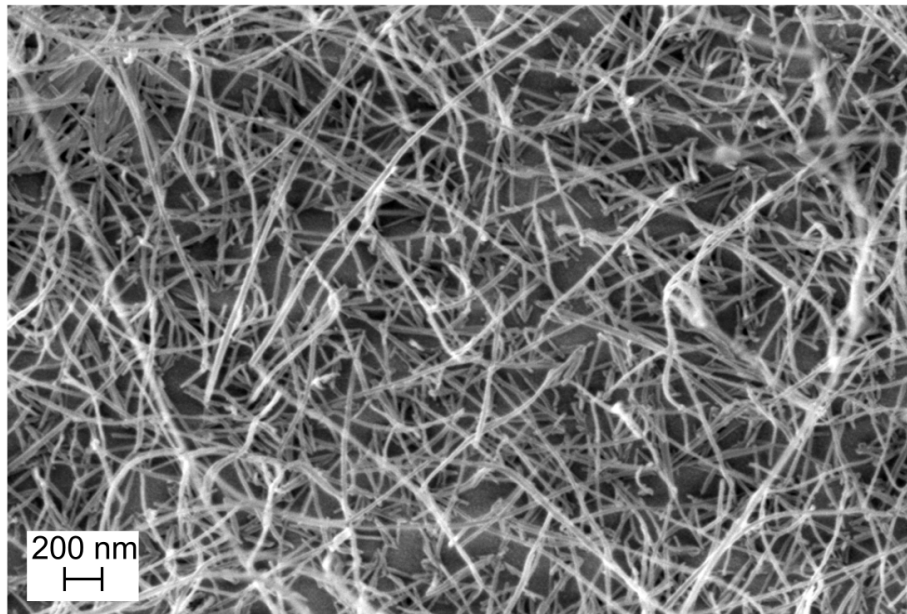


Figure 6.3.: SEM image of 20 nm QM1 on 10 nm C_{60} (sample 1). The image was taken by Mona Sedighi (Dresden Center for Nanoanalysis (DCN)) with an acceleration voltage of 500 V using an inlens detector.

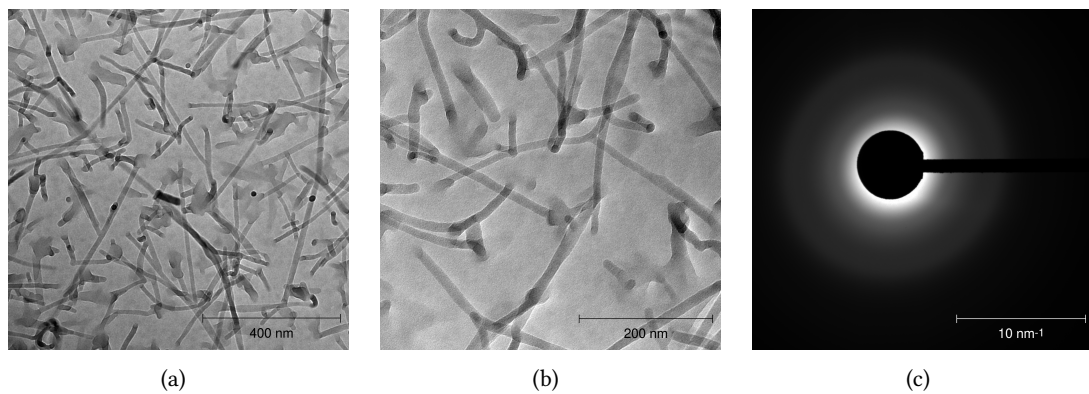


Figure 6.4.: (a) & (b) TEM images of 20 nm QM1 on 10 nm C_{60} (sample 1) taken in bright field mode and (c) diffraction mode on the area of (b). The measurements were taken by Mona Sedighi (DCN).

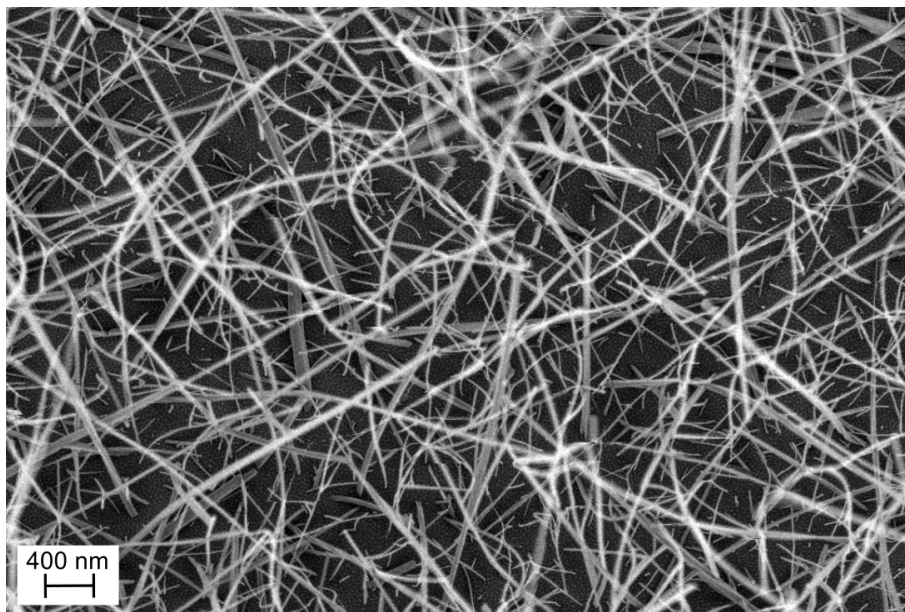


Figure 6.5.: SEM image of sample 2. The acceleration voltage was 700 V. The image was taken by Mona Sedighi (DCN) with an inlens detector.

shows the absorbance of the film. For comparison, the absorbance of a 50 nm and a 20 nm thick QM1 layer grown on glass is plotted. The absorption spectrum of the transferred sample is in good agreement with other samples. Figure 6.7(b) shows a SEM image of a film from sample 3 transferred on a copper TEM grid. Also in this case, QM1 forms nanowires when deposited on the KBr crystal. However, the diameter and length vary strongly. Upon deposition of QM1 on KBr, nanowires with a diameter of up to 300 nm are observed. Nevertheless, also wires with diameters of tens of nanometers are visible.

GIXRD

Figure 6.8(a) shows the GIXRD measurement on sample 4. A useful background measurement is hardly possible, considering the growth in nanowires. The nanowire growth does not allow to find one critical angle, where the X-ray beam couples into a (uniform) layer, since the material-air interface is not a smooth plane. Small signals are visible at 13.5° , 23.6° , and 26.5° . These angles correspond to 1.88 \AA^{-1} , 1.67 \AA^{-1} , and 0.98 \AA^{-1} in agreement with the strongest peaks from the ED measurements. Figure 6.8(b) shows the XRR measurement of the 40 nm sample. The absence of Kiessig fringes indicates a high surface roughness, which is reasonable considering the observed nanowire growth.

6. QM1

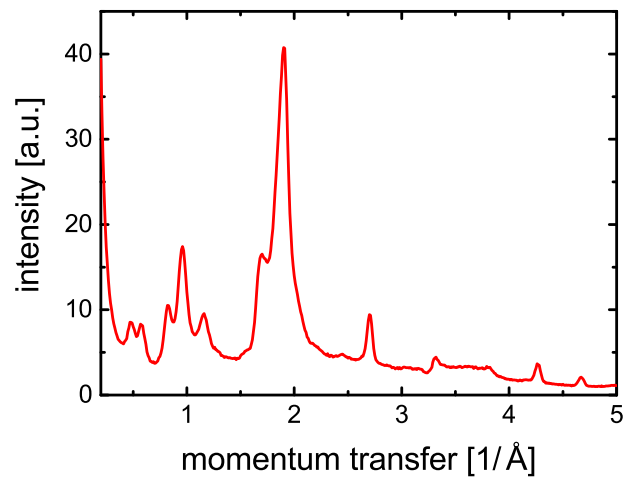
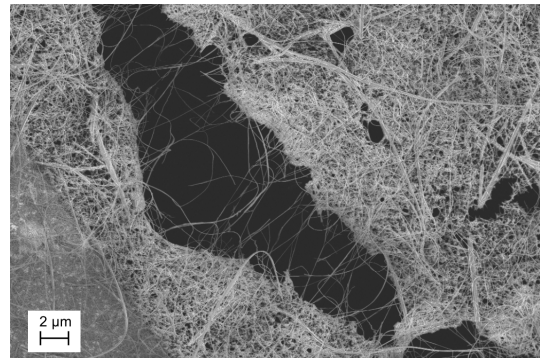
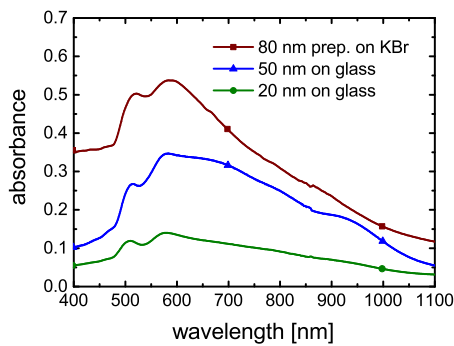


Figure 6.6.: Electron diffraction pattern of a 80 nm thick QM1 layer on a copper TEM grid, transferred from a KBr crystal. The measurement was done by Eric Müller (IFW Dresden).



(a)

(b)

Figure 6.7.: (a) Absorption spectra of 80 nm QM1 (sample 3) prepared on KBr and transferred to glass in comparison to QM1 layers directly grown on glass. The 50 nm sample was prepared and measured by Annette Petrich (IAPP). (b) SEM image of the film of sample 3 transferred to a TEM grid. SEM measurement by Mona Sedighi (DCN).

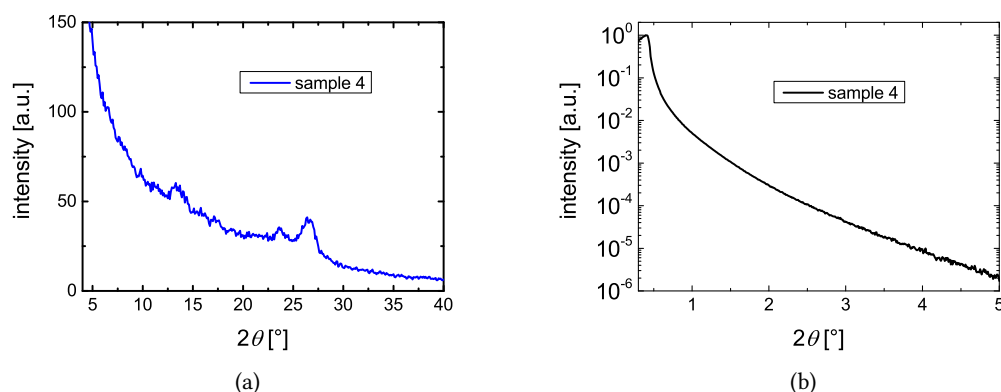


Figure 6.8.: (a) GIXRD measurement on 40 nm QM1 (sample 4). (b) XRR measurement of sample 4. The sample was measured by Dr. Lutz Wilde (Fraunhofer IPMS-CNT).

Discussion

The formation of nanowires through self assembly of small molecules is known in literature.[148] Guo *et al.* summarized several studies that had investigated favorable factors for nanowire growth.[148] One class of molecules, which can exhibit a one-dimensional growth, are molecules with an intramolecular charge transfer.[158] The charge transfer for QM1 was proven by Milián *et al.* using Raman as well as IR spectroscopy and is furthermore reported by Inoue *et al.*[22, 153] Furthermore, the charge transfer manifests itself in the large dipole moment (15.6 D) of QM1. In contrast to literature, where nanowires are usually formed from solution, template methods, or vapor phase deposition, the nanowires for QM1 form upon thermal vacuum deposition.[148] In addition, the formation of the nanowires is not limited to a certain substrate, since the nanowires are formed on ITO, KBr, glass, and C_{60} . A detailed explanation of the absorption of the QM1 thin film with its shifted absorption peaks and the long broad shoulder needs further investigations. X-ray diffraction on QM1 single crystals would be critical to get insight into the molecular arrangement. However, the preparation of QM1 single crystals that are large enough for this investigation was not possible yet. Based on the results so far, the observed blue shift of the two absorption peaks is a clear indicator for an H-aggregation of the molecules.[27] The formation of nanowires in H-aggregates was also reported by Fang *et al.*[31] In that work, the authors observed the formation of semicrystalline BMBBCP nanowires with ≈ 70 nm diameter and a blueshift in the absorption using a melt-assisted wetting method.[31] The reported blueshifts of 45 nm (390 nm to 345 nm) and 13 nm (243 nm to 230 nm) correspond to 415 meV and 288 meV. This would be well below the 650 meV for QM1, indicating a stronger interaction for the QM1 molecules.³ A second aspect of the absorption spectrum is the long shoulder towards the IR.

³In 2011, Kim *et al.* reported on H-aggregation of oligothiophene-derivates in thin film transistors. Based on the changes from the absorption in solution to the absorption in thin film, blue shifts of over 1 eV were observed.[159]

6. QM1

A possible explanation are oblique aggregates, where the QM1 molecules are arranged under a certain slippage angle and the J-band contributes to the absorption (see section 2.2.1). For H-aggregation, the slippage angle is between 54.7° and 90° , at which 90° corresponds to a perfect H-aggregate. For angles below 90° , the J-band is not completely suppressed and the H- and the J-band contribute to the absorption. The ratio of the contribution depends then on the slippage angle and therefore net transition moments of the aggregate.[27] In addition, two other effects might influence the broad shoulder of the QM1 thin film absorption: the presence of a non-aggregated phase of QM1 and the quantum size effect that is observed for nanostructures and leads to a formation of a long shoulder depending on the size of the nanowires.[30, 149, 150]

6.2.3. Blends with C_{60}

The following paragraph focuses on the properties of the blend of QM1 and C_{60} . This combination is interesting with regard to BHJ solar cells. Figure 6.9 presents an SEM image of sample 5 – a blend of QM1 with C_{60} (20 nm, 0.3 Å/s, 1:1). The image shows nanowires with 10-30 nm diameter that are several hundred nanometers long. Additionally, a grain structure is visible with grain sizes of several tens of nanometers. Based on the results of the previous measurements on QM1 single layers, we attribute the nanowires to QM1. The grain structure is attributed to C_{60} . [157] However, contributions of QM1 to the grains cannot be excluded. In comparison, Figure 6.10 shows an SEM image of a QM1: C_{60} blend layer (sample 6), prepared at the processing conditions (30 nm, 0.6 Å/s, 1:2) yielding the highest power conversion efficiency in the solar cell. In this case, the nanowires are thinner and shorter compared to the sample, presented in Figure 6.9. The thinner and shorter nanowires suggest that the higher C_{60} content and the higher deposition rate hinder the nanowire formation.

Figure 6.11(a) depicts the diffraction patterns of QM1: C_{60} blend layers (samples 7-10) at different deposition rates obtained by GIXRD. The diffraction patterns of a neat C_{60} layer (gray) and a neat QM1 layer (black) are plotted for comparison. The blend layer patterns show maxima at 10.9° , 19.8° , and 26.3° . The first two maxima can be assigned to C_{60} . The maximum at 26.3° fits to the maximum of the neat QM1 layer. Figure 6.11(b) shows the corresponding XRR measurements for samples 7-10. In contrast to the neat QM1 layer, all samples exhibit Kiessig fringes, indicating a smoother surface for the blend layers. As the amplitude of the fringes increases with deposition rate, we conclude a smoothing of the blend layer surface with increasing donor deposition rate.

Following the discussion about the crystallinity, we analyze the absorption of QM1: C_{60} blend layers. Figure 6.12(a) shows the absorption of 20 nm thick blend layers of QM1 and C_{60} in different mixing ratios on 5 nm C_{60} . For the analysis of the spectra, the absorption of the neat layer and QM1 in DMSO is plotted in the background of the graph. The absorption of C_{60} reaches up to 700 nm with the last significant maximum at approximately 450 nm. From 550 nm onwards, the absorption of C_{60} is strongly decreased (see Figure 3.2). Therefore, QM1 gives the main contribution to the absorption spectrum for wavelengths higher than 550 nm. Accordingly, the narrow minimum at 550 nm for the 1:1 sample is caused by the aggregated QM1 as the comparison the neat QM1 layer shows. For an increasing content of C_{60} in the blend layer, one can see that the minimum at 550 nm is broader and more pronounced, while

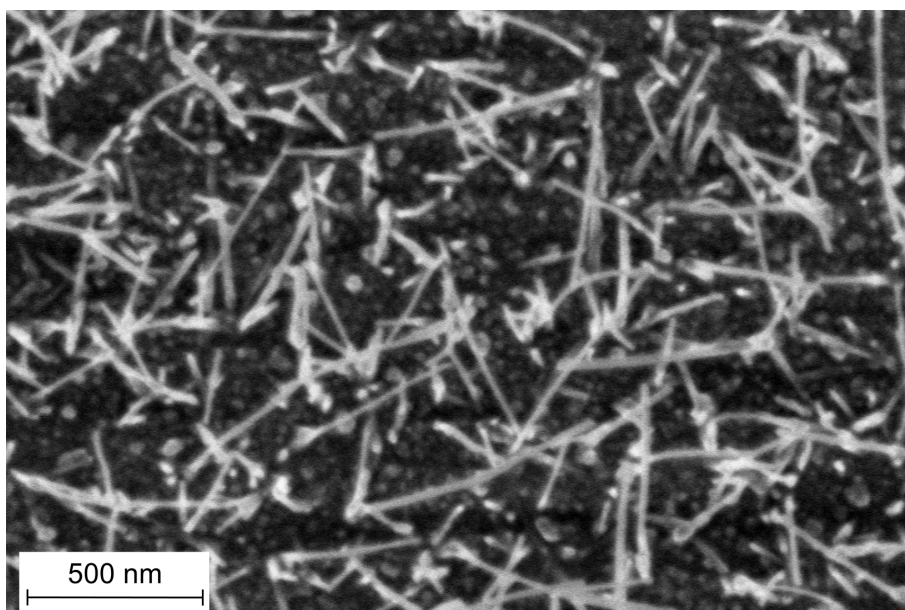


Figure 6.9.: SEM image of 20 nm QM1:C₆₀ in a mixing ratio of 1:1 (sample 5). The image was taken by Mona Sedighi (DCN) with an acceleration voltage of 1 kV.

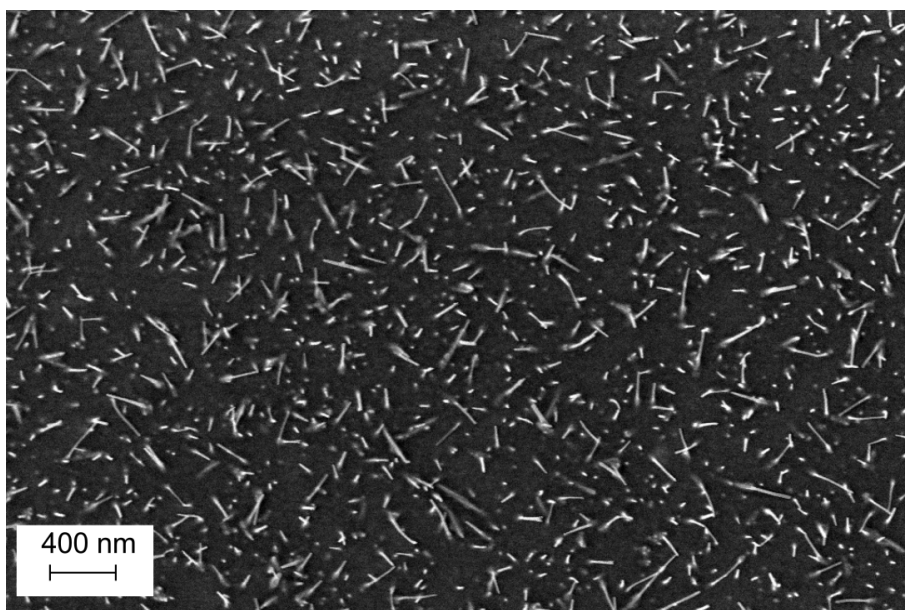


Figure 6.10.: SEM image of 30 nm QM1:C₆₀ in a mixing ratio of 1:2 (sample 6). The image was taken by Mona Sedighi (DCN) with an acceleration voltage of 1 kV.

6. QM1

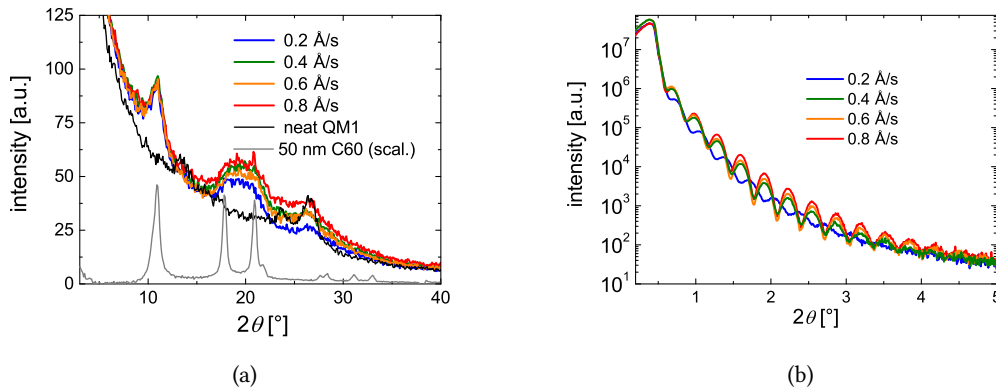


Figure 6.11.: (a) GIXRD measurements on QM1:C₆₀ blends in a 1:1 mixing ratio deposited with different deposition rates (samples 7-10). Results are compared with intrinsic QM1 (black) and C₆₀ (gray). (b) The corresponding XRR measurements. Measurements by Dr. Lutz Wilde (Fraunhofer IPMS-CNT).

the maximum at 450 nm is slightly increased. The decrease and broadening of the minimum suggests a reduction of the aggregated QM1 molecules, because the double peak structure with the minimum at 550 nm vanishes and the broad minimum between 500 nm and 600 nm is caused by the shoulder of the C₆₀ absorption peak at 450 nm and the non-aggregated QM1. In return, the maximum of the blend layer absorption shifts to around 800 nm, which indicates a more dominant absorption from non-aggregated molecules. For an explanation of the development of the region between 900 nm and 1100 nm, further investigations are needed. Figure 6.12(b) shows the development of the blend absorption for a 1:1 mixing ratio for different donor deposition rates. The absorption of the blend between 600 nm and 1100 nm is increased for deposition rates higher than 0.2 Å/s. The increase is accompanied by a reduction of the peak at 500 nm, which is expected to be absorption of aggregated QM1. Similar to the development with increasing C₆₀ content, the increased deposition rates point to a reduced aggregation of QM1 in the blend.

6.3. Solar cells

Here, we study the application of QM1 as a donor in heterojunction solar cells with C₆₀. At the beginning, QM1-C₆₀ PHJ solar cells are briefly discussed. The second part describes the steps during the optimization of the BHJ solar cells regarding efficiency. The third section covers aging measurements. Finally, we investigate the lifetime of those devices in aging experiments.

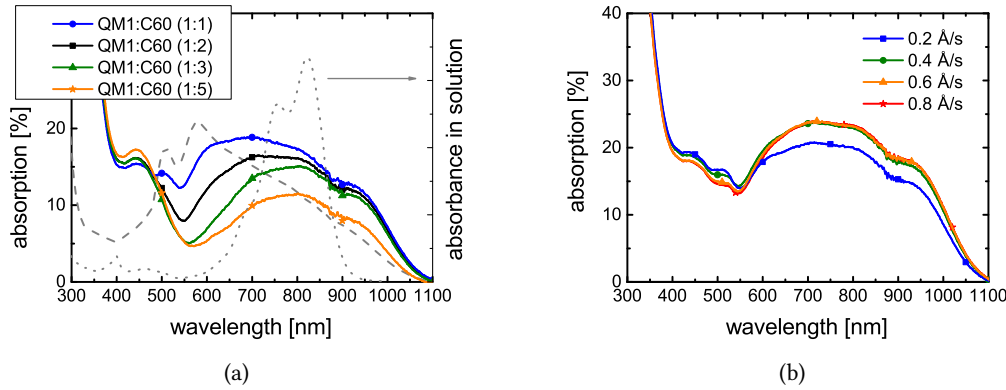


Figure 6.12.: (a) Absorption of 20 nm thick QM1:C₆₀ blends with different mixing ratios. For comparison the absorption spectrum of neat QM1 layer (dashed line) and the absorbance of QM1 in solution (points). (b) Absorption of QM1:C₆₀ blends in a 1:1 mixing ratio for different donor deposition rate.

6.3.1. PHJ

For the PHJ solar cell, the following stack structure is tested: glass | ITO | n-C₆₀ (5 nm, 3 wt% W₂(hpp)₄) | C₆₀ (15 nm) | QM1 (6 nm) | HTL (5 nm) | p-HTL (40 nm, 10 wt% F6-TCNNQ) | F6-TCNNQ (2 nm) | Al (100 nm). Since the determination of the *IP* by UPS is not possible, the *IP* is estimated to get an idea for the selection of the HTL.⁴ Preliminary tests showed that V_{oc} is in the range of 0.3-0.4 V for a heterojunction with C₆₀. It is known from literature that a good approximation for V_{oc} is $V_{oc} \approx EA_A - IP_D - 0.6$ V.[109] Therefore, we can estimate the *IP* to be between 4.9 eV and 5.0 eV and BF-DPB is selected as HTL. Figure 6.13(a) shows the *jV* curve of the PHJ solar cell. The *jV* curve has a large S-kink, which leads to a *FF* of 17% and a reduced j_{sc} of 1.8 mA/cm². In combination with the low V_{oc} , the η_{PCE} is only 0.1%. An S-kink can be a hint for an insufficient charge carrier extraction, which might be caused by the relatively loose nanowire growth of QM1. In addition, upright standing nanowires lead to high surface roughness causing problems, like e.g. short circuits. Nevertheless, between 600 nm and 1100 nm the EQE displays a contribution of QM1 to the current, as shown in Figure 6.13(b). As further tests on the PHJ solar cell did not bring significant progress, we focus our work on BHJ solar cells.

6.3.2. BHJ

Within the optimization of the BHJ solar cells, the following variations are tested:

- mixing ratio of QM1:C₆₀: 1:1, 1:2, 1:3

⁴The *IP* was later determined to be (4.95 ± 0.35) eV. Details can be found in the Appendix (see section A.2 in the Appendix).

6. QM1

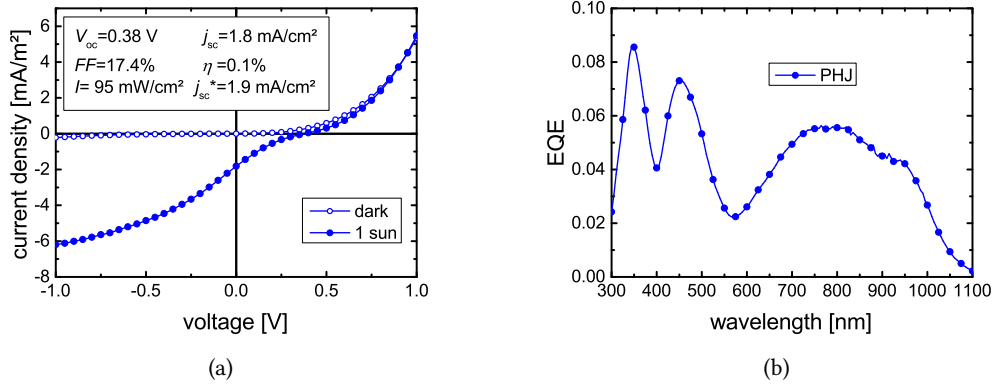


Figure 6.13.: (a) jV curve of a PHJ with QM1-C₆₀ in darkness and under illumination. (b) EQE of the PHJ.

- donor rate variation 0.2 Å/s, 0.4 Å/s, **0.6 Å/s**, 0.8 Å/s
- HTL: **BF-DPB**, Spiro-OMe-TAD, BPAPF
- ETL: **Bis-HFI-NTCDI**, C60
- blend layer thickness variation: 15 nm, 20 nm, 25 nm, **30 nm**, 35 nm, 40 nm.

The best parameter in each aspect is set in boldface. At the beginning the mixing ratio of the blend is optimized. BF-DPB and Spiro-OMe-TAD are tested as suitable candidates for HTL.

Mixing ratio

The solar cell stack is glass | ITO | n-C₆₀ (5 nm, 3 wt% W₂(hpp)₄) | C₆₀ (15 nm) | donor:C₆₀ (30 nm, different mixing ratios) | HTL (5 nm) | p-HTL (40 nm, 10 wt% F6-TCNNQ) | F6-TCNNQ (2 nm) | Al (100 nm) with BF-DPB or Spiro-OMe-TAD as HTL. Table 6.2 shows the jV characteristics of the solar cells. The solar cells designed with BF-DPB as HTL instead of Spiro-OMe-TAD perform better in every aspect and are discussed in the following. Figure 6.14(a) presents the jV curves of the solar cells with BF-DPB as HTL. The difference in the jV characteristics between solar cells with different mixing ratios is small. The V_{oc} of ≈ 0.4 V and the FF of 32% are comparable for all devices with BF-DPB as HTL. Though a FF of 32% is rather bad, it is an improvement compared to the PHJ device. The major difference between the devices is found in j_{sc} . Here, the 1:2 sample has the highest j_{sc} with 7.7 mA/cm², which leads to a η_{PCE} of 1.0%. The 1:1 device with 7.3 mA/cm² and 0.9% is slightly worse. Figure 6.14(b) shows the EQE for the devices. As for the QM1:C₆₀ blend layer absorption, a broad maximum is visible, which reaches from 600 nm to 1100 nm. For the 1:2 sample, the EQE reaches a maximum of 23% for the region around 800 nm. While the height of the EQE at these wavelengths is rather moderate in comparison to other NIR absorbers, the fact that the EQE is at 970 nm still at 20% is outstanding.[130, 139, 160, 161] The EQEs of the 1:1 and

the 1:3 device are smaller than for the 1:2 device. Due to the higher QM1 content of the 1:1 device, we can deduce that the IQE is higher for the 1:2 device.

Additionally, the insertion of a 3 nm interlayer of neat QM1 between the blend and the intrinsic HTL layer is tested for all solar cell configurations. However, as for the PHJ solar cells in many configurations the interlayer leads to a worsening of the performance or even to an S-kink formation (not shown).

Table 6.2.: Overview about blend ratio variation of QM1:C₆₀ solar cells. The deposition rates for QM1 are 0.4 Å/s for the 1:1 devices and 0.2 Å/s for the 1:2 devices and 1:3 devices.

HTL	ratio	j_{sc} mA/cm ²	V_{oc} V	FF %	η_{PCE} %	Sat	I_{ill} mW/cm ²	j_{sc}^* mA/cm ²
BF-DPB	1:1	7.3	0.40	32	0.9	1.8	103	7.0
	1:2	7.7	0.41	32	1.0	1.8	104	7.4
	1:3	6.5	0.41	32	0.8	1.9	104	6.3
Spiro-OMe-TAD	1:1	0.3	0.29	11	0.0	32	–	–
	1:2	5.9	0.38	29	0.6	2.1	102	5.8
	1:3	4.7	0.37	27	0.5	2.3	102	4.6

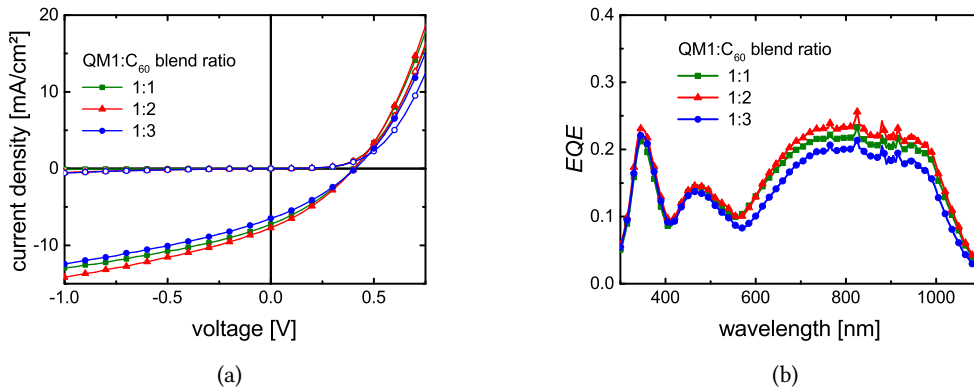


Figure 6.14.: (a) jV curves of the devices with BF-DPB as HTL from Table 6.2 and (b) the corresponding EQEs. The noise between 800 nm and 900 nm stems from a problem with the xenon lamp in the EQE measurement setup at that time.

Rate variation

Even in a blend with C₆₀, QM1 grows in crystalline nanowires of several 100 nm length sticking out of the blend as shown in Figure 6.10. These nanowires are expected to have a negative influence on the solar cell. The aim is to reduce the nanowire growth and decrease the surface

6. QM1

roughness by evaporating at higher deposition rates. The success of this approach is proven by XRR measurements presented in Figure 6.11(b) showing a reduction of the roughness for higher deposition rates. Accordingly, higher donor deposition rates (0.2 Å/s, 0.4 Å/s, 0.6 Å/s, and 0.8 Å/s) are tested in devices. Since the difference between the best (1:2) and the second best mixing ratio (1:1) is rather small, both mixing ratios are investigated. The stack for the tests is glass | ITO | n-C₆₀ (5 nm, 3 wt% W₂(hpp)₄) | C₆₀ (15 nm) | donor:C₆₀ (30 nm, different mixing ratios and deposition rates) | BF-DPB (5 nm) | p-BF-DPB (40 nm, 10 wt% F6-TCNNQ) | F6-TCNNQ (2 nm) | Al (100 nm). The results are summarized in Table 6.3. For both blend ratios, a donor deposition rate of 0.6 Å/s gives the best power conversion efficiency. Once again, the devices with a 1:1 ratio have a lower current density, despite the higher content of QM1. Also the V_{oc} is again slightly lower than in the 1:2 samples. The results for the FF vary depending on the deposition rate. For the 1:1 and 1:2 devices prepared with a 0.2 Å/s QM1 deposition rate, the FF is significantly lower than for the devices processed at higher donor deposition rates. For the 1:2 devices the higher donor deposition rates give approximately the same FF of 43-44%. For the 1:1 devices, 0.6 Å/s deposition rate is needed to achieve such a plateau, which is attributed to the higher QM1 content. The best η_{PCE} of 1.8% is achieved for the 1:2 device at 0.6 Å/s.

Table 6.3.: Overview about rate dependent evaporation of 1:1 and 1:2 OSCs.

ETL and blend ratio	rate Å/s	j_{sc} mA/cm ²	V_{oc} V	FF %	η_{PCE} %	Sat	I_{ill} mW/cm ²	J_{sc}^* mA/cm ²
n-C ₆₀ 1:1	0.2	2.4	0.39	17	0.2	3.4	97	2.4
	0.4	7.8	0.41	41	1.3	1.5	101	7.7
	0.6	8.9	0.42	46	1.7	1.4	102	8.7
	0.8	8.5	0.42	45	1.6	1.5	101	8.4
n-C ₆₀ 1:2	0.2	7.7	0.42	37	1.2	1.5	104	7.4
	0.4	9.4	0.43	44	1.7	1.5	105	8.9
	0.6	9.9	0.43	44	1.7	1.8	106	9.4
	0.8	9.3	0.42	43	1.6	1.5	105	8.9
n-Bis-HFI-NTCDI 1:2	0.2	7.7	0.42	38	1.2	1.5	104	7.4
	0.4	9.3	0.43	44	1.7	1.4	105	8.9
	0.6	9.5	0.43	44	1.7	1.4	105	9.1
	0.8	9.2	0.43	44	1.7	1.4	104	8.8

In a second measurement series, the 1:2 blend ratio is tested in combination with n-doped Bis-HFI-NTCDI as ETL. Table 6.3 depicts the results of this measurement series. The corresponding jV and EQE curves are presented in Figure 6.15. The difference to the n-C₆₀ as ETL is rather small. However, due to planning error the doping ratio of n-Bis-HFI-NTCDI is 3 wt% instead of normally 7 wt%. This may hinder the full potential of Bis-HFI-NTCDI as ETL layer. Therefore, the following thickness variation is prepared with a 7 wt% n-Bis-HFI-NTCDI layer.

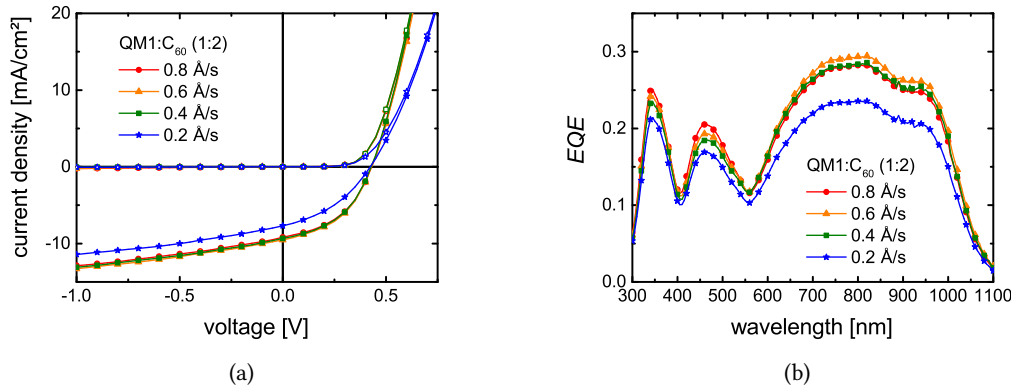


Figure 6.15.: (a) jV curves and (b) EQE curves of QM1:C₆₀ devices in a mixing ratio of 1:2 with n-Bis-HfI-NTCDI as ETL and p-BF-DPB as HTL.

Thickness variation

In a last optimization step, the blend layer thickness is varied in steps of 5 nm from 15 nm to 40 nm. Additionally, the BF-DPB thickness is varied to higher thicknesses to optimize the absorption in the blend layer. The devices presented here are prepared with a different QM1 batch. However, the new batch gives comparable results to the old batch (not shown). The device structure is glass | ITO | n-Bis-HfI-NTCDI (5 nm, 7 wt% W₂(hpp)₄) | C₆₀ (15 nm) | QM1:C₆₀ (varied thickness, 1:2) | BF-DPB (5 nm) | p-BF-DPB (varied thickness, 10 wt% F6-TCNNQ) | F6-TCNNQ (2 nm) | Al (100 nm). Table 6.4 presents the results for the thickness variation with an HTL thickness of 50 nm. Figure 6.16 shows the corresponding jV and EQE curves. The thickness increase of the QM1:C₆₀ blend leads to an increase of the current density, while the FF decreases. The EQE shows an increase in the range between 600 nm and 1100 nm for the increase in blend layer thickness, which is expected for an increasing blend layer thickness. As a result, the thicker devices have an EQE of nearly 20% from 600 nm to 1000 nm. The EQE peak at 450-500 nm decreases, probably because the absorption maximum of the optical field in the device moves from the intrinsic C₆₀ layer to the blend layer due to the increasing blend layer thickness. In section A.2 of the Appendix, we present an assessment of the IQE of the QM1:C₆₀ solar cells. We find that j_{sc} is limited due to recombination and a lower boundary of the IQE of 30-40% for devices with 60 nm BF-DPB thickness.

6.3.3. Aging

The jV measurements of the thickness variation series was repeated four days after the initial measurement. Between the measurements, the solar cells were located in a shelf at dark, ambient conditions. The results are presented in Table 6.5. The current density has decreased and the decrease cannot be explained by the small reduction in intensity in comparison to the first measurement.

6. QM1

Table 6.4.: Overview of the QM1:C₆₀ (1:2) blend thickness variation.

blend thickness nm	j_{sc} mA/cm ²	V_{oc} V	FF %	η_{PCE} %	Sat	I_{ill} mW/cm ²	j_{sc}^* mA/cm ²
15	6.5	0.44	53	1.6	1.3	97	6.6
20	7.7	0.45	52	1.8	1.3	102	7.6
25	8.8	0.45	50	1.9	1.4	104	8.4
30	9.4	0.45	49	1.9	1.4	106	8.9
35	9.7	0.45	46	1.9	1.4	106	9.2
40	9.9	0.45	44	1.8	1.4	106	9.3

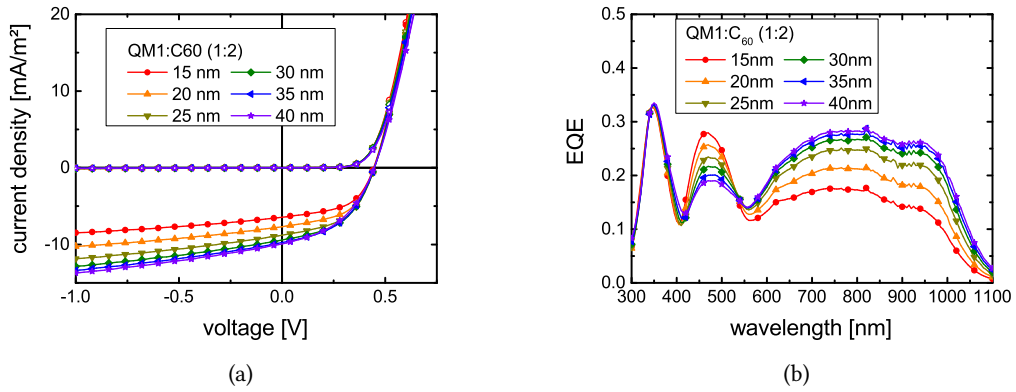


Figure 6.16.: (a) jV curves of the blend layer thickness variation and (b) the corresponding EQE.

Table 6.5.: Second measurement of the QM1:C₆₀ blend thickness variation.

blend thickness nm	j_{sc} mA/cm ²	V_{oc} V	FF %	η_{PCE} %	Sat	I_{ill} mW/cm ²	j_{sc}^* mA/cm ²
15	6.2	0.44	52	1.5	1.3	96	6.5
20	7.4	0.44	52	1.7	1.3	100	7.4
25	8.5	0.44	50	1.8	1.4	103	8.3
30	9.0	0.44	48	1.8	1.4	104	8.7
35	9.3	0.44	46	1.8	1.4	105	8.9
40	9.4	0.44	43	1.7	1.4	105	9.0

Since the solar cells already show a decrease in efficiency after several measurements, the device with 35 nm blend thickness is aged in a climate chamber. Figure 6.17(b) shows the development of the normalized IV parameters. The corresponding IV curves are displayed in Figure 6.17(a). The solar cell has a glass-glass encapsulation and is aged at 38 °C and 50%

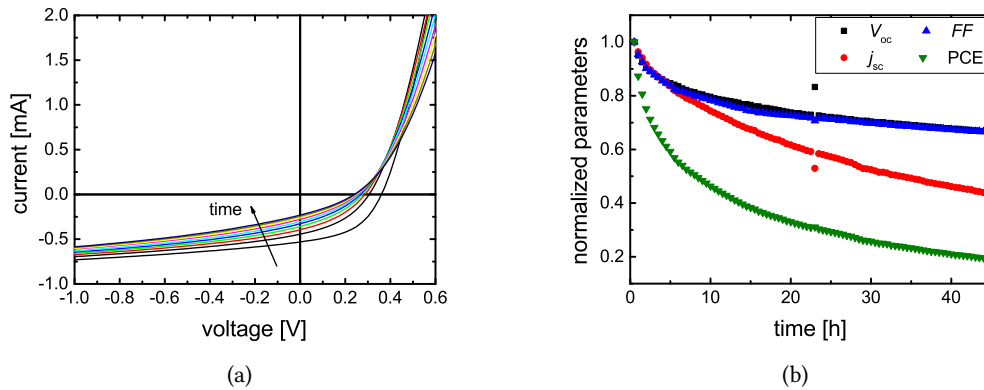


Figure 6.17.: (a) Development of the IV curves during the aging. (b) Development of the jV characteristics during aging at $38\text{ }^{\circ}\text{C}$ and 50% humidity. The aging measurement was performed by Dr. Frederik Nehm (IAPP).

relative humidity at open circuit voltage. The device is illuminated by a SOL 2000 sun simulator (Hönle uv technology) at ≈ 1 sun. The solar cell degrades to 50% of the initial power conversion efficiency within approximately 8 h. The decrease of the parameters happens likewise in V_{oc} and fill factor; I_{sc} decreases even stronger. The amount of water and oxygen that permeates the glass-glass encapsulation during this time scale is negligible. Therefore, we conclude that the degradation is caused by intrinsic factors. Considering the strong tendency of QM1 to form aggregates, a possible reason for the degradation is phase segregation of the QM1: C_{60} blend layer, due to the elevated temperature.[162]

6.4. Conclusion

In this chapter, QM1 is thermally evaporated in single and blend layers with C_{60} for the application in organic solar cells. SEM measurements show a growth of neat QM1 in nanowires on C_{60} , glass, ITO, and KBr substrates. The diameter of the nanowires depends on the evaporation conditions and sublayer and is between 10 nm and 300 nm. The length of the nanowires is between several hundred nanometers and a few microns. In addition, the growth of QM1 nanowires on a heated substrate ($T_{sub}=100\text{ }^{\circ}\text{C}$) was verified. This large range of processing conditions (different sublayers, substrate temperatures during the deposition, deposition rates) shows that QM1 has an extraordinary strong tendency to grow in nanowires. This tendency is related to the large dipole moment of the QM1 molecule of 15.6 D, which leads to a strong dipole-dipole interaction between the molecules. The crystallinity of the nanowires was demonstrated using electron diffraction measurements. X-ray measurements on QM1 single crystals were so far not possible as the preparation of crystals that are sufficiently large for a measurement proved to be difficult. However, the formation of the nanowires is accompanied by a large blue shift of the absorption maximum (650 meV) in comparison to

6. QM1

the absorption spectrum in solution. This is a clear indicator for H-aggregation of the QM1 molecules. The strength of the blue shift of 650 meV is remarkable, as it indicates an interaction between the molecules, which is stronger than the usual Van-der-Waals forces. With an absorption maximum at 824 nm in solution and an absorption that spans up to 1100 nm in the thin film, QM1 is a suitable candidate for an NIR absorber. For this reason, blend layers with the acceptor C₆₀ were tested. SEM measurements on QM1:C₆₀ layers showed that QM1 forms also nanowires in blend layers, proving again the strong tendency of QM1 molecule to form nanowires. The absorption of the QM1:C₆₀ blend layers show an even enhanced absorption in the NIR spectrum. However, an explanation for the changes in absorption between neat QM1 and blends with C₆₀ need further investigations. Solar cells with PHJs of QM1 and C₆₀ are inefficient with a η_{PCE} of approximately 0.1%. For the optimization of the BHJ solar cell, variations of the mixing ratio, the deposition rate, and the blend layer thickness were conducted. The best results were achieved for a QM1:C₆₀ blend layer with a mixing ratio of 1:2 and moderate QM1 deposition rate of 0.6 Å/s. However, the differences in power conversion efficiency for deposition rates of 0.4 Å/s and 0.8 Å/s are rather small. For deposition rates below this plateau, such as 0.2 Å/s, a significant decrease in all fingerprints was observed. The same rate dependence was measured for the devices with a QM1:C₆₀ mixing ratio of 1:1. The highest achieved η_{PCE} was 1.9% with a remarkable EQE of over 19% from 600 nm to 1000 nm. The low *FF* (<50%) in combination with the relatively high saturations (*Sat*>1.3) indicate a problem with the charge carrier extraction. The lifetime of the solar cell is limited to a few hours despite a glass-glass encapsulation under 38 °C and 50% relative humidity and constant illumination.

It has a certain sense of irony that a solar cell, which achieves EQEs of 19% at 1000 nm, uses nanowires formed by H-aggregation, which is usually associated with a blue shift of the absorption. J-aggregation would be the preferable aggregation mechanism as this aggregation type leads to an enhancement of the red shifted J-band. Furthermore, the absorption of J-aggregates tends to be spectrally narrowed.[26] An absorption from 600 nm to 1000 nm is good for a single cell. However, NIR absorbers for high power conversion efficiency solar cells have to function in an ensemble of absorbers in tandem solar cells. Therefore, a narrow strong absorption is more useful than a moderate broad absorption. In order to investigate whether a J-aggregation is possible, vapor phase deposition should be tested. This technique, which uses an inert carrier gas such as nitrogen or argon, is well established for the preparation of nanowires from small molecules and has more free process parameters to adjust the growth of the wires.[148, 163, 164]

7. Investigations on co-evaporant induced crystallization

This chapter presents the main results on the work with co-evaporated additives as means to enhance the crystallinity in organic thin films. Using PDMS as additive, we examine the technique and correct assumptions on the evaporation of PDMS, find problems in the detection of liquid additives with QCMs, and address misconceptions in the determination of the volatilization temperature. Using GIXRD, we demonstrate that the method leads to a strong increase in crystallinity when applied to ZnPc:C₆₀ blend layers. Applied to solar cells, we can achieve an increase in short circuit current density and fill factor, which is normally achieved through a higher substrate temperature or lower deposition rate. Parts of this chapter are published in reference [165], Copyright 2015, reprinted with permission from Elsevier.

7.1. Introduction

7.1.1. Motivation

Achieving a suitable morphology of organic thin films is an important prerequisite for efficient organic solar cells, especially for donor-acceptor blends in bulk heterojunction solar cells.[76, 166, 167] The bulk heterojunction concept overcomes the difference in length scale between the optical absorption length and the exciton diffusion length in organic semiconductors and, hence, enables higher short circuit current densities than planar heterojunctions.[74] Besides chemical tailoring of molecules, the processing conditions have a major influence on the morphology. For some DA combinations, the scale of phase separation is too small, hindering charge carrier extraction.[76] In solution-processed solar cells, solvent additives are widely used to overcome this issue or to influence the morphology in general.[168–172] Using vacuum processing, the most common methods to solve this problem are substrate heating during the deposition and a low material deposition rate.[34, 77, 167, 173] However, both processing conditions contradict an inexpensive large-scaled production, aiming for high throughput in a roll-to-roll process. A low deposition rate reduces the velocity of the roles and high substrate temperatures require time periods for heating and cool down. In addition, the use of plastic foils allows only a limited temperature treatment.[174]

7.1.2. Preliminary work in literature

Kaji *et al.* [166, 175] developed the method of “co-evaporant induced crystallization”, which provides a remedy for these problems. Liquid additives like polydimethylsiloxane, which is shown in Figure 7.1, or alkyldiphenylethers were co-evaporated during the deposition of

7. Investigations on co-evaporant induced crystallization

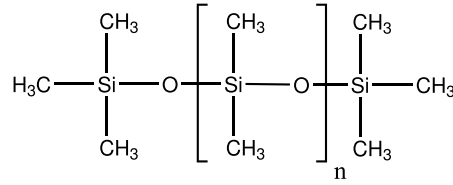


Figure 7.1.: Molecular structure of polydimethylsiloxane (PDMS).

DA blend layers. The authors state that additives do not remain in the co-evaporated layer due to the additional substrate heating, which ensures a complete desorption of the additive molecules from the substrate. Tests in organic solar cells showed a remarkable increase in efficiency for solar cells with 400 nm thick absorber layers, focusing on a maximum absorption of light.

The authors investigated nine different co-evaporants on the $H_2Pc:C_{60}$ system. They observed that the “[...] short-circuit current density appears to rise rapidly as the molecular mass of the co-evaporant becomes comparable to the mass of blend H_2Pc and C_{60} molecules.”[166] Among the different co-evaporants, PDMS41 achieved the best results and improved j_{sc} also for lead phthalocyanine: C_{60} , aluminum-chlorophthalocyanine: C_{60} , and rubrene: C_{60} . [166] In order to identify a suitable substrate temperature for the re-evaporation of the co-evaporant molecules, the volatilization temperature (T_{vol}) was determined. The volatilization temperature is defined as the substrate temperature where the rate of the adsorbed co-evaporant molecules equals the rate of the desorbed molecules, bringing the system in a steady state. Figure 7.2(a) shows the setup, proposed by Kaji *et al.* for the determination of T_{vol} . [175] The setup is comparable to the configuration used for standard tooling purposes with one QCM as a reference and one temperature controlled QCM, which is equipped with a heater. Figure 7.2(b) shows the thickness development of both QCMs over time at constant evaporation rate. The temperature of the heatable QCM is displayed as well. The control QCM has a linear increase in thickness over time. The same behavior is also observed for the heatable QCM up to 400 s, which corresponds to a QCM temperature of $\approx 35^\circ C$. Afterwards, the curve flattens and subsequently decreases. The authors interpret the maximum at $48^\circ C$ as the aforementioned equilibrium between incoming and desorbing molecules, and consequently $48^\circ C$ as the volatilization temperature.

In order to explain the increase in crystallinity, Kaji *et al.* proposed a mechanism that is shown in Figure 7.3. Figure 7.3(a) shows incoming ball- and disc shaped absorber molecules heading towards the substrate during the deposition process. The red arrows indicate the direction of the momentum of the molecules. Since the momentum is orthogonal to the substrate, it should not contribute to the mobility of the absorber molecules on the substrate. The idea of Kaji *et al.* is displayed in Figure 7.3(b), in which the co-evaporant is evaporated during the deposition of the blend layer. Here, a vapor of heavy co-evaporant molecules provides collision centers for the incoming absorber molecules in front of the substrate. This vapor is created by re-evaporation of the co-evaporant molecules from the heated substrate surface. The substrate temperature is set above the volatilization temperature to ensure that all co-evaporant molecules re-evaporate from the substrate and avoid any condensation of

the co-evaporant molecules on the substrate.[166] The collisions between the incoming absorber molecules and the re-evaporated co-evaporant molecules lead to a direction change of the momentum of the incoming absorber molecules. Thus, the absorber molecules have on average a higher horizontal component of the momentum parallel to the substrate surface. This should increase the mobility of the absorber molecules on the substrate and, therefore, also increase the crystallinity of the blend layers.[166] Based on this model, the authors formulate a couple of criteria to the co-evaporant.[166] The co-evaporant ...

- ... must remain liquid in vacuum at RT.
- ... should not decompose during the evaporation.
- ... must be volatile when heated.
- ... should have a molecular mass, that “ [...] is large relative to that of the blend molecules.”[166]

7.2. Analysis of PDMS

Kaji *et al.* achieved the highest gain in short circuit current density by using PDMS41 as co-evaporant. The commercial name of PDMS41 is KF96-50cs, a product of Shin-Etsu Silicones. [166] The “50cs” refers to the viscosity of the PDMS. Due to problems purchasing this material, a PDMS with the same viscosity, “ELBESIL Öl B50” was chosen. At first, the mass distribution of the silicone oil is investigated by MALDI-ToF-MS. These measurements were performed and evaluated by Dr. Karin Sahre (IPF, Dresden). Figure 7.4 presents the signals of the molecules as a function of mass per charge.

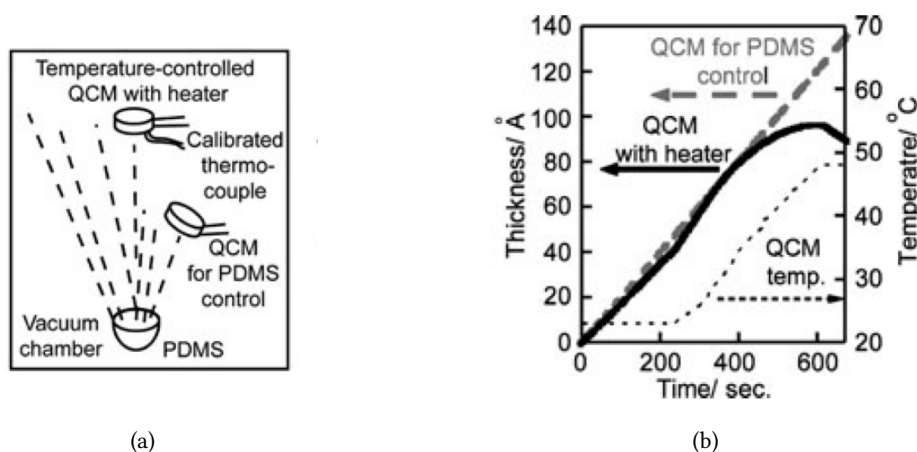


Figure 7.2.: (a) Setup for the determination of T_{vol} . (b) Measurement curves for the determination of T_{vol} . Figures reproduced with permission from ref. [175]. Copyright (2013) Taylor & Francis.

7. Investigations on co-evaporant induced crystallization

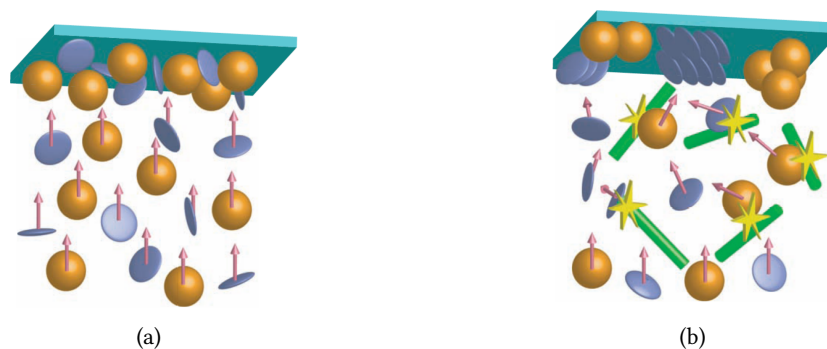


Figure 7.3.: (a) Cartoon of the incoming molecules on a substrate during conventional deposition. (b) Cartoon of the deposition of molecules during a co-evaporant induced crystallization. Figures reproduced with permission from ref. [166]. Copyright (2011) WILEY-VCH Verlag GmbH & Co. KGaA, Weinheim.

One can see that the signals are arranged in a broad distribution, which ranges from 800 u up to nearly 14000 u. Hence, the distribution contains all PDMS oligomers investigated by Kaji *et al.*: PDMS13 (1126.38 g/mol), PDMS41 (3202.68 g/mol), and PDMS87 (6613.77 g/mol). The maximum of the mass distribution is at 1890 u, which corresponds to approximately 23 repetition units. PDMS23 has a molecular weight of 1867.91 g/mol. In addition with the molecular weight of sodium (22.99 g/mol) and less one hydrogen atom (1.01 g/mol), the molecule has a mass of 1889.89 g/mol. The sodium stems from the NaTFAC, which was added to enhance the ionization of the molecules. The inset of Figure 7.4 shows a detailed view around the maximum from 1600 u to 2150 u. One can clearly see that the distances between the single peaks correspond to the molecular mass of the PDMS repetition unit of 74.15 g/mol.

In a follow-up experiment, the distribution of the PDMS molecules upon evaporation is investigated. Therefore, pyrolysis-GC-MS measurements were performed by Eileen Schierz and PD Dr. Alben Lederer (both IPF, Dresden). The PDMS is heated up to 300 °C and 500 °C. Figure 7.5(a) presents the recorded mass spectra at a retention time of 22 minutes for 500 °C. Since the mass spectra do not significantly change at different retention times or different pyrolysis temperatures, this configuration is exemplarily discussed. The most prominent mass peaks are arranged in two patterns. These patterns correspond to two series of PDMS oligomers that are presented in Figures 7.5(b) and 7.5(c). Figure 7.5(b) presents cyclic siloxanes with the masses 207 u, 281 u, 355 u, and 429 u. Figure 7.5(c) shows linear siloxanes, which account for the masses 73 u, 147 u, 221 u, 295 u, 369 u, and 443 u. The deviations between the proposed structures and the mass peaks are approximately 0.1 u and within the experimental error.

In addition, the presented mass patterns are in agreement with the work of Ballistreri *et al.*[176] There, the authors investigated PDMS with a molar weight of 22000 u in a pyrolysis experiment and found two evaporation regimes depending on the temperature. The lower one, between temperatures of 150 °C and 250 °C, was attributed to different low mass

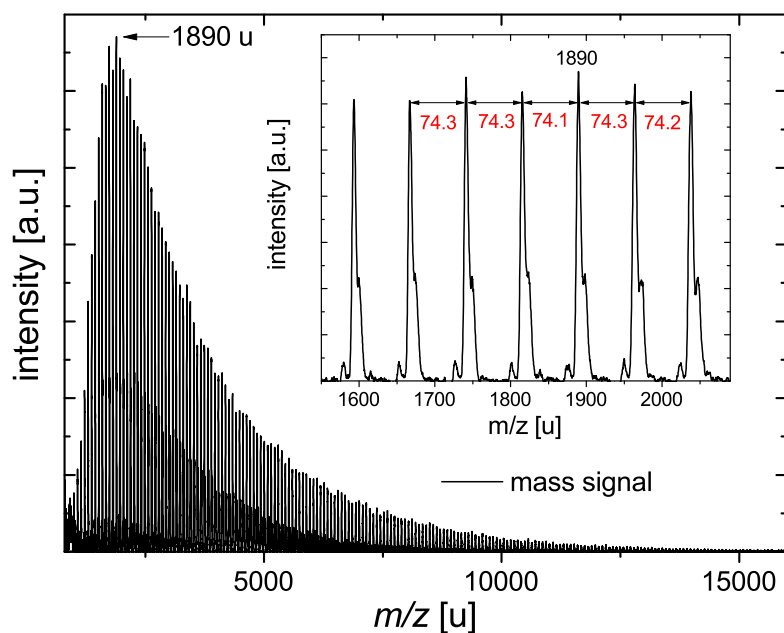


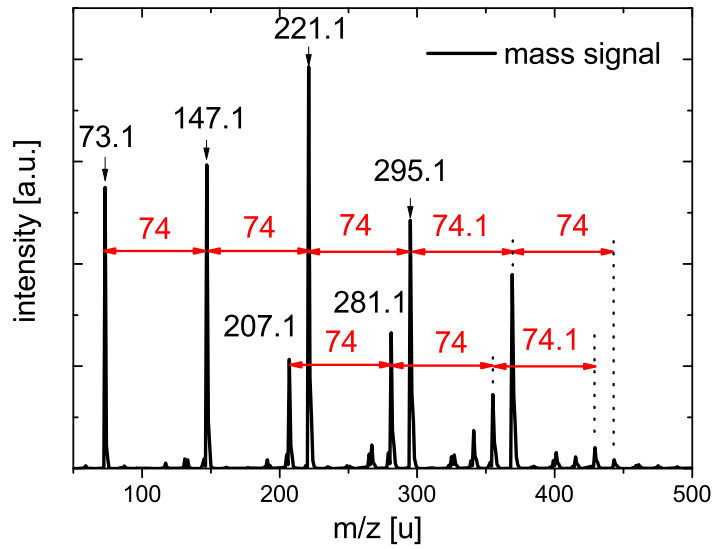
Figure 7.4.: MALDI-ToF-MS spectrum of the used PDMS in a matrix of dithranol with NaT-FAc as salt. The inset shows a detailed view around the maximum of the mass signals at 1890 u. The difference between the mass signals is approximately 74.2 u. Measurement and evaluation was done by Dr. Karin Sahre (Leibniz Institute of Polymer Research (IPF), Dresden).

oligomers with structures similar to the ones presented in Figure 7.5(b) and 7.5(c). The authors interpreted these oligomers to be remainders from the synthesis and had remained in the polymer. At approximately 400 °C, the fragmentation of the actual polymer began. These fragments have the same molecular structures as the oligomers that were initially present in the material.[176]

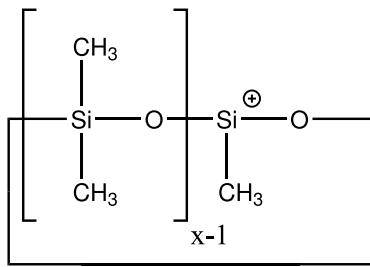
On the course of many PDMS evaporations within the underlying work, the evaporation temperature increased from 125 °C to 220 °C. After replacing the PDMS, the evaporation temperature was again approximately 125 °C. Therefore, we conclude that the evaporation took place in the lower temperature regime.

One can conclude that the initial mass distribution of the PDMS oligomers above approximately 450 u is irrelevant, because only oligomers below this mass are evaporated. For this reason, “ELBESIL Öl B50” is a suitable substitute to KF96-50cs. Kaji *et al.* claimed in their work that the ideal co-evaporant should be heavier than the co-deposited blend molecules.[166] The positive results of the three (heavy) PDMS molecules worked in favour for this assumption. Since the actual evaporated fragments have masses below 450 u, large molecular masses

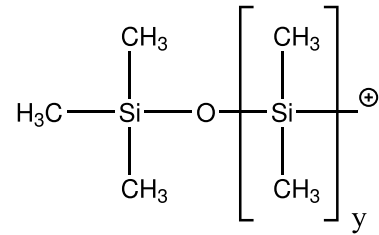
7. Investigations on co-evaporant induced crystallization



(a)



(b)



(c)

Figure 7.5.: (a) Mass spectra after a retention time of 22 min of the evaporated PDMS, obtained from pyrolysis-GC-MS. The pyrolysis temperature was 500 °C. The measurements were performed by Eileen Schierz and PD Dr. Alben Lederer (IPF, Dresden). Plausible molecular structure for different masses (b) $m(x=3)=207$ u, $m(x=4)=281$ u and (c) $m(y=0)=73$ u, $m(y=1)=147$ u, $m(y=2)=221$ u. Adapted from ref. [176].

seem to be of minor importance for the co-evaporant induced crystallization. The findings are also in agreement with data of Kaji *et al.*[166] The authors presented short circuit current densities from solar cells co-evaporated with PDMS13, PDMS41, and PDMS81. According to our findings and the work of Ballistreri *et al.*, these three siloxanes should have the same effect upon co-evaporation.[176] And indeed, all short circuit current densities are approximately 11 - 12 mA/cm². Taking into account the different substrate temperatures during the

deposition of the blend layers, these values appear to be approximately the same.

7.3. Detection of PDMS with QCMs and volatilization temperature

In the first part of this section, the detection of PDMS with quartz crystal microbalances is investigated. The second part proves that a method to determine the volatilization temperature based on QCMs is highly error prone. An alternative approach by means of LDI-ToF-MS is successfully applied and it is shown that PDMS remains in co-evaporated layers.

At the beginning, common tooling experiments are performed. The PDMS is evaporated at a constant evaporation rate and monitored by two QCMs. One reference QCM (QCM_{ref}) is put to the position where the substrate is normally located. The second QCM (QCM_2) is fixed in the chamber and used for the detection of the PDMS at normal evaporations. QCM_2 is heatable in order to perform the tests for the volatilization temperature. A detailed description of the setup can be found in the Experimental chapter (Figure 3.7(b)). The setup is similar to the one in Figure 7.2(a), with the difference that the heatable QCM in our setup is closer to the crucible than the reference QCM.

Figure 7.6(a) presents tooling curves at QCM temperatures of 20 °C, 30 °C, and 45 °C. The PDMS read-out of QCM_2 is plotted as a function of the thickness, recorded at the reference QCM. The curves start linear for all three temperatures, then become sublinear and exhibit a saturation-like behavior. The saturation sets in at lower thicknesses, when the QCM_2 temperature is higher. In Figure 7.6(b), QCM_2 is adjusted at two different inclination angles: $20^\circ \pm 10^\circ$ and 0° to 5° . The curves reveal that the more horizontally aligned QCM has a delayed saturation behavior.

Figure 7.7 presents a situation after finishing the PDMS evaporation. In this graph, the thickness monitored at QCM_{ref} and QCM_2 is depicted as a function of time after finishing the PDMS evaporation. The point of origin for the time axis is set to five minutes after the heating of the PDMS source was turned off to ensure that no PDMS is evaporated anymore. The temperature of QCM_2 is plotted on the right axis to prove that the decrease is not temperature driven ($\Delta T < 1$ K). The decrease in thickness for both QCMs is clearly visible. For QCM_2 , the monitored thickness drops from approximately 2000 Å to 200 Å in 160 minutes. Also the thickness recorded by QCM_{ref} decreases slightly by approximately 17%.

In this context, QCM_{ref} as a reference has to be discussed, since all presented phenomena should also be present for the reference. QCM_{ref} has a larger distance to the PDMS source. Therefore, less PDMS is deposited and the flattening behavior sets in later. In addition, QCM_{ref} is located on the substrate holder and is horizontally aligned, which again delays saturation effects. All three phenomena can be explained by the reasonable assumption that the PDMS condenses after the evaporation again into a liquid state. Hence, the flattening of the PDMS thickness can be explained by the liquid PDMS flowing off the QCM. The saturation of the thickness is then an equilibrium between the income of the deposited PDMS and the flowing off or other kinds of desorption of the QCM. The faster flattening of the

7. Investigations on co-evaporant induced crystallization

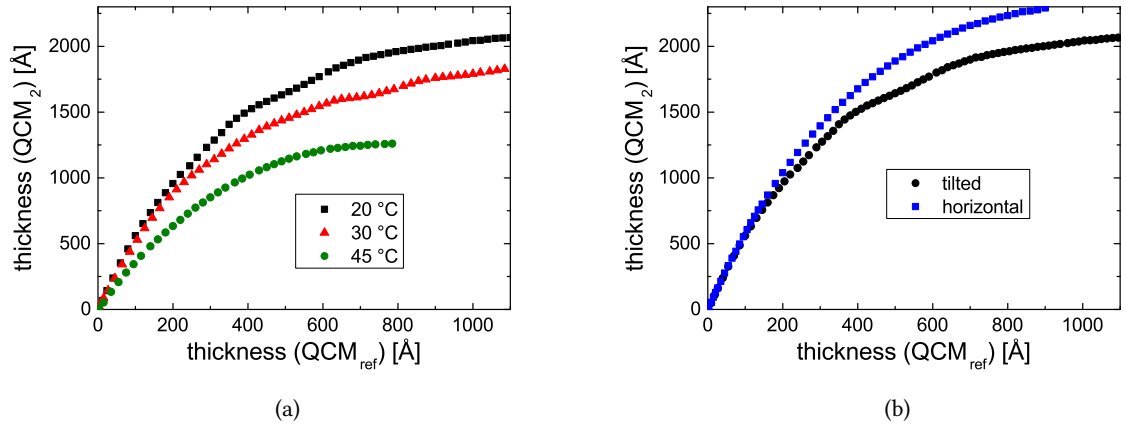


Figure 7.6.: (a) PDMS thickness read-out from QCM₂ and QCM_{ref} at different temperatures of QCM₂. (b) PDMS read-out from QCM₂ for different alignments of the quartz in the vacuum chamber as a function of the read-out from QCM_{ref}.

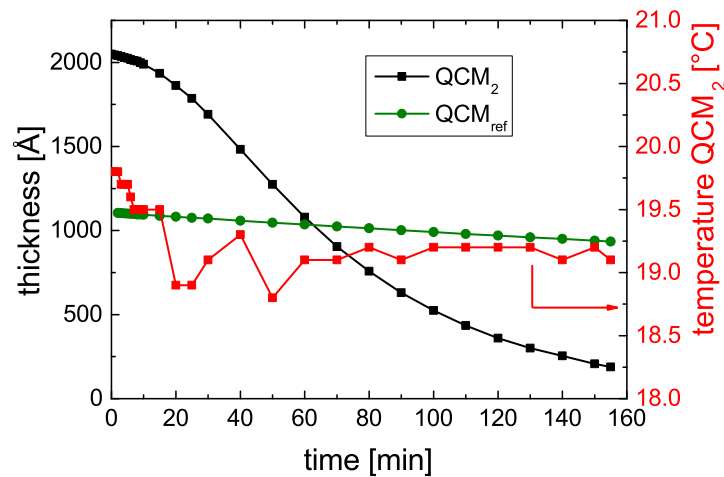


Figure 7.7.: Development of the monitored PDMS thickness of the (tilted) QCM₂ and QCM_{ref} starting 5 min after PDMS evaporation was terminated (heating switched off). The lines are a guide to the eye.

thickness curves at higher QCM temperatures can be explained by the lower viscosity of the liquid PDMS at elevated temperatures. The angular dependence of the flattening is a consequence of an inclined plane, at which a higher downhill-slope force is present. After the evaporation of the PDMS has stopped, the income of the PDMS vanishes and only the drain and other desorption mechanisms are present. For these reasons, a precise control of

7.3. Detection of PDMS with QCMs and volatilization temperature

the PDMS rate is difficult. Accordingly, the control of the PDMS thickness is only accurate for smaller layer thicknesses. Now, the volatilization temperature is determined according to the protocol proposed by Kaji. For this purpose, a tooling configuration is prepared again. The PDMS is evaporated at a constant rate monitored by the reference quartz, while QCM₂ is gradually heated. Figure 7.8 presents the results. The read-out of the heated QCM₂ (d_2) is plotted as a function of the thickness monitored on QCM_{ref} (d_{ref}).

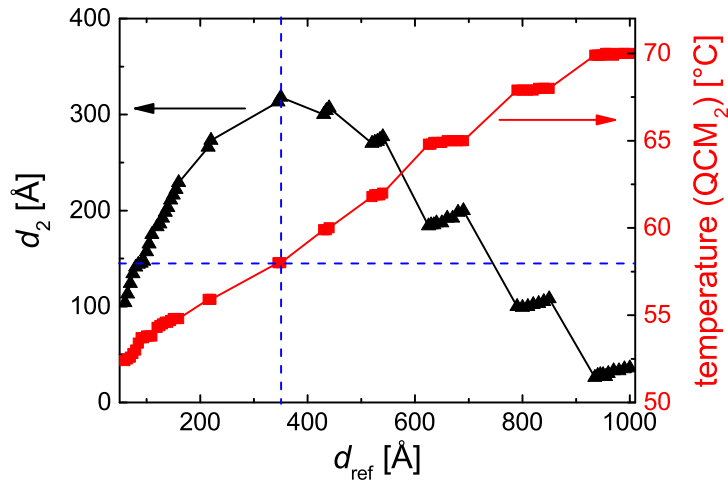


Figure 7.8.: Black triangles represent the thickness development monitored by the heated QCM₂ (d_2) plotted as a function of the thickness on the reference monitor QCM_{ref} (d_{ref}). Red squares show the temperature of QCM₂. The solid red/black lines between the data points are a guide to the eye. The blue dashed lines indicate the temperature of the thickness maximum monitored by QCM₂.

The dependence of d_2 on d_{ref} remains linear up to 180 Å, which corresponds to a QCM₂ temperature of 55 °C. This is the expected behavior for two quartzes monitoring the same evaporation source. A further increase in QCM temperature leads to a sublinear increase of d_2 and to a maximum at 58 °C, indicated by the dashed blue line. However, this procedure neglects the temperature dependence of the resonance frequency (f_0) of a QCM.[97] f_0 shifts towards higher frequencies when its temperature increases (see Figure 3.8).[97] As a consequence, the recorded layer thickness decreases. The effect becomes relevant for temperature changes above 30-40 °C. Therefore, we stabilize the QCM₂ temperature to avoid temperature induced f_0 -shifts to check whether T_{vol} is achieved. Plateaus of constant temperature can be seen around 435 Å, 530 Å, 620 Å, 800 Å, and 1000 Å. For each plateau, an increase in thickness is monitored, proving that T_{vol} is not achieved up to 70 °C, despite a negative rate intermittently displayed by QCM₂.

A more sensitive but time-consuming way to determine T_{vol} is to check for the absence of PDMS in co-evaporated layers determined by mass spectrometry. We apply LDI-ToF-MS measurements to scan for remainders of PDMS in the co-evaporated layer. A 30 nm thick

7. Investigations on co-evaporant induced crystallization

co-evaporated C_{60} layer is prepared at a substrate temperature of $80\text{ }^{\circ}\text{C}$ on an ITO substrate. The PDMS evaporation rate is 0.2 \AA/s and a factor five lower than in the above paragraph. The LDI-ToF measurements were performed by Dr. Florian Wölzl (IAPP). Figure 7.9 shows the detected LDI-ToF-MS signals.

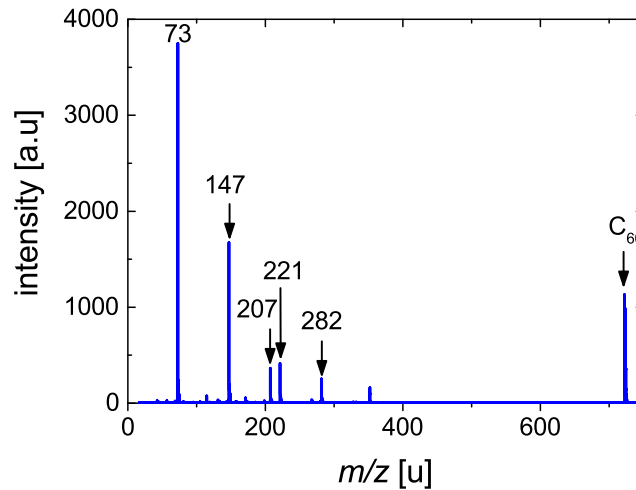


Figure 7.9.: LDI-ToF-MS measurement on a 30 nm thick C_{60} layer co-evaporated with PDMS at $T_{\text{sub}}=80\text{ }^{\circ}\text{C}$. Measurement performed by Dr. Florian Wölzl (IAPP).

Remainders of PDMS at masses of 73 u, 147 u, 207 u, 221 u, and 282 u are detected in the sample and are in good agreement with the results of the pyrolysis-GC-MS measurements. The absence of PDMS oligomers with higher masses might be related to the different desorption methods and the differences in the evaporation of the PDMS. In the pyrolysis method, the PDMS was evaporated rather quickly at high temperatures, while for the co-evaporated samples the PDMS was heated to $T=161\text{ }^{\circ}\text{C}$ for a constant rate. Hence, heavier molecules did not have enough energy to fly and are absent in the sample. These results prove that T_{vol} is not achieved here up to a substrate temperature of $80\text{ }^{\circ}\text{C}$ at a PDMS evaporation rate of 0.2 \AA/s .

Two additional samples with 30 nm thick C_{60} on ITO are prepared at $T_{\text{sub}}=56\text{ }^{\circ}\text{C}$, both without co-evaporation of PDMS. One sample was produced in the MTC, the other in a vacuum chamber of UFO 1, which never contained PDMS. Both samples exhibit no PDMS patterns (not shown).

The detection of PDMS with a QCM is insufficient due to non linear behavior and saturation for high deposited thicknesses. Based on the results for differently inclined QCMs, the different saturation at different QCM temperatures, and the decrease of thickness after ending the PDMS evaporation, we conclude that this is caused by condensing of the PDMS to the liquid form with all listed drawbacks. Accordingly, this behavior should be a property of all liquids evaporated in vacuum and is difficult to control.

7.4. Morphology effects of PDMS co-evaporation with ZnPc:C₆₀ blend layers

We showed that the method to determine the volatilization temperature by Kaji *et al.* ignores the temperature dependence of an AT-cut quartz and, therefore, underestimates the volatilization temperature. Even if the temperature of the QCM is stabilized to check for a stagnant rate, the handiness of the method decreases with increasing quartz temperature, as the slope of the resonance frequency shift increases with temperature. Accordingly, the margins for a “stable” temperature decrease. LDI-ToF-MS as an alternative method was successfully tested and detected remainders of PDMS in the co-evaporated sample, despite a substrate temperature significantly higher than the proposed volatilization temperature of 58 °C and a factor five lower PDMS deposition rate compared to the volatilization test with the QCMs.

The finding that the volatilization temperature is not achieved indicates the incorporation of PDMS in the organic thin film. In addition, the vapor formation in front of the substrate might not be as dense as expected for substrate temperatures well above the volatilization temperature. In combination with the decomposition of the PDMS in oligomers with masses below 450 u, the model of heavy collision centers in front of the substrate becomes less plausible. Accordingly, the effect of PDMS located on the substrate during the layer formation should be considered, e.g., acting as nucleation centers or changes in the surface energy, similar to the effect of additives used for solution processing.

We proceed with low substrate temperatures, knowing that the PDMS is incorporated. Graham *et al.* used PDMS as an additive for solution processed small molecule solar cells.[171, 172] Depending on the concentration of PDMS, it increased or decreased the feature size of the blend layers of 1-EtHx:PCBM or 1-C7:PCBM.[171] Hence, we do not expect a negative effect of the incorporated PDMS per se.

7.4. Morphology effects of PDMS co-evaporation with ZnPc:C₆₀ blend layers

We co-evaporate PDMS with ZnPc:C₆₀ blend layers. This material system was chosen, because its properties are expected to be quite similar to the H₂Pc:C₆₀ system, which was investigated by Kaji *et al.*[166] In addition, ZnPc:C₆₀ served also a standard system at the IAPP and was thoroughly investigated.[92, 173, 177, 178]

Note that the blend layer thickness of co-evaporated layers with PDMS refers only to the total thickness of the donor and the acceptor. The PDMS thickness is not included here, as its exact value is difficult to determine as explained in the previous section. The actual blend layer thickness depends on the given processing conditions. For a PDMS co-evaporated layer with a cumulative material deposition rate of, e.g., 1.6 Å/s and a PDMS evaporation rate of 0.2 Å/s, the actual layer thickness might be larger by approximately 10%.

We use GIXRD in order to demonstrate the increase in crystallinity of a ZnPc:C₆₀ blend layer upon PDMS co-evaporation. Figure 7.10 shows the GIXRD measurements of three 100 nm thick ZnPc:C₆₀ blend layers in a mixing ratio of 1:1 by volume. The blend layer, co-evaporated with PDMS, as well as the reference are deposited in the MTC on heated

7. Investigations on co-evaporant induced crystallization

substrates with a deposition rate of 0.8 \AA/s for ZnPc as well as C_{60} . Table 7.1 summarizes the detailed processing conditions. The reference sample has a rather sharp peak at 7° with a shoulder at 8.1° and a broad amorphous halo around 19° . The 7° peak can be attributed to ZnPc, which can exist in different crystalline phases.[167] Commonly reported for ZnPc thin films are the metastable α -phase and the β -phase, which occurs at higher temperatures. Since both phases have a Bragg reflex at approximately 7° , a more precise attribution is difficult. The broad shoulder at 8.1° in the reference sample is comparable to a peak observed by Schünemann *et al.*[167] The authors explained it as an overlap of the ZnPc peak at 7° and the C_{60} peak at 10.9° . The amorphous halo is a convolution of several Bragg reflexes of C_{60} . The PDMS co-evaporated sample exhibits more pronounced Bragg reflexes (10.9° , 17.8° , and 20.9°) compared to the reference sample, which can be attributed to the fcc C_{60} phase.[102] The shoulder at 8.1° vanished nearly completely for the blend co-evaporated with PDMS. Instead, the C_{60} reflex at 10.9° and the 7° peak are sharpened, which indicates an increase in crystallinity for C_{60} . Instead of the broad halo around 19° , two sharp Bragg reflexes are observed at 17.8° and 20.9° .

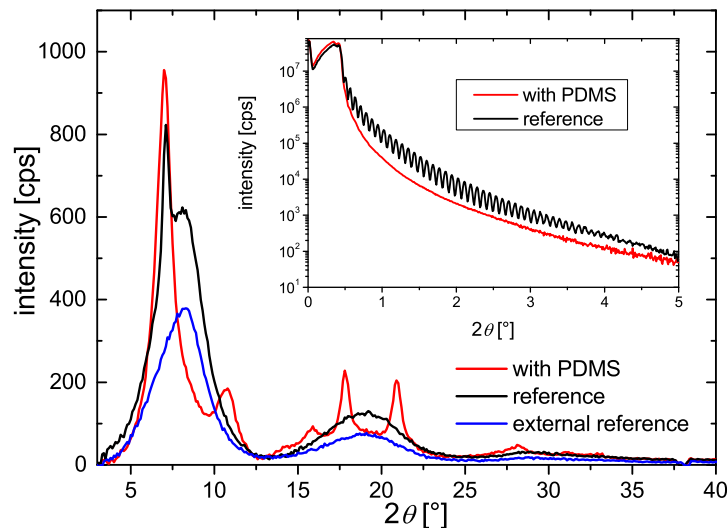


Figure 7.10.: GIXRD measurements on 100 nm thick ZnPc: C_{60} (mixing ratio 1:1 by volume, $R=0.8 \text{ \AA/s}$, $T_{\text{sub}}=54 \text{ }^\circ\text{C}$) samples. One of the samples was co-evaporated with PDMS (red line), which is compared to a reference sample without PDMS (black line) and an external reference (blue line). The external reference was evaporated at another vacuum chamber (UFO 1), which had never contact to PDMS. The inset shows the XRR measurements for the co-evaporated sample and the reference. The measurements were performed by Dr. Lutz Wilde (Fraunhofer IPMS-CNT).

Table 7.1.: Processing conditions of the 100 nm ZnPc:C₆₀ (1:1, by volume) blend layers. The substrate temperature during deposition was 54 - 56 °C. The PDMS was deposited at a rate of 0.2 Å/s. The C₆₀ of the internal and external reference stem from different batches.

sample	chamber	PDMS	PDMS dep. [Å/s]	material dep. rate [Å/s]
int. reference	MTC	no	–	0.8
ext. reference	UFO 1	no	–	0.8
coevap1	MTC	yes	0.2	0.4
coevap2	MTC	yes	0.2	0.8
coevap3	MTC	yes	0.2	1.2

The inset of Figure 7.10 presents X-ray reflectometry measurements of the co-evaporated and the reference sample. An increased surface roughness of the co-evaporated sample is indicated by the absence of Kiessig fringes, which is not unusual for an increased crystalline film growth.

External reference An external reference was prepared for GIXRD measurements. External means that the sample had no contact to the vacuum chamber (MTC) where the PDMS was evaporated. Therefore, an unwanted incorporation of PDMS into this sample can be excluded. Figure 7.10 shows the GIXRD measurement of a 100 nm ZnPc:C₆₀ sample (external reference) produced in another vacuum chamber (UFO 1), which never contained PDMS. Table 7.1 gives the processing details for the external reference. The comparison between both reference samples reveals that the external reference has comparable features at around 20° and 8.1°, but shows no distinct Bragg reflex at 7°. This reflex is attributed to ZnPc crystallites, which are not present in the external reference. The external reference is furthermore in agreement with the work of Schünemann *et al.*, who presented qualitatively similar diffraction patterns for 150 nm thick ZnPc:C₆₀ layers on 5 nm C₆₀ prepared at substrate temperatures of 30 °C and 100 °C.[167] Therefore, we conclude that although no direct evaporation of the PDMS took place during the preparation of the reference sample, an influence of the PDMS on the morphology cannot be excluded, leading to an enhanced crystallization of ZnPc in comparison to the external reference. This was unexpected, because a LDI-ToF measurement on a C₆₀ layer without direct co-evaporation of PDMS did not show a PDMS peak pattern.

Schünemann *et al.* investigated the development of the crystallinity of ZnPc:C₆₀ blend layers upon substrate heating.[167] The highest substrate temperature investigated in their work was 140 °C, the deposition rate for both materials was 0.3 Å/s.[167] A qualitative comparison between their diffractograms and the one of the blend layer with PDMS shows sharper Bragg reflexes for C₆₀ for our samples. This indicates that the crystallization upon co-evaporation of PDMS for this material system is stronger than an increase of the substrate temperature by 80 K, despite the significantly higher deposition rate of 0.8 Å/s.

7. Investigations on co-evaporant induced crystallization

Coherence length Two additional samples (coevap1 and coevap3) with varied material deposition rates (0.4 Å/s and 1.2 Å/s) were co-evaporated with PDMS to test the influence of the material deposition rate. The evaporation rate of the PDMS was kept constant at 0.2 Å/s. Further details are listed in Table 7.1. Figure 7.11(a) depicts the results. In order to quantify the increase in crystallinity, we evaluate the coherence length of C₆₀ and ZnPc using the Scherrer equation. For this purpose, the 7° peak from ZnPc and the 17.8° and 20.9° peaks from C₆₀ of the co-evaporated samples are analyzed. An evaluation of the reference samples is not possible due to the overlap of the broad Bragg reflexes. Figure 7.11(b) presents the coherence lengths in dependence of the material deposition rates.

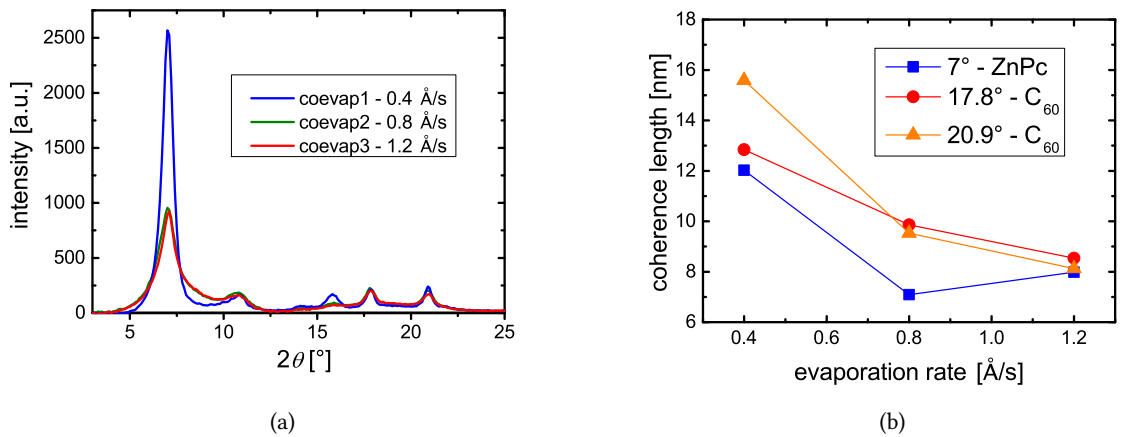


Figure 7.11.: (a) GIXRD measurements of 100 nm thick ZnPc:C₆₀ layers (1:1) for different deposition rates (0.4 Å/s, 0.8 Å/s, 1.2 Å/s). Measurement performed by Dr. Lutz Wilde (Fraunhofer IPMS-CNT). (b) Calculated coherence lengths using the Scherrer equation (see equation (3.5)) for the 7° ZnPc peak and the 17.8° and 20.9° C₆₀ peaks. The connecting lines are a guide for the eye.

The Bragg reflexes of C₆₀ exhibit a continuous sharpening with decreasing deposition rate. Therefore, the coherence length increases from 8-9 nm for a material deposition rate of 1.2 Å/s to 13-16 nm for 0.4 Å/s. The experimental uncertainty can be estimated from the difference between the 20.9° and 17.8° peak of C₆₀. While the deviations for the higher rates are rather small, the difference for 0.4 Å/s is 3 nm. The coherence length of ZnPc stays the same for a decrease from 1.2 Å/s to 0.8 Å/s, since a decline from 8 nm to 7 nm is within the experimental uncertainty, and increases to 12 nm for 0.4 Å/s material deposition rate. Accordingly, we conclude that a decrease of the deposition rate during the co-evaporation with PDMS leads to a higher crystallinity for both materials in the blend.

Figure 7.12 shows the corresponding absorption measurements of the blend layers. The major difference between the internal reference and the PDMS co-evaporated layers is an increased absorption in the spectral region of C₆₀ (around 450 nm) and a relative change in the height of the ZnPc absorption maxima in the range between 550 nm and 750 nm – the so

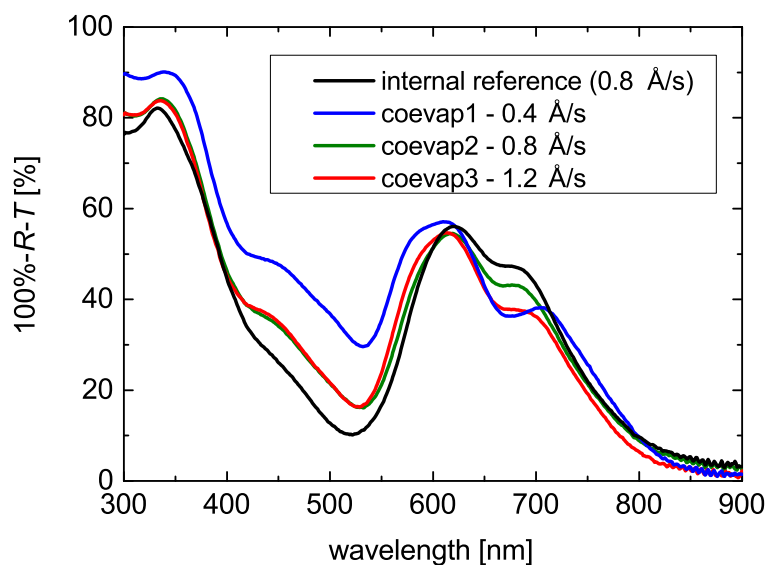


Figure 7.12.: Absorption measurements of samples listed in Table 7.1.

called Q-band. For the PDMS co-evaporated samples, the lower energetic peak in the Q-band is significantly smaller than the higher energetic peak of the Q-band. The 0.4 Å/s sample exhibits the largest difference between both peaks. Note that the lower energetic Q-band peak of the 0.8 Å/s sample is higher than for the 1.2 Å/s sample, which correlates with the higher coherence length of the 1.2 Å/s sample.

Zawadzka *et al.* reported similar Q-band curvatures in the absorption spectrum for post annealing experiments on neat ZnPc single layers at 150 °C.[179] The authors compared the absorption of a ZnPc sample as deposited at RT to the absorption of a post annealed sample at 150 °C and 250 °C.[179] The absorption of the 250 °C sample showed the characteristic Q-band of β -ZnPc with a significantly larger absorption of the lower energetic Q-band peak compared to the higher energetic Q-band peak. The phase transition from α -phase to β -phase appears after longer post annealing treatments for temperatures over approximately 220 °C [94] or is immediately induced for elevated substrate temperatures ($T_{\text{sub}}=150$ °C) during the deposition [180]. Therefore, the change in absorption is another indicator that the co-evaporated PDMS has a similar effect on the ZnPc:C₆₀ blend as elevated substrate temperatures during the deposition. In addition, Iwatsu *et al.* reported a transition from α - to β -phase for evaporated ZnPc thin films in the vapor of several alcohols.[181]

7.5. Usage in organic solar cells

Kaji *et al.* tested their method on solar cells with 400 nm thick blend layers.[166] The authors argued that these unusually thick blend layers could produce higher photocurrents

7. Investigations on co-evaporant induced crystallization

Table 7.2.: Device parameters of the measurement series. The measurement took place at the UFO sun under a nominal intensity of 100 mW/cm^2 for the Si reference diode and is not mismatch corrected.

OSC	bulk	j_{sc} [mA/cm^2]	V_{oc} [V]	FF [%]	η_{PCE} [%]
A	78 nm (PDMS)	10.2	0.48	41	2.0
B	80 nm ref	8.0	0.49	30	1.2
C	44 nm (PDMS)	10.2	0.47	41	2.0
D	40 nm ref	8.5	0.52	32	1.4
E	200 nm (PDMS)	10.7	0.42	40	1.7
F	200 nm ref	6.1	0.50	34	1.0

due to greater light absorption. Instead of using the method to enable very thick blend layers for maximum currents, we are more interested in this method as a means to influence the morphology. Therefore, we tested smaller blend thicknesses of 40 nm, 80 nm, and 200 nm. Another reason for the smaller thicknesses is the saturation found for larger quantities of PDMS on QCMs.

Six solar cells are fabricated incorporating the previously characterized blends. The devices have the following stack: ITO | 20 nm C_{60} | ZnPc: C_{60} (1:1, rate = 0.8 \AA/s) | 10 nm BF-DPB | 30 nm BF-DPB (p-doped with 10 wt% F_6 -TCNNQ) | 2 nm F_6 -TCNNQ | 100 nm Al. The organic layers were prepared in the MTC. Afterwards, the samples were transferred in a box with a nitrogen atmosphere to UFO 1, which is located in another building, for the deposition of the aluminum contact. Since the MTC is not attached to a glovebox, the samples had contact to air for approximately 10 - 20 s. Table 7.2 provides an overview of the prepared samples. Devices A, C, and E are prepared by co-evaporation of PDMS at a deposition rate of 0.2 \AA/s simultaneously to the ZnPc and C_{60} deposition. In contrast, devices B, D, and F were prepared without addition of PDMS and serve as references. The substrate temperature during the deposition of the blend layer was $T_{sub}=54 \text{ }^\circ\text{C}$ for all devices. The characterization of the devices took place shortly after the deposition of the metal contact on the sun simulator in the glovebox of UFO 1. Table 7.2 summarizes the results, the corresponding jV -curves are presented in Figure 7.13.

Since the trend for all device pairs is similar, we exemplarily discuss the jV characteristics of device A and B, which are displayed in Figure 7.13(a). Device A exhibits an increased j_{sc} of 10.2 mA/cm^2 compared to device B with 8.0 mA/cm^2 . In addition, the FF increased from 30% for device B to 41% for device A. The higher FF indicates an improved charge carrier transport. In conjunction with the higher crystallinity, shown by GIXRD measurements, and the increased j_{sc} , these are indications for a larger phase separation. The optimization of the performance through a higher crystallinity was described by Schünemann *et al.*[167] Yet, the increase in crystallinity was achieved by a further increase of the substrate temperature to $140 \text{ }^\circ\text{C}$, which our protocol avoids. The overall cell performance increases from 1.2% for device B to 2.0% for device A. Figure 7.13(b) presents the EQE of both devices. The compari-

son of the EQE spectra¹ shows similarities to the absorption spectra of the blend layers. For device A, the higher energetic Q-band peak of ZnPc is stronger than the lower energetic one in comparison to device B. In addition, the EQE between 400 nm and 500 nm is considerably higher than for device B.

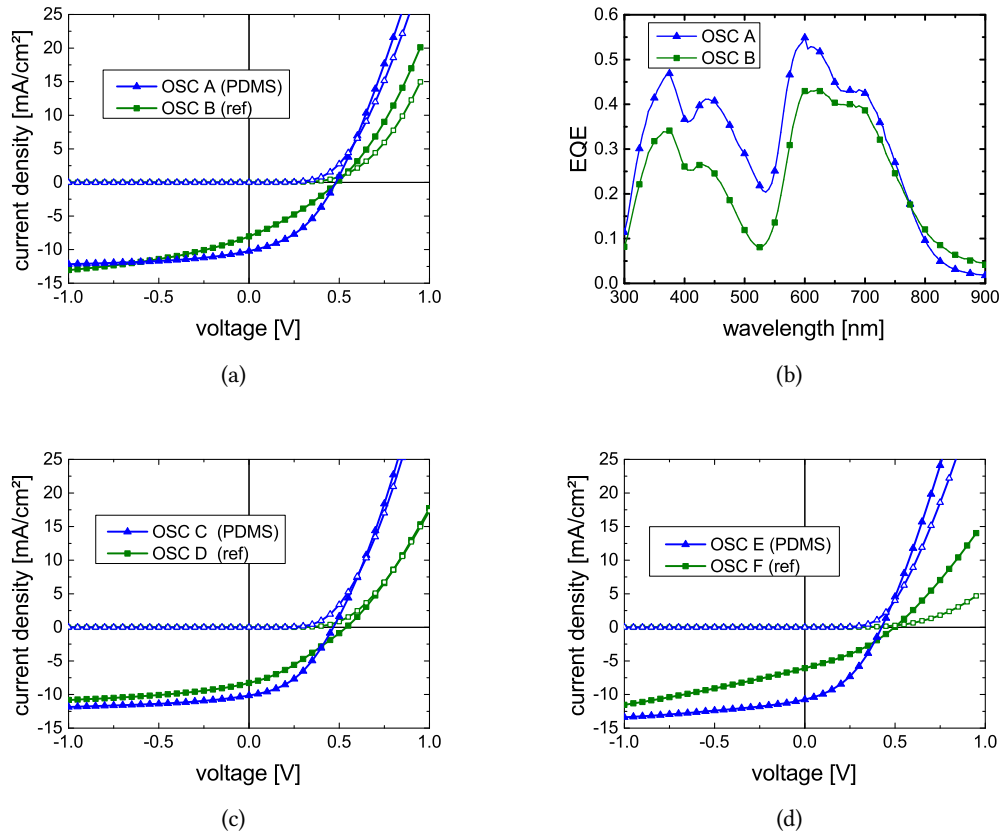


Figure 7.13.: (a) jV characteristics of device A (blue triangles) and device B (green squares). Solid symbols indicate the measurement under illumination, open symbols measurements in the dark. (b) EQE of device A and B. (c), (d) jV measurements of devices C-F. Processing conditions similar to device A/B.

The positive effect of co-evaporation induced crystallization is also demonstrated for devices with thinner (40 nm) and thicker (200 nm) BHJ layers. Each co-evaporated OSC showed a significantly decreased series resistance, which is visible in the steeper slope of the current in forward direction. Though V_{oc} is lower for the co-evaporated OSCs, their power conversion efficiency is higher compared to the respective references, which is caused by a higher j_{sc} and higher FF . Both parameters were rather unaffected by the thickness variation. Unfortunately, the devices exhibited fast degradation, resulting in an S-kink in the mismatch

¹The EQE was measured on encapsulated devices, which showed already an S-kink.

7. Investigations on co-evaporant induced crystallization

corrected measurement after encapsulation. We address this degradation to the air contact between the p-doped layer and the metal contact. One explanation might be that the air contact leads to oxygen and water deposition on the hole transport layer and gradually corrodes the critical organic-aluminum interface. In order to hinder the degradation, a second series of samples was prepared with the difference that the exposure to air was done before the deposition of the p-doped BF-DPB layer. We assumed that the influence of the water and oxygen might be less harmful directly in that case. Furthermore, after the transfer the samples could gas out for several days under ultra high vacuum in UFO 1 ($p \leq 10^{-7}$ mbar). The measurement series reproduced the observed trends, however, without showing the expected increase in lifetime. The results are presented in section A.3 in the Appendix. Accordingly, a further investigation of the devices was not meaningful.

7.6. PDMS co-evaporation applied to DTDCTB and DCV₂-5T-Me(3,3) blends

We apply the technique of PDMS co-evaporation to two other material systems to investigate whether the observed trends can be transferred to other materials. DTDCTB:C₆₀ is tested, because this material system showed no change in GIXRD diffractograms upon substrate heating (compare chapter 4). Therefore, PDMS is co-evaporated to test an alternative method to increase the crystallinity in blend systems. Figure 7.14(a) shows the GIXRD diffractograms of a sample co-evaporated with PDMS compared to a reference sample. The co-evaporated sample is processed at $T_{\text{sub}}=75$ °C, 25 K below the substrate temperature of the reference sample. A comparison between both graphs suggests that PDMS has no influence on this material system.

DCV₂-5T-Me(3,3):C₆₀ is chosen as the other material system, because it achieves its best performance at elevated substrate temperatures. Figure 7.14(b) shows the results. Despite the lower substrate temperature during evaporation and the lower film thickness, the diffractogram of the PDMS co-evaporated sample shows significantly sharper Bragg peaks than the reference sample, which was deposited at $T_{\text{sub}}=90$ °C. The peaks at 17.9°, 20.9°, and the shoulder at 11.0° can be attributed to C₆₀.

7.7. Conclusion

In this chapter, the method of co-evaporant induced crystallization of organic blend layers was investigated. We chose PDMS as additive and measured the evaporation of low mass PDMS oligomers (<450 u), regardless of the initial mass distribution. We determined the mass distribution of the PDMS oligomers by pyrolysis-GC-MS in the evaporated gas phase and detected a similar mass pattern in the co-evaporated C₆₀ layers by LDI-ToF-MS. An insufficient detection of PDMS with QCM was demonstrated due to the liquid phase of the PDMS. In addition, we found that the method to determine the volatilization temperature is error prone due to the temperature dependence of the resonance frequency of the quartz.

²The PDMS rate is 0.02 Å/s, because the DCV₂-5T-Me(3,3) was deposited with a rate of 0.1 Å/s.

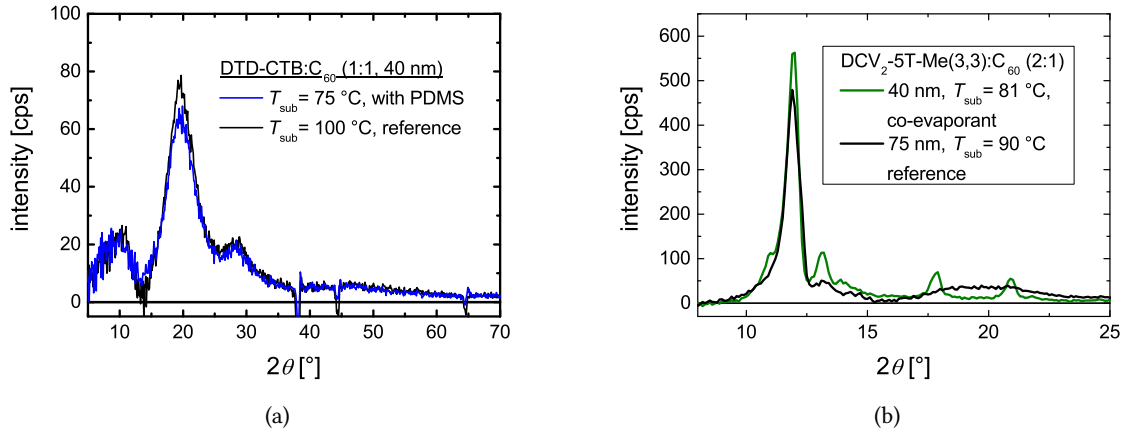


Figure 7.14.: GIXRD measurements on (b) DTDCTB:C₆₀ with (PDMS rate ≈ 0.1 Å/s) and without co-evaporation of PDMS. The reference sample was produced in UFO 1 by Jacob König-Otto (IAPP). (a) DCV₂-5T-Me(3,3):C₆₀ diffractograms with (PDMS rate ≈ 0.02 Å/s) and without co-evaporation.² The reference sample was processed on UFO 1 by Dr. Chris Elschner (IAPP). The GIXRD measurements were performed by Dr. Lutz Wilde (Fraunhofer IPMS-CNT).

LDI-ToF as a possible alternative for the determination of T_{vol} was presented. We proceeded at substrate temperatures below T_{vol} , and co-evaporated PDMS in ZnPc:C₆₀ blend layers, accepting the incorporation of PDMS into the blend layer. A strong crystallization was detected by GIXRD, in accordance with the work of Kaji *et al.*[166]. The gains in crystallinity were quantified for different material deposition rates, determining the coherence length by using the Scherrer equation. The GIXRD patterns and the absorption spectra of the PDMS co-evaporated ZnPc:C₆₀ blends indicate that the co-evaporation induces a morphology that is usually achieved at much higher substrate temperatures during the deposition and for lower material deposition rates. Tests in solar cells showed an increase of short circuit current density and fill factor, despite the incorporation of PDMS. Furthermore, the co-evaporation of PDMS was tested on two additional material systems. For the system that is known to respond to substrate heating (DCV₂-5T-Me(3,3):C₆₀), an increase in crystallinity was observed, whereas for the system, which does not respond to substrate heating (DTDCTB:C₆₀), no change was visible in GIXRD. This is a further indicator that PDMS co-evaporation induces a change in morphology that is similar to a deposition of the blend at higher substrate temperature.

In summary, the co-evaporation of PDMS is a powerful method to increase the crystallinity of blend layers despite higher material deposition rates and lower substrate temperatures. However, due to the liquid state of the PDMS an insufficient detection via QCM hinders a precise control of the deposition. Therefore, the necessary control of the morphology for

7. Investigations on co-evaporant induced crystallization

bulk heterojunctions is not satisfactory. Accordingly, a further usage of this method can only be useful with a suitable detection of the liquids, or the usage of solid additives should be tested, to enable a precise control via QCM.

8. Conclusion and Outlook

This chapter summarizes the results of the thesis and suggests approaches for further investigations. New materials were investigated and a very broad infrared absorber was found, as well as another donor material with extraordinary low non-radiative voltage losses in solar cells with C_{60} . Furthermore, we studied the method of "co-evaporant induced crystallization" and applied it to $ZnPc:C_{60}$ solar cells. The summary starts with the investigation of the peculiar behavior of the fill factor of DTDCTB: C_{60} solar cells.

DTDCTB The performance of DTDCTB: C_{60} solar cells is studied as a function of blend layer thickness and substrate temperature during the deposition. We find that the fill factor with increasing DTDCTB: C_{60} thickness depends strongly on the substrate temperature during the deposition. Three regimes are identified: At RT, the fill factor increases up to 50 nm blend layer thickness and stays constant up to 70 nm. In a medium temperature regime around 85 °C, an S-kink is present, which keeps the fill factor constantly below 25%. In the high temperature regime at ≈ 100 -110 °C, the fill factor drops monotonically, as usually observed for an increase of the blend layer thickness in organic solar cells. We attribute this behavior to a morphological change in the blend layer. However, we can only exclude an increase in crystallinity or a change in the average alignment of the molecules as reasons for the change. Furthermore, the peculiar behavior of the $FF(d)$ dependence could neither be explained by a higher mobility of the charge carriers at room temperature nor by a significantly increased charge carrier lifetime nor by a significant change in the recombination behavior. The presented measurements can only exclude approaches to an explanation of the behavior of $FF(d)$ for the different substrate temperatures. For a conclusive explanation of this behavior, further investigations are necessary.

A promising starting point for further studies are TEM measurements to gather more information about the morphology, besides the crystallinity of the blend layer. TEM measurements in combination with an energy dispersive X-ray detector (EDX) can provide information about the phase separation of the blend layer without crystalline phases.[182] This might help to identify the difference in morphology for the different substrate temperatures during the deposition.

Benzothiadiazole derivatives Three new molecules, TTF, CNTF, and PRTF, are tested in thin films and solar cells. They are designed to overcome the low thermal stability of DTDCTB. For PRTF, a strong increase in sublimation yield is achieved. However, all derivatives have a reduced absorption as compared to DTDCTB, making it difficult to achieve comparable short circuit currents. Furthermore, the devices incorporating the new materials have lower fill factors and are more sensitive to higher blend layer thicknesses as DTDCTB: C_{60}

8. Conclusion and Outlook

devices. The highest power conversion efficiency is achieved for PRTF with 3.8%, which is clearly lower than the 4.9% of the DTDCTB:C₆₀ devices. However, we find for PRTF that the difference between the open-circuit voltage and the CT-state energy ($\Delta V_{oc}=0.54$ V) is exceptionally low as compared to typical voltage losses in organic solar cells. This is the result of low non-radiative recombination losses ($\Delta V_{nonrad}=0.26$ V).

The origin of the low non-radiative recombination losses deserves further investigation and might lead to a future design rule for materials that enable higher open circuit voltages. Investigations on solar cells with a low donor content (≈ 5 mol%) are one possibility to exclude the influence of the morphology and allow an assignment to either morphology or a molecular property.

QM1 QM1 is investigated in single and blend layers with C₆₀ for application in organic solar cells. SEM measurements show a growth of QM1 in nanowires on different sublayers with nanowire lengths between several hundred nanometers and a few microns. The extraordinary strong preference for nanowire formation of QM1 is related to the large dipole moment of the QM1 molecule of 15.6 D, which leads to a strong dipole-dipole interaction between the molecules. The formation of the crystalline nanowires is accompanied by a large blue shift of the absorption maximum (650 meV) in comparison to the absorption spectrum in solution. This is a clear indicator for H-aggregation of the QM1 molecules. The strength of the blue shift of 650 meV is remarkable, as it indicates an interaction between the molecules much stronger than for the usual Van-der-Waals forces.

With an absorption maximum at 824 nm in solution and an absorption that spans up to 1100 nm in the thin film, QM1 is a suitable candidate for an NIR absorber. For this reason, we optimized blend layers with the acceptor C₆₀ in solar cells. The highest achieved power conversion efficiency is 1.9% with a remarkable EQE of over 19% from 600 nm to 1000 nm.

It has a certain sense of irony that a solar cell achieving EQEs of 19% at 1000 nm uses nanowires formed by H-aggregation, which is usually associated with a blue shift of the absorption. J-aggregation would be the preferable aggregation mechanism as this aggregation type leads to an enhancement of the red shifted J-band. Furthermore, the absorption of J-aggregates tends to be spectrally narrowed.[26] A broad absorption from 600 nm to 1000 nm is beneficial for a single cell. However, NIR absorbers for high power conversion efficiency solar cells have to function in an ensemble of absorbers in tandem solar cells. Therefore, a narrow strong absorption is more useful than a moderate broad absorption. In order to investigate whether J-aggregation could be achieved, vapor phase deposition should be tested. This technique, which uses an inert carrier gas such as nitrogen or argon, is well established for the preparation of nanowires from small molecules and allows more process parameters to adjust the growth of the wires.[148, 163, 164] In addition, QM1 nanowires should be investigated in an organic field effect transistor in order to check, whether the strong interaction of the QM1 molecules leads to a high mobility of the charge carriers.

PDMS “Co-evaporant induced crystallization” is a method to increase the crystallinity of blend layers in vacuum deposited organic solar cells and was invented by Kaji *et al.*[166,175] The method is investigated using PDMS as the liquid co-evaporant. We refute several assumptions of Kaji’s explanation for the increase in crystallinity, such as that the co-evaporant molecules do not stay in the co-evaporated layer, that the co-evaporant molecules should be heavier than the absorber molecules and do not decompose. Therefore, PDMS should rather be considered as an additive instead of a co-evaporant. Furthermore, we demonstrate that the evaporation rate of liquid additives in general cannot be precisely detected. However, this control is a necessary requirement for such a method, since the size of the crystalline phases has to be adjusted to the exciton diffusion length of the material.

We co-evaporate PDMS with ZnPc:C₆₀ blend layers and show a significant increase of the crystallinity for the sample with co-evaporated PDMS. The GIXRD patterns indicate a higher coherence length of the ZnPc as well as C₆₀ phases within the blend layer, especially for lower deposition rates of the materials. The co-evaporated solar cells show a behavior similar to solar cells processed at a higher substrate temperature. Further tests on other material systems indicate that the method works only for material combinations, where also substrate heating is beneficial for an increased crystallinity. Nevertheless, the method of “co-evaporant induced crystallization” leads to tremendous increase of the crystallinity without slowing down the deposition rate or increasing the substrate temperature. This is beneficial for a large scale production on flexible substrates. As the co-evaporant stays in the blend layer, it acts more like an additive, which is very common in solution processed organic solar cells.

However, for a further application of the method, liquid substances have to be avoided to ensure a precise detection of the additive with QCMs. Accordingly, molecular structures comparable to the identified PDMS fragments have to be found that have a solid aggregate state and keep it when exposed to vacuum. Furthermore, the role of the additive in the crystallization process has to be better understood to specify further requirements to the additives.

A. Appendix

A.1. DTDCTB

A.1.1. Sublayers

Table A.1.: Fingerprints of the devices with different HTL sublayers shown in Table 4.2 and Figure 4.7. The layers below the blend are for stack 1: ITO | NDP9 | p-BPAPF | BPAPF, stack 2: ITO | NDP9 | p-BPAPF | BPAPF | DTDCTB, and stack 3: ITO | MoO₃ | DTDCTB.

stack	d nm	T_{sub} °C	j_{sc} mA/cm ²	V_{oc} V	FF %	I_{ill} mW/cm ²	j_{sc}^* mA/cm ²	η_{PCE} %
1	50	100	4.0	0.68	32	99	4.0	0.9
1	40	100	7.4	0.82	38	98	7.6	2.4
1	30	100	6.2	0.82	41	96	6.4	2.2
1	30	RT	5.9	0.82	55	100	5.9	2.7
1	40	RT	6.9	0.83	57	101	6.8	3.2
1	50	RT	7.8	0.83	58	102	7.7	3.7
2	50	100	8.0	0.79	35	100	8.0	2.2
2	40	100	7.5	0.81	42	99	7.6	2.6
2	30	100	6.5	0.80	45	97	6.8	2.4
2	30	RT	5.5	0.82	55	100	5.5	2.5
2	40	RT	6.7	0.83	57	102	6.6	3.1
2	50	RT	7.5	0.83	58	103	7.3	3.5
3	50	100	7.8	0.82	33	99	7.8	2.1
3	40	100	7.6	0.82	40	98	7.8	2.6
3	30	100	6.8	0.82	44	96	7.0	2.6
3	30	RT	5.7	0.82	56	100	5.7	2.6
3	40	RT	6.8	0.82	58	101	6.7	3.2
3	50	RT	7.7	0.82	59	102	7.6	3.7

A.1.2. Solar cell set 2

ITO | NDP9 (2 nm) | p-BPAPF (30 nm, 10 wt% NDP9) | BPAPF (5nm) | DTDCTB:C₆₀ (var. blend thickness, var. substrate temp.) | C₆₀ (20 nm) | n-Bis-HFI-NTCDI (15 nm, 7 wt%) | Al (100 nm).

A. Appendix

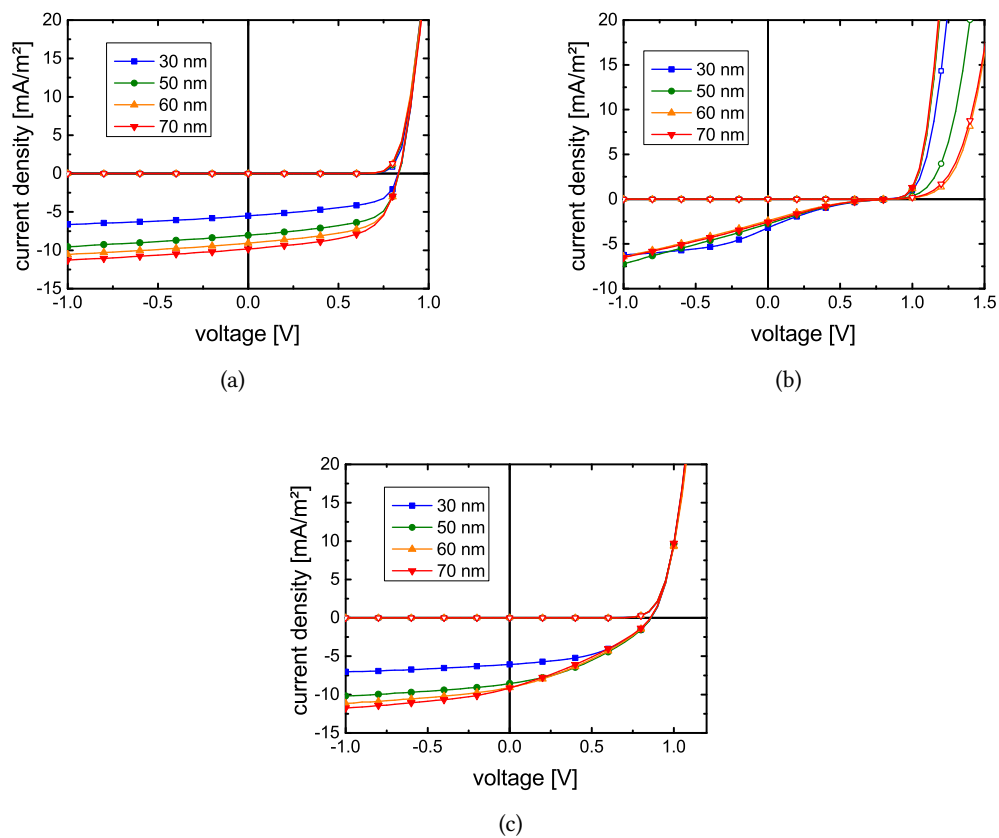
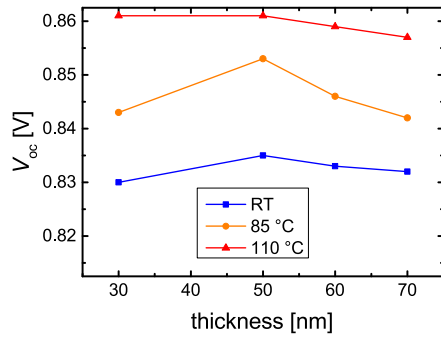
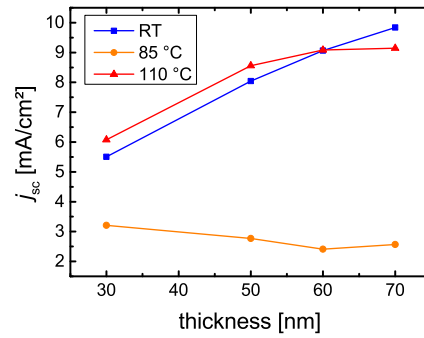


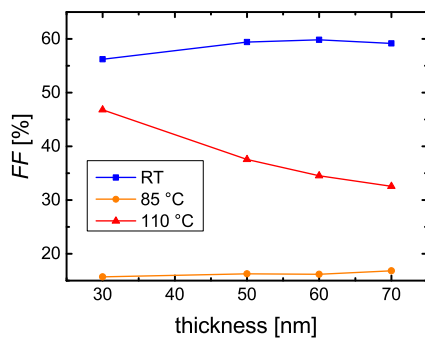
Figure A.1.: jV curves in dark and under illumination for blend layer thicknesses of 30/50/60/70 nm deposited at (a) RT, (b) 85 °C, and (c) 110 °C.



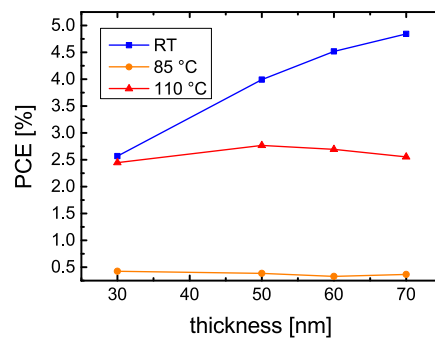
(a)



(b)



(c)



(d)

Figure A.2.: Fingerprints of the jV curves presented in Figure A.1. The lines are a guide to the eye.

A. Appendix

A.1.3. IS on ITO | blend | Al devices

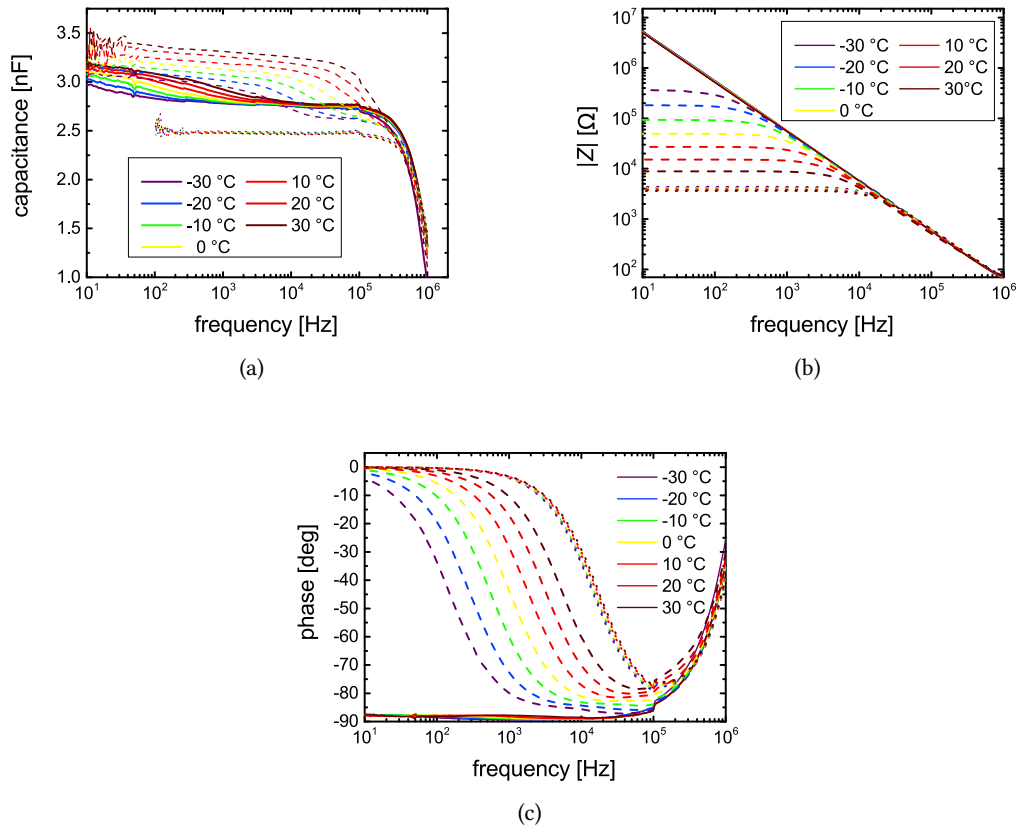


Figure A.3.: Temperature dependent (a) Cf , (b) Zf , (c) phase- f plot of the ITO | DTDCTB:C₆₀ (100 nm) | Al devices produced at RT (solid lines), 85 °C (dashed lines), and 110 °C (dotted lines).

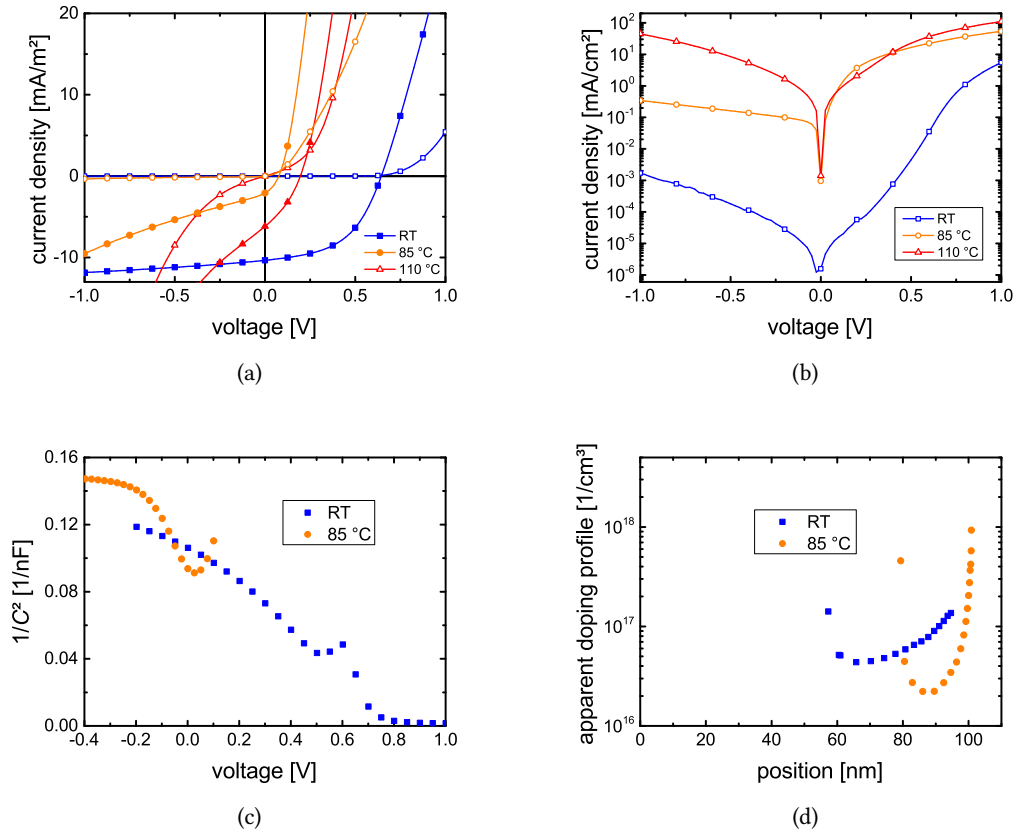


Figure A.4.: (a) jV characteristics of the m-i-m devices in the dark and under illumination (1sun). (b) The dark jV curves in log-plot. (c) The corresponding $C-V$ curves in Mott-Schottky plot and the (c) corresponding apparent doping profile.

A.1.4. IS on complete solar cells

Figure A.5 shows the temperature dependent Cf , modulus- f , and phase- f plot of the solar cells of set 1 with 100 nm blend layer thickness. The comparison to the simplified ITO | DTDCTB:C₆₀ (100 nm) | Al samples shows significantly different responses in the Cf plot. While the simplified devices have a comparable capacitance at the high frequency capacitance plateau, the height of the high frequency plateau for the RT solar cell is nearly two times higher than for the 85 °C and 110 °C solar cells. Though the Cf response changes with temperature, it is not comparable to a trap response as observed in Figure A.3 for the simplified m-i-m devices. As the interpretation of the Cf response is difficult, due to the additional (doped) layers, we investigate different blend layer thicknesses to pinpoint the reason for the differences in capacitance to the blend layer. Figure A.6 shows the Cf spectra of the devices from set 2 with (a) 30 nm and (b) 70 nm blend layer thickness. For both blend layer thicknesses, the increased capacitance of the RT device is visible. For a further

A. Appendix

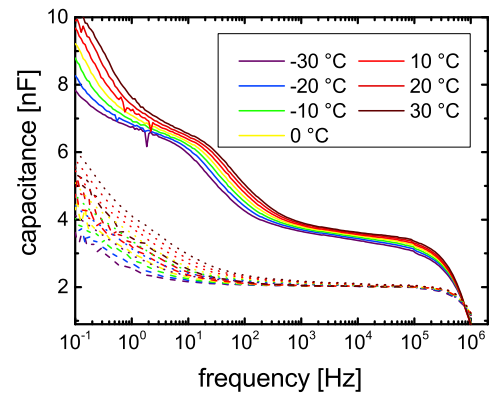
evaluation, we apply an equivalent circuit, consisting of a capacitor with a parallel resistor and an additional resistor in series, as described in the Experimental chapter (3.3.11). For the fitting only the frequencies over $5 \cdot 10^3$ Hz are considered in order to avoid a contribution of trap states. To get information about the bulk properties, we assume that the intrinsic layer in the solar cell acts like several independent plate capacitors connected in series:

$$\frac{1}{C} = \frac{1}{C_1} + \frac{1}{C_2} + \frac{1}{C_3} + \dots = \frac{1}{\epsilon_0 \epsilon_r A} d + \text{const.} \quad (\text{A.1})$$

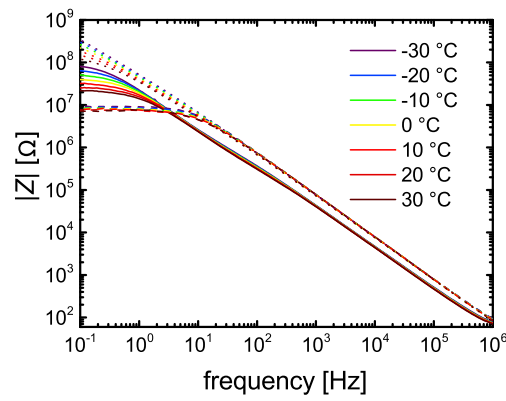
Figure A.6(c) shows the inverse capacitance as a function of the blend layer thickness. Assuming a plate capacitor, we fit the slope and with the knowledge of blend layer thickness d and area A , we obtain the dielectric constant of the blend layer. The values are summarized in Table A.2. While the blend layers of the 85 °C and 100 °C devices have a comparable ϵ_r of 4.4 (4.2), the blend layer of the RT device has an ϵ_r of 6.8. The higher ϵ_r of the RT device could reduce bimolecular recombination, due to a higher screening of the electric field and a smaller capture radius.[183] This might be an explanation for the higher fill factor. However, the difference in ϵ_r is not found for the simplified devices and as mentioned above the interpretation neglects the interaction or influence of the doped transport layers.

Table A.2.: Overview of the fitted slopes from Figure A.6(c) and calculated relative permittivities.

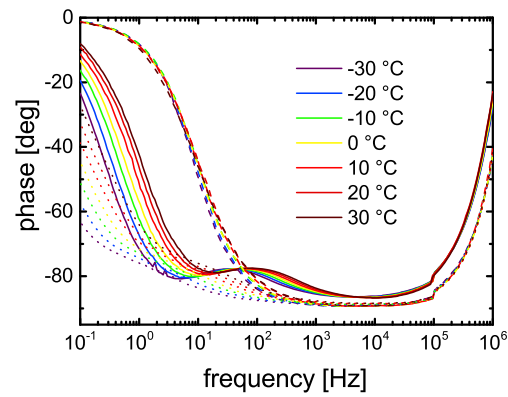
substrate temperature	RT	85 °C	110 °C
slope [$10^{15}/(\text{Fm})$]	2.58	4.01	4.22
ϵ_r	6.8	4.4	4.2



(a)



(b)



(c)

Figure A.5.: Temperature dependent (a) Cf , (b) Zf , (c) phase- f plot of devices with 100 nm DTDCTB: C_{60} thickness from set 1 produced at RT (solid lines), 85 °C (dashed lines), and 110 °C (dotted lines).

A. Appendix

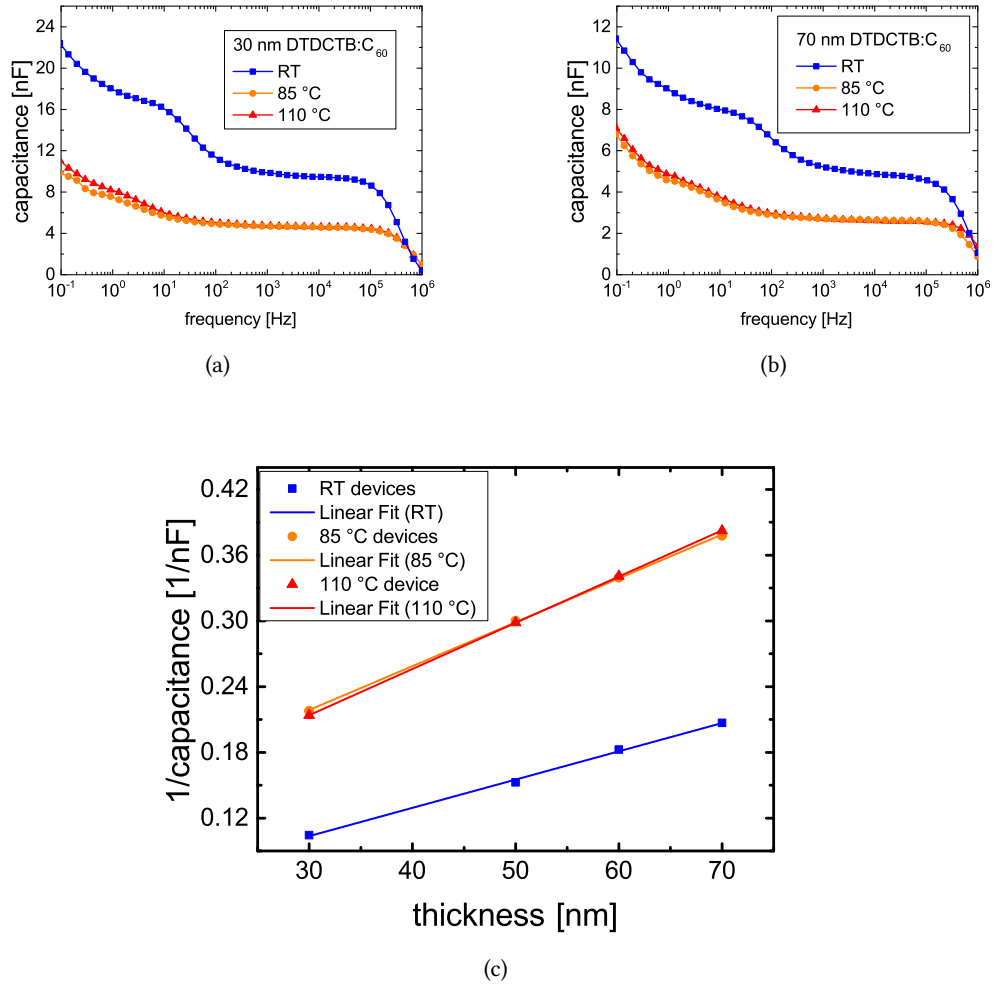


Figure A.6.: Cf spectra of solar cells with (a) 30 nm and (b) 70 nm thick blend layers from set 2 (with intrinsic BPAPF layer). (c) Inverse capacitances, obtained from the fitting of the Cf spectra with the equivalent circuit, as function of the blend layer thickness. The data points were fitted with a linear function.

A.1.5. sensitive EQE

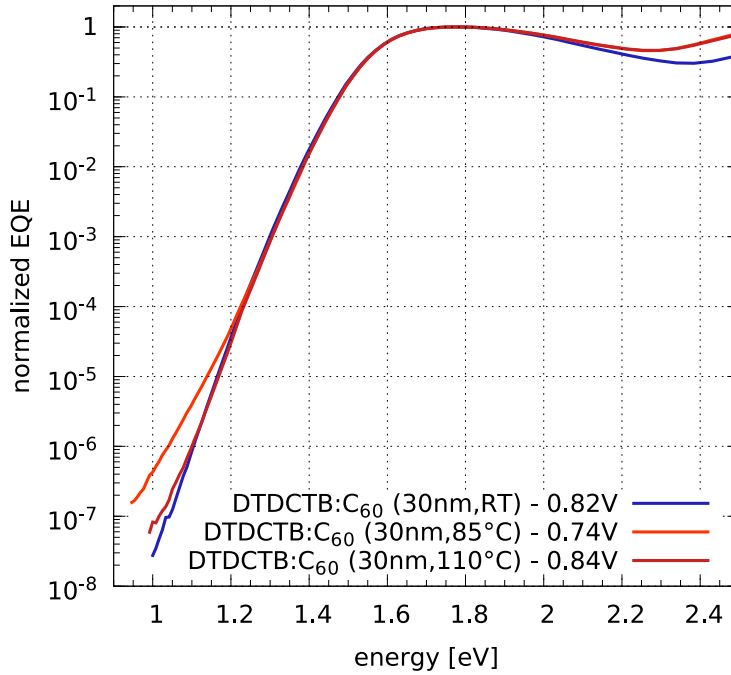


Figure A.7.: Sensitive EQE measurements on the 30 nm thick devices of set 1. The measurement and evaluation was performed by Johannes Benduhn (IAPP).

A.2. QM1

Determination of IP

Due to the nanowire formation of QM1 on C_{60} , a determination of the IP is not possible, since the signal of the underlying C_{60} hinders an evaluation of the QM1 signal. In order to determine the IP , we apply a method suggested by Widmer *et al.*[109] This method makes use of the linear temperature dependence of V_{oc} , which allows an extrapolation to 0 K and the determination of an effective gap. With the knowledge of the EA of the acceptor, the determination of the IP of the donor is possible. The measurement is performed with the 1:2 sample (BF-DPB as HTL) shown in Table 6.2. The measurement was performed by Anton Kirch and evaluated by Dr. Johannes Widmer (both IAPP). V_{oc} for 0 K is extrapolated to (0.95 ± 0.05) V. Under the assumption of an EA of C_{60} of (4.0 ± 0.3) eV, the IP of QM1 is (4.95 ± 0.35) eV.

IQE

Figure A.8 shows the EQE and absorption of various QM1:C₆₀ solar cells with different blend layer thicknesses. While the absorption of the solar cells in the NIR still increases with increasing blend layer thickness, the EQE saturates. For this reason, we conclude that j_{sc} is limited by recombination. Furthermore, a lower boundary for the internal quantum efficiency of 30-40% can be estimated, depending on the blend layer thickness.

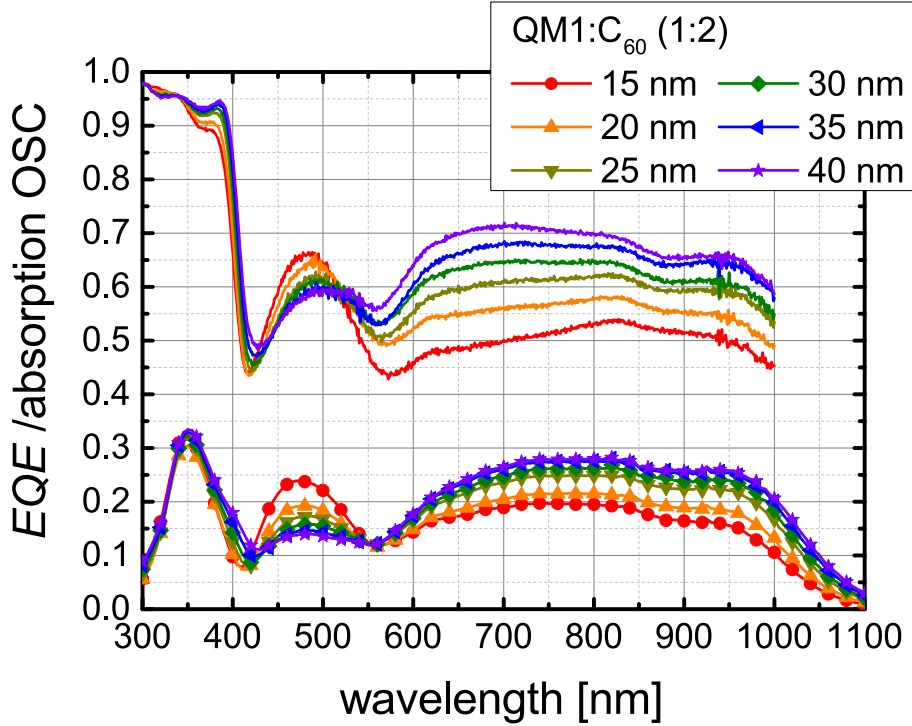


Figure A.8.: Absorption (lines) and EQE (lines with symbols) of QM1:C₆₀ solar cells with the following stack: ITO | n-Bis-HfI-NTCDI (5 nm, 7 wt% W₂(hpp)₄) | C₆₀ (15 nm) | QM1:C₆₀ (1:2, 30 nm, rate(QM1)=0.6 Å/s) | BF-DPB (5 nm) | p-BF-DPB (60 nm, 10 wt% F₆-TCNNQ) | F₆-TCNNQ (2 nm) | Al (100 nm).

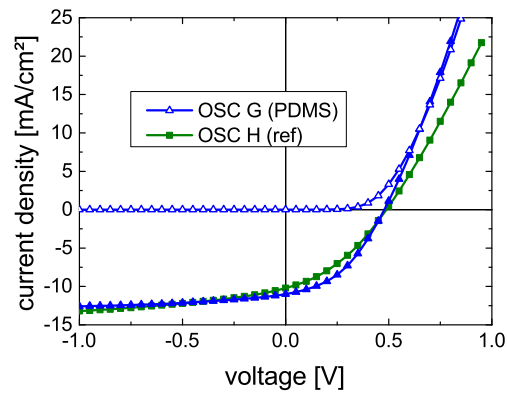
A.3. PDMS

Measurement series 2 was exposed to air before the deposition of the p-doped BF-DPB layer. The results are shown in Table A.3 and Figure A.9. With exception of device L with (1 day) there was a waiting time of 4-5 days in vacuum between the deposition of the intrinsic BF-DPB layer and the following p-BF-DPB layer.

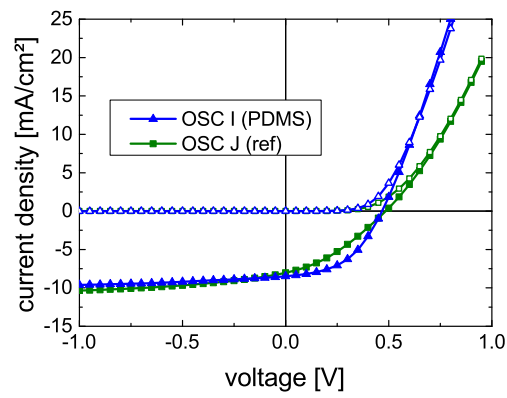
Table A.3.: Device parameters of measurement series 2.

OSC	bulk	j_{sc} [mA/cm ²]	V_{oc} [V]	FF [%]	η_{PCE} [%]
G	80 nm (PDMS)	11.3	0.48	42	2.3
H	80 nm ref	10.5	0.49	36	1.9
I	40 nm (PDMS)	8.8	0.47	47	1.9
J	40 nm ref	8.3	0.52	34	1.4
K	200 nm (PDMS)	8.8	0.43	42	1.6
L	200 nm ref	6.6	0.45	35	1.1

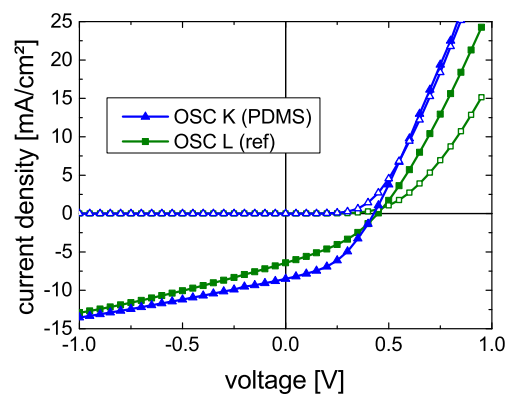
A. Appendix



(a)



(b)



(c)

Figure A.9.: jV measurements of OSCs G-L.

B. Lists

Table B.1.: Acronyms

acronym	meaning
AFM	atomic force microscopy
BHJ	bulk heterojunction
CS	charge separated state
CT	charge transfer
DCN	Dresden Center for Nanoanalytics
ED	electron diffraction
EQE	external quantum efficiency
ETL	electron transport layer
FET	field effect transistor
GC	gas chromatography
GIWAXS	grazing-incidence small-angle scattering
GIXRD	grazing incidence X-ray diffraction
HBEC	high binding energy cut-off
HTL	hole transport layer
HOMO	highest occupied molecular orbital
IAPP	Institute for Applied Photophysics
IPMS	(Fraunhofer) Institute for Photonic Microsystems
IQE	internal quantum efficiency
IR	infra red
IS	impedance spectroscopy

B. Lists

ISE	Institute for Solar Energy Systems
LDI-ToF-MS	Laser desorption/ionization time-of-flight mass spectrometer
LUMO	lowest unoccupied molecular orbital
MALDI-ToF-MS	Matrix assisted Laser desorption/ionization time-of-flight mass spectrometer
MM	mismatch
MPP	maximum power point
MS	mass spectrometry
MTC	material test chamber
NIR	near infra red
OPV	organic photovoltaics
OSC	organic solar cell
OTRACE	open circuit corrected charge carrier extraction
PHJ	planar heterojunction
QCM	quartz crystal microbalance
SEM	scanning electron microscope
TEM	transmission electron microscope
UHV	ultra high vacuum
UPS	ultraviolet photoelectron spectroscopy
UV	ultraviolet light
vis	visible light
XPS	X-ray photoelectron spectroscopy
XRR	X-ray reflectometry

Table B.2.: Materials

Al	aluminum
Au	gold
Bis-HfI-NTCDI	N,N-Bis(fluoren-2-yl)-naphthalenetetracarboxylic diimide
BF-DPB	N,N'-((Diphenyl-N,N'-bis)9,9,-dimethyl-fluoren-2-yl)-benzidine
BPAPF	9,9-bis[4-(N,N-bis-biphenyl-4-yl-amino)phenyl]-9H-fluorene
C ₆₀	Buckminster Fullerene C ₆₀
C ₆₀ F ₃₆	
C ₇₀	Buckminster Fullerene C ₇₀
C ₇₀ F ₅₆	
DTDCTB	2-[7-(5-N,N-ditolylaminothiophen-2-yl)-2,1,3-benzothiadiazol-4-yl]methylenemalononitrile
CNTF	(Z)-4-(1-cyano-2-(7-(5-(di-p-tolylamino)thiophen-2-yl)benzo-2,1,3-thiadiazol-4-yl)vinyl)-2,3,5,6-tetrafluorobenzonitrile
DCV ₂ -5T-Me(3, 3)	2,2'-((3'',4''-dimethyl-[2,2':5':2'':5'':2''':5''',2''''-quinquthiophene]-5,5''-diyl)bis(methanylylidene))dimalononitrile
DMSO	Dimethyl sulfoxide
F ₆ TCNNQ	2,2'-(perfluoronaphthalene-2,6-diylidene)dimalononitrile
F ₁₆ ZnPc	Zinc 1,2,3,4,8,9,10,11,15,16,17,18,22,23,24,25-hexadecafluoro-29H,31H-phthalocyanine
ITO	indium tin oxide
KBr	potassium bromide
MoO _x	molybdenum oxide
NaTFAc	sodium trifluoroacetate
NGX1	2-(dicyanomethylene)-5'-(1,3-dithiol-2-ylidene)-5,5'-dihydro-Delta2,2'-bithiophene
NMP	N-Methyl-2-pyrrolidone
NDP9	commerical p-dopand from Novaled

B. Lists

NTCDA	1,4,5,8-naphthalenetetacarboxylic dianhydride
PDMS	poly dimethyl siloxane
PRTF	(Z)-3-(7-(5-(di-p-tolylamino)thiophen-2-yl)benzo-2,1,3-thiadiazol-4-yl)-2-(perfluoropyridin-4-yl)acrylonitrile
Spiro-OMe-TAD	2,2',7,7'-Tetrakis[N,N-di(4-methoxyphenyl)amino]-9,9'-spirobifluorene
TFTF	(Z)-3-(7-(5-(di-p-tolylamino)thiophen-2-yl)benzo-2,1,3-thiadiazol-4-yl)-2-(2,3,5,6-tetrafluoro-4-(trifluoromethyl)phenyl)acrylonitrile
W ₂ (hpp) ₄	tetrakis(1,3,4,6,7,8-hexahydro-2H-pyrimido[1,2-a]pyrimidinato)ditungsten (II)
ZnPc	zinc phtalocyanine

Table B.3.: Symbols

a	material constant (Lennard Jones potential)
A, A^*	acceptor, excited acceptor
$A(\lambda)$	absorption
A'	voltage slope over time (OTRACE, see Fig.3.15)
AM	air mass
AM1.5G, AM1.5D	see section 2.3.1
b	material constant (Lennard Jones potential)
c	speed of light
C	capacitance
CT_x	charge transfer state
d	thickness
D, D^*	donor, excited donor
D_E	exciton diffusion length
EA	electron affinity
E	energy
E_B	binding energy
E_e	electron energy
E_F	Fermi energy
$E_{F,e}$	Quasi-Fermi level of the electrons
$E_{F,h}$	Quasi-Fermi level of the holes
E_{HOMO}	energy of the HOMO level
E_h	hole energy
E_{kin}	kinetic energy
E_{LUMO}	energy of the LUMO level
E_{sim}	illumination spectrum of the sun simulator
E_{sun}	AM1.5G spectrum

B. Lists

E_t	energy of the trap level
$\langle E_\infty \rangle$	equilibrium energy (Bässler model)
f	frequency
f_{CT}	measure for the number of charge transfer states
$f(E)$	distribution function
\vec{F}, F	electric field
FF	fill factor
h	Planck constant
\hbar	reduced Planck constant
i	initial site (Bässler model)
i	small current (impedance spectroscopy)
I_{ill}	illumination intensity
I	current
I_{sc}	short current
I_{MPP}	current at the maximum power point
I_{ph}	photocurrent
I_S	saturation current
IP	ionization potential
j	final site (Bässler model)
j	current density
j_0	dark saturation current density
j_{inj}	injection current density
j_{sc}	short circuit current density
j_{sc}^*	short circuit current density normalized to 100 mW/cm ²
J_{ov}	spectral overlap (Dexter/Förster transfer)
k	transfer rate
k	extinction coefficient
k_B	Boltzmann constant

K	constant (Dexter transfer)
K	shape factor (Scherrer equation)
l	length
l_0	thickness of the atmosphere
L	measure for the average orbital radius (Dexter transfer)
L_{abs}	characteristic absorption length
L_{D}	exciton diffusion length
L_{coh}	coherence length
m^*	reduced mass
n_e	electron density
n_p	hole density
n_{id}	diode ideality factor
n	refractive index
N_{C}	effective density of states of the conduction band
N_{V}	effective density of states of the valence band
OD	absorbance
$\overline{P_e}$	average electron polarization energy
$\overline{P_h}$	average hole polarization energy
P_{MPP}	maximum power
PCE	power conversion efficiency
q	charge
r	distance
$R(\lambda)$	reflectance
R_{RMS}	root-mean-square roughness
R_{ji}	distance between sites i and j
R_{p}	parallel resistance
R_{s}	series resistance
S_x	singlet state

B. Lists

S	Spin
Sat	saturation
SR	spectral response
t	time
t_{max}	time of maximum current density (OTRACE, see Fig. 3.15)
T_x	triplet state
T	temperature
T_A	absorber temperature
T_S	sun temperature
T_0	ambient temperature
T_{sub}	substrate temperature during the deposition
$T(\lambda)$	transmittance
v	small voltage (impedance spectroscopy)
V	voltage
V_{oc}	open circuit voltage
V_{rad}	maximum theoretical V_{oc} under the assumption that all charge carriers recombine radiatively
V_{MPP}	voltage at the maximum power point
V_0	open circuit voltage at 0 K
$V(r)$	potential
W	band width
W_{ij}	transition rate between the site i and j (Miller-Abrahams equation)
Z	impdance
α	angle
γ	overlap factor (Miller Abrahams equation)
δ^+	positive partial charge
δ^-	negative partial charge
$\Delta_{2\theta}$	Full width at half maximum

ΔV_{nonrad}	nonradiative voltage losses
ΔV_{rad}	radiative voltage losses
ϵ_0	vacuum permittivity
ϵ_r	relative permittivity
η_{PCE}	power conversion efficiency
η_{A}	probability of photon absorption
η_{ED}	probability that an exciton reaches a heterojunction
η_{CT}	probability that an exciton at the heterojunction is split into free charge carriers
η_{CC}	probability that a free charge carrier created at the heterojunction is collected at the electrode
η_{max}	thermodynamic maximum power conversion efficiency
θ_a	angle between molecules (Förster transfer)
λ	wavelength
λ_{reorg}	reorganization energy
μ	mobility or chemical potential
μ_e, μ_p	electron mobility, hole mobility
μ_0	mobility for a disorder free material
ν	average wave number (Förster transfer)
ν	frequency
ν_0	attempt hopping frequency
ξ_d^{A}	oscillator strength for acceptor transition
ξ_d^{D}	oscillator strength for donor transition
$\rho(E)$	density of states
σ	conductivity, diagonal disorder (Bässler model)
Σ	off diagonal disorder parameter (Bässler model)
τ	lifetime
Φ_{EL}	excess electroluminescence
Φ_{BB}	black body spectrum at ambient conditions

B. Lists

ω angular frequency

ω angle of incidence (GIXRD, XRR)

Bibliography

- [1] Heliatek GmbH press release (21.09.16), <http://www.heliatek.com/en/news/news/details/heliatek-raises-80-million-322>. Accessed on 04.11.16.
- [2] N. Espinosa, M. Hösel, D. Angmo, F. C. Krebs. Solar cells with one-day energy payback for the factories of the future. *Energy & Environmental Science*, 5(1), 2012, pp. 5117–5132. doi:10.1039/C1EE02728J
- [3] Heliatek GmbH press release (08.02.16), <http://www.heliatek.com/en/news/news/details/heliatek-sets-new-organic-photovoltaic-world-record-efficiency-of-13-2-228>. Accessed on 04.11.16.
- [4] H. R. Christen. Grundlagen der organischen Chemie. Aarau : Sauerländer; Frankfurt am Main: Diesterweg-Salle, 3rd edition, 1975
- [5] R. Steudel. Chemie der Nichtmetalle. Walter de Gruyter Berlin New York, 3rd edition, 2008
- [6] H. Suzuki. Electronic Absorption Spectra and Geometry of Organic Molecules. Academic Press New York London, 1967
- [7] P. G. Parejo, M. Zayat, D. Levy. Highly efficient UV-absorbing thin-film coatings for protection of organic materials against photodegradation. *Journal of Materials Chemistry*, 16(22), 2006, pp. 2165–2169. doi:10.1039/B601577H
- [8] M. Sun Ryu, H. Jin Cha, J. Jang. Improvement of operation lifetime for conjugated polymer:fullerene organic solar cells by introducing a UV absorbing film. *Solar Energy Materials and Solar Cells*, 94(2), 2010, pp. 152–156. doi:10.1016/j.solmat.2009.08.011
- [9] M. Schwoerer, H. C. Wolf. Organische Molekulare Festkörper. Weinheim: WILEY-VCH-Verlag, 2005
- [10] H. Haken, H. Wolf. Molekülphysik und Quantenchemie - Einführung in die experimentellen und theoretischen Grundlagen. Springer-Verlag Berlin, 5th edition, 2005
- [11] M. L. Tang, Z. Bao. Halogenated Materials as Organic Semiconductors. *Chemistry of Materials*, 23(3), 2011, pp. 446–455. doi:10.1021/cm102182x
- [12] D. Schlettwein, K. Hesse, N. E. Gruhn, P. A. Lee, K. W. Nebesny, N. R. Armstrong. Electronic Energy Levels in Individual Molecules, Thin Films, and Organic Heterojunctions of Substituted Phthalocyanines. *The Journal of Physical Chemistry B*, 105(21), 2001, pp. 4791–4800. doi:10.1021/jp001912q

Bibliography

- [13] R. Fitzner, E. Reinold, A. Mishra, E. Mena-Osteritz, H. Ziehlke, C. Körner, K. Leo, M. Riede, M. Weil, O. Tsaryova, A. Weiß, C. Urich, M. Pfeiffer, P. Bäuerle. Dicyanovinyl-Substituted Oligothiophenes: Structure-Property Relationships and Application in Vacuum-Processed Small Molecule Organic Solar Cells. *Advanced Functional Materials*, 21(5), 2011, pp. 897–910. doi:10.1002/adfm.201001639
- [14] Y.-H. Chen, L.-Y. Lin, C.-W. Lu, F. Lin, Z.-Y. Huang, H.-W. Lin, P.-H. Wang, Y.-H. Liu, K.-T. Wong, J. Wen, D. J. Miller, S. B. Darling. Vacuum-Deposited Small-Molecule Organic Solar Cells with High Power Conversion Efficiencies by Judicious Molecular Design and Device Optimization. *Journal of the American Chemical Society*, 134(33), 2012, pp. 13616–13623. doi:10.1021/ja301872s
- [15] C. K. Chan, E.-G. Kim, J.-L. Brédas, A. Kahn. Molecular n-Type Doping of 1,4,5,8-Naphthalene Tetracarboxylic Dianhydride by Pyronin B Studied Using Direct and Inverse Photoelectron Spectroscopies. *Advanced Functional Materials*, 16(6), 2006, pp. 831–837. doi:10.1002/adfm.200500402
- [16] C. Falkenberg. Optimizing Organic Solar Cells - Transparent Electron Transport Materials for Improving Device Performance. Ph.D. thesis, TU Dresden, 2011. <http://nbn-resolving.de/urn:nbn:de:bsz:14-qucosa-89214>
- [17] S.-H. Hwang, Y. K. Kim, Y. Kwak, C.-H. Lee, J. Lee, S. Kim. Improved performance of organic light-emitting diodes using advanced hole-transporting materials. *Synthetic Metals*, 159(23), 2009, pp. 2578–2583. doi:10.1016/j.synthmet.2009.09.015
- [18] C.-W. Ko, Y.-T. Tao. 9,9-Bis{4-[di-(p-biphenyl)aminophenyl]}fluorene: a high T_g and efficient hole-transporting material for electroluminescent devices. *Synthetic Metals*, 126(1), 2002, pp. 37–41. doi:10.1016/S0379-6779(01)00492-1
- [19] P. K. Koech, A. B. Padmaperuma, L. Wang, J. S. Swensen, E. Polikarpov, J. T. Darsell, J. E. Rainbolt, D. J. Gaspar. Synthesis and Application of 1,3,4,5,7,8-Hexafluorotetracyanonaphthoquinodimethane (F6-TNAP): A Conductivity Dopant for Organic Light-Emitting Devices. *Chemistry of Materials*, 22(13), 2010, pp. 3926–3932. doi:10.1021/cm1002737
- [20] N. Liu, Y. Morio, F. Okino, H. Touhara, O. V. Boltalina, V. K. Pavlovich. Electrochemical properties of C₆₀F₃₆. *Synthetic Metals*, 86(1), 1997, pp. 2289–2290. doi:10.1016/S0379-6779(97)81130-7
- [21] V. Malytskyi, J.-J. Simon, L. Patrone, J.-M. Raimundo. Thiophene-based push-pull chromophores for small molecule organic solar cells (SMOSCs). *RSC Advances*, 5(1), 2015, pp. 354–397. doi:10.1039/C4RA11664J
- [22] B. Milián, E. Ortí, V. Hernández, J. T. López Navarrete, T. Otsubo. Spectroscopic and theoretical study of push-pull chromophores containing thiophene-based quinonoid structures as electron spacers. *The Journal of Physical Chemistry B*, 107(44), 2003, pp. 12175–12183. doi:10.1021/jp0354651

- [23] M. C. R. Delgado, K. R. Pigg, D. A. da Silva Filho, N. E. Gruhn, Y. Sakamoto, T. Suzuki, R. M. Osuna, J. Casado, V. Hernández, J. T. L. Navarrete, N. G. Martinelli, J. Cornil, R. S. Sánchez-Carrera, V. Coropceanu, J.-L. Brédas. Impact of Perfluorination on the Charge-Transport Parameters of Oligoacene Crystals. *Journal of the American Chemical Society*, 131(4), 2009, pp. 1502–1512. doi:10.1021/ja807528w
- [24] R. Ruiz, D. Choudhary, B. Nickel, T. Toccoli, K.-C. Chang, A. C. Mayer, P. Clancy, J. M. Blakely, R. L. Headrick, S. Iannotta, G. G. Malliaras. Pentacene Thin Film Growth. *Chemistry of Materials*, 16(23), 2004, pp. 4497–4508. doi:10.1021/cm049563q
- [25] F. Würthner, T. E. Kaiser, C. R. Saha-Möller. J-Aggregate: von ihrer zufälligen Entdeckung bis zum gezielten supramolekularen Aufbau funktioneller Farbstoffmaterialien. *Angewandte Chemie*, 123(15), 2011, pp. 3436–3473. doi:10.1002/ange.201002307
- [26] A. Eisfeld, J. Briggs. The J- and H-bands of organic dye aggregates. *Chemical Physics*, 324(2), 2006, pp. 376–384. doi:10.1016/j.chemphys.2005.11.015
- [27] M. Kasha. Energy transfer mechanisms and the molecular exciton model for molecular aggregates. *Radiation Research*, 20(1), 1963, pp. 55–70. doi:10.2307/3571331
- [28] G. Lanzani. The Photophysics behind Photovoltaics and Photonics. Wiley-VCH Verlag GmbH & Co. KGaA., 1st edition, 2012
- [29] L. Huang, M. Stolte, H. Bürckstümmer, F. Würthner. High-Performance Organic Thin-Film Transistor Based on a Dipolar Organic Semiconductor. *Advanced Materials*, 24(42), 2012, pp. 5750–5754. doi:10.1002/adma.201202441
- [30] A. Patra, C. G. Chandaluri, T. Radhakrishnan. Optical materials based on molecular nanoparticles. *Nanoscale*, 4(2), 2012, pp. 343–359. doi:10.1039/C1NR11313E
- [31] Q. Fang, F. Wang, H. Zhao, X. Liu, R. Tu, D. Wang, Z. Zhang. Strongly coupled excitonic states in H-aggregated single crystalline nanoparticles of 2,5-bis(4-methoxybenzylidene) cyclopentanone. *The Journal of Physical Chemistry B*, 112(10), 2008, pp. 2837–2841. doi:10.1021/jp710262q
- [32] C. Schünemann, D. Wynands, K.-J. Eichhorn, M. Stamm, K. Leo, M. Riede. Evaluation and Control of the Orientation of Small Molecules for Strongly Absorbing Organic Thin Films. *The Journal of Physical Chemistry C*, 117(22), 2013, pp. 11600–11609. doi:10.1021/jp400604j
- [33] A. A. Günther, J. Widmer, D. Kasemann, K. Leo. Hole mobility in thermally evaporated pentacene: Morphological and directional dependence. *Applied Physics Letters*, 106(23), 2015, pp. –. doi:10.1063/1.4922422
- [34] M. Vogel, J. Strotmann, B. Johnev, M. C. Lux-Steiner, K. Fostiropoulos. Influence of nanoscale morphology in small molecule organic solar cells. *Thin Solid Films*, 511–512, 2006, pp. 367–370. doi:10.1016/j.tsf.2005.12.030

Bibliography

- [35] C. Koerner, C. Elschner, N. C. Miller, R. Fitzner, F. Selzer, E. Reinold, P. Bäuerle, M. F. Toney, M. D. McGehee, K. Leo, M. K. Riede. Probing the effect of substrate heating during deposition of DCV4T:C60 blend layers for organic solar cells. *Organic Electronics*, 13(4), 2012, pp. 623–631. doi:10.1016/j.orgel.2011.12.017
- [36] J. Simon, J.-J. André. *Molecular Semiconductors - Photoelectrical Properties and Solar Cells*. Springer Berlin Heidelberg, 1985
- [37] S. M. Sze. *Physics of Semiconductor Devices 2nd Edition*. New York: Wiley, 1981
- [38] A. W. Hains, Z. Liang, M. A. Woodhouse, B. A. Gregg. Molecular Semiconductors in Organic Photovoltaic Cells. *Chemical Reviews*, 110(11), 2010, pp. 6689–6735. doi:10.1021/cr9002984
- [39] I. Hill, A. Kahn, Z. Soos, R. Pascal, Jr. Charge-separation energy in films of π -conjugated organic molecules. *Chemical Physics Letters*, 327(3–4), 2000, pp. 181 – 188. doi:10.1016/S0009-2614(00)00882-4
- [40] P. Peumans, A. Yakimov, S. R. Forrest. Small molecular weight organic thin-film photodetectors and solar cells. *Journal of Applied Physics*, 93(7), 2003, pp. 3693–3723. doi:10.1063/1.1534621
- [41] H. Bäessler. Charge Transport in Disordered Organic Photoconductors a Monte Carlo Simulation Study. *physica status solidi (b)*, 175(1), 1993, pp. 15–56. doi:10.1002/pssb.2221750102
- [42] N. Tessler, Y. Preezant, N. Rappaport, Y. Roichman. Charge Transport in Disordered Organic Materials and Its Relevance to Thin-Film Devices: A Tutorial Review. *Advanced Materials*, 21(27), 2009, pp. 2741–2761. doi:10.1002/adma.200803541
- [43] V. Coropceanu, J. Cornil, D. A. da Silva Filho, Y. Olivier, R. Silbey, J.-L. Brédas. Charge Transport in Organic Semiconductors. *Chemical Reviews*, 107(4), 2007, pp. 926–952. doi:10.1021/cr050140x
- [44] J. Y. Lee, S. Roth, Y. W. Park. Anisotropic field effect mobility in single crystal pentacene. *Applied Physics Letters*, 88(25), 2006, pp. -. doi:10.1063/1.2216400
- [45] C. Reese, Z. Bao. High-Resolution Measurement of the Anisotropy of Charge Transport in Single Crystals. *Advanced Materials*, 19(24), 2007, pp. 4535–4538. doi:10.1002/adma.200701139
- [46] M. Schrader, R. Fitzner, M. Hein, C. Elschner, B. Baumeier, K. Leo, M. Riede, P. Bäuerle, D. Andrienko. Comparative Study of Microscopic Charge Dynamics in Crystalline Acceptor-Substituted Oligothiophenes. *Journal of the American Chemical Society*, 134(13), 2012, pp. 6052–6056. doi:10.1021/ja300851q
- [47] Y. C. Cheng, R. J. Silbey, D. A. da Silva Filho, J. P. Calbert, J. Cornil, J. L. Brédas. Three-dimensional band structure and bandlike mobility in oligoacene single crystals: A

- theoretical investigation. *The Journal of Chemical Physics*, 118(8), 2003, pp. 3764–3774. doi:10.1063/1.1539090
- [48] T. Oyamada, H. Sasabe, C. Adachi, S. Murase, T. Tominaga, C. Maeda. Extremely low-voltage driving of organic light-emitting diodes with a Cs-doped phenyldipyrenylphosphine oxide layer as an electron-injection layer. *Applied Physics Letters*, 86(3), 2005, pp. –. doi:10.1063/1.1852707
- [49] M. Kröger, S. Hamwi, J. Meyer, T. Riedl, W. Kowalsky, A. Kahn. P-type doping of organic wide band gap materials by transition metal oxides: A case-study on Molybdenum trioxide. *Organic Electronics*, 10(5), 2009, pp. 932–938. doi:10.1016/j.orgel.2009.05.007
- [50] R. Meerheim, S. Olthof, M. Hermenau, S. Scholz, A. Petrich, N. Tessler, O. Solomeshch, B. Lüssem, M. Riede, K. Leo. Investigation of C₆₀F₃₆ as low-volatility p-dopant in organic optoelectronic devices. *Journal of Applied Physics*, 109(10), 2011, pp. –. doi:10.1063/1.3590142
- [51] K. Walzer, B. Maennig, M. Pfeiffer, K. Leo. Highly Efficient Organic Devices Based on Electrically Doped Transport Layers. *Chemical Reviews*, 107(4), 2007, pp. 1233–1271. doi:10.1021/cr050156n
- [52] I. Salzmann, G. Heimel. Toward a comprehensive understanding of molecular doping organic semiconductors (review). *Journal of Electron Spectroscopy and Related Phenomena*, 204, Part A, 2015, pp. 208–222. doi:10.1016/j.elspec.2015.05.001
- [53] S. Olthof, S. Mehraeen, S. K. Mohapatra, S. Barlow, V. Coropceanu, J.-L. Brédas, S. R. Marder, A. Kahn. Ultralow Doping in Organic Semiconductors: Evidence of Trap Filling. *Physical Review Letters*, 109, 2012, p. 176601. doi:10.1103/PhysRevLett.109.176601
- [54] P. Würfel. Physik der Solarzellen. Spektrum Akademischer Verlag Heidelberg Berlin, 2nd edition, 2000
- [55] B. P. Rand, D. P. Burk, S. R. Forrest. Offset energies at organic semiconductor heterojunctions and their influence on the open-circuit voltage of thin-film solar cells. *Physical Review B*, 75, 2007, p. 115327. doi:10.1103/PhysRevB.75.115327
- [56] C. W. Schlenker, M. E. Thompson. The molecular nature of photovoltage losses in organic solar cells. *Chemical Communications*, 47(13), 2011, pp. 3702–3716. doi:10.1039/C0CC04020G
- [57] B. Maennig, J. Drechsel, D. Gebeyehu, P. Simon, F. Kozłowski, A. Werner, F. Li, S. Grundmann, S. Sonntag, M. Koch, K. Leo, M. Pfeiffer, H. Hoppe, D. Meissner, N. Sariciftci, I. Riedel, V. Dyakonov, J. Parisi. Organic p-i-n solar cells. *Applied Physics A*, 79(1), 2004, pp. 1–14. doi:10.1007/s00339-003-2494-9

Bibliography

- [58] K. Vandewal, K. Tvingstedt, A. Gadisa, O. Inganas, J. V. Manca. On the origin of the open-circuit voltage of polymer-fullerene solar cells. *Nature Materials*, 8(11), 2009, pp. 904–909. doi:10.1038/nmat2548
- [59] C. M. Proctor, M. Kuik, T.-Q. Nguyen. Charge carrier recombination in organic solar cells. *Progress in Polymer Science*, 38(12), 2013, pp. 1941–1960. doi:10.1016/j.progpolymsci.2013.08.008
- [60] NREL. Reference Solar Spectral Irradiance: ASTM G-173. [Http://rredc.nrel.gov/solar/spectra/am1.5/ASTMG173/ASTMG173.html](http://rredc.nrel.gov/solar/spectra/am1.5/ASTMG173/ASTMG173.html), accessed on 26.11.15
- [61] W. Shockley, H. J. Queisser. Detailed Balance Limit of Efficiency of p-n Junction Solar Cells. *Journal of Applied Physics*, 32(3), 1961, pp. 510–519. doi:10.1063/1.1736034
- [62] P. I. Djurovich, E. I. Mayo, S. R. Forrest, M. E. Thompson. Measurement of the lowest unoccupied molecular orbital energies of molecular organic semiconductors. *Organic Electronics*, 10(3), 2009, pp. 515–520. doi:10.1016/j.orgel.2008.12.011
- [63] T. Kirchartz, T. Agostinelli, M. Campoy-Quiles, W. Gong, J. Nelson. Understanding the thickness-dependent performance of organic bulk heterojunction solar cells: the influence of mobility, lifetime, and space charge. *The Journal of Physical Chemistry Letters*, 3(23), 2012, pp. 3470–3475. doi:10.1021/jz301639y
- [64] W. Tress, K. Leo, M. Riede. Influence of Hole-Transport Layers and Donor Materials on Open-Circuit Voltage and Shape of I–V Curves of Organic Solar Cells. *Advanced Functional Materials*, 21(11), 2011, pp. 2140–2149. doi:10.1002/adfm.201002669
- [65] W. Tress, A. Merten, M. Furno, M. Hein, K. Leo, M. Riede. Correlation of Absorption Profile and Fill Factor in Organic Solar Cells: The Role of Mobility Imbalance. *Advanced Energy Materials*, 3(5), 2013, pp. 631–638. doi:10.1002/aenm.201200835
- [66] W. Tress, K. Leo, M. Riede. Photoconductivity as loss mechanism in organic solar cells. *physica status solidi (RRL) – Rapid Research Letters*, 7(6), 2013, pp. 401–405. doi:10.1002/pssr.201307039
- [67] K. Vandewal, S. Albrecht, E. T. Hoke, K. R. Graham, J. Widmer, J. D. Douglas, M. Schubert, W. R. Mateker, J. T. Bloking, G. F. Burkhard, A. Sellinger, J. M. J. Fréchet, A. Amassian, M. K. Riede, M. D. McGehee, D. Neher, A. Salleo. Efficient charge generation by relaxed charge-transfer states at organic interfaces. *Nature Materials*, 13(1), 2014, pp. 63–68. doi:10.1038/nmat3807
- [68] S. H. Park, A. Roy, S. Beaupre, S. Cho, N. Coates, J. S. Moon, D. Moses, M. Leclerc, K. Lee, A. J. Heeger. Bulk heterojunction solar cells with internal quantum efficiency approaching 100%. *Nature Photonics*, 3(5), 2009, pp. 297–302. doi:10.1038/nphoton.2009.69

- [69] R. Schueppel, C. Uhrich, M. Pfeiffer, K. Leo, E. Brier, E. Reinold, P. Baeuerle. Enhanced Photogeneration of Triplet Excitons in an Oligothiophene-Fullerene Blend. *ChemPhysChem*, 8(10), 2007, pp. 1497–1503. doi:10.1002/cphc.200700306
- [70] D. Veldman, S. C. J. Meskers, R. A. J. Janssen. The Energy of Charge-Transfer States in Electron Donor-Acceptor Blends: Insight into the Energy Losses in Organic Solar Cells. *Advanced Functional Materials*, 19(12), 2009, pp. 1939–1948. doi:10.1002/adfm.200900090
- [71] U. Rau. Reciprocity relation between photovoltaic quantum efficiency and electroluminescent emission of solar cells. *Physical Review B*, 76, 2007, p. 085303. doi:10.1103/PhysRevB.76.085303
- [72] K. Vandewal, K. Tvingstedt, A. Gadisa, O. Inganäs, J. V. Manca. Relating the open-circuit voltage to interface molecular properties of donor:acceptor bulk heterojunction solar cells. *Physical Review B*, 81, 2010, p. 125204. doi:10.1103/PhysRevB.81.125204
- [73] C. W. Tang. Two-layer organic photovoltaic cell. *Applied Physics Letters*, 48(2), 1986, pp. 183–185. doi:10.1063/1.96937
- [74] M. Hiramoto, H. Fujiwara, M. Yokoyama. Three-layered organic solar cell with a photoactive interlayer of codeposited pigments. *Applied Physics Letters*, 58(10), 1991, pp. 1062–1064. doi:10.1063/1.104423
- [75] J. Meiss, M. Hummert, H. Ziehlke, K. Leo, M. Riede. Organic solar cells with very high fill factor and voltage using tetrapropyl-tetraphenyl-diindenoperylene as green donor. *physica status solidi (RRL) – Rapid Research Letters*, 4(11), 2010, pp. 329–331. doi:10.1002/pssr.201004310
- [76] A. Opitz, J. Wagner, W. Brütting, I. Salzmann, N. Koch, J. Manara, J. Pflaum, A. Hinderhofer, F. Schreiber. Charge Separation at Molecular Donor-Acceptor Interfaces: Correlation Between Morphology and Solar Cell Performance. *Selected Topics in Quantum Electronics, IEEE Journal of*, 16(6), 2010, pp. 1707–1717. doi:10.1109/JSTQE.2010.2048096
- [77] D. Wynands, M. Levichkova, K. Leo, C. Uhrich, G. Schwartz, D. Hildebrandt, M. Pfeiffer, M. Riede. Increase in internal quantum efficiency in small molecular oligothiophene: C60 mixed heterojunction solar cells by substrate heating. *Applied Physics Letters*, 97(7), 2010, p. 3503. doi:10.1063/1.3475766
- [78] F. Yang, S. R. Forrest. Photocurrent Generation in Nanostructured Organic Solar Cells. *ACS Nano*, 2(5), 2008, pp. 1022–1032. doi:10.1021/nn700447t
- [79] M. M. Hawkeye, M. J. Brett. Glancing angle deposition: Fabrication, properties, and applications of micro- and nanostructured thin films. *Journal of Vacuum Science & Technology A*, 25(5), 2007, pp. 1317–1335. doi:10.1116/1.2764082

Bibliography

- [80] J. G. Van Dijken, M. D. Fleischauer, M. J. Brett. Controlled nanostructuring of CuPc thin films via glancing angle deposition for idealized organic photovoltaic architectures. *Journal of Materials Chemistry*, 21, 2011, pp. 1013–1019. doi:10.1039/C0JM03026K
- [81] E. Siebert-Henze, V. G. Lyssenko, J. Fischer, M. Tietze, R. Brueckner, T. Menke, K. Leo, M. Riede. Electroabsorption studies of organic p-i-n solar cells: Increase of the built-in voltage by higher doping concentration in the hole transport layer. *Organic Electronics*, 15(2), 2014, pp. 563–568. doi:10.1016/j.orgel.2013.12.009
- [82] E. Siebert-Henze, V. G. Lyssenko, J. Fischer, M. Tietze, R. Brueckner, M. Schwarze, K. Vandewal, D. Ray, M. Riede, K. Leo. Built-in voltage of organic bulk heterojunction p-i-n solar cells measured by electroabsorption spectroscopy. *AIP Advances*, 4(4), 2014. doi:10.1063/1.4873597
- [83] D. Nanova, M. Scherer, F. Schell, J. Zimmermann, T. Glaser, A. K. Kast, C. Krekeler, A. Pucci, W. Kowalsky, R. R. Schröder, R. Lovrinčić. Why Inverted Small Molecule Solar Cells Outperform Their Noninverted Counterparts. *Advanced Functional Materials*, 25(41), 2015, pp. 6511–6518. doi:10.1002/adfm.201502943
- [84] T. Menke. Molecular Doping of Organic Semiconductors - A Conductivity and Seebeck study. Ph.D. thesis, TU Dresden, 2013. <http://nbn-resolving.de/urn:nbn:de:bsz:14-qucosa-121305>
- [85] W. Zhao, A. Kahn. Charge transfer at n-doped organic-organic heterojunctions. *Journal of Applied Physics*, 105(12), 2009. doi:10.1063/1.3153962
- [86] W. Gao, A. Kahn. Controlled *p*-doping of zinc phthalocyanine by coevaporation with tetrafluorotetracyanoquinodimethane: A direct and inverse photoemission study. *Applied Physics Letters*, 79(24), 2001, pp. 4040–4042. doi:10.1063/1.1424067
- [87] Y.-L. Tung, S.-W. Lee, Y. Chi, Y.-T. Tao, C.-H. Chien, Y.-M. Cheng, P.-T. Chou, S.-M. Peng, C.-S. Liu. Organic light-emitting diodes based on charge-neutral Os(ii) emitters: generation of saturated red emission with very high external quantum efficiency. *Journal of Materials Chemistry*, 15(4), 2005, pp. 460–464. doi:10.1039/B414636K
- [88] P. Schulz, E. Edri, S. Kirmayer, G. Hodes, D. Cahen, A. Kahn. Interface energetics in organo-metal halide perovskite-based photovoltaic cells. *Energy & Environmental Science*, 7(4), 2014, pp. 1377–1381. doi:10.1039/C4EE00168K
- [89] T. Menke, D. Ray, J. Meiss, K. Leo, M. Riede. In-situ conductivity and Seebeck measurements of highly efficient n-dopants in fullerene C60. *Applied Physics Letters*, 100(9), 2012. doi:<http://dx.doi.org/10.1063/1.3689778>
- [90] C. Körner. Oligothiophene Materials for Organic Solar Cells - Photophysics and Device Properties. Ph.D. thesis, TU Dresden, 2012. <http://nbn-resolving.de/urn:nbn:de:bsz:14-qucosa-121509>

- [91] D. Wynands. Strategies for Optimizing Organic Solar Cells: Correlation Between Morphology and Performance in DCV6T-C60 Heterojunctions. Ph.D. thesis, TU Dresden, 2010. <http://nbn-resolving.de/urn:nbn:de:bsz:14-qucosa-65084>
- [92] C. Schünemann. Organic Small Molecules: Correlation between Molecular Structure, Thin Film Growth, and Solar Cell Performance. Ph.D. thesis, TU Dresden, 2012
- [93] C. Elschner. Structural Investigations of Disordered Organic Thin Films. Ph.D. thesis, TU Dresden, 2013. (Image of the temperature distribution of on a heated substrate in Fig. 3.11)
- [94] M. Kozlik, S. Paulke, M. Gruenewald, R. Forker, T. Fritz. Determination of the optical constants of α - and β -zinc (II)-phthalocyanine films. *Organic Electronics*, 13(12), 2012, pp. 3291 – 3295. doi:10.1016/j.orgel.2012.09.030
- [95] R. Meerheim, C. Körner, K. Leo. Highly efficient organic multi-junction solar cells with a thiophene based donor material. *Applied Physics Letters*, 105(6), 2014. doi:10.1063/1.4893012
- [96] P. Freitag. White Top-Emitting OLEDs on Metal Substrates. Ph.D. thesis, TU Dresden, 2010. <http://nbn-resolving.de/urn:nbn:de:bsz:14-qucosa-70756>
- [97] G. Sauerbrey. Verwendung von Schwingquarzen zur Wägung dünner Schichten und zur Mikrowägung. *Zeitschrift für Physik*, 155(2), 1959, pp. 206–222. doi:10.1007/BF01337937
- [98] M. W. Nielen. Maldi time-of-flight mass spectrometry of synthetic polymers. *Mass Spectrometry Reviews*, 18(5), 1999, pp. 309–344. doi:10.1002/(SICI)1098-2787(1999)18:5<309::AID-MAS2>3.0.CO;2-L
- [99] M. Mann, R. C. Hendrickson, A. Pandey. Analysis of Proteins and Proteomes by Mass Spectrometry. *Annual Review of Biochemistry*, 70(1), 2001, pp. 437–473. doi:10.1146/annurev.biochem.70.1.437
- [100] M. Möbus, N. Karl. The growth of organic thin films on silicon substrates studied by X-ray reflectometry. *Thin Solid Films*, 215(2), 1992, pp. 213–217. doi:10.1016/0040-6090(92)90440-M
- [101] H. Kiessig. Untersuchungen zur Totalreflexion von Röntgenstrahlen. *Annalen der Physik*, 402(6), 1931, pp. 715–768. doi:10.1002/andp.19314020607
- [102] C. Elschner, A. A. Levin, L. Wilde, J. Grenzer, C. Schroer, K. Leo, M. Riede. Determining the C60 molecular arrangement in thin films by means of X-ray diffraction. *Journal of Applied Crystallography*, 44(5), 2011, pp. 983–990. doi:10.1107/S002188981103531X
- [103] J. Rivnay, R. Noriega, R. J. Kline, A. Salleo, M. F. Toney. Quantitative analysis of lattice disorder and crystallite size in organic semiconductor thin films. *Physical Review B*, 84(4), 2011, p. 045203. doi:10.1103/PhysRevB.84.045203

Bibliography

- [104] F. Roth, A. König, J. Fink, B. Büchner, M. Knupfer. Electron energy-loss spectroscopy: A versatile tool for the investigations of plasmonic excitations. *Journal of electron spectroscopy and related phenomena*, 195, 2014, pp. 85–95. doi:10.1016/j.elspec.2014.05.007
- [105] L. J. A. Koster, V. D. Mihailetschi, H. Xie, P. W. M. Blom. Origin of the light intensity dependence of the short-circuit current of polymer/fullerene solar cells. *Applied Physics Letters*, 87(20), 2005. doi:10.1063/1.2130396
- [106] A. K. K. Kyaw, D. H. Wang, V. Gupta, W. L. Leong, L. Ke, G. C. Bazan, A. J. Heeger. Intensity Dependence of Current–Voltage Characteristics and Recombination in High-Efficiency Solution-Processed Small-Molecule Solar Cells. *ACS Nano*, 7(5), 2013, pp. 4569–4577. doi:10.1021/nn401267s
- [107] L. Fang, F. Holzmueller, T. Matulaitis, A. Baasner, C. Hauenstein, J. Benduhn, M. Schwarze, A. Petrich, F. Piersimoni, R. Scholz, O. Zeika, C. Koerner, D. Neher, K. Vandewal, K. Leo. Thermally Stable Fluorine-Containing Low-Energy- Gap Organic Dyes with Low Voltage Losses for Organic Solar Cells. *Synthetic Metals*, 2016. doi:10.1016/j.synthmet.2016.10.025
- [108] V. Shrotriya, G. Li, Y. Yao, T. Moriarty, K. Emery, Y. Yang. Accurate Measurement and Characterization of Organic Solar Cells. *Advanced Functional Materials*, 16(15), 2006, pp. 2016–2023. doi:10.1002/adfm.200600489
- [109] J. Widmer, M. Tietze, K. Leo, M. Riede. Open-Circuit Voltage and Effective Gap of Organic Solar Cells. *Advanced Functional Materials*, 23(46), 2013, pp. 5814–5821. doi:10.1002/adfm.201301048
- [110] T. Kirchartz, W. Gong, S. A. Hawks, T. Agostinelli, R. C. MacKenzie, Y. Yang, J. Nelson. Sensitivity of the Mott–Schottky analysis in organic solar cells. *The Journal of Physical Chemistry C*, 116(14), 2012, pp. 7672–7680. doi:10.1021/jp300397f
- [111] T. Walter, R. Herberholz, C. Müller, H. Schock. Determination of defect distributions from admittance measurements and application to Cu (In, Ga) Se₂ based heterojunctions. *Journal of Applied Physics*, 80(8), 1996, pp. 4411–4420. doi:10.1063/1.363401
- [112] S. Khelifi, K. Decock, J. Lauwaert, H. Vrielinck, D. Spoltore, F. Piersimoni, J. Manca, A. Belghachi, M. Burgelman. Investigation of defects by admittance spectroscopy measurements in poly (3-hexylthiophene):(6, 6)-phenyl C₆₁-butyric acid methyl ester organic solar cells degraded under air exposure. *Journal of Applied Physics*, 110(9), 2011, p. 094509. doi:10.1063/1.3658023
- [113] A. Baumann, J. Lorrmann, D. Rauh, C. Deibel, V. Dyakonov. A New Approach for Probing the Mobility and Lifetime of Photogenerated Charge Carriers in Organic Solar Cells Under Real Operating Conditions. *Advanced Materials*, 24(32), 2012, pp. 4381–4386. doi:10.1002/adma.201200874

- [114] J. Lorrmann, B. H. Badada, O. Inganäs, V. Dyakonov, C. Deibel. Charge carrier extraction by linearly increasing voltage: Analytic framework and ambipolar transients. *Journal of Applied Physics*, 108(11), 2010, 113705. doi:10.1063/1.3516392
- [115] A. Foertig, J. Kniepert, M. Gluecker, T. Brenner, V. Dyakonov, D. Neher, C. Deibel. Nongeminate and geminate recombination in PTB7: PCBM solar cells. *Advanced Functional Materials*, 24(9), 2014, pp. 1306–1311. doi:10.1002/adfm.201302134
- [116] M. Wolf, H. Rauschenbach. Series resistance effects on solar cell measurements. *Advanced Energy Conversion*, 3(2), 1963, pp. 455–479. doi:10.1016/0365-1789(63)90063-8
- [117] K. Tvingstedt, C. Deibel. Temperature Dependence of Ideality Factors in Organic Solar Cells and the Relation to Radiative Efficiency. *Advanced Energy Materials*, 6(9), 2016. doi:10.1002/aenm.201502230
- [118] L.-Y. Lin, Y.-H. Chen, Z.-Y. Huang, H.-W. Lin, S.-H. Chou, F. Lin, C.-W. Chen, Y.-H. Liu, K.-T. Wong. A low-energy-gap organic dye for high-performance small-molecule organic solar cells. *Journal of the American Chemical Society*, 133(40), 2011, pp. 15822–15825. doi:10.1021/ja205126t
- [119] X. Che, X. Xiao, J. D. Zimmerman, D. Fan, S. R. Forrest. High-Efficiency, Vacuum-Deposited, Small-Molecule Organic Tandem and Triple-Junction Photovoltaic Cells. *Advanced Energy Materials*, 4(18), 2014. doi:10.1002/aenm.201400568
- [120] O. L. Griffith, X. Liu, J. A. Amonoo, P. I. Djurovich, M. E. Thompson, P. F. Green, S. R. Forrest. Charge transport and exciton dissociation in organic solar cells consisting of dipolar donors mixed with C₇₀. *Physical Review B*, 92(8), 2015, p. 085404. doi:10.1103/PhysRevB.92.085404
- [121] J. Otto. Optimierung und Charakterisierung organischer Solarzellen auf Basis von DTDCTB Heteroübergängen, 2013. Master's thesis, TU Dresden
- [122] M. Lenes, L. Koster, V. Mihailetschi, P. Blom. Thickness dependence of the efficiency of polymer:fullerene bulk heterojunction solar cells. *Applied Physics Letters*, 88(24), 2006, pp. 243502–243502. doi:10.1063/1.2211189
- [123] S. Nunomura, X. Che, S. R. Forrest. Charge Trapping in Mixed Organic Donor–Acceptor Semiconductor Thin Films. *Advanced Materials*, 26(45), 2014, pp. 7555–7560. doi:10.1002/adma.201403198
- [124] D. Cheyins, M. Kim, B. Verreet, B. P. Rand. Accurate spectral response measurements of a complementary absorbing organic tandem cell with fill factor exceeding the subcells. *Applied Physics Letters*, 104(9), 2014, p. 093302. doi:10.1063/1.4867261
- [125] Y. Park, V. Choong, Y. Gao, B. R. Hsieh, C. W. Tang. Work function of indium tin oxide transparent conductor measured by photoelectron spectroscopy. *Applied Physics Letters*, 68(19), 1996, pp. 2699–2701. doi:10.1063/1.116313

Bibliography

- [126] K. Sugiyama, H. Ishii, Y. Ouchi, K. Seki. Dependence of indium–tin–oxide work function on surface cleaning method as studied by ultraviolet and x-ray photoemission spectroscopies. *Journal of Applied Physics*, 87(1), 2000, pp. 295–298. doi:10.1063/1.371859
- [127] X. Jiang, F. Wong, M. Fung, S. Lee. Aluminum-doped zinc oxide films as transparent conductive electrode for organic light-emitting devices. *Applied Physics Letters*, 83(9), 2003, pp. 1875–1877. doi:10.1063/1.1605805
- [128] L. Spada, Q. Gou, M. Vallejo-López, A. Lesarri, E. J. Cocinero, W. Caminati. Weak C–H···N and C–H···F hydrogen bonds and internal rotation in pyridine–CH₃F. *Physical Chemistry Chemical Physics*, 16(5), 2014, pp. 2149–2153. doi:10.1039/C3CP54430C
- [129] E. Kryachko, S. Scheiner. CH···F Hydrogen Bonds. Dimers of Fluoromethanes. *The Journal of Physical Chemistry A*, 108(13), 2004, pp. 2527–2535. doi:10.1021/jp0365108
- [130] S. Kraner, J. Widmer, J. Benduhn, E. Hieckmann, T. Jägeler-Hoheisel, S. Ullbrich, D. Schütze, K. S. Radke, G. Cuniberti, F. Ortman, M. Lorenz-Rothe, R. Meerheim, D. Spoltore, K. Vandewal, C. Koerner, K. Leo. Influence of side groups on the performance of infrared absorbing aza-BODIPY organic solar cells. *physica status solidi (a)*, 212(12), 2015, pp. 2747–2753. doi:10.1002/pssa.201532385
- [131] C. Hauenstein. Charakterisierung und Optimierung von Donator-Akzeptor-Absorbermolekülen in organischen Solarzellen, 2015. Bachelor thesis, TU Dresden
- [132] M. L. Tietze, W. Tress, S. Pfützner, C. Schünemann, L. Burtone, M. Riede, K. Leo, K. Vandewal, S. Olthof, P. Schulz, A. Kahn. Correlation of open-circuit voltage and energy levels in zinc-phthalocyanine: C₆₀ bulk heterojunction solar cells with varied mixing ratio. *Physical Review B*, 88(8), 2013, p. 085119. doi:10.1103/PhysRevB.88.085119
- [133] K. Vandewal, Z. Ma, J. Bergqvist, Z. Tang, E. Wang, P. Henriksson, K. Tvingstedt, M. R. Andersson, F. Zhang, O. Inganäs. Quantification of Quantum Efficiency and Energy Losses in Low Bandgap Polymer: Fullerene Solar Cells with High Open-Circuit Voltage. *Advanced Functional Materials*, 22(16), 2012, pp. 3480–3490. doi:10.1002/adfm.201200608
- [134] F. Holz Müller, N. Gräßler, M. Sedighi, E. Müller, M. Knupfer, O. Zeika, K. Vandewal, C. Koerner, K. Leo. H-aggregated small molecular nanowires as near infrared absorbers for organic solar cells. *Organic Electronics*, 45, 2017, pp. 198–202. doi:10.1016/j.orgel.2017.03.009
- [135] M. A. Green, K. Emery, Y. Hishikawa, W. Warta, E. D. Dunlop. Solar cell efficiency tables (Version 45). *Progress in photovoltaics: research and applications*, 23(1), 2015, pp. 1–9. doi:10.1002/pip.2573
- [136] M. Riede, T. Mueller, W. Tress, R. Schueppel, K. Leo. Small-molecule solar cells—status and perspectives. *Nanotechnology*, 19(42), 2008, p. 424001. doi:10.1088/0957-4484/19/42/424001

- [137] H.-S. Shim, H. J. Kim, J. W. Kim, S.-Y. Kim, W.-I. Jeong, T.-M. Kim, J.-J. Kim. Enhancement of near-infrared absorption with high fill factor in lead phthalocyanine-based organic solar cells. *Journal of Materials Chemistry*, 22(18), 2012, pp. 9077–9081. doi:10.1039/C2JM30417A
- [138] R. F. Bailey-Salzman, B. P. Rand, S. R. Forrest. Near-infrared sensitive small molecule organic photovoltaic cells based on chloroaluminum phthalocyanine. *Applied Physics Letters*, 91(1), 2007, p. 3508. doi:10.1063/1.2752992
- [139] F. Yang, R. R. Lunt, S. R. Forrest. Simultaneous heterojunction organic solar cells with broad spectral sensitivity. *Applied Physics Letters*, 92(5), 2008, p. 053310. doi:10.1063/1.2839408
- [140] S. Y. Leblebici, L. Catane, D. E. Barclay, T. Olson, T. L. Chen, B. Ma. Near-infrared azadipyromethenes as electron donor for efficient planar heterojunction organic solar cells. *ACS applied materials & interfaces*, 3(11), 2011, pp. 4469–4474. doi:10.1021/am201157d
- [141] Q. Song, Y. Jiao, Z. Wang, X. Zhang. Tuning the Energy Gap by Supramolecular Approaches: Towards Near-Infrared Organic Assemblies and Materials. *Small*, 12(1), 2016, pp. 24–31. doi:10.1002/smll.201501661
- [142] F. Meng, K. Chen, H. Tian, L. Zuppiroli, F. Nuesch. Cyanine dye acting both as donor and acceptor in heterojunction photovoltaic devices. *Applied Physics Letters*, 82(21), 2003, pp. 3788–3790. doi:10.1063/1.1579133
- [143] M. Hiramoto, K. Kitada, K. Iketaki, T. Kaji. Near infrared light driven organic pin solar cells incorporating phthalocyanine J-aggregate. *Applied Physics Letters*, 98(2), 2011, p. 023302. doi:10.1063/1.3534804
- [144] K. Yokoyama, T. Kaji, M. Hiramoto. Double co-deposited layered organic photovoltaic cells with sensitivity from visible to near-infrared regions. *Japanese Journal of Applied Physics*, 52(4S), 2013, p. 04CR06. doi:10.7567/JJAP.52.04CR06
- [145] K. C. Deing, U. Mayerhöffer, F. Würthner, K. Meerholz. Aggregation-dependent photovoltaic properties of squaraine/P₆₁BM bulk heterojunctions. *Physical Chemistry Chemical Physics*, 14(23), 2012, pp. 8328–8334. doi:10.1039/c2cp40789b
- [146] G. Chen, H. Sasabe, W. Lu, X.-F. Wang, J. Kido, Z. Hong, Y. Yang. J-aggregation of a squaraine dye and its application in organic photovoltaic cells. *Journal of Materials Chemistry C*, 1(40), 2013, pp. 6547–6552. doi:10.1039/c3tc31243g
- [147] S. Brück, C. Krause, R. Turrisi, L. Beverina, S. Wilken, W. Saak, A. Lützen, H. Borchert, M. Schiek, J. Parisi. Structure–property relationship of anilino-squaraines in organic solar cells. *Physical Chemistry Chemical Physics*, 16(3), 2014, pp. 1067–1077. doi:10.1039/c3cp54163k

Bibliography

- [148] Y. Guo, L. Xu, H. Liu, Y. Li, C.-M. Che, Y. Li. Self-Assembly of Functional Molecules into 1D Crystalline Nanostructures. *Advanced Materials*, 27(6), 2015, pp. 985–1013. doi:10.1002/adma.201403846
- [149] H.-B. Fu, J.-N. Yao. Size effects on the optical properties of organic nanoparticles. *Journal of the American Chemical Society*, 123(7), 2001, pp. 1434–1439. doi:10.1021/ja0026298
- [150] Y. S. Zhao, D. Xiao, W. Yang, A. Peng, J. Yao. 2, 4, 5-triphenylimidazole nanowires with fluorescence narrowing spectra prepared through the adsorbent-assisted physical vapor deposition method. *Chemistry of materials*, 18(9), 2006, pp. 2302–2306. doi:10.1021/cm060102+
- [151] S. Inoue, S. Mikami, Y. Aso, T. Otsubo, T. Wada, H. Sasabe. Donor-acceptor-substituted heteroquinoid chromophores as novel nonlinear optics. *Synthetic Metals*, 84(1), 1997, pp. 395–396. doi:10.1016/S0379-6779(97)80799-0
- [152] R. Gompper, H.-U. Wagner, E. Kutter. Ketenderivate, XIII. Stabile p-Chinodimethane, I: Synthesen und Eigenschaften. *Chemische Berichte*, 101(12), 1968, pp. 4123–4143. doi:10.1002/cber.19681011212
- [153] S. Inoue, S. Mikami, K. Takimiya, T. Otsuho, Y. Aso. Syntheses, structures, and spectroscopic properties of push-pull heteroquinoid compounds. *Heterocycles*, 71(2), 2007, pp. 253–268. doi:10.3987/COM-06-10848
- [154] A. D. Becke. Density-functional exchange-energy approximation with correct asymptotic behavior. *Physical Review A*, 38, 1988, pp. 3098–3100. doi:10.1103/PhysRevA.38.3098
- [155] C. Lee, W. Yang, R. G. Parr. Development of the Colle-Salvetti correlation-energy formula into a functional of the electron density. *Physical Review B*, 37, 1988, pp. 785–789. doi:10.1103/PhysRevB.37.785
- [156] W. Liptay. Electrochromism and solvatochromism. *Angewandte Chemie International Edition in English*, 8(3), 1969, pp. 177–188. doi:10.1002/anie.196901771
- [157] A. Garitagoitia Cid, M. Sedighi, M. Löffler, W. F. van Dorp, E. Zschech. Energy-Filtered Backscattered Imaging Using Low-Voltage Scanning Electron Microscopy: Characterizing Blends of ZnPc-C₆₀ for Organic Solar Cells. *Advanced Engineering Materials*, 18(6), 2016, pp. 913–917. doi:10.1002/adem.201600063
- [158] Y. Li, T. Liu, H. Liu, M.-Z. Tian, Y. Li. Self-assembly of intramolecular charge-transfer compounds into functional molecular systems. *Accounts of chemical research*, 47(4), 2014, pp. 1186–1198. doi:10.1021/ar400264e
- [159] S.-o. Kim, T. K. An, J. Chen, I. Kang, S. H. Kang, D. S. Chung, C. E. Park, Y.-H. Kim, S.-K. Kwon. H-Aggregation Strategy in the Design of Molecular Semiconductors for Highly Reliable Organic Thin Film Transistors. *Advanced Functional Materials*, 21(9), 2011, pp. 1616–1623. doi:10.1002/adfm.201002367

- [160] L. Dou, Y. Liu, Z. Hong, G. Li, Y. Yang. Low-bandgap near-IR conjugated polymers/molecules for organic electronics. *Chemical reviews*, 115(23), 2015, pp. 12633–12665. doi:10.1021/acs.chemrev.5b00165
- [161] A. Zitzler-Kunkel, M. R. Lenze, N. M. Kronenberg, A.-M. Krause, M. Stolte, K. Meerholz, F. Würthner. NIR-Absorbing Merocyanine Dyes for BHJ Solar Cells. *Chemistry of Materials*, 26(16), 2014, pp. 4856–4866. doi:10.1021/cm502302s
- [162] B. Ray, M. A. Alam. A compact physical model for morphology induced intrinsic degradation of organic bulk heterojunction solar cell. *Applied Physics Letters*, 99(3), 2011, p. 033303. doi:10.1063/1.3610460
- [163] Y. S. Zhao, H. Fu, A. Peng, Y. Ma, D. Xiao, J. Yao. Low-Dimensional Nanomaterials Based on Small Organic Molecules: Preparation and Optoelectronic Properties. *Advanced Materials*, 20(15), 2008, pp. 2859–2876. doi:10.1002/adma.200800604
- [164] J.-J. Chiu, C.-C. Kei, T.-P. Perng, W.-S. Wang. Organic semiconductor nanowires for field emission. *Advanced Materials*, 15(16), 2003, pp. 1361–1364. doi:10.1002/adma.200304918
- [165] F. Holzmueller, L. Wilde, F. Wölzl, C. Koerner, K. Vandewal, K. Leo. Co-evaporant induced crystallization of zinc phthalocyanine: C₆₀ blends for solar cells. *Organic Electronics*, 27, 2015, pp. 133–136. doi:10.1016/j.orgel.2015.08.031
- [166] T. Kaji, M. Zhang, S. Nakao, K. Iketaki, K. Yokoyama, C. W. Tang, M. Hiramoto. Co-evaporant Induced Crystalline Donor: Acceptor Blends in Organic Solar Cells. *Advanced Materials*, 23(29), 2011, pp. 3320–3325. doi:10.1002/adma.201101305
- [167] C. Schünemann, D. Wynands, L. Wilde, M. P. Hein, S. Pfützner, C. Elschner, K.-J. Eichhorn, K. Leo, M. Riede. Phase separation analysis of bulk heterojunctions in small-molecule organic solar cells using zinc-phthalocyanine and C₆₀. *Physical Review B*, 85, 2012, p. 245314. doi:10.1103/PhysRevB.85.245314
- [168] J. Peet, J. Y. Kim, N. E. Coates, W. L. Ma, D. Moses, A. J. Heeger, G. C. Bazan. Efficiency enhancement in low-bandgap polymer solar cells by processing with alkane dithiols. *Nature Materials*, 6(7), 2007, pp. 497–500. doi:10.1038/nmat1928
- [169] C. Li, Y. Chen, Y. Zhao, H. Wang, W. Zhang, Y. Li, X. Yang, C. Ma, L. Chen, X. Zhu, Y. Tu. Acceptor-donor-acceptor-based small molecules with varied crystallinity: processing additive-induced nanofibril in blend film for photovoltaic applications. *Nanoscale*, 5(20), 2013, pp. 9536–9540. doi:10.1039/C3NR03048B
- [170] J. A. Love, C. M. Proctor, J. Liu, C. J. Takacs, A. Sharenko, T. S. van der Poll, A. J. Heeger, G. C. Bazan, T.-Q. Nguyen. Film Morphology of High Efficiency Solution-Processed Small-Molecule Solar Cells. *Advanced Functional Materials*, 23(40), 2013, pp. 5019–5026. doi:10.1002/adfm.201300099

Bibliography

- [171] K. R. Graham, J. Mei, R. Stalder, J. W. Shim, H. Cheun, F. Steffy, F. So, B. Kippelen, J. R. Reynolds. Polydimethylsiloxane as a macromolecular additive for enhanced performance of molecular bulk heterojunction organic solar cells. *ACS applied materials & interfaces*, 3(4), 2011, pp. 1210–1215. doi:10.1021/am2000328
- [172] K. R. Graham, P. M. Wieruszewski, R. Stalder, M. J. Hartel, J. Mei, F. So, J. R. Reynolds. Improved Performance of Molecular Bulk-Heterojunction Photovoltaic Cells through Predictable Selection of Solvent Additives. *Advanced Functional Materials*, 22(22), 2012, pp. 4801–4813. doi:10.1002/adfm.201102456
- [173] S. Pfuetzner, C. Mickel, J. Jankowski, M. Hein, J. Meiss, C. Schuenemann, C. Elschner, A. A. Levin, B. Rellinghaus, K. Leo, M. Riede. The influence of substrate heating on morphology and layer growth in C₆₀:ZnPc bulk heterojunction solar cells. *Organic Electronics*, 12(3), 2011, pp. 435–441. doi:10.1016/j.orgel.2010.12.007
- [174] V. Zardetto, T. M. Brown, A. Reale, A. Di Carlo. Substrates for flexible electronics: A practical investigation on the electrical, film flexibility, optical, temperature, and solvent resistance properties. *Journal of Polymer Science Part B: Polymer Physics*, 49(9), 2011, pp. 638–648. doi:10.1002/polb.22227
- [175] T. Kaji, S. Nakao, M. Hiramoto. Effect of Co-evaporant Induced Crystallization on Needle Growth of Phthalocyanine Thin Films. *Molecular Crystals and Liquid Crystals*, 578(1), 2013, pp. 63–67. doi:10.1080/15421406.2013.804376
- [176] A. Ballistreri, D. Garozzo, G. Montaudo. Mass spectral characterization and thermal decomposition mechanism of poly(dimethylsiloxane). *Macromolecules*, 17(7), 1984, pp. 1312–1315. doi:10.1021/ma00137a003
- [177] T. Mönch, T. S. Sherkar, L. J. Anton Koster, P. Friederich, M. Riede, P. Formanek, C. Koerner, K. Vandewal, W. Wenzel, K. Leo. Experimental and theoretical study of phase separation in ZnPc:C₆₀ blends. *Organic Electronics*, 27, 2015, pp. 183–191. doi:10.1016/j.orgel.2015.09.023
- [178] W. Tress, S. Pfuetzner, K. Leo, M. Riede. Open circuit voltage and IV curve shape of ZnPc:C₆₀ solar cells with varied mixing ratio and hole transport layer. *Journal of Photonics for Energy*, 1(1), 2011, p. 011114. doi:10.1117/1.3556726
- [179] A. Zawadzka, P. Płóciennik, I. Czarnecka, J. Sztupecka, Z. Łukasiak. The effects of annealing process influence on optical properties and the molecular orientation of selected organometallic compounds thin films. *Optical Materials*, 34(10), 2012, pp. 1686 – 1691. doi:10.1016/j.optmat.2012.02.035
- [180] B. Maennig, M. Pfeiffer, A. Nollau, X. Zhou, K. Leo, P. Simon. Controlled *p*-type doping of polycrystalline and amorphous organic layers: Self-consistent description of conductivity and field-effect mobility by a microscopic percolation model. *Phys. Rev. B*, 64, 2001, p. 195208. doi:10.1103/PhysRevB.64.195208

- [181] F. Iwatsu, T. Kobayashi, N. Uyeda. Solvent effects on crystal growth and transformation of zinc phthalocyanine. *The Journal of Physical Chemistry*, 84(24), 1980, pp. 3223–3230. doi:10.1021/j100461a018
- [182] T. Moench, P. Friederich, F. Holzmueller, B. Rutkowski, J. Benduhn, T. Strunk, C. Koenner, K. Vandewal, A. Czyrska-Filemonowicz, W. Wenzel, K. Leo. Influence of Meso and Nanoscale Structure on the Properties of Highly Efficient Small Molecule Solar Cells. *Advanced Energy Materials*, 6(4), 2016, p. 1501280. doi:10.1002/aenm.201501280
- [183] M. Hirade, T. Yasuda, C. Adachi. Effects of intramolecular donor–acceptor interactions on bimolecular recombination in small-molecule organic photovoltaic cells. *The Journal of Physical Chemistry C*, 117(10), 2013, pp. 4986–4991. doi:10.1021/jp400386q

C. Acknowledgements

Abschließend möchte ich denjenigen danken ohne deren Unterstützung diese Arbeit nicht möglich gewesen wäre. Vielen Dank an Prof. Leo für die Gelegenheit meine Dissertation am IAPP unter hervorragenden Bedingungen schreiben zu können und die Unterstützung während der Anfertigung der Arbeit. Ich danke Prof. Deibel, der sich bereit erklärt hat, das Zweitgutachten zu übernehmen und für seine freundliche Einladung in das OPKM Seminar nach Chemnitz. Ein besonderer Dank gilt Dr. Christian Körner, welcher als OSOL-Gruppenleiter die Arbeit mitbetreut hat und von dem ich viel über die Charakterisierung von Solarzellen und Materialien gelernt habe. Vielen Dank auch an Dr. Moritz Riede und Prof. Koen Vandewal für ihre Hinweise und Ratschläge am Anfang bzw. gegen Ende der Promotion. Für die Finanzierung dieser Arbeit danke ich weiterhin dem BMBF im Rahmen der Programme MEDOS und Innoprofile 2.2 sowie der Graduiertenakademie der TU Dresden.

Vielen Dank an Sven Kunze und Andreas Büst für die Instandhaltung der Geräte, insbesondere des launenhaften UFO1, die Reinigung der Substrate und technischen Support jeder Art. Ich danke dem Lesker Team: Tobias Günther, Andreas Wendel und Caroline Walde für die Prozessierung der Leskerruns sowie die zeitnahe Verkapselung der UFO- und MTC-Proben (auch noch in den Abendstunden). Vielen Dank an Johanna Katzschner, Eva Schmidt, Jutta Hunger, Julia Barth, Dr. Annette Polte, Dr. Angelika Wolf, Dr. Christian Zschalig, Carla Schmidt und Dr. Hartmut Fröb für jegliche Unterstützung im Umgang mit Formularen, Anträgen und sonstiger Bürokratie. Weiterhin danke ich Kai Schmidt und Peter Leumer für ihre Hilfe rund um die IT.

Vielen Dank an die anderen Piloten des UFO1 insbesondere Dr. Max Tietze und Martin Schwarze für unterhaltsame Stunden im Labor. Da es ohne neue Materialien nichts zu charakterisieren gäbe, gilt mein Dank den Personen, die die Materialien herstellen und aufreinigen: Dr. Olaf Zeika, Nico Gräßler, Lijia Fang und Annette Petrich. Vielen Dank auch an Jacob König-Otto, Christoph Hauenstein und Daniel Schütze für die Hilfe bei der Herstellung und Untersuchung von Proben.

Da Materialcharakterisierung sich zu einem Zehnkampf entwickeln kann und sich viele Feinheiten/Tücken in den Spezialdisziplinen nur mit viel Erfahrung erkennen lassen, gilt mein Dank jenen Spezialisten, die mich mit Einweisungen, Messungen und Diskussionen unterstützt haben: Insbesondere Natalia Sergeeva für die Einweisung in diverse Messmethoden rund ums Impedanzspektrometer, Sascha Ullbrich für zeitabhängige Messungen (zusammen mit André Nascimento), die Fertigstellung des OSOLMage, Tipps zu Podcasts und die Einrichtung des Burger-Newsletters, Toni Meyer für die Instandhaltung des IV- und EQE-Roboters, den Mismatch calculator und Diskussionen über OP, Jens Jankowski für OFET Messungen, Marco Höppner für seinen Vortrag über Nanowires zur richtigen Zeit, Dr. Florian Wölzl und Dr. Norwid Rasmus Behrnd für die Durchführung von und Diskussion über LDI-ToF-MS, Martin Schwarze und Dr. Max Tietze für UPS Messungen, Ludwig Bormann

C. Acknowledgements

für seine Ratschläge zum neuen Shimadzu, Felix Lemke für einen Nachmittag am Spektrometer, Till Jägeler-Hoheisel für Hinweise im Umgang mit den Absorptionsmessungen am IV-Roboter, Johannes Benduhn für viele sEQE Messungen, Dr. Johannes Widmer für temperaturabhängige IV-Messungen (zusammen mit Anton Kirch) und ausführliche Diskussion von "OSOL1247 Sx5 0x5", Frederik Nehm für Alterungsmessungen; Dr. Reinhard Scholz für DFT-Rechnungen, Dr. Chris Elschner für Diskussionen rund um die Morphologie; Andreas Hofacker für seine Hinweise zu Ladungstransport und Zustandsdichte; Dr. Stefan Kraner für etliche Diskussionen über die relative Permittivität und Dr. Tobias Mönch für Diskussionen und Ratschläge auch abseits von Morphologie und AFM. Further, I would like to thank Yoonseok Park for conversations during the day, introducing me into Korean culture, taking care of the plants in the office, and being a great office mate in general; Vasilis Nicolis for a great time in Thessaloniki; Dr. Kyung-Geun Lim for the introduction into spin coating and Dr. Donato Spoltore for discussions and cooking tasty Italian food. Mein Dank gilt weiterhin den Leuten, die meine Arbeit mit Messungen außerhalb des Instituts unterstützt haben: Dr. Alben Lederer, Dr. Karin Sahre und Eileen Schierz für Massenspektrometriemessungen, Mona Sedighi für SEM und TEM Messungen, Prof. Martin Knupfer und Eric Müller für ED und EELS-Messungen, Dr. Carsten Hinrichs und Dr. Eva Bittrich für Ellipsometriemessungen, Dr. Scott Himmelberger für GIWAXS Messungen, Dr. Fortunato Piersimoni für Elektrolumineszenzmessungen sowie Dr. Lutz Wilde für unzählige GIXRD und XRR Messungen.

Vielen Dank für kritische Anmerkungen und das Korrekturlesen von mehr oder weniger Teilen der Dissertation an Prof. Leo, Christian, Koen, Tobias, Natalia, Andreas, Ludwig, Sascha, Norwid, Scott, Mona, Dr. Karin Sahre, Olaf, Nico, Martin und Franz.

Vielen Dank an alle derzeitigen und ehemaligen Büromitbewohner der Bey95 für die angenehme Arbeitsatmosphäre im Büro. Nach über sechs Jahren als 95er wage ich es nicht alle Namen einzeln aufzuzählen, da ich befürchte einige zu vergessen. Allerdings möchte ich Christian und Max für die Stiftung der Palmen danken, die das Büro erst richtig gemütlich gemacht haben. Vielen Dank auch an die Mitglieder der OSOL-Gruppe für das kritische Anhören meiner Vorträge im Rahmen von work presentations oder test talks sowie Ratschlägen im Sci-Coff. Weiterhin danke ich dem Team BS für viele kurzweilige Montagabende und der 11:35 bzw. 11:20 Essensgruppe für entspannte Mittagspausen.

Vielen Dank an alle Sportsfreunde des JuJutsu Uni-Sports der TU Dresden für den Ausgleich nach der Arbeit.

Abschließend danke ich meinen Freunden und meiner Familie und ganz besonders meinen Eltern für die fortwährende Unterstützung.

Erklärung der Selbstständigkeit

Diese Dissertation wurde am Dresden Integrated Center for Applied Physics and Photonic Materials / Institut für Angewandte Physik/Photophysik der Fakultät Mathematik und Naturwissenschaften an der Technischen Universität Dresden unter wissenschaftlicher Betreuung von Prof. Dr. Karl Leo angefertigt.

Hiermit versichere ich, dass ich die vorliegende Arbeit ohne unzulässige Hilfe Dritter und ohne Benutzung anderer als der angegebenen Hilfsmittel angefertigt habe. Die aus fremden Quellen direkt oder indirekt übernommenen Gedanken sind als solche gekennzeichnet. Diese Arbeit wurde bisher weder im Inland noch im Ausland in gleicher oder ähnlicher Form einer anderen Prüfungsbehörde vorgelegt.

Weiterhin versichere ich, dass weder ein früheres erfolgloses Promotionsverfahren stattgefunden hat noch ein weiteres Promotionsverfahren anhängig ist. Ich erkenne die Promotionsordnung der Fakultät Mathematik und Naturwissenschaften der Technischen Universität Dresden vom 23.03.2011 in der aktuellen Fassung mit den durch den Fakultätsrat beschlossenen Änderungen vom 15.06.2011 und 18.06.2014 an.

Felix Holzmüller